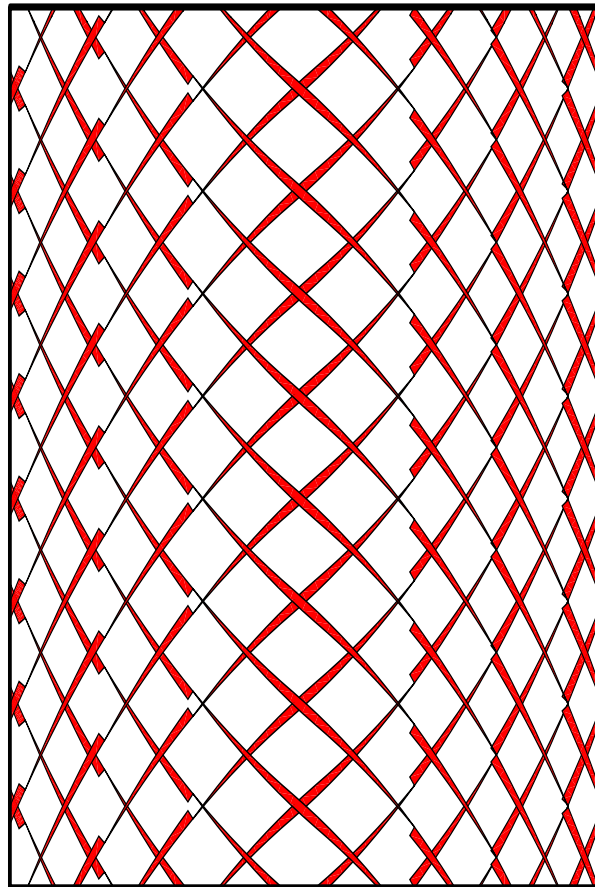


MASTER OF SCIENCE THESIS

A methodology to predict the stiffness properties and buckling load of manufacturable variable stiffness panels

Vibhas Mishra



Faculty of Aerospace Engineering · Delft University of Technology

A methodology to predict the stiffness properties and buckling load of manufacturable variable stiffness panels

MASTER OF SCIENCE THESIS

For obtaining the degree of Master of Science in Aerospace Engineering
at Delft University of Technology

Vibhas Mishra

29 May 2017



Copyright © Vibhas Mishra
All rights reserved.



DELFT UNIVERSITY OF TECHNOLOGY
FACULTY OF AEROSPACE ENGINEERING
DEPARTMENT OF AEROSPACE STRUCTURES AND MATERIALS

GRADUATION COMMITTEE

Dated: 29 May 2017

Chair holder:

Prof. Dr. Chiara Bisagni

Committee members:

Prof. Dr. Chiara Bisagni

Dr. Boyang Chen

Dr. Calvin Rans

Dr. Daniël Peeters

Abstract

Automated fibre placement technology has made possible to place bands of composite fibre tows along curvilinear path to create laminates with spatially varying stiffness properties called variable stiffness panels. These panels have shown improvement in stiffness properties, buckling load and post buckling failure load, over conventional straight fibre laminates. However, automated fibre placement machines can allow a minimum radius of curvature for fibre steering. Due to this, bands of fibre tows with same orientations are placed next to each other to produce a panel. This placement strategy gives rise to mismatch between the two bands and leads to fibre angular distortion. It can also lead to thickness build up but, to maintain the constant thickness of the panel, fibre tows are cut perpendicular to the placement direction which give rise to the defects called tow drop defects. Tow drop defects are the resin rich areas. In recent years, optimization of the variable stiffness panels for different load cases have been studied. These studies do not account for tow drop defects during optimization. To take account of these defects on the properties of the variable stiffness panels certain finite element approaches were proposed. For applying these approaches, location and geometry of the tow drop defects need to be identified in the variable stiffness panels. Based on it, property assignment to the mesh elements were done. However, the location and geometry of tow drops are dependent on fibre angle, width of the fibre tows and number of fibre tows in a band and can vary for different configuration of variable stiffness panel. It involves excessive computational effort to determine the location and geometry of the tow drop defects in the panels and analyze it. This makes it difficult to integrate the finite element approaches to optimization study. Thus, there is a need to develop a methodology which could make this integration possible.

This research focuses on developing a methodology which could take account of the effect of tow drop defects on the properties of different variable stiffness panels without knowing the location and geometry of the tow drop defects in the panels. The estimation of the tow drop defects will be done through fibre angle gradient present in the panels. The effect of tow drop defects will be estimated on the stiffness properties and buckling load of the different variable stiffness panels.

To achieve this goal three major steps were performed. Firstly, a material model was developed which was dependent upon the variables on which the geometries of the tow drop defects were

dependent. To generate a material model a straight fibre ply with no defect was assumed as baseline ply. Then, the straight fibre ply with tow drop defects embedded in it was considered and it was analyzed through periodic homogenization approach. Homogeneous elastic properties of the ply with defect was evaluated. The change in the elastic properties of the ply with defect and baseline ply was evaluated. It was termed as knock-down factors. A correlation between the knock-down factors and the geometrical parameters was developed. Through which the material properties of ply with any defect configuration can be evaluated. Secondly, a complete variable stiffness panel model was developed and analysis was carried out by the existing finite element approach called defect layer method. In defect layer method, the mesh elements were generated on the geometry of the panel and for each element, volume fraction of the resin inside an element was evaluated. Based on it, properties were assigned to an element. For this approach, the location and geometry of the tow drop defects in the variable stiffness panels need to be evaluated. Uniform end shortening analysis were performed on the panel. Effective elastic modulus and buckling load of the panels with different configuration were evaluated from the analysis. These results were taken as reference results to compare it to the predicted results. Lastly, finite element analysis of the variable stiffness panels with developed methodology was done. For the analysis, estimation of the geometrical parameters of tow drop defect in the variable stiffness panels was made through fibre angle gradient. Based on it, properties were assigned to the mesh elements through material model developed in first stage of the thesis. From the finite element analysis, effective elastic modulus and buckling load of the various variable stiffness panel was evaluated and compared it to the reference results generated in second stage of the thesis.

It was found that the knock-down factors were dependent upon the fibre angular distortion and volume fraction of the tow drop defects. The maximum error observed in the developed correlation was 10% . The results generated from defect layer method were compared to the results reported in the literature to verify the developed model. The comparison showed that the results were comparable and model can be used to generate results for other configurations. Lastly, for all the configurations studied, the elastic modulus evaluated through the developed methodology were under predicted, than the results obtained from defect layer method. Thus, elastic modulus were predicted on the conservative side. However, the buckling load evaluated from the developed methodology were over predicted than the defect layer method results. For all configurations studied in this research, minimum 50% of the effect of tow drop defect on buckling load of the variable stiffness panels was captured by the developed methodology. Also, it was shown that the estimation of the tow drop defects can be done through fibre angle gradients and no determination of the tow drop defect location and geometries is required. Moreover, the element used for the developed methodology was 8 times larger than the elements used in defect layer method. This made the process even less computational intensive.

Acknowledgments

I would like to thank and express my gratitude towards my supervisors Dr. Chiara Bisagni, Dr. Mostafa Abdalla and Dr. Daniël Peeters, for their valuable guidance during the course of this thesis.

Also, I would like to thank my fellow colleagues, my parents, my girlfriend, my brother and my friends for their love and support which made my journey as a master student memorable.

Delft, University of Technology
29 May 2017

Vibhas Mishra

“Today’s scientists have substituted mathematics for experiments, and they wander off through equation after equation, and eventually build a structure which has no relation to reality”

— *Nikola Tesla*

Table of Contents

Acknowledgments	ix
Glossary	xxiii
1 Introduction	1
2 Background	3
2.1 Automated Fibre Placement	3
2.1.1 Historic development of AFP	3
2.1.2 Process description	4
2.1.3 Advantages and disadvantages of AFP	4
2.2 Variable Stiffness Panel	5
2.2.1 Development of concept of VSP	5
2.2.2 Curvilinear path definition	6
2.2.3 Manufacturing and manufacturing constraints	8
2.2.4 Process induced defects	11
3 State of the Art	13
3.1 Analysis of Conventional Composite Laminate	13
3.1.1 Classical laminate theory	14
3.1.2 Analysis in <i>Abaqus</i>	16
3.2 Analysis of Variable Stiffness Panels	17
3.2.1 FE analysis of the ideal VSP	17
3.2.2 FE implementation of process induced defects in VSP model	18
3.3 Studies on VSPs and Process Induced Defects	20
3.3.1 Comparison of VSPs and straight fibre laminates	20
3.3.2 Studies on process induced defects in conventional laminates	22

3.3.3	Studies on process induced defects in VSP	24
3.4	Periodic Homogenization Approach	25
3.4.1	Homogenization	25
3.4.2	Methodology of periodic homogenization	27
3.4.3	Knock-down factors	30
3.4.4	Applicability of periodic homogenization	30
3.5	Motivation	32
4	Micro-Mechanical Modelling	33
4.1	Types of Cuts	33
4.2	Micro-mechanical Models of Cuts	35
4.2.1	Basic assumption and models	35
4.2.2	FE implementation	37
4.2.3	Knock-down factors	46
4.3	Results from Micro-Mechanical Models	47
4.3.1	Range of variables	47
4.3.2	Displacement plots	48
4.3.3	Homogeneous stiffness tensor	48
4.3.4	Comparison between pixelation and modified defect layer method	53
4.3.5	Calculations of knock-down factors	54
4.3.6	Knock-down factors for zipper cuts	59
4.3.7	Knock-down factors for single sided cuts	65
4.4	Correlation Development	67
4.4.1	Correlation for zipper cuts	69
4.4.2	Correlation for single sided cuts	72
4.4.3	Error calculations	73
5	Macro-Mechanical Modelling	75
5.1	Development of the Model	75
5.1.1	Single sided cuts	78
5.1.2	Zipper cuts	80
5.2	FE implementation	81
5.2.1	Mesh generation	81
5.2.2	Property assignment	81
5.2.3	Load cases and boundary conditions	82
5.2.4	Stiffness and buckling Load calculations	83
5.3	Results	84

6 Smearing Methodology	91
6.1 Methodology	91
6.1.1 Single sided cuts	91
6.1.2 Zipper Cuts	95
6.2 FE implementation	96
6.2.1 Mesh generation	96
6.2.2 Property assignment	97
6.2.3 Load cases	98
6.3 Results	100
6.3.1 Lamina results	100
6.3.2 Laminate results	113
6.4 Applicability of Smearing Methodology	119
7 Conclusions and Recommendations	121
7.1 Conclusions	121
7.2 Recommendations	123
References	124
References	125
A Appendix A	129
A.1 <i>.poly</i> file in <i>Triangle</i>	129
A.2 Python file for data extraction	130
A.3 Nodal forces and displacement plots	133
A.4 Interpolation function for single sided cuts	139
A.4.1 Interpolation function for Material 1	139
A.4.2 Interpolation function for Material 2	141
B Appendix B	145
B.1 Lamina results for zipper cuts	145

List of Figures

2.1	Different composite manufacturing processes	4
2.2	AFP systems representation	5
2.3	Definition of reference course	6
2.4	Representation of a ply of VSP	7
2.5	Parallel Method	8
2.6	Shifting Method	9
2.7	Strategies to produce a ply of VSP through shifting method	10
2.8	Intraply gap and overlap defect	11
2.9	Coverage parameter [1]	11
2.10	Other defects that can be generated by AFP [2]	12
3.1	Conventional Laminate	14
3.2	Ply coordinate system and global coordinate system	15
3.3	Section of the laminate	16
3.4	Schematic of a VSP laminate	17
3.5	A ply of VSP with tow drop defects and the mesh generated on it.	18
3.6	Micromechanical model and load cases to evaluate effective properties from micro-mechanical model	19
3.7	Element covering defect and composite area of single ply of VSP	20
3.8	Models for different defects proposed <i>Li et al</i> [3]	23
3.9	Effect of tow drop and overlap on the ideal VSP design shown by <i>Nik et al.</i> [4]	25
3.10	Schematic representation of heterogeneous, equivalent homogeneous material and representative volume element	27
3.11	Representation of a RVE	28
3.12	Specimen studied and result presented by <i>Suquet</i> [5]	31
4.1	Tow drop defects generated due to single sided cuts	34

4.2	Different types of tow drop strategy studied in this thesis and different type defects generated	34
4.3	Infinite models of different cuts	35
4.4	RVE for single sided cuts	36
4.5	RVE for zipper cuts	37
4.6	Ideal RVE selected for different cuts	38
4.7	Node generation on the RVE of Zipper cuts	38
4.8	Sample Meshes	39
4.9	Regions in the zipper cut RVE	40
4.10	An element covering three regions of the zipper cut RVE	41
4.11	Implementation of periodic boundary condition in <i>Abaqus</i>	43
4.12	Body subjected to the displacement	44
4.13	Baseline Ply	46
4.14	Displacement plots for Loadcase 1, 2 and 3. Displacements are in millimeters	49
4.15	Displacement plots for Loadcase 4, 5 and 6. Displacements are in millimeters	50
4.16	Dimensions of zipper cut RVE selected to calculate the homogeneous stiffness tensor.	51
4.17	Loadcase 1	52
4.18	Convergence Study: Comparison between pixelation and modified defect layer method.	54
4.19	Chosen RVE of zipper cut: RVE1	55
4.20	Chosen RVE of single sided cut: RVE2	57
4.21	Knock-down factors from ideal RVEs of zipper cuts for Material 1	61
4.22	Knock-down factors from RVEs of zipper cuts with defects for Material 1	62
4.23	Knock-down factors from ideal RVEs of zipper cuts for Material 2	63
4.24	Knock-down factors from RVE of zipper cuts with defects for Material 2	64
4.25	Knock-down factors from ideal RVEs of single sided cuts	66
4.26	Knock-down factors from RVEs of single sided cuts with defects for Material 1	67
5.1	Representation of a VSP ply	77
5.2	Two course which are placed on the plate with shifting method (Blue lines - shifted course, Black lines - reference course)	78
5.3	Numbering of tow edges of reference course	79
5.4	Intersecting courses and tow dropping	80
5.5	The defect generated in the ply with single sided cut strategy.	81
5.6	The defect generated in a ply with zipper cut strategy.	82
5.7	Dimensions of panel	83
5.8	Fibre angle of reference curve compared between the ply $(46 -1.57)$ and equivalent studied ply $< 46 60 >$	87
5.9	Comparison between tow drop area between the reported and equivalent ply	89
6.1	The schematic representation of single sided cuts	92

6.2	RVE for single sided cuts	93
6.3	Intersection of two courses of equal course width	94
6.4	The schematic representation of zipper cuts	95
6.5	Intersection of two courses of equal course width	96
6.6	An element of the finite element mesh	97
6.7	Dimensions of the panel	98
6.8	Effective modulus of straight fibre panels with configuration $[\pm\theta_0]_{4s}$ in y' direction as a function of θ_0	101
6.9	Single Sided Cuts (Material 1): Results of normalized elastic modulus (E_y/E_0) and volume fraction of tow drop defect (v_f) obtained from the modified defect layer method and smearing methodology for plies with center angle $T_0 = 10^\circ$ and $T_0=20^\circ$ and for various edge angle T_1	105
6.10	Single Sided Cuts (Material 1): Results of normalized elastic modulus (E_y/E_0) and volume fraction of tow drop defect (v_f) obtained from the modified defect layer method and smearing methodology for plies with center angle $T_0 = 30^\circ$ and $T_0=40^\circ$ and for various edge angle T_1	106
6.11	Single Sided Cuts (Material 1): Results of normalized elastic modulus (E_y/E_0) and volume fraction of tow drop defect (v_f) obtained from the modified defect layer method and smearing methodology for plies with center angle $T_0 = 50^\circ$ and $T_0=60^\circ$ and for various edge angle T_1	107
6.12	Single Sided Cuts (Material 1): Results of normalized elastic modulus (E_y/E_0) and volume fraction of tow drop defect (v_f) obtained from the modified defect layer method and smearing methodology for plies with center angle $T_0 = 70^\circ$ and $T_0=80^\circ$ and for various edge angle T_1	108
6.13	Single Sided Cuts (Material 2): Results of normalized elastic modulus (E_y/E_0) and volume fraction of tow drop defect (v_f) obtained from the modified defect layer method and smearing methodology for plies with center angle $T_0 = 10^\circ$ and $T_0=20^\circ$ and for various edge angle T_1	109
6.14	Single Sided Cuts (Material 2): Results of normalized elastic modulus (E_y/E_0) and volume fraction of tow drop defect (v_f) obtained from the modified defect layer method and smearing methodology for plies with center angle $T_0 = 30^\circ$ and $T_0=40^\circ$ and for various edge angle T_1	110
6.15	Single Sided Cuts (Material 2): Results of normalized elastic modulus (E_y/E_0) and volume fraction of tow drop defect (v_f) obtained from the modified defect layer method and smearing methodology for plies with center angle $T_0 = 50^\circ$ and $T_0=60^\circ$ and for various edge angle T_1	111
6.16	Single Sided Cuts (Material 2): Results of normalized elastic modulus (E_y/E_0) and volume fraction of tow drop defect (v_f) obtained from the modified defect layer method and smearing methodology for plies with center angle $T_0 = 70^\circ$ and $T_0=80^\circ$ and for various edge angle T_1	112
6.17	Steering effect on the elastic modulus and buckling load	115
6.18	Convergence study of smearing methodology	117
6.19	Element size comparison in smearing	118
6.20	Tow drop defects in different VSP plies	120
A.1	Components of <i>.poly</i> file	130

A.2	Loadcase 2	134
A.3	Loadcase 3	135
A.4	Loadcase 4	136
A.5	Loadcase 5	137
A.6	Loadcase 6	138
B.1	Zipper Cuts (Material 1): Results of normalized elastic modulus (E_y/E_0) and volume fraction of tow drop defect (v_f) obtained from the modified defect layer method and smearing methodology for plies with center angle $T_0 = 10^\circ$ and $T_0=20^\circ$ and for various edge angle T_1	146
B.2	Zipper Cuts (Material 1): Results of normalized elastic modulus (E_y/E_0) and volume fraction of tow drop defect (v_f) obtained from the modified defect layer method and smearing methodology for plies with center angle $T_0 = 30^\circ$ and $T_0=40^\circ$ and for various edge angle T_1	147
B.3	Zipper Cuts (Material 1): Results of normalized elastic modulus (E_y/E_0) and volume fraction of tow drop defect (v_f) obtained from the modified defect layer method and smearing methodology for plies with center angle $T_0 = 50^\circ$ and $T_0=60^\circ$ and for various edge angle T_1	148
B.4	Zipper Cuts (Material 1): Results of normalized elastic modulus (E_y/E_0) and volume fraction of tow drop defect (v_f) obtained from the modified defect layer method and smearing methodology for plies with center angle $T_0 = 70^\circ$ and $T_0=80^\circ$ and for various edge angle T_1	149
B.5	Zipper Cuts (Material 2): Results of normalized elastic modulus (E_y/E_0) and volume fraction of tow drop defect (v_f) obtained from the modified defect layer method and smearing methodology for plies with center angle $T_0 = 10^\circ$ and $T_0=20^\circ$ and for various edge angle T_1	150
B.6	Zipper Cuts (Material 2): Results of normalized elastic modulus (E_y/E_0) and volume fraction of tow drop defect (v_f) obtained from the modified defect layer method and smearing methodology for plies with center angle $T_0 = 30^\circ$ and $T_0=40^\circ$ and for various edge angle T_1	151
B.7	Zipper Cuts (Material 2): Results of normalized elastic modulus (E_y/E_0) and volume fraction of tow drop defect (v_f) obtained from the modified defect layer method and smearing methodology for plies with center angle $T_0 = 50^\circ$ and $T_0=60^\circ$ and for various edge angle T_1	152
B.8	Zipper Cuts (Material 2):Results of normalized elastic modulus (E_y/E_0) and volume fraction of tow drop defect (v_f) obtained from the modified defect layer method and smearing methodology for plies with center angle $T_0 = 70^\circ$ and $T_0=80^\circ$ and for various edge angle T_1	153

List of Tables

3.1	Laminates studied by <i>Fayazbakhsh et al</i> [6]	24
4.1	Material 1 Properties : Material system IM7/8552	39
4.2	Material 2 Properties : Material system G40-800/5276-1	40
4.3	Load cases to evaluate a homogeneous stiffness tensor	44
4.4	Range of variables	47
4.5	Chosen RVEs	48
5.1	Properties of AS4/977-3 Material System	84
5.2	Comparison between the stiffness results numerically (Num.) and experimentally (Exp.) calculated by <i>Wu et al</i> [7], and the numerical results generated from the analysis of the developed macro-mechanical model	85
5.3	Comparison of the buckling load results of ideal VSP reported by <i>Wu et al</i> [7], and the numerical results generated from the analysis of developed macro-mechanical model.	85
5.4	Laminates studied by <i>Fayazbakhsh et al</i> [6]	86
5.5	Material 2 Properties : Material System G40-800/5276-1	86
5.6	Configuration of Laminates studied in this thesis equivalent to the laminates studied by <i>Fayazbakhsh et al</i> [6]	86
5.7	Comparison between the normalized stiffness results of ideal VSP, reported by <i>Fayazbakhsh et al</i> [6] and results generated by analysis of the equivalent laminates	87
5.8	Comparison between the normalized stiffness results of tow drop VSP, reported by <i>Fayazbakhsh et al</i> [6] and results generated by analysis of the equivalent laminates. The equivalent laminates were generated from single sided and zipper cut strategy. Percentage difference from the respective ideal VSP is presented in bracket	88
5.9	Percentage volume fraction of defects, in the panels reported by <i>Fayazbakhsh et al</i> [6] and calculated for the equivalent panels generated by single sided and zipper cut strategy	88
5.10	Comparison between the normalized buckling load results of ideal VSP, reported by <i>Fayazbakhsh et al</i> [6] and results generated by analysis of the equivalent laminates	88

5.11 Comparison between the normalized buckling load results of tow drop VSP reported by <i>Fayazbakhsh et al</i> [6] and results generated by analysis of the equivalent laminates. The equivalent laminates were generated from single sided and zipper cut strategy. Percentage difference from the respective ideal VSP is presented in bracket	89
6.1 Material 1 Properties : Material system IM7/8552	99
6.2 Material 2 Properties : Material system G40-800/5276-1	99
6.3 Configuration of Laminates studied in this thesis equivalent to the laminates studied by <i>Fayazbakhsh et al</i> [6]	99
6.4 Configuration of Laminates studied in this thesis equivalent to the laminates studied by <i>Fayazbakhsh et al</i> [6]	113
6.5 Normalized elastic modulus results for tow drop VSP from modified defect layer method (DLM) and smearing methodology for Material 1. Percentage in bracket shows the percentage difference between the value and ideal case value.	113
6.6 Normalized buckling load results for tow drop VSP from modified defect layer approach (DLM) and smearing methodology for Material 1. Percentage in bracket shows the percentage difference between the value and ideal case value.	113
6.7 Normalized elastic modulus results for tow drop VSP from modified defect layer method (DLM) and smearing methodology for Material 2. Percentage in bracket shows the percentage difference between the value and ideal case value.	114
6.8 Normalized buckling load results for tow drop VSP from modified defect layer approach (DLM) and smearing methodology for Material 2. Percentage in bracket shows the percentage difference between the value and ideal case value.	114
6.9 Percentage volume fraction results for tow drop VSP from smearing methodology. 'Diff.' represents percentage difference between DLM and smearing results.	115
6.10 Results obtained by modified defect layer (DLM) and smearing method of optimum laminate reported by <i>Tatting et al</i> [8] for Material 1. Percentage in bracket shows the percentage difference between the value and ideal case value.	116
6.11 Results obtained by modified defect layer (DLM) and smearing method of optimum laminate reported by <i>Tatting et al</i> [8] for Material 2. Percentage in bracket shows the percentage difference between the value and ideal case value.	117

Glossary

List of Acronyms

AFP	Automated Fibre Placement
VSP	Variable Stiffness Panel
FE	Finite Element
CLT	Classical Laminate Theory
RVE	Representative Volume Element

List of Symbols

(x^*, y^*)	Point coordinates on reference curve
(x', y')	Point coordinates inside a course
θ'	Fibre Angle inside a course
θ^*	Fibre Angle on reference curve
ϕ	Angle between global coordinate axis and ply coordinate axis
r	Perpendicular distance from the reference course
κ	Curvature
T_0	Angle at the center of the plate
T_1	Angle at the edge of the plate
σ	Stress vector
ϵ	Strain vector
Q	Stiffness tensor
M	Transformation matrix
V	Volume of the RVE
n	Normal vector
Σ	Average stress vector
E	Average strain vector
Q_{hom}	Homogeneous stiffness tensor
Q_o	Baseline stiffness tensor

λ	Eigen value or knock-down factor
θ	Fibre angular distortion
t_w	Tow width
n_t	Number of tows in a course
w	Width of the RVE
w_c	Course width
U	Internal energy density
d_s	Shift distance
v_f	Volume fraction of resin

Chapter 1

Introduction

Manufacturing of composite material structures with complicated geometries has been a pertinent challenge in aerospace industry. With development of Automated Fibre Placement (AFP) technology, these challenges had been overcoming to a certain extent. An advantage provided by this technology is to place band of fibres on curved surfaces and along curvilinear path [9]. This advantage enabled many researchers to develop structures, like Variable Stiffness Panels (VSPs), with improved mechanical performance compared to conventional straight fibre laminates. *Tatting et al* [8] and *Lopes et al* [10] [11] studied VSPs and showed improvement in buckling load, first-ply failure load and post buckling load over traditional straight fibre laminates. However, the major concern raised were on the accountability of the process induced defects on mechanical properties of variable stiffness panels.

The process induced defects get generated due to the manufacturing constraints posed by AFP machine during production of fibre steered panels. The defects generated can be of many forms such as intraply overlaps and gaps, tow drops, or local fibre buckling. The geometry and size of the process induced defects are dependent upon various design and production variables. Some of the variables like fibre angle, tow width and course width can be controlled by the designers, however others, like material defects, are completely random. The defects generated in straight fibre laminates are due to random variables and can be avoided by best industrial practices. For the case of steered fibre, certain defects such as local fibre buckling can be avoided by maintaining the right radius of curvature, however, defects such as tow drops and overlaps, generates periodically and inevitably in the panels. Over the last two decades, researchers have explored, experimentally and numerically, the effect of different process induced defects on the properties of steered fibre laminates. *Sawicki et al* [12] studied experimentally the effect of intraply overlaps and gaps, on compressive strength of composite laminates with straight fibres. They reported maximum reduction of 27% in the compressive strength of the laminate. Furthermore, *Blom et al* [13] showed that the tow drop defects deteriorated the stiffness properties of the VSPs. Moreover, the vicinity of tow drop defects were the probable sites for the failure initiation. These studies clearly showed the effect of different process induced defects on the properties of the composite laminates.

In the recent years, studies were focused to optimize the steered panel designs. In one such

study, *Lopes et al* [11] have optimized ideal VSPs design for maximum buckling load. The optimization was done through Finite Element (FE) method. Thereafter, the optimized design was analyzed numerically to account for the defects. It suggests that the accountability of the defects were not taken during the optimization process. To analyze the VSPs with defects numerically, FE methodologies like pixelation and defect layer method were proposed by *Blom et al* [13] and *Fayazbakhsh et al* [6], respectively. Integration of these methodology with the optimization process could make the optimization process more versatile. Through this integration the optimization could be done with consideration of defects. The direct use of the pixelation and defect layer method for optimization is problematic as it involves a computational intensive step to identify the locations and geometry of the defects in the VSPs. Thus, there is a need to develop a method to predict the properties of VSPs, which takes account of the generated defects and is less computational intensive.

For the conventional laminate, to take account for defects like intraply gap and overlap, generated randomly, on laminate properties, *Li et al* [3] proposed a 3D modeling technique. This technique parameterized the geometry of defects like intraply gap and overlap into geometric parameters. By selecting these parameters, laminate with defects of any layup could be numerically modeled and analyzed. Taking motivation from this study, a micro-mechanical model of defects generated in a variable stiffness ply was developed. These models were parameterized into the design and production variables, on which the geometry of the defects were dependent. Furthermore, micro-mechanical models were studied by periodic homogenization approach. Through this analysis, homogeneous elastic properties were evaluated. Moreover, from these properties knock-down factors caused by the defects on the elastic properties of the ply were evaluated. The knock-down factors were further correlated to the design and production variables. These correlation were then used to predict mechanical properties of variable stiffness lamina and laminate through a developed FE methodology termed Smearing. The predicted results from smearing were then compared to the full panel analysis done by defect layer method.

This thesis is divided into six subsequent chapters. Chapter 2 gives overview of AFP systems, concept of VSPs and process induced defects. Chapter 3 gives the state of the art with focus on numerical methods, which have been used to analyze variable stiffness panels and process induced defects generated in it. Chapter 4 is on the development of micro-mechanical model of the defects in a single ply. And also covers evaluation of homogeneous property, knockdown factors and development of correlation. Chapter 5 covers the development of full VSP model. The model is termed as macro-mechanical model in this thesis. Chapter 6 introduces the smearing methodology and its applicability. Finally, chapter 7 gives the conclusion from the results obtained and recommendations for further research.

Chapter 2

Background

This chapter gives a brief overview on the Automated Fibre Placement (AFP) process which is discussed in Section 2.1. Furthermore, in Section 2.2 the concept of the Variable Stiffness Panels (VSPs) is discussed .

2.1 Automated Fibre Placement

2.1.1 Historic development of AFP

During the 1960s, the production of the composites were done through Manual Layup or Hand-Layup method. This process involves laying of the fibres on the mould by hand. For improvement in the productivity and reliability of the composite structure, automation in production process was realized. Onward 1970s, various automated processes like Filament Winding and Automated Tape Laying were developed. Filament winding machines were used to place fibres over rotating mandrels. The fibres used in the process were in the form of tows as shown in Figure 2.1a. The process was mainly used to produce cylindrical parts. Whereas, Automated Tape Layup process involved placement and compaction of the large tape on the surface of the mould through a robotic roller to produce composite structure as shown in Figure 2.1b. The Automated Tape layup machines can cut these tape to various lengths and the subsequent tapes can be placed next to each other in order to produce a ply. The typical tape width used in the process were 75mm, 150mm and 300mm. This was used to develop flat and curved geometries. Both processes, Filament winding and Automated Tape Layup, were used to produce high quality composite structure, with better reliability and lesser material wastage than Manual Layup method [9]. However, these processes were limited to produce parts with relatively simpler geometries like single curved surface, flat surface or cylindrical surfaces. Also, Filament Winding machines lacked fibre placement on the concave surfaces and Automated Tape Layup lacked high fibre steering capabilities. In order to overcome these limitations Automated Fibre Placement (AFP) systems were developed. The AFP systems were introduced in the 1980s. These systems were logical combination of the Filament

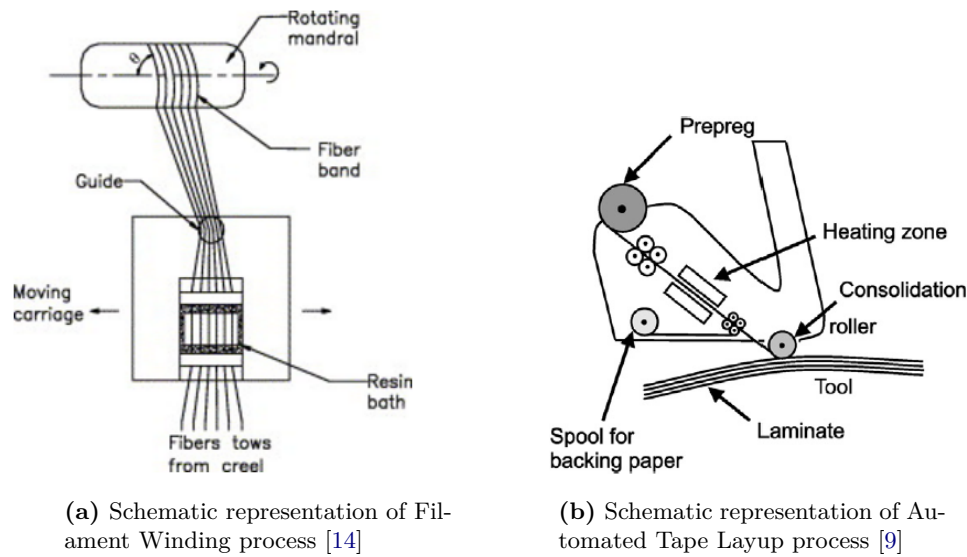


Figure 2.1: Different composite manufacturing processes

Winding and Automated Tape Layup process [9]. The capability to place individual fibres of Filament Winding and compaction and cut-restart operation of Automated Tape Layup were logically combined in AFP. Through this process the fibres can be placed along curvilinear path on complex geometries like doubly curved surface.

2.1.2 Process description

An AFP system delivers a band of fibres on the mould surface through a computer controlled roller. The band of the fibres is called course and the course consist of the smaller units called tow as shown in Figure 2.2a. These tows are delivered by a tow payout system. A typical tow width can be equal to 3.2 mm, 6.4 mm and 12.7 mm. The tow are then formed as courses. These courses are heated up and placed on the mould surface with the help of a compaction roller as shown in Figure 2.2b. The AFP systems have the capability of cut and restart individual tows. This means that a tow can be cut through a cutter if it is not required to be placed on the mould surface and if the tow is further required to be placed on the mould the tow feed can be restarted. This operation brings a flexibility to place variable course width on the mould surface, which was lacking in the Automated Tape Layup systems.

2.1.3 Advantages and disadvantages of AFP

The use of small tows and individual tow cut and restart capability of the AFP provides flexibility to place fibres on complex geometries. Furthermore, *Measom et al* [15] have shown that the complex part production from AFP can reduce material wastage from 62% to 6% and productivity can be increased 450% over the component made through Filament Winding and Manual Layup method. Moreover, similar results were reported by *Pasanen et al* [16], they showed cost reduction of 43% for AFP over Manual Layup. However, AFP machines have not

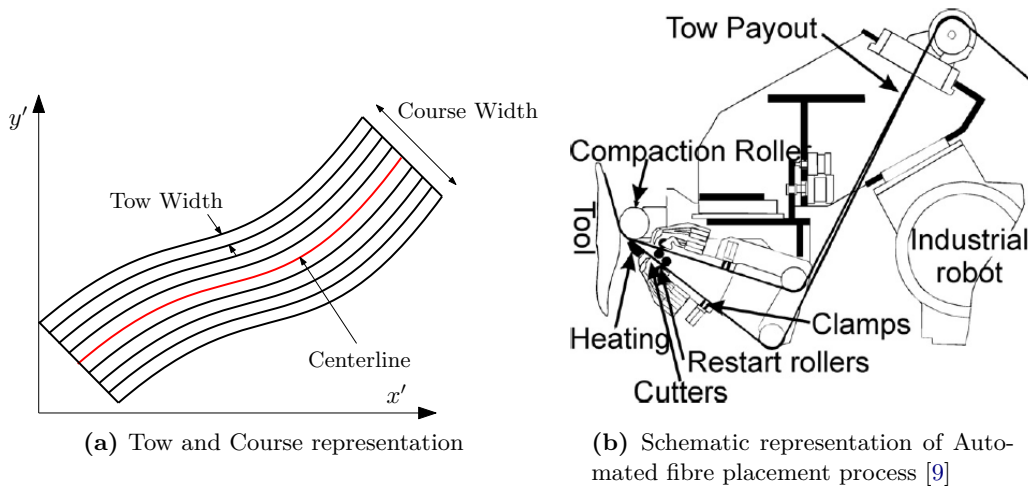


Figure 2.2: AFP systems representation

shown major increase in productivity compared to the Automated Tape Layup machines [9]. Also, the initial cost of the AFP systems are very high. The raised productivity and lesser material wastage are not good enough to break even the initial cost associated with the AFP systems in lesser time frame [9].

2.2 Variable Stiffness Panel

2.2.1 Development of concept of VSP

The structure with variable stiffness was build by *Yau et al* [17] without AFP machines. They inserted a metal pin in the woven fabric before curing and produced a laminate with open hole. The compressive strength property of the laminate was reported better than the laminate with drilled hole. The improvement of the properties was associated to the load path continuity and higher volume fraction of fibres around the hole. Furthermore, *Hyer et al* [18] studied the effect of fibre angle variation on the buckling properties of the laminates with the hole. The result showed improved buckling resistance due to the steering of the fibres around the hole. Following these study, researchers proposed different design of structure in which the fibres were made to follow the constant load or constant principal stress path in order to improve the performance of the laminate [19]. However, manufacturability of these structure remained a greater challenge. During this time period, in order to integrate the production technique available and standardize the design methodology of steered panels, *Gürdal et al* [20] proposed a definition of the curvilinear path along which the fibres can be placed and variable stiffness plies can be produced by AFP. The VSPs produced and tested based on the concept of *Gürdal et al* [20] have shown improved in-plane properties and buckling load over the conventional straight fibre laminates [7]. Thus, existing AFP technology enabled researchers to produce laminate with complicated shapes which have better performance than the conventional laminate. The following sub-sections will discuss the curvilinear path definition, manufacturability of the VSPs and process induced defects.

2.2.2 Curvilinear path definition

This section is dedicated to the definition of curvilinear path proposed by *Gürdal et al* [20] which can be traced by AFP machines. They defined a reference curve along which centerline of a course can be placed as shown in Figure 2.3a. A and B are the general point on the reference curve. The $x - y$ coordinate system is the global coordinate system and $x' - y'$ coordinate system is the ply coordinate system. ϕ is angle between the global and ply coordinate system. θ is the angle of the tangent at point B with respect x -axis of the global coordinate system. Similarly, θ' is the angle of the tangent at point B with respect to the x' -axis in the local coordinate system. (x^*, y^*) are the coordinate of a general point on the reference curve in global coordinate system. Keeping ϕ constant, the reference curve can be generated by varying θ' .

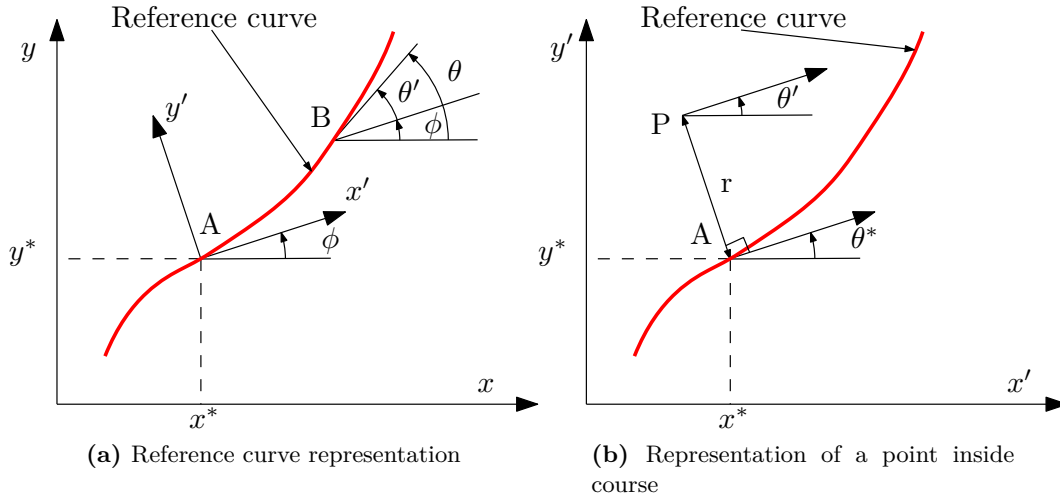


Figure 2.3: Definition of reference course

Now, reference curve only give the points of the centerline of the course. The course also have finite width. To generate the points in the course through the reference curve Figure 2.3b can be referred. In this figure, ϕ is assumed to be zero, thus, the ply coordinate system is the global coordinate system. Point P is the general point in the reference course. Point A is the point on reference curve. The normal drawn on the reference curve at point A passes through point P. The tangent at point A makes θ^* angle with the x' -axis. Fibre angle at point P is equal to θ' with respect to x' -axis. The coordinate of the point P and A are given by (x', y') and (x^*, y^*) . respectively. The coordinates and other parameters of the point P can be defined as in Eq. (2.1).

$$\begin{aligned}
 x' &= x^* - r \sin(\theta^*(x^*)) & \theta'(x', y') &= \theta^*(x^*) \\
 y' &= y^*(x^*) + r \cos(\theta^*(x^*)) & \kappa'(x', y') &= \kappa^*(x^*)/[1 - r\kappa^*(x^*)]
 \end{aligned} \tag{2.1}$$

Here, r represents the perpendicular distance of the point P from the reference curve and maximum value of r is equal to half of the course width. κ^* and κ' represents the curvature of reference curve at point A and curvature at point P respectively. The curvature is defined as

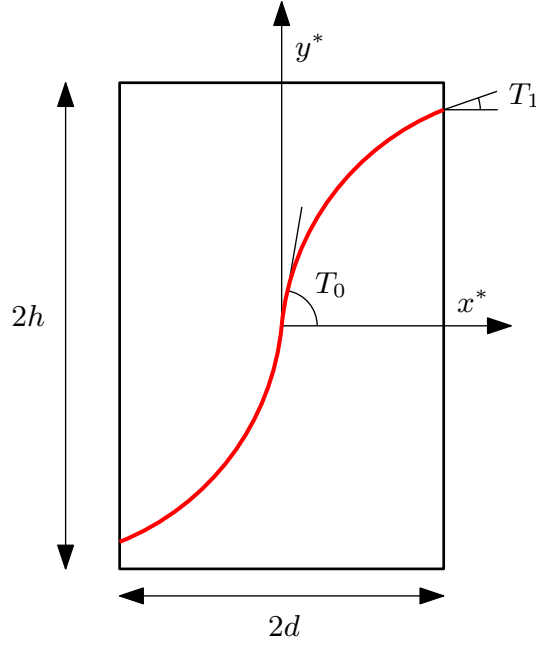


Figure 2.4: Representation of a ply of VSP

the inverse of the radius of curvature at a particular point. $y^*(x^*)$ and $\theta^*(x^*)$ are the single valued function which could be chosen by the designer.

Now, restricting the discussion to the reference curve, thus $r = 0$, it can be assumed that coordinates (x', y') are equivalent to (x^*, y^*) . The function which could define the reference curve are $\theta^*(x^*)$. *Gürdal et al* [20] assumed the linear fibre angle variation along x^* -axis. For a ply with dimensions as shown in Figure 2.4, the expression for linear fibre angle variation can be represented by Eq. (2.2).

$$\theta^*(x^*) = \begin{cases} T_0 + (T_1 - T_0)\left(\frac{x^*}{d} - k\right), & k: \text{even} \\ T_0 + (T_0 - T_1)\left(\frac{x^*}{d} - k\right), & k: \text{odd} \end{cases} \quad \text{where, } k = \text{floor}\left[\frac{x^*}{d}\right] \quad (2.2)$$

Here, T_0 and T_1 are the angle of the fibre at the center and edge ($x^* = d$) of a ply with respect to x^* . The corresponding $y^*(x^*)$ is represented in Eq. (2.3).

$$y^*(x^*) = \begin{cases} kS + \frac{d}{(T_0 - T_1)} \ln \left[\frac{\cos(\theta^*(x^*))}{\cos(T_0)} \right], & k: \text{even} \\ kS + \frac{d}{(T_1 - T_0)} \ln \left[\frac{\cos(\theta^*(x^*))}{\cos(T_1)} \right], & k: \text{odd} \end{cases} \quad \text{where, } S = \frac{d}{(T_0 - T_1)} \ln \left[\frac{\cos(T_0)}{\cos(T_1)} \right] \quad (2.3)$$

Thus, a course can be placed along this reference curve through AFP system. The center line of the course will meet the reference curve. This course is termed as reference course. The placement of the reference course can be repeated to generate the complete ply. The representation of the variable stiffness ply in the layup definition of the laminate is given by the notation $\langle T_0|T_1 \rangle$. Also, other definitions of the reference curve are available in the

literature. *Blom et al* [13] used constant curvature path for their theoretical model. The angle variation defined by them is given in Eq. (2.4). The representation of the variable stiffness ply with constant curvature reference curve is given by (T_0, κ^*) .

$$\sin(\theta^*) = \sin(T_0) + \kappa^* |x^*| \quad (2.4)$$

2.2.3 Manufacturing and manufacturing constraints

There are two methods to generate a single ply of VSP, one is the parallel method and other is the shifting method. In case of the parallel method the subsequent course is placed adjacent to the reference course and no gaps and overlaps are allowed between them, as shown in Figure 2.5a. This process is repeated to generate the entire ply. The advantage of this method is that there is no gap and overlap generation. However, this process changes the centerline of the every course from the reference curve as shown in Figure 2.5b. Thus, the radius of curvature of the fibres changes. Due to this, it becomes difficult to maintain the constraint suggested by *Nagendra et al* [21]. They suggested that the radius of curvature of the fibres should be minimum 635mm in order to prevent out of plane wrinkling of the fibre at the inner edge. The minimum radius of curvature requirement is dependent upon the AFP machines. It can vary from 400mm to 1000mm depending upon the material, rate at which material is laid and specification of the machine [22].

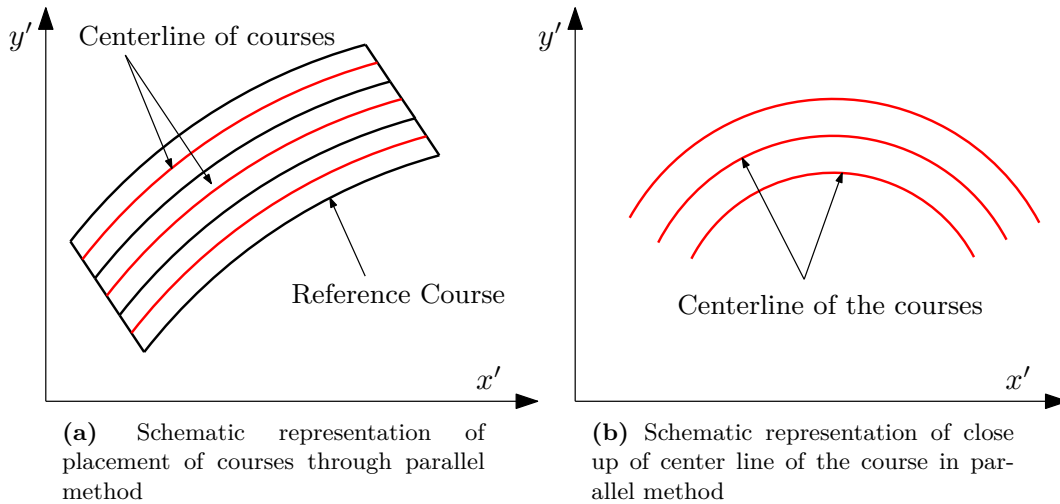


Figure 2.5: Parallel Method

In shifting method, reference curve is shifted in the direction perpendicular (y' in Figure 2.6a) to the axis along which the fibre angle is varying (x' in Figure 2.6a). The curvature of the courses does not change during the production, as shown in Figure 2.6b. Thus, it is easy to control the radius of curvature of the ply during production. Therefore, shifting method is preferred for production. However, the curve of one side of the course does not coincide with the curve of the subsequent course and form a mismatch, as shown in Figure 2.6a. These mismatches are unavoidable during the production and the type of defects generated due

to these mismatches are dependent upon the type of strategies chosen to produce a ply by shifting method.

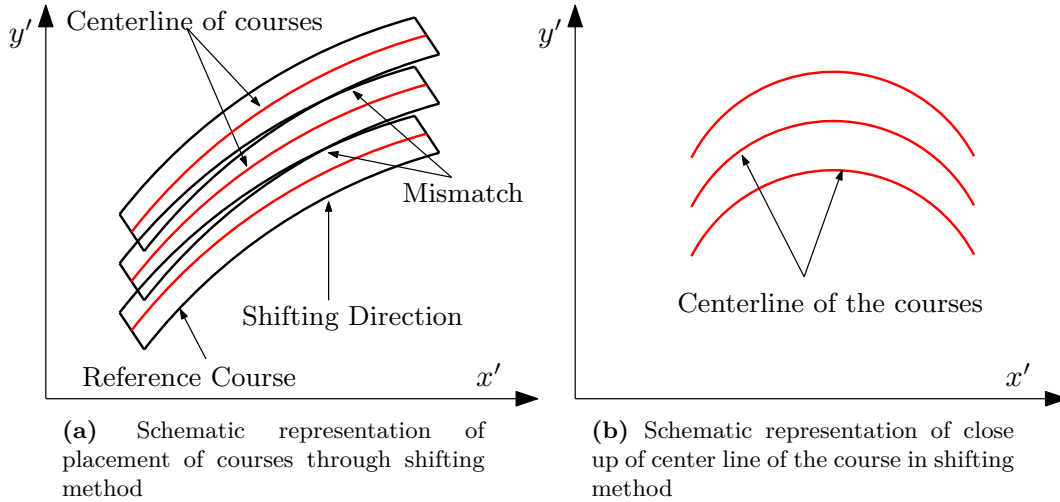
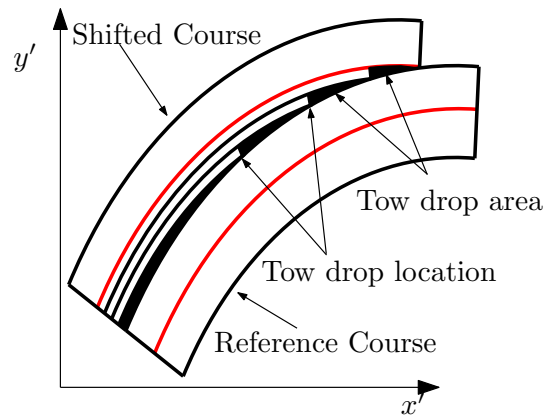
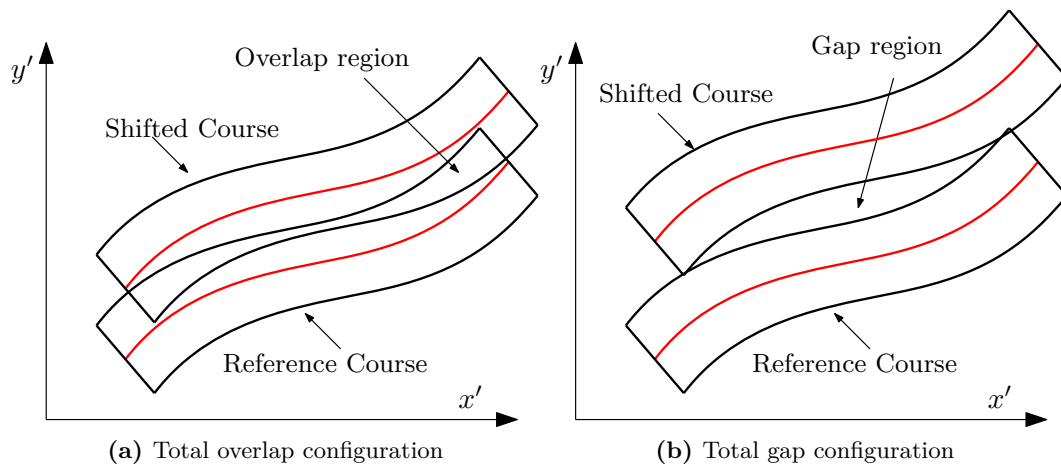


Figure 2.6: Shifting Method

One such strategy is the total overlap strategy, in which the shifted course leave no gaps between the ply, however, there exist a overlap between the two courses as shown in Figure 2.7a. Due to this the ply becomes thicker at locations where overlap is present. Another strategy is the total gap strategy where no overlaps are permitted as shown in Figure 2.7b. Since the total gap strategy leads to very large resin pockets this strategy is generally not used. The third strategy takes the advantage of the cut-restart option of AFP. This is called tow drop strategy. In this strategy, tows are dropped at the intersection of two courses through which panel with uniform thickness can be produced. However, This process gives rise to tow drop defects which are in the structure as shown in Figure 2.7c. These tow drop locations are resin rich and are referred as tow drop areas. Furthermore, there are strategies to cut the tow. Generally, single sided tow cutting strategy is employed. In this case, tows are cut from only one of the courses at the intersection. Single sided cuts were studied by *Blom et al* [13]. The other strategy is double sided cut strategy. In this strategy, the tows are dropped on both side of the intersecting courses. The tow drop is done at the location where the shifted reference curve meets the tows of the course. This strategy was illustrated in the work of *Nik et al* [4]. However, this strategy generates greater tow drop area compared to the single sided cut strategy, therefore, these cuts were not further studied. The tow drop defects generated by single and double sided cut strategies are shown in Figure 2.7d and Figure 2.7e. It can be observed from set of figures in Figure 2.7 that the production of VSP through shifting method leads to periodic defect generation in the VSP.

In the tow drop strategy, there is a possibility of generating fibres with length less than the minimum fibre length allowed by the machine. The constraint is mentioned in the optimization study of *Tatting et al* [8]. Minimum fibre length is distance between the roller head and the cutter of the AFP machine. It depends on machine specification. 5 inches was the minimum length considered by *Tatting et al* [8]. If this condition does not get fulfilled, then there will be occurrence of an unaccounted gaps or overlaps in the laminate.



(c) Small tow drop defects generated due to tow dropping



(d) Tow drop defects generated due to single sided cut strategy [4]



(e) Tow drop defects generated due to double sided cut strategy [4]

Figure 2.7: Strategies to produce a ply of VSP through shifting method

2.2.4 Process induced defects

Process induced defects are the defects that are generated in the structure during the production phase of the structure. The generation of the process induced defects are not only limited to the steered panels but can be formed in the panels with straight fibres. *Croft et al* [23] and *Sawicki et al* [12] studied the defect, which could be present in a straight fibre laminates, such as intra-ply gaps, overlaps, gap/overlap and twisted tow. These defects are caused due to the Material and Machine tolerances, or twisted, missing or spliced tows placed in the process. The defects are parallel to the fibre direction and its size could be as large as 1.5 times the tow width [23]. The main consequences of these defects are the out-of-plane fibre waviness generated in the consecutive stacked plies and thickness variation at the defect location. These consequence causes major effect on the stiffness and strength properties of the laminate. However, the consequences could be mitigated with different manufacturing practices like maintaining close tolerances, staggering techniques [3], use of the hard surface tooling during production and employing alternate stacking sequences for laminate production [24].

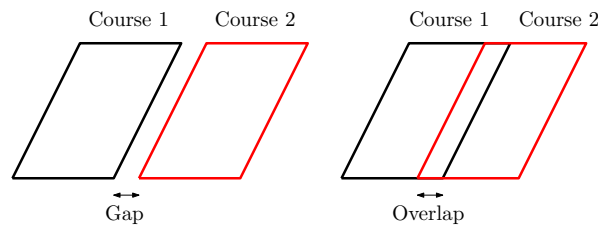


Figure 2.8: Intraply gap and overlap defect

For the case of steered fibres, the defects can be generated in the VSPs, when it is produced by shifting method. These manufacturing issues were studied by *Gürdal et al* [1] and *Kim et al* [2]. *Gürdal et al* [1] focussed on the defects generated through tow drop and complete overlap strategy. For the case of tow drop, the defect generation is dependent on the different parameters like coverage parameter, pre existing arc length of the tow and the nearest course which has to be cut. The coverage parameter is a parameter which determines the percentage of the coverage of the boundary by the tows as shown in Figure 2.9.

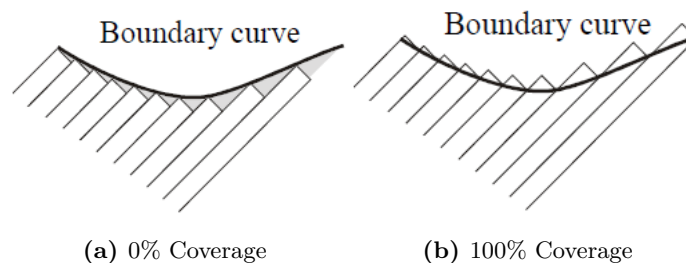


Figure 2.9: Coverage parameter [1]

0% shows no coverage and 100% denotes total coverage of the boundary. The coverage could be in between two scenarios. With choice of these coverage parameters the resin percentage

in the tow drop area could vary from 100% to 0%. For 100% coverage case, local overlapping defects can be formed, and for 0% case, tow drop area with resin rich regions are formed. For the case of total overlap strategy, the thickness build up in the panel is the issue which makes the part of the panels stiffer. The build up can be homogenized by staggering techniques. In staggering process, subsequent plies can be shifted to a certain distance, which would produce the same fibre orientation but due to the presence of overlaps at staggered location the effect of build up could be subdued. This approach also helps with the tow drop strategy to disperse tow drops at different locations. Moreover, an interweaving technique suggested by *Gürdal et al* [1] can also be employed, which can further reduce the thickness variation and spread the defects more uniformly in the laminate. However, these techniques cannot fully eliminate the tow drop and overlap defects that are generated in the process. Moreover, overlaps are avoided during manufacturing of the laminates as aerospace industries have strict guidelines to avoid overlap formation in the structure [24].

Additional defects that were highlighted by *Kim et al* [2] were the local defects such as local buckling, thinning, thickening and local bending as shown in Figure 2.10. The causes of these defects can be different like tow width variation, variation of tension force and tow length variation across the tow. However, these defects can be avoided by maintaining the right curvature and tension in the fibre.

Case	Deformed shape	Defects
Perfect condition		Local buckling Thickening Thinning
Width variation		Local buckling Thickening Thinning
Tension variation		Local bending Thinning
Feed length variation		Local buckling Thickening Thinning

Figure 2.10: Other defects that can be generated by AFP [2]

Chapter 3

State of the Art

This chapter reviews the studies done on the Variable Stiffness Panels (VSPs) and process induced defects generated in it. The studies are both experimental and numerical. Since, the thesis is focused on the numerical methodology development, thus, major attention is given to numerical approaches. Firstly in section 3.1, Classical Laminate Theory (CLT) is discussed, which is used for analysis of the conventional straight fibre laminates. The discussion of CLT is important as it will be further used to analyze steered panels. Moreover, procedure to perform laminate analysis in *Abaqus* is also discussed. Section 3.2 will focus FE analysis of VSPs. In this section, firstly, finite element methodology to analyze ideal VSP has been described. Ideal VSP is a term given to the panels in which no manufacturing defects have been considered. Thereafter, pixelation and defect layer method are discussed through which the process induced defects are incorporated in the finite element models. Section 3.3 is on the studies conducted on the VSPs. Studies on comparison of optimized steered panel designs with conventional laminates are discussed. In these studies, researchers evaluated the optimum VSP design for certain load case and then compared it to the straight fibre laminates. The optimization was performed on the ideal VSPs. Moreover, different studies which shows the effect of the process induced defects on variable stiffness panels are discussed. In section 3.4, homogenization approach has been discussed, which was used to evaluate the properties from the micro-mechanical models of the defects in this research. And finally, a motivation to conduct this research is discussed in section 3.5.

3.1 Analysis of Conventional Composite Laminate

A brief overview of the CLT has been given in section 3.1.1. This theory is used to analyse the laminate shown in Figure 3.1 . Furthermore, the procedure to conduct the analysis in *Abaqus* is discussed in section 3.1.2.

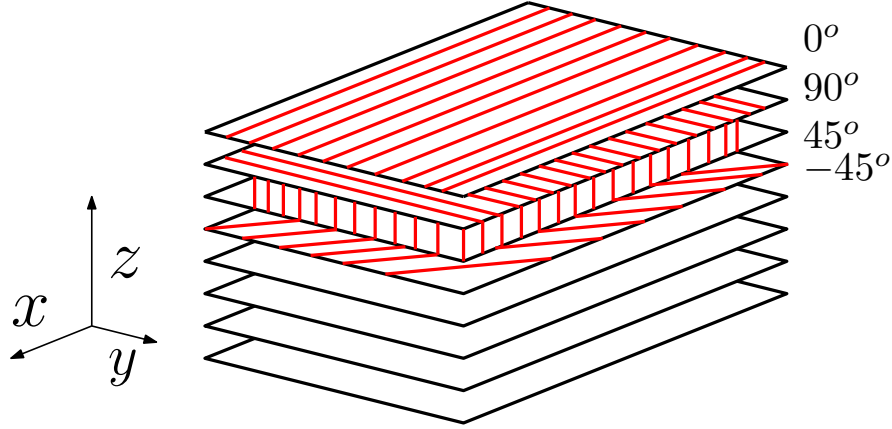


Figure 3.1: Conventional Laminate

3.1.1 Classical laminate theory

Composite materials are anisotropic materials, however, the laminates shown in Figure 3.1 can be treated as a stack of plies and each ply behaves as an orthotropic material. For orthotropic material the Hooke's law reduces to the Eq. (3.1) assuming plane stress conditions.

$$\begin{bmatrix} \sigma_1 \\ \sigma_2 \\ \tau_{12} \end{bmatrix} = \begin{bmatrix} Q_{11} & Q_{12} & 0 \\ Q_{21} & Q_{22} & 0 \\ 0 & 0 & Q_{66} \end{bmatrix} \begin{bmatrix} \epsilon_1 \\ \epsilon_2 \\ \gamma_{12} \end{bmatrix} \quad (3.1)$$

Eq. (3.1) can also be expressed in a compact version as in shown Eq. (3.2)

$$\boldsymbol{\sigma} = \mathbf{Q}\boldsymbol{\epsilon} \quad (3.2)$$

Here, $\boldsymbol{\sigma}$ and $\boldsymbol{\epsilon}$ are the stress and strain vector. And \mathbf{Q} is the stiffness tensor as shown in Eq. (3.3).

$$\boldsymbol{\sigma} = \begin{bmatrix} \sigma_1 \\ \sigma_2 \\ \sigma_{12} \end{bmatrix} \quad \boldsymbol{\epsilon} = \begin{bmatrix} \epsilon_1 \\ \epsilon_2 \\ \gamma_{12} \end{bmatrix} \quad \mathbf{Q} = \begin{bmatrix} Q_{11} & Q_{12} & 0 \\ Q_{21} & Q_{22} & 0 \\ 0 & 0 & Q_{66} \end{bmatrix} \quad (3.3)$$

The individual components of the stiffness tensor are given in Eq. (3.4).

$$\begin{aligned} Q_{11} &= \frac{E_1}{1 - \nu_{12}\nu_{21}} \\ Q_{22} &= \frac{E_2}{1 - \nu_{21}\nu_{12}} \\ Q_{12} = Q_{21} &= \frac{\nu_{12}E_1}{1 - \nu_{12}\nu_{21}} \\ Q_{66} &= G_{12} \end{aligned} \quad (3.4)$$

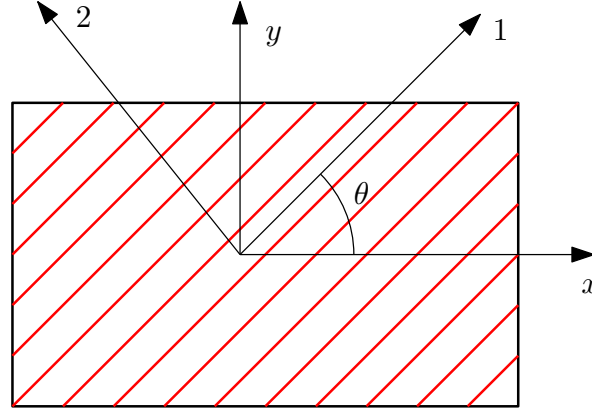


Figure 3.2: Ply coordinate system and global coordinate system

Where, E_1 and E_2 are the elastic modulus of a ply along the fibre and perpendicular to the fibre direction. ν_{12} and ν_{21} are the possions ratio and G_{12} is the shear modulus of a ply.

Assuming that all plies are made of same fibre and matrix, then stiffness properties of all plies can be evaluated from the Eq. (3.4). However, the stiffness tensor evaluated will be oriented in the ply coordinate system, 1 – 2, as shown in Figure 3.2. To orient the ply properties in the global coordinate system $x - y$, transformation is applied to the stiffness tensor as given in Eq. (3.5).

$$\mathbf{Q}_{xy} = \mathbf{M}(\theta)\mathbf{Q}\mathbf{M}(\theta)^T \quad (3.5)$$

Here, $\mathbf{M}(\theta)$ is the transformation matrix which is dependent on angle made by the fibres to the $x - axis$ of the global coordinate system as shown in Figure 3.2. The $\mathbf{M}(\theta)$ matrix is given in Eq. (3.6). The transformed matrix \mathbf{Q}_{xy} is the stiffness matrix of a ply in the x-y coordinate system. Now, for laminate shown in Figure 3.1, the stiffness tensor of different plies with fibre orientation such as 45° and 90° , can be evaluated through Eq. (3.5).

$$\mathbf{M}(\theta) = \begin{bmatrix} \cos^2(\theta) & \sin^2(\theta) & 2 \cos(\theta) \sin(\theta) \\ \sin^2(\theta) & \cos^2(\theta) & -2 \cos(\theta) \sin(\theta) \\ -\cos(\theta) \sin(\theta) & \cos(\theta) \sin(\theta) & \cos^2(\theta) - \sin^2(\theta) \end{bmatrix} \quad (3.6)$$

To analyse complete laminate, Kirchhoff plate theory is applied, which assumes for a plate, the cross-section of the plate remains plane post deformation and perpendicular to the neutral axis. Thus, through the thickness deformation of the plate could be mapped through the deformation of the neutral plane. Therefore, for the symmetric and balanced laminate shown in Figure 3.1 with through thickness section shown in Figure 3.3, deformation relation can be written as in Eq. (3.7). This relation is superposition of strains produced by extension and bending.

$$\boldsymbol{\epsilon} = \boldsymbol{\epsilon}_0 + z\boldsymbol{\kappa} \quad (3.7)$$

where, $\boldsymbol{\epsilon}_0$ is the strain vector of the neutral plane and $\boldsymbol{\kappa}$ is the curvature of the plate along z coordinate.

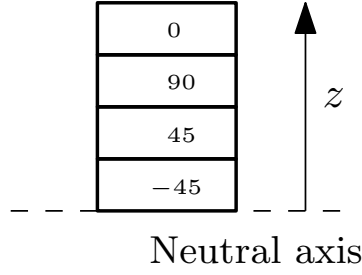


Figure 3.3: Section of the laminate

After assuming this, for the laminate the normal forces and the moments on the plates could be represented as shown in Eq. (3.8) and Eq. (3.9).

$$\mathbf{N} = \int_{-\frac{t}{2}}^{\frac{t}{2}} \boldsymbol{\sigma} dz = \int_{-\frac{t}{2}}^{\frac{t}{2}} \mathbf{Q}_{xy}(\boldsymbol{\epsilon}_0 + z\boldsymbol{\kappa}) dz \quad (3.8)$$

$$\mathbf{M} = \int_{-\frac{t}{2}}^{\frac{t}{2}} \boldsymbol{\sigma} z dz = \int_{-\frac{t}{2}}^{\frac{t}{2}} \mathbf{Q}_{xy}(\boldsymbol{\epsilon}_0 + z\boldsymbol{\kappa}) z dz \quad (3.9)$$

where, \mathbf{N} and \mathbf{M} are the normal force and moment vectors in reference coordinate system. The equations can be reduced down to Eq. (3.10).

$$\begin{bmatrix} \mathbf{N} \\ \mathbf{M} \end{bmatrix} = \begin{bmatrix} \mathbf{A} & \mathbf{B} \\ \mathbf{B} & \mathbf{D} \end{bmatrix} \begin{bmatrix} \boldsymbol{\epsilon}_0 \\ \boldsymbol{\kappa} \end{bmatrix} \quad (3.10)$$

where, \mathbf{A} , \mathbf{B} and \mathbf{D} are given as in Eq. (3.11).

$$\begin{aligned} \mathbf{A} &= \int_{-\frac{t}{2}}^{\frac{t}{2}} \mathbf{Q}_{xy} dz \\ \mathbf{B} &= \int_{-\frac{t}{2}}^{\frac{t}{2}} \mathbf{Q}_{xy} z dz \\ \mathbf{D} &= \int_{-\frac{t}{2}}^{\frac{t}{2}} \mathbf{Q}_{xy} z^2 dz \end{aligned} \quad (3.11)$$

The combination of \mathbf{A} , \mathbf{B} and \mathbf{D} matrix shown in Eq. (3.10) is termed as ABD matrix. Thus, after calculating ABD matrix of the laminate, for a particular deformation of the composite laminate the corresponding force or moment generated in the laminate can be calculated or vice versa.

3.1.2 Analysis in *Abaqus*

Abaqus does the calculation shown in Eq. (3.11) through itself. It provides a interface in which definition of the layup, material, boundary condition and loads are provided which gives desired output. To analyze the laminate, shown in Figure 3.1, following steps need to be executed in *Abaqus* to do the analysis.

1. Generation of the 2D-element mesh on the plate surface. The element choice can defer from user to user. General elements used with plane stress conditions are S3 (Triangle) and S4R (Quadrilateral).
2. Assignment of the property to each layer. Thus, E_1 , E_2 , G_{12} and ν_{12} need to be provided. *Abaqus* also allows users to input directly the components of the stiffness matrix \mathbf{Q} for property assignment.
3. Assignment of orientation of layers to the elements. Since, the laminate is straight fibre laminate each element will be have the same layup. Thus, same layup is provided to all the elements.
4. Application of the boundary condition and load.
5. Submission for analysis.

3.2 Analysis of Variable Stiffness Panels

This section is dedicated to the Finite Element (FE) methodologies used to analyse the variable stiffness panels with and without defects. The VSPs without defects are termed as ideal VSPs. Section 3.2.1 is dedicated to the FE analysis of the ideal VSPs. Section 3.2.2 is dedicated to the methods to account for process induced defects in the VSPs.

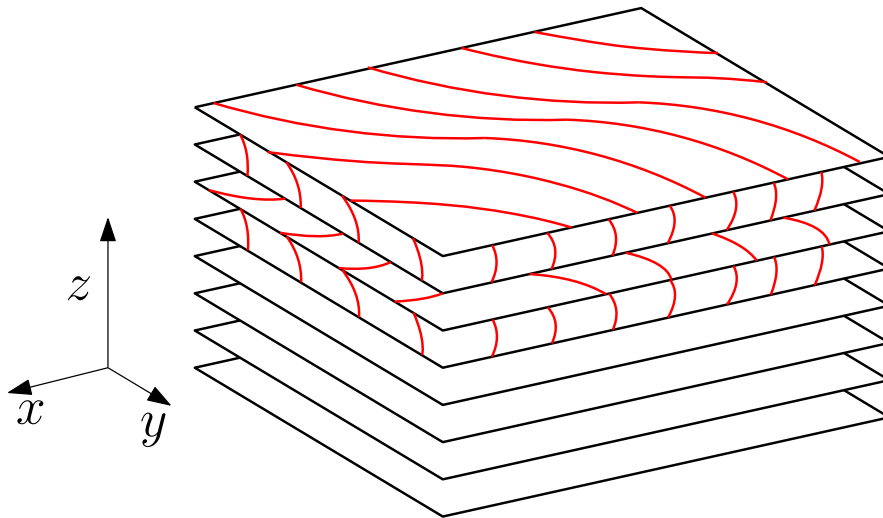


Figure 3.4: Schematic of a VSP laminate

3.2.1 FE analysis of the ideal VSP

If the conventional laminate, in Figure 3.1, is replaced by the VSP, as shown in Figure 3.4, the analysis through *Abaqus* becomes complicated. VSP laminate can be analysed through CLT, but, FE method differs from the conventional laminates. The initial process of the mesh generation and property assignment remains the same as it was in the case of conventional laminate. However, the layup definition changes for every element in the case of VSP. At

every location of the VSP, fibre orientation will be different in every ply. Thus, for every element, a different layup has to be assigned based on the position of the element. The process of assigning each element a different layup is termed as element stacking. In order to provide different layup for the element, firstly, the coordinate of the centroid of an element is evaluated. Based on the coordinate of the centroid, the fibre orientation is calculated for every ply. Then, the layup is provided to that element. This is repeated for every element of the mesh. This methodology assumes that the course intersection is smooth and no defects have been formed in the laminate.

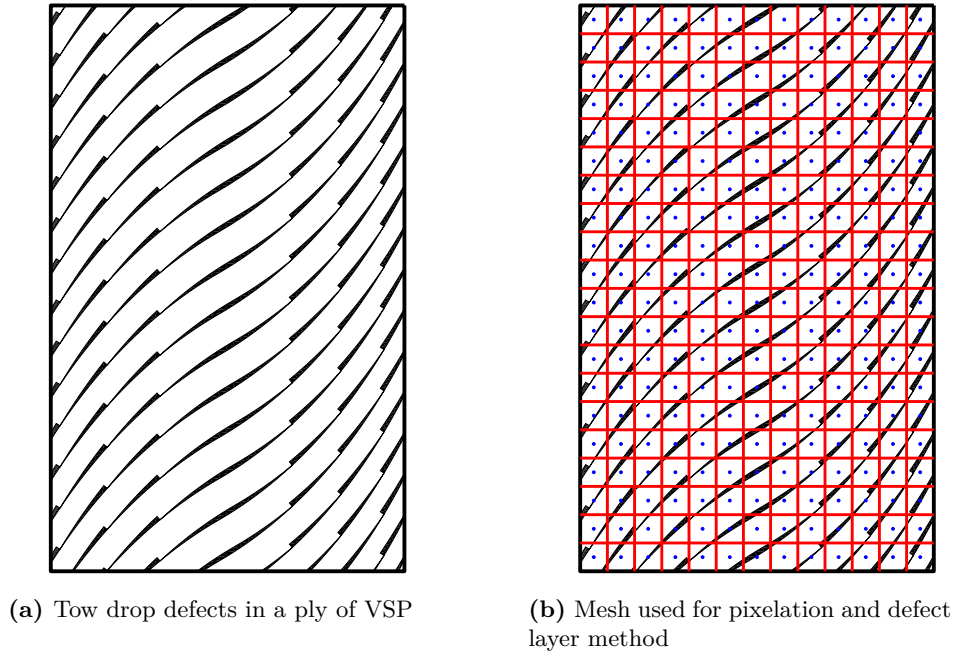


Figure 3.5: A ply of VSP with tow drop defects and the mesh generated on it.

3.2.2 FE implementation of process induced defects in VSP model

There are two approaches which were discussed in the literature to incorporate defects in the FE model of the VSP. The two approaches are termed as the Pixelation and the Defect Layer Method. Pixelation method was used by *Blom et al* [13]. For the FE analysis of the VSP with defects, defect geometry of the tow drop or overlap was created for every ply in the panel. The tow drop defect generation in a variable stiffness ply is shown in Figure 3.5a. Thereafter, a 2D-mesh was generated on the laminate as shown in Figure 3.5b. The mesh is shown in red lines. In order to find the stacking for every element, coordinates of the centroid of the element was evaluated. Centroids are represented by blue dots in Figure 3.5b. Now, every centroid were checked for every ply whether it lies in the tow drop region or in the composite region. If the centroid lies in the composite region of a particular ply then at the same position of the element stack composite properties are given with the orientation. But, if the centroid lies in the tow drop region then at that position resin properties are given in the element stack. The resin properties are isotropic and does not require any orientation

definition. Through this approach account of the tow drop area was taken in the FE model of the VSP by *Blom et al* [13]. For the overlap defects, the centroid of each element are checked, whether it lies in the overlap region. If centroid is found in the overlap region then the thickness of the element is given twice than the thickness of the ply. Identification of the centroid in the overlap region is done by checking if the coordinates lies in the two consecutive courses. Since, the overlap defects are not considered in the thesis, thus, the procedure of identification of overlap region is not discussed further. The element size used in pixelation approach should be small enough to capture the tow drop defects in the panel this brings more computational effort to predict the properties of the VSP with defects. Reduction of the computational effort motivated *Fayazbakhsh et al* [6] to propose Defect Layer Method. In this approach, generation of defect geometry and mesh are the common step as described in pixelation. For the incorporation of the defects in the VSP small micro-mechanical model ($0.254\text{mm} \times 0.254\text{mm}$) was developed. The model is shown in the Figure 3.6a. The center part of the micro-mechanical model could be gap or overlap depending on the strategy from which VSP with the defects are produced.

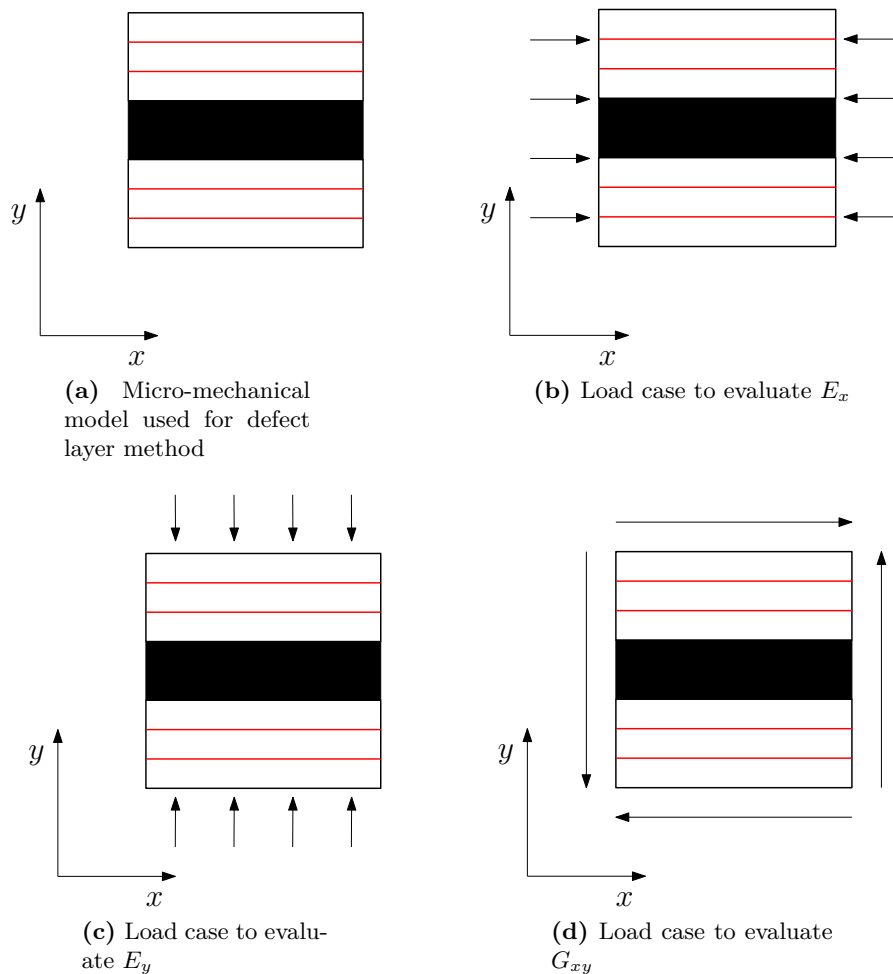


Figure 3.6: Micromechanical model and load cases to evaluate effective properties from micro-mechanical model

From these micro-mechanical models effective modulus like E_x , E_y and G_{xy} were calculated from the load cases shown in Figure 3.6. Uniform traction condition were applied to the micro-mechanical model in each load case. The properties were calculated from 0% to 100% volume fraction of the gaps or overlaps in the micro-mechanical model. A mathematical correlation was developed between the different effective properties and volume fraction of the defects. Now, this correlation was used further to assign properties to the FE mesh.

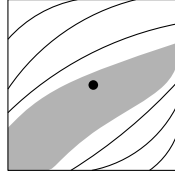


Figure 3.7: Element covering defect and composite area of single ply of VSP

An element from the 2D mesh is shown in Figure 3.7. The element covers the defect area, which is grey shaded portion. The rest of the area in element is the composite area. The area of the element is given by A_{ele} and the defect area covered by element is A_{def} . Now, the volume fraction of defect is equal to $\frac{A_{def}}{A_{ele}}$. Based on this volume fraction, the effective properties are assigned to this element from the developed correlation. This process is repeated for every ply to create the element stack. and further it is repeated for every element. The results reported by *Fayazbakhsh et al* [6] shows that the defect layer method has shown better convergence than the pixelation approach.

3.3 Studies on VSPs and Process Induced Defects

In this section, studies on variable stiffness panels and process induced defects have been reviewed. This section aims to understand the current state of the art. Section 3.3.1 reviews the research which compares the conventional and variable stiffness panels. In this section, terms like constant thickness or tow drop VSPs have been used. These terms were used in literature for terminology. Thus, have been taken similarly for the consistency. No tow drop defects have been considered for these analysis. However, overlap defects have been studied by the researchers and the VSPs with this defect are termed as overlap VSPs. Thereafter, different studies on process induced defects have been reviewed. Effect of process induced defects have been studied by researchers on both laminates, i.e, the conventional laminates and the VSPs. Thus, Section 3.3.2 and Section 3.3.3 reviews studies on the conventional laminates and the VSPs respectively.

3.3.1 Comparison of VSPs and straight fibre laminates

Tatting et al [8] have shown that a remarkable improvement in the buckling load is observed for VSPs with holes over traditional straight fibre laminate with a hole. In their study, they selected top 5 designs of the VSPs which were optimized for the maximum buckling load by Rayleigh-Ritz method. The VSPs had linear fibre angle variation. For each VSP, constant thickness and overlap cases were studied and each panel, with and without hole, was

analyzed by FE approach. The results showed improvement of approximately 20% and 60% for the constant thickness and overlap VSP case, respectively, over the traditional straight fibre laminates. The analysis of the open hole case, showed uniform stress distribution around the hole for the all the VSP. The increase in the buckling loads were attributed to the stiffness steering to the edge of the panel. This made the region near the edge responsible for the load transfer. The region near the edges were well supported thus, buckling load for the VSPs increased.

Jegley et al [25] tested one of the optimized design under compression loading. The configuration of the tested laminate was $([\pm 45/\pm < 45|60 >_2 / \pm < 30|15 > / \pm < 45|60 >]_s)$. The laminate was produced with holes using tow drop and total overlap method. The results were qualitatively similar to the FE analysis results produced by *Tatting et al* [8]. In a follow up study, *Jegley et al* [26] bolster the claim that the buckling load has improved due to the diversion of the load towards the edges of the panel with holes rather than the increase in the bending stiffness of the panel. The same panel was tested under compression load with change in the position of the hole in the panel. The hole was shifted to the higher stiffness region of the panel. With the same bending stiffness, the panel with hole in the higher stiffness region showed lower buckling load. Thus, it was shown experimentally that the dispersion of load transfer towards the edges was the main cause of buckling load improvement. In a similar study, to measure the effectiveness of the steered fibre laminates over straight fibre laminates under compression load *Wu et al* [7] performed experimental and numerical work on one VSP laminate $[\pm 45/\pm < 30|60 >_4]_s$. They showed different properties like pre buckling stiffness, critical point for instability and failure load improved for the steered fibre laminates compared to the conventional laminates. They also suggested to incorporate pre stress condition in the VSP laminate for more accurate results.

Furthermore, *Lopes et al.* [10] considered the same laminates as considered by *Jegley et al* [25] and carried out a numerical study to investigate the first-ply failure load and buckling load improvement. The improvement in the buckling load was reported as 10.7% and 35.8% for constant thickness and overlap case respectively compared to the straight fibre laminate. And the first ply failure load was increased by 24.8% and 33.9% for both previous cases respectively. To further understand the failure of the same panel *Lopes et al* [27] conducted a progressive failure study on the panels. They also calculated the open hole effect on the properties of the laminates. For the VSP without hole, buckling load result showed an increase of 50.7% and 93.0% for the tow drop and overlap case and final failure load showed an increase of 25.2% and 41.2% for the respective cases. For the VSP with hole the improvement in buckling load was reduced to 42.0% and 90.3% for the two cases and final failure load improvement reduced to 13.4% and 55.5% respectively for two cases compared to the conventional straight fibre laminates.

Recently, *Wu et al* [28] studied the general variable stiffness long laminates (aspect ratio 20) with three edges simply supported and one free long edge. They considered non-linear variation of the fibres on the plate to optimize the path of the fibres on the plate in more general way. They selected certain control points on the plate. Fibre angles at control points were controlled by them. The fibre path on the laminate was generated by Lagrangian polynomials with the help of control points. Rayleigh-Ritz methodology was used to evaluate the buckling load for the different configuration and was further compared to the FE results. An increase of 255% in buckling load was reported for the optimized design compared to the quasi-isotropic laminate. *Raju et al* [29] studied the similar long laminates with linear fibre

variation. They developed a new methodology to predict the buckling load of the laminates through differential quadrature method. The developed methodology showed comparable results with the FE analysis of the laminates. Furthermore, to analyse the variable stiffness plies in the sandwich structure, *Coburn et al* [30] performed a buckling analysis of sandwich panels with different cores. The cores were selected from very high transverse rigidity to very low transverse rigidity. The optimized panel, with core having high transverse shear modulus (approximately more than 500MPa), showed an increase of 80% in the buckling load compared to the straight fibres sandwich panels. However, panels with core having low transverse shear modulus showed shear crimping as major mode for failure. Also, for this case, the straight fibre sandwich panel had better performance than the variable stiffness sandwich panels.

3.3.2 Studies on process induced defects in conventional laminates

Sawicki et al [5] studied the composite panels under compression test in order to understand the physical behaviour of the composite around intra-ply gaps and overlaps. They attributed the reduction in strength to out-of-plane waviness. Furthermore, the failure mechanism in vicinity of the defects was found to be matrix dominated and inter laminar shear stress was major contributor to the failure mechanism. They also concluded that a particular size of the defect acts as a threshold value, upto which the reduction increases with the rise of the defect size but afterwards there is no significant change in the strength reduction. They also found that only one defect can be responsible for the strength reduction of the panel.

Further, *Croft et al* [23], from their experimental work concluded that the effect of the defects at the lamina level are not significant than at laminate level. At lamina level, from compression load case, they found similar results as reported by *Sawicki et al* [12], however, from the tension test they found no significant change in the ultimate strength with respect to the baseline configuration. This was explained by the microscopic images of the defects. The microscopic images showed that in the tension specimen, the resin rich area was not purely resin rich, whereas some of the fibres had squeezed into this region which had enforced the region. Therefore, it had not altered the lamina's ultimate tension strength. From the shear test, they concluded that the configuration which leads to more out of plane waviness in the laminate will result into greater strength reduction. At the laminate level, from the tension test of open hole specimen, they found that defects play insignificant role in failure of the laminate than stress concentration generated by the open hole. However, for the compression test, the out of plane waviness of the ply leads to the micro buckling of the fibres and hence, plays a vital role in the failure of the laminate.

Later, *Lan et al* [24] had studied two cross ply laminate samples, one without alternate stacking sequence and other with alternate stacking sequence, and both with defects. Every samples were prepared with and without caul plate. They had shown that the laminate without alternate stacking and manufactured without caul plate had very high apparent stiffness at the position, where defects had been present. This was due to thickness reduction at that area. This attracted more load to it. However, the load carrying capacity of the section was drastically reduced, thus, leading to the early failure. However, the same sample prepared with caul plate had lesser effects of defects on laminate properties. This temperate effect was due to the overall uniformity of the laminate thickness caused by caul plate. For the case of samples with alternate stacking sequence caul plate does not play any major role

in strength and stiffness properties of laminates because the thickness aberration along the laminate were not prominent.

In order to model microstructure of these laminates numerically *Li et al* [3] proposed a 3D meshing tool which could produce microstructure automatically for laminates with any stacking sequence of a straight fibre laminate. For modelling of the gaps and overlap in a ply *Li et al.* [3] parametrized the features of the gaps and overlaps in different parameters. The model proposed by them is shown in Figure 3.8. For gaps three parameters, namely, A_{gap} , B_{gap} and R_{gap} were proposed. A_{gap} represents the transition length, B_{gap} represents the length from where the material has flown in the gap and R_{gap} represents the length of the resin rich pocket. Similarly, for the overlaps two parameters $A_{overlap}$ and $H_{overlap}$ was proposed where, former is the transition length and later is the total increase in the thickness due to the overlap. The values of these parameters were chosen in order to make the model of the microstructure for the laminate more realistic. The choice was also dependent on the production technique of the laminate, whether it is made from hard or soft tooling.

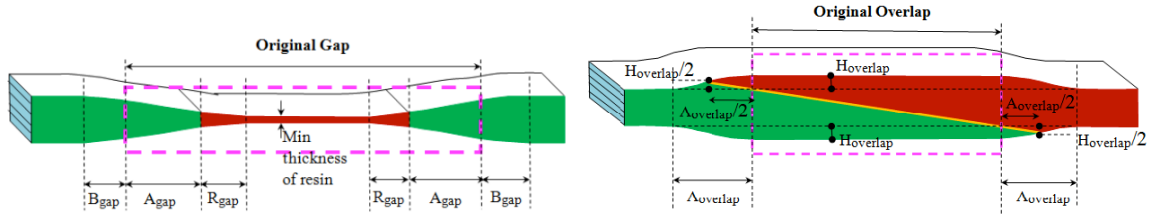


Figure 3.8: Models for different defects proposed *Li et al* [3]

For checking the reliability of the model, pristine model of layup $[45/90/-45/0]_{3s}$ was created and tested in tension and compression, which showed good resemblance with experimental results. Furthermore, progressive failure analysis was carried out under tension and compression load with different defect sizes, staggering sequence and position of the defects. The conclusion drawn by them were, firstly, comparison of the hard and soft tooling laminate showed that the failure occurred due to delamination in both cases which initiated at the center of the laminate and progressed towards the edges of the laminate which ultimately led to full failure of the laminate. However, hard tooling mitigated the effect of out-of-plane waviness due to intraply defects and increased the tolerance of laminate to damage initiation. It also improved maximum strength and post damage behavior. Secondly, the effect of orientation of the gap and overlap on the laminate property in tension and compression revealed that the 45° or -45° orientation effect the laminate properties the worst. Also, it was found that the staggering of these defects helps to mitigate the out of plane waviness which results into low strength knock-down. And lastly, from the investigation on the influence of defect size, stagger distance and stagger repeat it was concluded that for both isolated gap and overlap, there is a threshold of the defect size after which the effect of the defects remain constant. The threshold values proposed are $2(A_{gap} + R_{gap})$ and $2(A_{overlap})$. Furthermore, it was concluded that the negative staggering distance has the worst effect on the properties of the laminate as it promotes more undulation in the fibres. Positive stagger and stagger repeat had minimal influence on the laminate. It was also concluded that overlaps have greater sensitivity towards the staggering pattern than the gaps which means the gaps allow the movement of the resin

in the laminate during curing which may uniform the thickness variation contrary to overlaps thus different staggering pattern may result different results for laminates with overlaps.

3.3.3 Studies on process induced defects in VSP

A theoretical model was presented by *Blom et al* [13] in order to incorporate the tow drop area in the FE analysis of the laminate. The model was based on the assumption that the tow drop occurs at one side of the steered fibre. FE analysis was done through pixelation method. The reported result shows that the stiffness reduction of the panel is directly proportional to the tow drop area and these tow drop area are the reason for the failure initiation in the laminate. They had also shown that the staggering improves the properties of the laminate, whether in the ideal VSP, or in the panel which contains tow drop. Later, *Lopes et. al.* [11] predicted through numerical study a significant reduction in post buckling first ply failure load of optimized ideal VSP($[\pm < 0|80 >]_{6s}$) due to the tow drop defects. They reported a reduction of 18% in the failure load due to tow drop defects.

Label	Configuration
A	$[\pm(47, 0.48)/ \pm (46, -1.57)/ \pm (55, -1.57)/ \pm (52, -1.57)]_s$
B	$[\pm(47, 0.48)/ \pm (42, -1.57)/ \pm (60, -1.57)/ \pm (64, -1.57)]_s$
Baseline	$[45/0/ - 45/90]_{2s}$

Table 3.1: Laminates studied by *Fayazbakhsh et al* [6]

Fayazbakhsh et. al. [6] have developed defect layer method to study VSP defects. Through this method, they studied two VSP designs. The configuration of two VSP and baseline design are shown in Table 3.1. Design A is optimized design for maximum buckling load and Design B was optimized design for same stiffness as of the baseline and higher buckling load than baseline. The designs were studied with and without process induced defects. Effect of both tow drop and overlap were studied on ideal design. Stiffness loss of 15.1% and 14.0% were reported due to tow drop from ideal A and B design. Similarly, Buckling load reduction of 12.4% and 12.2% was reported due to tow drop defect from ideal A and B design. However, for the overlap case, improvement in the properties were reported. Stiffness increased by 9.6% and 11% and Buckling load increased by 29.9% and 30.5% over ideal A and B design respectively. Recently, *Nik et al* [4] carried out an optimization study, in which they considered the effect of design and manufacturing parameters such as the center (T_0) and edge (T_1) angle and tow and course width respectively, on the stiffness and buckling properties of the VSP. They also concluded that process induced defects such as tow drop deteriorates properties of the VSP and overlap alleviates them. They also showed that with consideration of these defects, for different design cases, the in plane stiffness of the panel could be alleviated but buckling properties can be kept constant, which made it necessary to include these defects in the optimization process. The design set they considered was evaluated by the pareto frontier method. The ideal VSP properties of the design set and the effect of different process induced defects on the design set is shown in Figure 3.9.

Recently, *Falco et. al.* [31] had conducted the experimental study to understand the effect of angle discontinuity caused by tow drop defect on the properties of the laminate. They calculated the maximum fibre angle discontinuity in the VSP design by varying different

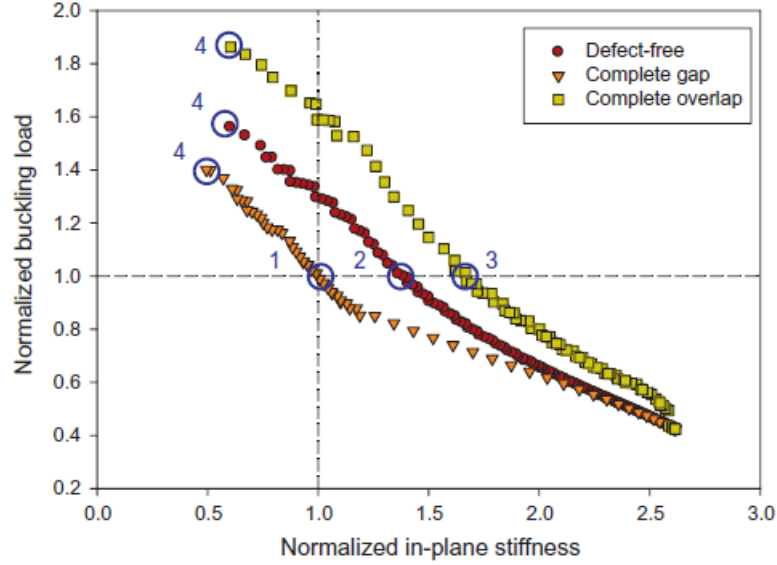


Figure 3.9: Effect of tow drop and overlap on the ideal VSP design shown by *Nik et al.* [4]

design and manufacturing parameters. The maximum angular discontinuity in the fibre angle was reported 12° . Thereafter, the triangular shaped defect was made in the laminate with same angular discontinuity and with 0% and 100% coverage parameter. They reported 20% decrease in the strength of the laminates with non-staggered defects. However, staggering improved the strength properties and the reduction was only 10%.

3.4 Periodic Homogenization Approach

This sections gives a brief overview about the periodic homogenization approach. This approach is used in this thesis to evaluate the effect of defects on the VSP through micro-mechanical models. Thus, it is important to discuss it. Firstly, in general, Homogenization process is discussed in section 3.4.1. Thereafter, the methodology of periodic homogenization approach is discussed in section 3.4.2, which could be applied to the micro-mechanical model for evaluation of the homogeneous stiffness properties. In section 3.4.3, evaluation of knock-down factors caused by defects on the properties of material is discussed. In section 3.4.4, different studies have been reviewed in which periodic homogenization is used for property evaluation. Also, applicability of the periodic homogenization approach has been reviewed.

3.4.1 Homogenization

Homogenization is a process to replace a heterogeneous material with a fictitious homogeneous material which takes account of all the heterogeneity in the replaced material and has the same average response as the heterogeneous material. An example of this work is shown by *Hill* [32]. Through basic assumptions like constant stress and constant strain in the composite material Reuss and Voigt estimate of the elastic constants of the composite material can be evaluated. For a composite material with isotropic individual component A and B having bulk

modulus as κ_A and κ_B and rigidity modulus as μ_A and μ_B , then the Reuss and the Voigt estimates of the elastic constants of composite material is given by Eq. (3.12) and Eq. (3.13).

$$\begin{aligned}\frac{1}{\kappa_R} &= \frac{c_A}{\kappa_A} + \frac{\kappa_B}{E_B} \\ \frac{1}{\mu_R} &= \frac{c_A}{\mu_A} + \frac{c_B}{\mu_B}\end{aligned}\tag{3.12}$$

$$\begin{aligned}\kappa_V &= c_A \kappa_A + c_B \kappa_B \\ \mu_V &= c_A \mu_A + c_B \mu_B\end{aligned}\tag{3.13}$$

Here, (κ_R, μ_R) , and (κ_V, μ_V) are the Reuss and Voigt estimates of the elastic constants of the composite material respectively. c_A and c_B are the volume fraction of the individual component in the composite. The assumptions, on which the estimates are evaluated, are not true in real life scenario and the elastic constants differ from these values. *Hill* [32] showed that the real elastic property of the composite material are bounded between the Reuss and the Voigt estimates of the elastic property. It was also, proved in his work that the young's modulus of the composite material is between the bound shown in Eq. (3.14).

$$E_R \leq E \leq E_V\tag{3.14}$$

Here, E is the young's modulus of the composite material and E_R and E_V are the estimates of the young's modulus of the composite material evaluated through Eq. (3.12) and Eq. (3.13). The evaluation of E , or other elastic constants or, properties for a composite material, with consideration of the material heterogeneity is called Homogenization. The average response of the homogenized material would be same as the average response of the composite material but local response could differ.

The evaluation of the Reuss and Voigt estimates is also homogenization process, however, the properties of various composites are not accurately measured with it. Thus, better approximation methods were required to evaluate the composite properties. One such method is statistically choosing the small region in the heterogeneous material and apply appropriate boundary condition on it to determine the properties from the statistically chosen region and the properties will be representation of the complete heterogeneous material. The defect layer method approach is the example of this approach. The boundary condition, however, used were uniform traction, which suggest it gives the Reuss estimates of the properties. The other boundary condition is periodic boundary condition used by *Suquet* [5]. However, the boundary conditions was only limited to the periodic media. Another boundary condition proposed by *Hazanov et al* [33] was the mixed boundary condition. In the mixed boundary condition, the boundary of the statistically chosen region is partially subjected to displacement and partially to traction. *Hazanov et al* [33] studied a problem under three different conditions, one with static traction, other with static displacement and third with mixed condition. Thereafter, the order relationship was evaluated between the different result. It was found that with the mixed boundary condition, the effective properties were found to be bounded between the results found by other two boundary conditions.

Later, *Terada et al* [34] showed that the periodic boundary condition is also suitable to predict the composite properties which do not show periodicity. They applied the periodic boundary condition on the material without periodicity and concluded that the periodic homogenization approach is better for approximation than the static traction and static displacement boundary conditions. Furthermore, *Van der Sluis et al* [35] compared the periodic and mixed boundary conditions in their study. They studied material with heterogeneous micro-structure and applied the two boundary conditions. They concluded that the periodic boundary conditions give better result than the mixed boundary condition for their problem.

Thus, different researchers have shown that the periodic boundary condition are better for approximation than the other boundary conditions like static traction, static displacement and mixed-boundary condition. And it is also applicable for the periodic and non-periodic material, thus, this methodology could be used further for study of the micro-structure of the VSPs.

3.4.2 Methodology of periodic homogenization

Representative volume element

Representative volume element is a region which statistically represents the complete macroscopic media. The choice of the region is dependent on the researcher and the macroscopic law is dependent on the choice of this region. For a periodic media, this region is the unit cell which periodically generates the entire region. Now, in a homogenized material at a particular point \mathbf{x} shown in Figure 3.10, the system variables are equivalent to the system variables evaluated in RVE. It takes the heterogeneity in the material into account through a microscopic variable \mathbf{y} . The system variables which are additive in nature can be averaged in the RVE. It will be equal to the system variables at \mathbf{x} . The system variables can be any quantity like stress or strain.

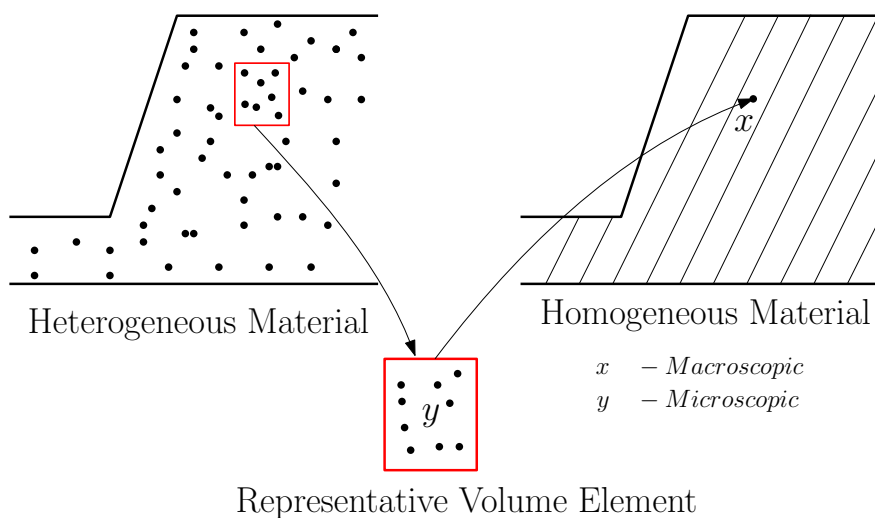


Figure 3.10: Schematic representation of heterogeneous, equivalent homogeneous material and representative volume element

The system variables inside the RVE can vary and are dependent upon \mathbf{y} . The system variables in the RVE could be considered as an oscillating function, which could be represented in two parts one is the averaged part and other an oscillating part. If the system variables are averaged in the RVE, then the average part will be equivalent to the average in the RVE and the average of the oscillating part over the entire RVE is zero. Therefore, for a RVE, Eq. (3.15) can be written.

$$\begin{aligned}\Sigma_{ij} &= \frac{1}{V} \int_V \sigma_{ij} dy = \langle \sigma_{ij} \rangle \\ E_{ij} &= \frac{1}{V} \int_V \epsilon_{ij} dy = \langle \epsilon_{ij} \rangle\end{aligned}\quad (3.15)$$

Here, $\langle . \rangle$ stands for the averaging operator, Σ and E represents macroscopic stress and strain tensor, respectively, σ and ϵ represents microscopic stress and strain tensor, respectively. 'ij' indices represent the components of the tensor. V represents the volume of the RVE.

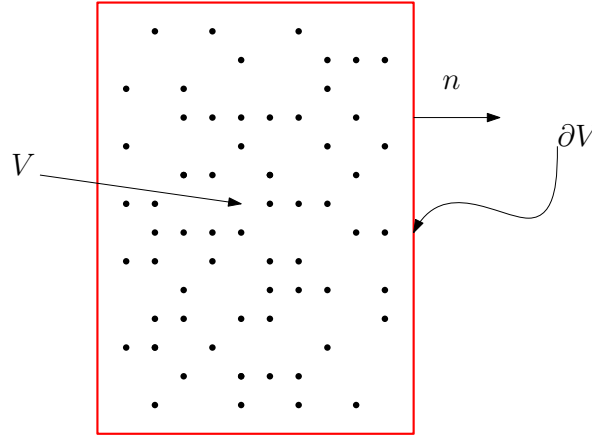


Figure 3.11: Representation of a RVE

Constitutive equation and boundary conditions

Suquet [5] defined homogenization as procedure which relates Σ and E (and possibly their derivatives with respect to the time and other parameters), by means of Eq. (3.15), and of micro constitutive law as given by Eq. (3.16).

$$\begin{aligned}div(\sigma) &= \mathbf{o} \\ \langle \sigma \rangle &= \Sigma \quad or \quad \langle \epsilon \rangle = E\end{aligned}\quad (3.16)$$

The above equation assumes that there are no surface or body forces on the media. Thus, if the average stress Σ or average strain E are known for the material then $div(\sigma) = \mathbf{o}$ can be solved in the RVE, which will give the average strain E or average stress Σ . In order to solve Eq. (3.16), boundary conditions on the RVE are required. The boundary conditions on the RVE, shown in Figure 3.11, for which the Eq. (3.15) and Eq. (3.16) can be solved are given as follows.

1. Uniform stress on boundary $\partial V : \boldsymbol{\sigma} \mathbf{n} = \boldsymbol{\Sigma} \mathbf{n}$ on ∂V
2. Uniform strain on boundary $\partial V : \mathbf{u} = \mathbf{E} \mathbf{y}$ on ∂V
3. Periodicity condition on boundary $\partial V : \boldsymbol{\sigma} \mathbf{n}$ anti periodic , $\mathbf{u} = \mathbf{E} \mathbf{y} + \mathbf{u}^*$, \mathbf{u}^* is periodic.

Where, ∂V represents the boundary of the RVE, \mathbf{u} represents the displacement vector in a RVE, \mathbf{u}^* is the oscillating component of the displacement vector \mathbf{u} and \mathbf{n} represents the normal vector to the surface ∂V . Uniform stress and uniform strain conditions will give the Reuss and Voigt estimates and the periodicity conditions will give the approximation of the composite material between the Reuss and Voigt estimates.

Homogenized stiffness tensor

For the linear elastic case, in a RVE the constitutive equation can be written as in Eq. (3.17)

$$\begin{aligned} \boldsymbol{\sigma}(\mathbf{y}) &= \mathbf{Q}(\mathbf{y}) : \boldsymbol{\epsilon}(\mathbf{y}) = \mathbf{Q}(\mathbf{y}) : (\mathbf{E} + \boldsymbol{\epsilon}^*(\mathbf{y})) \\ \text{div}(\boldsymbol{\sigma}) &= \mathbf{o}, \quad \text{and boundary condition} \end{aligned} \quad (3.17)$$

Here, $(:)$ represents the operation of tensor on another tensor. \mathbf{Q} is the stiffness tensor, it is dependent upon the individual components of the RVE and is also dependent on \mathbf{y} . $\boldsymbol{\epsilon}^*$ is the oscillating part of the microscopic strain tensor. Now, Eq. (3.17) can be solved over the RVE by all three boundary condition and with known average strain \mathbf{E} . Average $\boldsymbol{\sigma}$ over the RVE or the homogenized form can be written as in Eq. (3.18) and Eq. (3.19). The actual solution of the problem has not been presented here, however, it can be referred in the work of *Suquet* [5]

$$\boldsymbol{\Sigma} = \langle \boldsymbol{\sigma} \rangle = \langle \mathbf{Q} : \boldsymbol{\epsilon}(\mathbf{u}) \rangle = \langle \mathbf{Q} : \mathbf{D} : \mathbf{E} \rangle = \langle \mathbf{Q} : \mathbf{D} \rangle : \mathbf{E} \quad (3.18)$$

$$\boldsymbol{\Sigma} = \mathbf{Q}_{\text{hom}} : \mathbf{E} \quad \text{where} \quad \mathbf{Q}_{\text{hom}} = \langle \mathbf{Q} : \mathbf{D} \rangle \quad (3.19)$$

where, \mathbf{Q}_{hom} is the homogenized stiffness tensor and \mathbf{D} is the localization tensor. The homogenized stiffness tensor is the average equivalent of the stiffness tensor of the individual component inside the RVE. However, it is not the average of the stiffness tensor over the RVE. This is because stiffness is not an additive quantity. This homogenized stiffness tensor is dependent upon the boundary condition. For this thesis, periodic boundary conditions are chosen to evaluate the homogenized tensor.

The calculation of the \mathbf{Q}_{hom} can be done by the knowledge of the localization tensor \mathbf{D} . However, a simpler approach can be followed to evaluate \mathbf{Q}_{hom} . The internal energy density of the RVE can be calculated which will be equal to the expression shown in Eq. (3.20).

$$\begin{aligned} U &= \frac{1}{2} \mathbf{E}^T : \langle \mathbf{D}^T : \mathbf{Q} : \mathbf{D} \rangle : \mathbf{E} \\ \mathbf{Q}_{\text{hom}} &= \langle \mathbf{D}^T : \mathbf{Q} : \mathbf{D} \rangle \end{aligned} \quad (3.20)$$

Here, U is the internal energy density of the RVE. Thus, if the internal energy of the RVE is known then \mathbf{Q}_{hom} can be easily evaluated without knowing the localization tensor \mathbf{D} . The expression of the homogenized tensor in Eq. (3.19) and Eq. (3.20) are equivalent as proved by *Suquet* [5]. From the expression of homogenized stiffness tensor it could be concluded that the tensor is symmetric.

3.4.3 Knock-down factors

VSPs consist of the periodically generated defects. Thus, a small RVE can be chosen for it which can be analyzed through periodic homogenization approach and elastic properties of the VSP can be approximated without modeling the complete VSP. However, the geometry of the defects are dependent upon various variables such as tow width, course width and fibre angle distortion. Thus, RVE will differ for different panels. This will result into different knock-down on the properties of the variable stiffness panel. Thus, knock-down can be calculated and correlated to the variables on which the defect geometry are dependent.

Now, to calculate knock-down through the stiffness tensor which is evaluated through periodic homogenization a approach suggested by *Abdalla et al* [36] can be used. In this approach, a baseline stiffness tensor is chosen which corresponds to the ply with no defects. This stiffness can be denoted as \mathbf{Q}_o . Then, the stiffness tensor can be calculated through periodic homogenization approach for the ply which contains the defects. This is termed as \mathbf{Q}_{hom} . From these stiffness tensor eigen value problem shown in Eq. (3.21) can be solved.

$$(\mathbf{Q}_{hom} - \mathbf{Q}_o)\mathbf{T} = \lambda\mathbf{Q}_o\mathbf{T} \quad (3.21)$$

where, λ is the eigen value and can be thought of as ratio of change in the baseline tensor due to the defect to the baseline tensor. \mathbf{T} represents the vector along which the stiffness properties changes. λ and \mathbf{T} can represent the knock-down which the defects will cause on the property of the baseline composite with no defects. These λ and \mathbf{T} can further be correlated to the variables on which the defect geometry are dependent. This correlation should be valid on the entire range of the variables selected. Thus, through this correlation knock-down on the properties of the VSP can be easily calculated for different design, without further performing any homogenization methodology.

3.4.4 Applicability of periodic homogenization

Periodic homogenization approach has been used over the years by researchers to predict the homogenized elastic properties of the composite materials. *Suquet* [5] compared the results numerically generated from this approach for a perforated plate to the experimental results. The specimen presented in Figure 3.12a was tested for different angle α and Figure 3.12b shows the comparison between the experimental and numerical result generated by *Suquet* [5]. The comparison shows that periodic boundary condition gives good estimate of the elastic properties of the perforated plate specimen than uniform stress and strain boundary condition.

Hollister et al [37] compared the periodic homogenization method to the averaging approach, which assumes uniform stress or strain on the boundary, and concluded that for a one dimensional case all the approaches give the same and accurate estimate, however, for two and three dimensional periodic porous media cases the periodic homogenization gives more accurate results than the other averaging approaches. They calculated the stiffness properties of the porous periodic media from the FE analysis and compared the results with the estimates calculated by periodic homogenization and other averaging approaches. The estimates from periodic homogenization differed 30% compared FE analysis, whereas, for other averaging case the deviation was 70% compared to FE analysis. Also, *Gusev* [38] showed that the homogeneous behaviour of the composite at macroscopic level can be accurately predicted

by the periodicity condition. Furthermore, *Wang et al* [39] also used this methodology to calculate the elastic property of the woven composites. Their work shows a good agreement between the experimental and the numerical results. Through these studies it could be concluded that the periodic homogenization gives a reasonable estimate of the elastic property of the composite material. However, FE implementation of the homogenization boundary condition in commercial software is problematic. In the commercial softwares like *Abaqus* the periodic boundary condition can be imposed on periodic meshes. Periodic mesh means meshes should contain equal number of nodes and same pattern on opposite edges of the mesh. Due to these requirements the periodic boundary conditions can be applied to limited geometry cases like rectangle or parallelepiped. *Wu et al* [40] gave the systematic method to apply periodic boundary conditions on the rectangular shape geometry in *Abaqus*. However, different approaches have been proposed by the researchers which could be used in order to enforce the periodic boundary conditions on arbitrary meshes. *Nguyen et al* [41] suggested a polynomial interpolation implementation which could be applied to non-periodic meshes in order to impose the boundary conditions. The method have shown good accuracy and convergence rate to the solution which was produced by periodic meshes.

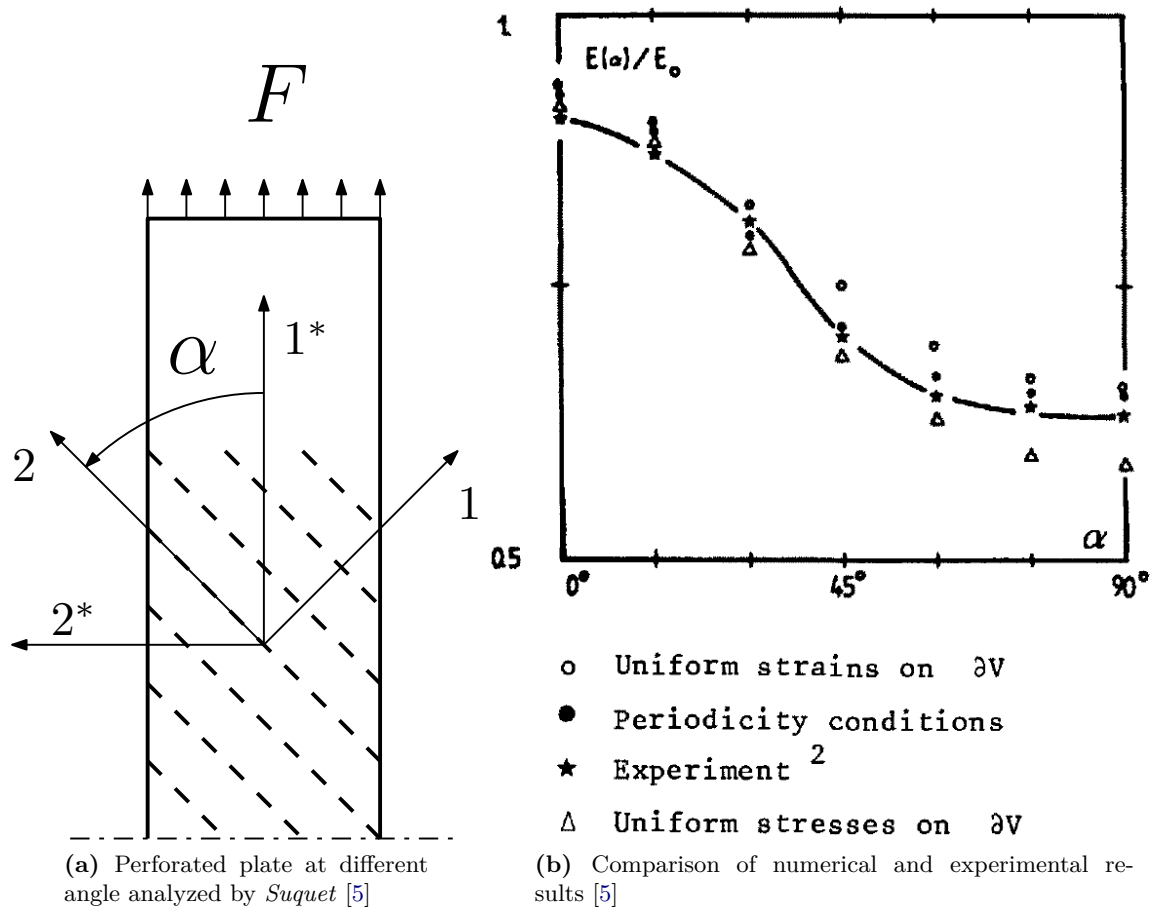


Figure 3.12: Specimen studied and result presented by *Suquet* [5]

3.5 Motivation

For incorporation of process induced defects in the FE analysis of VSP, Pixelation and Defect Layer Method are used. These strategies do not model the defects explicitly but gives property to the simple meshes depending on the position of the tow drop defects. Firstly, these strategies have not been proven to converge to the solution which can be found through explicit modeling of the defects. However, explicit modeling of the individual defect in the VSP will be complicated as the orientation and the position of the defects will be different for different plies. Thus, a gap has to be filled which involves proving the strategies like pixelation and defect layer method converges to the solutions, which are got from the explicit modeling of the defects in the VSP.

The strategies Pixelation and defect layer method involves a common step to identify the position of the tow drop location so that element stack can be formed. This process is computationally intensive. Thus, optimization studies are done on the ideal panels and the optimized design are tested with defects. However, the defects consideration in the optimization is missing and must be integrated to it . Thus, a methodology should be developed to take account of the defects in the VSP in computationally cheaper way. Smearing methodology discussed in this research focus to eliminate the step involving identification of the defects in VSP. It exploits the advantage of the periodic defects generation in the VSP in order to give accurate results of the manufacturable panels. Through this approach no geometry generation of the tow drop defects are needed. However, smearing methodology involves a common step with defect layer method which is micro-mechanical modeling of the defects. The micro-mechanical models used in smearing are modified version of the models used in the defect layer method. Also, constant load conditions are not used in determining the homogeneous property of the micro-mechanical model. Periodic Homogenization approach is used which gives satisfactory results for the periodic composite media through modeling a small periodic unit of the composite. Only tow drop defects have been studied in this research. Though the overlap defects give improved properties than the tow drop defects, it increases the weight of the structure. Also, the thickness uniformity is lost in the laminate, furthermore, overlap defects are avoided at industrial level. Thus, overlap defects have not been studied in this research.

Micro-Mechanical Modelling

This chapter is on the development of the micro-mechanical model of the tow drop defects in a single ply of a VSP. Tow drop defects from the single sided cut strategy were studied. Also, a different type of tow drop strategy was introduced. The strategy is termed as zipper cut strategy. The tow drop defects generated due to zipper cut strategy were also studied. The tow drop defects generated in the actual VSP has complicated geometry. Certain assumptions were made during micro-mechanical model development. These assumptions were made to simplify the geometry of micro-mechanical models and to overcome the limitation of FE implementation of periodic homogenization approach. Through these micro-mechanical models homogeneous stiffness tensor of composite with different defect configurations were evaluated. From the stiffness tensors the knock-down factors were evaluated. Thereafter, the knockdown factors were correlated to the design and production variables on which the defects were dependent. Furthermore, micro-mechanical models were studied firstly through explicit modeling of the defects. Thereafter, pixelation and defect layer method were used to study the models. A convergence study was performed to compare the existing strategy. In this chapter, terms like single sided cuts and zipper cuts are used, which refers to the defects generated due to the single sided cut strategy and zipper cut strategy.

4.1 Types of Cuts

The general type of tow drop strategy used during production of a VSP is the single sided tow drop strategy. This strategy has shown to develop lesser volume fraction of the resin rich area than the double sided cut strategy. The defect generated due to single sided cuts are shown in Figure 4.1. The defect generation is dependent upon the fibre angle distortion between the two courses and the tow width of the courses.

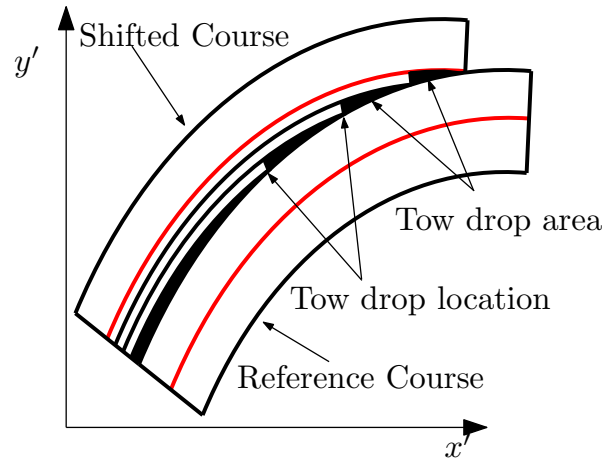


Figure 4.1: Tow drop defects generated due to single sided cuts

The defects generated can be represented as shown in Figure 4.2a. Figure 4.2a represents two courses intersecting at angle θ and have the tow width, t_w . The tows in the Course 1 are aligned to the y -axis and tows in the Course 2 are intersecting Course 1 at an angle θ . The courses shown are the straight lines, which is not the case in a VSP. The courses have the curvature which is assumed to be very large so that the intersections resemble the same way as shown in the Figure 4.2a. This assumption was made as radius of curvature can vary from 400mm to 1000mm for different AFP machines. And the tow width is typically 3.175mm, 6.35mm or 12.7mm, which is equivalent to the minimum defect size. Since, there is a difference of order between minimum defect size and the radius of curvature, thus, assumption of very large radius could be made.

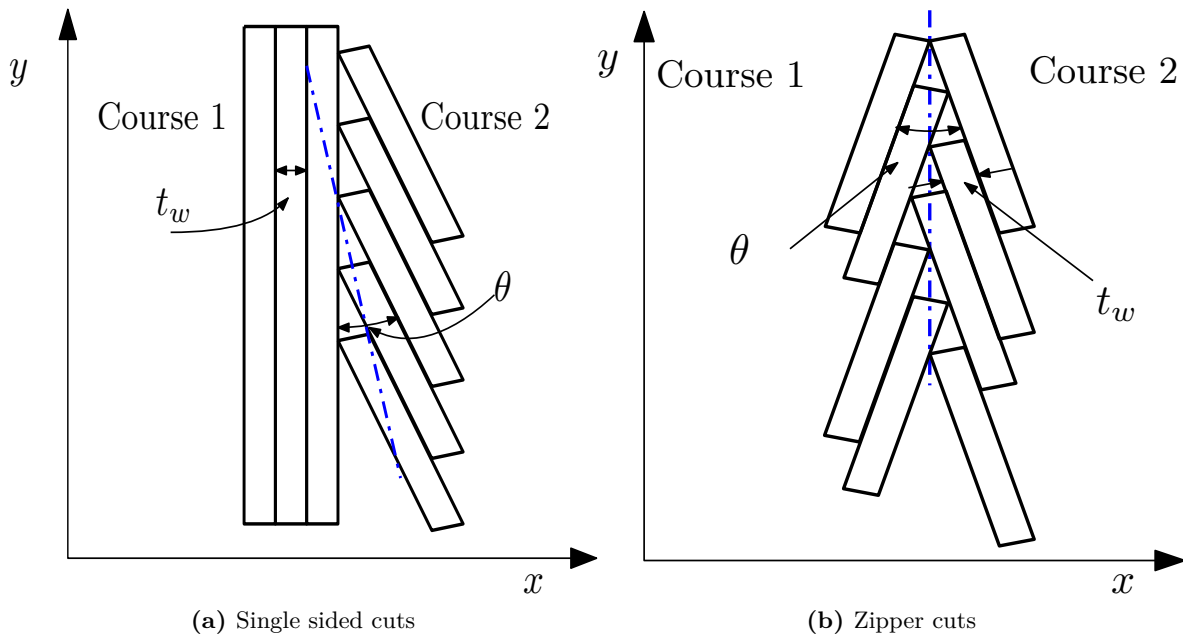


Figure 4.2: Different types of tow drop strategy studied in this thesis and different type defects generated

From Figure 4.2a it could be inferred that there is no symmetry in the single sided cuts. Also, the tows do not follow the fictitious blue intersection line. To eliminate this zipper cut strategy were introduced. The zipper cut strategy is shown in Figure 4.2b. It shows two courses meeting at same angle difference θ but the tow are dropped from both courses at the intersection. The two courses make the same angle with y -axis, which brings symmetry along the intersection. It also reduces the coupling between the different degree of freedom. Moreover, the tow drop defects generated are evenly distributed along the intersection line of the courses.

4.2 Micro-mechanical Models of Cuts

4.2.1 Basic assumption and models

The aim, here, is to develop a simplified ply model which could replace actual ply model of a VSP. The real geometries of the tow drop defects in VSP are complex and depends on different variables such as design variables like initial angle (T_0), final angle (T_1) and curvature (κ), and also manufacturing parameters like tow width (t_w) and number of tows in a course (n_t). In order to simplify the geometry of the tow drop defects, for micro-mechanical model, radius of curvature of the courses are assumed to be infinity. Thus, the cuts will resemble to the cuts shown in Figure 4.2a and Figure 4.2b. The cut geometries take account of the angle distortion which will be present in a ply due to mismatches of the courses, and the tow drop defects generated due to mismatch will be of the triangular shape. The width of the individual tows will correspond to the tow width used for the production of a ply. However, the cut geometry do not account for the fibre steering.

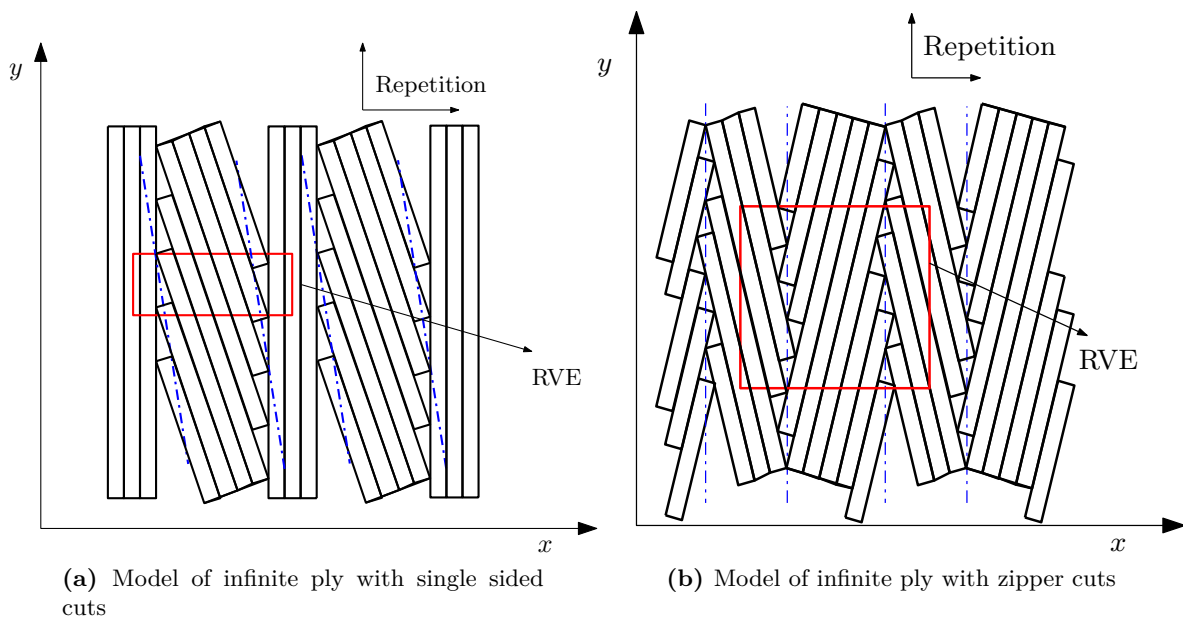


Figure 4.3: Infinite models of different cuts

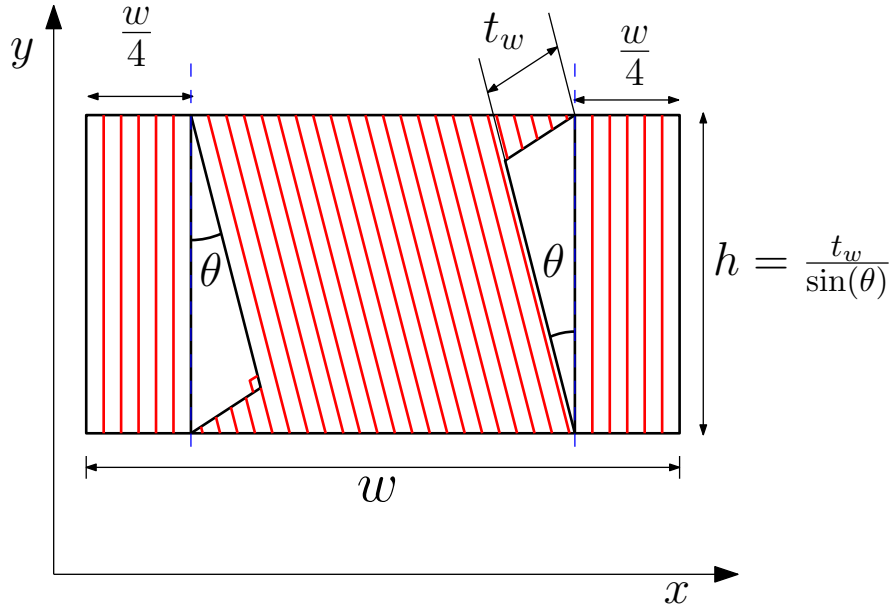


Figure 4.4: RVE for single sided cuts

Now, the repetition of the courses along x -axis will result into the straight fibre ply with angular distortion as shown in Figure 4.3. This is the simplified ply model which has been chosen for the study in this thesis. A ply in a VSP, thus has been approximated as the ply with infinite radius of curvature with embedded defects in it. Also, assuming that the repetition is also in the y direction. This means that the ply is infinite in x and y direction.

A RVE can be selected which represent the complete geometry of the tow drop defects in the approximated ply. The RVE should be such that it repeats itself to produce the entire ply and periodic homogenization can be applied on that. The red box shown in Figure 4.3 is the chosen RVE for the cuts. Magnified view of RVEs are shown in Figure 4.4 and Figure 4.5. The parameters of the RVEs signifies the different design and manufacturing parameters. The angle, θ , represents the fibre angular distortion which is controlled by T_0 and T_1 angles. The tow width, t_w , determines the size of the defect. And the width of the RVE signifies the number of tows, n_t , which are present in the course, or corresponds to the course width, w_c . Thus, changing these parameters individually will give rise to the different sizes of the defect which could be studied. Through these models effect of angular distortion, tow width and course width on the composite properties can be evaluated. However, the effect of angle steering is still missing. The red lines shown in these RVEs are the representation of the fibres inside the RVE. The length of the RVE, h , is dependent upon the tow width, t_w , and the angle, θ . This is because the length of the RVE will change as these two variable changes to maintain the periodicity.

Now, to isolate the effect of fibre angular distortion one more RVE, for both cuts, can be considered. As evident from the RVE, in Figure 4.4 and Figure 4.5, that the sole responsible for the defect geometry is the finite width of the tows. If the tow width is infinitely small, the only distortion in the laminate would be of the fibre angular distortion. Thus, by assuming tow width tending to zero, micro-mechanical models could be studied in which no defects are formed and only the effect of fibre angle distortion could be evaluated. The models for

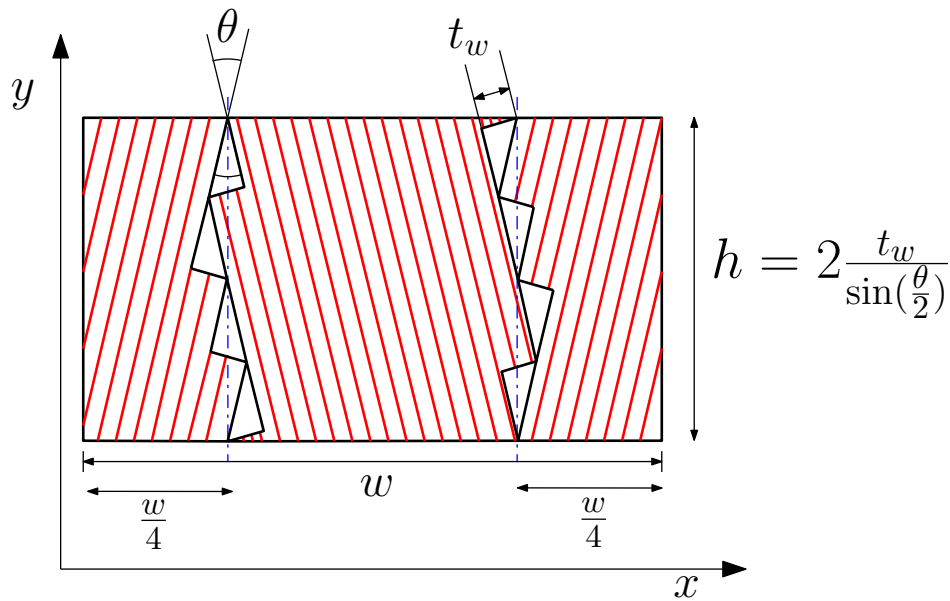


Figure 4.5: RVE for zipper cuts

the two different cuts with assumption of infinitely small tow width are shown in Figure 4.6. Thus, using both RVEs, which are with and without defects, the effect of the defect can be segregated. The RVEs with tow width equal to zero are termed as ideal RVEs.

4.2.2 FE implementation

The FE analysis of the micro-mechanical model of zipper cut with defects was done with three methods. Firstly, through explicit modelling of the defects and, then through pixelation and defect layer method. The defect layer method was slightly modified and is termed as modified defect layer method. The modified defect layer method involved calculation of the defect volume fraction in the element, however, the property assignment to the element was not done through creating the micro-mechanical models, as discussed in Section 3.2.2, but through linear interpolation of the properties of resin and composite. It is discussed, in-detail, later in this section. Once the comparison was drawn between the pixelation and modified defect layer method. The better approach was chosen to study ideal RVEs of zipper cuts. Furthermore, ideal RVEs, and RVEs with defect of single sided cuts was also studied with the better approach.

Mesh generation

In order to model explicitly the defects in the RVE, *Triangle* software was used. *Triangle* is a meshing tool which generates the triangular mesh elements on the user defined geometry. The software was developed by *Shewchuk* [42]. For the generation of the triangular mesh on the RVE, *.poly* file has to be generated and these file works as input files for the software. The generation of the mesh can be controlled by different handles which were described in the documentation of the *Triangle* software. For the zipper cut RVE with defects, the node generation was done on the different segments of the RVE as shown in Figure 4.7.

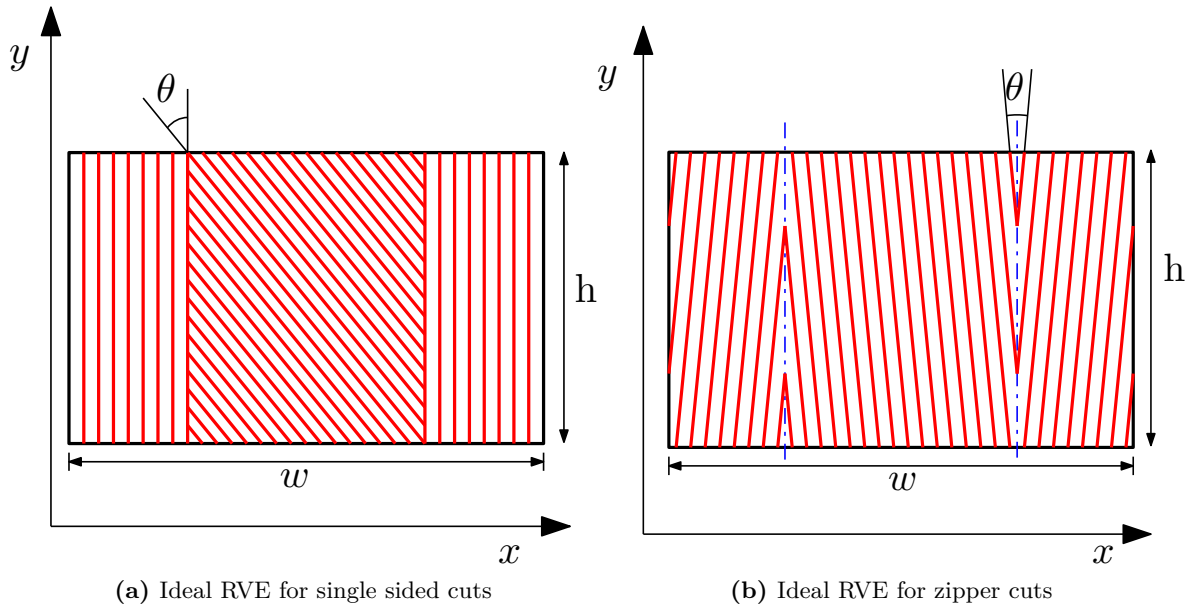


Figure 4.6: Ideal RVE selected for different cuts

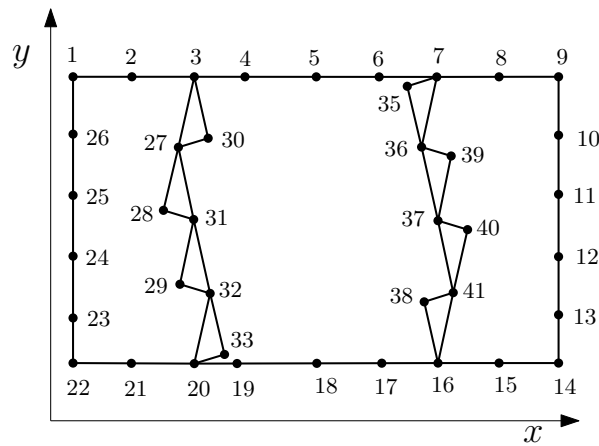
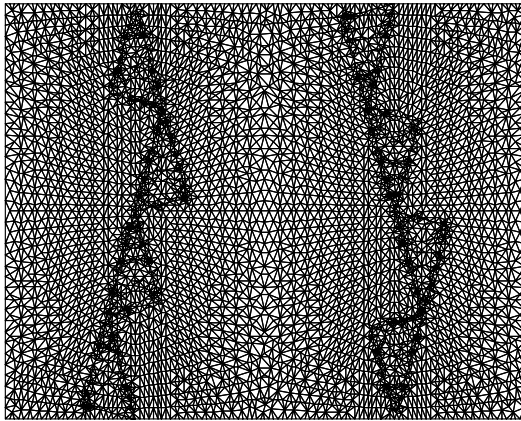


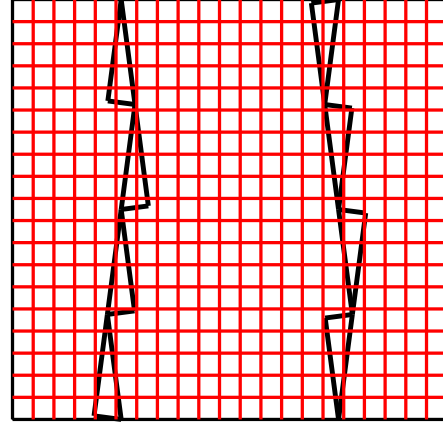
Figure 4.7: Node generation on the RVE of Zipper cuts

Every node was numbered and based on these numbers edges were defined which contains the geometry. A sample *.poly* file is shown in appendix Section A.1. In order to make the mesh periodic the pattern of nodes on the opposite edges of the RVE has to be same and should not get altered during the mesh generation process. *Triangle* provides a specific handle (-Y), which does not disturbs the nodes specified at the boundaries. The sample mesh generated on the RVE, from *Triangle* is shown in Figure 4.8a. The element type S3 was provided to these element. S3 2D-triangular element type for which plane stress condition is assumed.

For the pixelation and modified defect layer method square mesh was generated. The plane stress element type S4R were used for analysis. The sample square element mesh is shown in Figure 4.8b. Since for the single sided cut, explicit modeling approach was not used the mesh generated for this case were also simple square mesh. Furthermore, for the ideal RVEs



(a) Sample mesh on the RVE of Zipper cuts through *Triangle* software



(b) Sample mesh on the RVE of Zipper cuts for pixelation and modified defect layer method approach

Figure 4.8: Sample Meshes

of both cuts, simple square mesh was used for analysis.

Property assignment

The material properties used for the study are shown in Table 4.1 and Table 4.2. Hereafter, these material are termed as Material 1 and Material 2 respectively. The material properties of the composite are for the unidirectional layer ply. The property of the composite have subscript, 1 and 2, these subscript represents the direction. '1' and '2' stand for the direction along the fibres and perpendicular to the fibres. And '12' subscript represents the plane formed by '1' and '2' direction. The thickness of a ply is assumed to be 0.2mm. For the each method of FE analysis, the property assignment to the element were different. For explicit modeling method, the property were given to the element based on their position in the geometry. If the elements lies in the tow drop region the property of resin was given, else if the element lies in the composite region 1, 2 and 3 shown in Figure 4.9, properties of composite was given. The orientation of the composite was given based on the angle θ . If the element lies in region 1 and 3 shown in Figure 4.9, then orientation of was given as $\frac{\theta}{2}$, else for the region 2, orientation was given as $\frac{\theta}{2}$.

Composite		Resin	
E_1	161 GPa	E	11.4 GPa
E_2	11.4 GPa	ν	0.32
G_{12}	5.17 GPa	-	-
ν_{12}	0.32	-	-

Table 4.1: Material 1 Properties : Material system IM7/8552

Composite		Resin	
E_1	143 GPa	E	3.7 GPa
E_2	9.1 GPa	ν	0.3
G_{12}	4.8 GPa	-	-
ν_{12}	0.3	-	-

Table 4.2: Material 2 Properties : Material system G40-800/5276-1

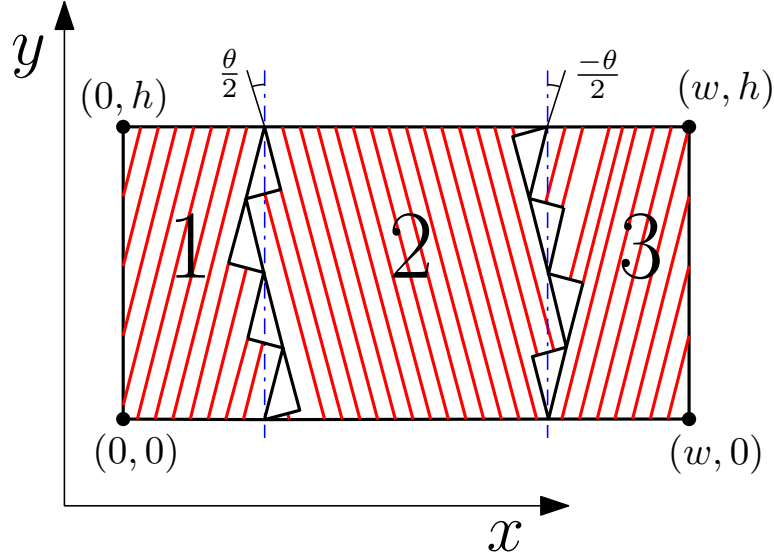


Figure 4.9: Regions in the zipper cut RVE

For the case of pixelation, as discussed in Section 3.2.2, the coordinates of the centroid of the element were calculated and then the coordinates were checked whether they lie inside the resin rich area or the composite. In order to evaluate, whether the centroid lies in the tow drop area of the micro-mechanical models, a *Matlab* function named *Inpolygon* was used. This function returns, 1, if the point lies in the polygon or at the edge of the polygon, else, 0. Thus, centroids were detected, whether, it lies inside the tow drop region or not and properties were assigned accordingly.

Defect layer method was modified for this research. Instead of calculating the modulus through the micro-mechanical model as discussed in Section 3.2.2, here, the properties were evaluated through linear interpolation of the properties between the composite and resin based on the volume fraction of the composite and resin present in the element. As shown in Figure 4.10, a element which covers the three region of the micro-mechanical model of zipper cuts. A_1 , A_2 and A_R are the areas which is covered by element in 1, 2 and tow drop region. Now, to evaluate the coordinates of the points, which form A_1 , A_2 and A_R , *Matlab* function *Polybool* was used. This function gives the coordinates of the points which form the area of two intersecting polygons. For example, A_1 is the intersecting region of element shown in Figure 4.10 and the region 1 shown in Figure 4.9. Similarly, points which form the areas A_2 and A_R were evaluated. The surface area calculation was done through *polyarea* function in *Matlab*. *Polyarea* function gives the area of any arbitrary polygon if the coordinates of the

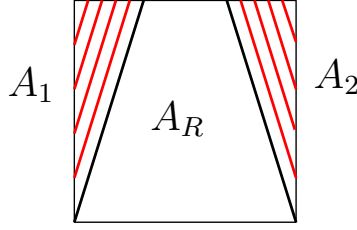


Figure 4.10: An element covering three regions of the zipper cut RVE

vertex of the polygon are known. The surface area of areas A_1 , A_2 and A_R were evaluated by this function. After, calculation of surface area the property to the element was assigned by following formula shown in Eq. (4.1).

$$\mathbf{Q}_e = \frac{A_1 \mathbf{Q}_{\frac{-\theta}{2}} + A_2 \mathbf{Q}_{\frac{\theta}{2}} + A_R \mathbf{Q}_R}{A_1 + A_2 + A_R} \quad (4.1)$$

Where, \mathbf{Q}_e is the stiffness tensor assigned to the element. $\mathbf{Q}_{\frac{-\theta}{2}}$, $\mathbf{Q}_{\frac{\theta}{2}}$ and \mathbf{Q}_R is the stiffness tensor of 1, 2 and tow drop regions respectively. This process was used to assign properties to every element, for the case of modified defect layer method.

Boundary condition

The boundary condition applied to the micro-mechanical models were periodic boundary conditions. To apply the periodic boundary condition on the RVE shown in the Figure 4.9, an average strain should be applied to the RVE. For two dimensional case and assuming plane stress condition, the displacement in the RVE can be written as in Eq. (4.2).

$$\begin{aligned} u(x, y) &= \epsilon_1 x + \frac{\epsilon_6}{2} y + \tilde{u}(x, y) \\ v(x, y) &= \epsilon_2 y + \frac{\epsilon_6}{2} x + \tilde{v}(x, y) \end{aligned} \quad (4.2)$$

Here, (u, v) are the displacement fields at point (x, y) . ϵ_1 and ϵ_2 are the average normal strains in x and y direction. ϵ_6 is the average engineering shear strain in the $x - y$ plane. Lastly, (\tilde{u}, \tilde{v}) are the oscillating component of the displacement at point (x, y) . Evaluating different strain components from the assumed displacement field Eq. (4.3), Eq. (4.4) and Eq. (4.5) will be obtained.

$$\epsilon_{xx}(x, y) = \frac{\partial u}{\partial x} = \epsilon_1 + \frac{\partial \tilde{u}}{\partial x} \quad (4.3)$$

$$\epsilon_{yy}(x, y) = \frac{\partial v}{\partial y} = \epsilon_2 + \frac{\partial \tilde{v}}{\partial y} \quad (4.4)$$

$$\epsilon_{xy}(x, y) = \frac{1}{2} \left(\frac{\partial u}{\partial y} + \frac{\partial v}{\partial x} \right) = \frac{\epsilon_6}{2} + \frac{1}{2} \left(\frac{\partial \tilde{u}}{\partial y} + \frac{\partial \tilde{v}}{\partial x} \right) \quad (4.5)$$

Now, integrating the Eq. (4.3) on both side with respect to x , from $x = 0$ to $x = w$, the Eq. (4.3) can be written as Eq. (4.6).

$$\int_0^w \epsilon_{xx}(x, y) dx = \int_0^w \frac{\partial u}{\partial x} dx = \int_0^w \epsilon_1 dx + \int_0^w \frac{\partial \tilde{u}}{\partial x} dx \quad (4.6)$$

Eq. (4.6) can be simplified to Eq. (4.7)

$$u(w, y) - u(0, y) = \epsilon_1 w + \tilde{u}(w, y) - \tilde{u}(0, y) \quad (4.7)$$

Now, due to periodicity in the RVE, opposite edges should behave similarly, thus, $\tilde{u}(w, y) = \tilde{u}(0, y)$ which reduce the Eq. (4.7) to Eq. (4.8)

$$u(w, y) - u(0, y) = \epsilon_1 w \quad (4.8)$$

Similarly, integrating the Eq. (4.4) along y , from $y = 0$ to $y = h$ and integrating Eq. (4.5) first along x and then along y with the same limits and applying the periodicity condition Eq. (4.9), Eq. (4.10) and Eq. (4.11).

$$v(x, h) - v(x, 0) = \epsilon_2 h \quad (4.9)$$

$$u(x, h) - u(x, 0) = \frac{\epsilon_6}{2} h \quad (4.10)$$

$$v(w, y) - v(0, y) = \frac{\epsilon_6}{2} w \quad (4.11)$$

Thus, Eq. (4.8)-(4.11) represent the boundary conditions which are to be applied on the FE periodic meshes. A method was described by *Wu et al* [40] in order to apply the periodic boundary conditions in *Abaqus*. The method suggest to generate a periodic mesh as shown in Figure 4.11. For a general node A on the left edge of the mesh, a pair node B exist on the right edge of the RVE. For these pair of nodes, a fictitious node C can be formed in the *Abaqus* and from node C, node A and B can be tied together. To tie the nodes **Equation* command was used. **Equation* command connects the displacement of the node A, B and C as shown in Eq. (4.12).

$$au_A + bu_B + cu_C = 0 \quad (4.12)$$

where, a , b and c are the coefficient which can be user defined. u_A , u_B and u_C represents the displacement of the nodes in x direction. By comparing Eq. (4.8) and Eq. (4.12), Eq. (4.13) can be written.

$$a = 1 \quad b = -1 \quad c = 1 \quad \text{and} \quad u_C = -\epsilon_1 w \quad (4.13)$$

Similarly, the displacement can be assigned to the different nodes and for different degree of freedom. Through this approach the periodic boundary condition can be applied to the RVE. The boundary condition can also be satisfied for a rigid body motion. Thus, to restrict the rigid body movement of the RVE left bottom corner node was restricted to move in all degree of freedom. The meshes for explicit modeling, pixelation and modified defect layer method case can be given the periodic boundary condition through this methodology.

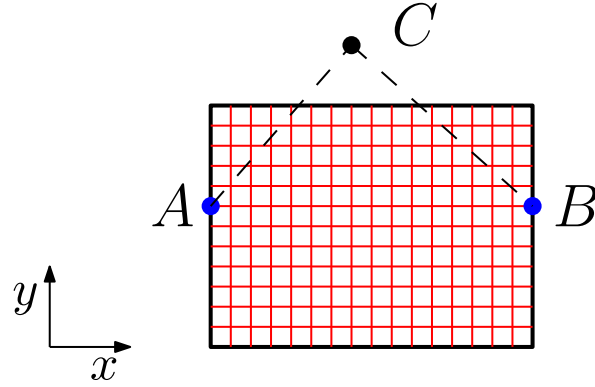


Figure 4.11: Implementation of periodic boundary condition in *Abaqus*

Load cases and evaluation of homogeneous properties

As mentioned in Section 3.4.2, if the average strain in the RVE is known then the calculation of the homogeneous stiffness tensor can be done through Eq. (3.20). Now in 2D case, the value of ϵ_1 , ϵ_2 and ϵ_6 can be user defined. The internal energy density equation for the 2D case can be written as.

$$U = \frac{1}{2} \langle \epsilon \rangle^T \mathbf{Q}_{hom} \langle \epsilon \rangle \quad (4.14)$$

where, U is the internal energy density, $\langle \epsilon \rangle$ is the average strain vector and \mathbf{Q}_{hom} is the homogeneous stiffness tensor of the RVE. The components of average strain vector and the homogeneous stiffness tensor can be written as in Eq. (4.15) and Eq. (4.16).

$$\langle \epsilon \rangle = \begin{bmatrix} \epsilon_1 \\ \epsilon_2 \\ \epsilon_6 \end{bmatrix} \quad (4.15)$$

$$\mathbf{Q}_{hom} = \begin{bmatrix} Q_{11}^{hom} & Q_{12}^{hom} & Q_{16}^{hom} \\ Q_{12}^{hom} & Q_{22}^{hom} & Q_{26}^{hom} \\ Q_{16}^{hom} & Q_{26}^{hom} & Q_{66}^{hom} \end{bmatrix} \quad (4.16)$$

Now, if the average strains are known, then these can be applied to the RVE and the internal energy density of the RVE can be calculated. This will enables us to compute the homogenized stiffness tensor from Eq. (4.14). In order to calculate the every component of the homogenized stiffness tensor, the Eq. (4.14) must be written in expanded form as shown in Eq. (4.17).

$$U = \frac{1}{2} [\epsilon_1 Q_{11}^{hom} \epsilon_1 + \epsilon_2 Q_{22}^{hom} \epsilon_2 + \epsilon_6 Q_{66}^{hom} \epsilon_6 + 2\epsilon_1 Q_{12}^{hom} \epsilon_2 + 2\epsilon_1 Q_{16}^{hom} \epsilon_6 + 2\epsilon_2 Q_{26}^{hom} \epsilon_6] \quad (4.17)$$

Now, if average state in a particular RVE is $\epsilon_1 = 1$ and $\epsilon_2 = \epsilon_6 = 0$, then Eq. (4.17) will be equivalent to Eq. (4.18). Therefore, if the internal energy density in that RVE is known the

Q_{11}^{hom} can be evaluated. To attain the average strain state in the RVE, the value of the ϵ_1 , ϵ_2 and ϵ_6 must be given in periodic boundary condition specified in Eq. (4.8)-(4.11). This is one load case to evaluate one component of the homogeneous stiffness tensor.

$$U = \frac{1}{2}[Q_{11}^{hom}] \quad (4.18)$$

Due to the symmetry of the homogeneous stiffness tensor, 6 load cases will be required in order to evaluate all components of the homogeneous stiffness tensor from a particular RVE. The six load cases are described in Table 4.3. Since, the composite material behave linear elastically, thus, linear elastic analysis was carried out for each load case in *Abaqus*.

Load Cases	1	2	3	4	5	6
ϵ_1	0.001	0	0	0.001	0.001	0
ϵ_2	0	0.001	0	0.001	0	0.001
ϵ_6	0	0	0.001	0	0.001	0.001

Table 4.3: Load cases to evaluate a homogeneous stiffness tensor

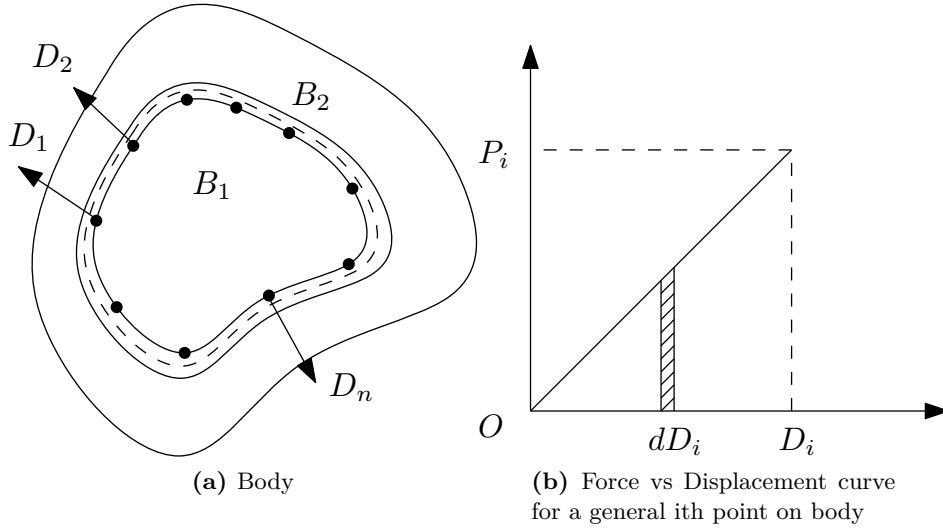


Figure 4.12: Body subjected to the displacement

Now, calculation of the internal energy density is still required to calculate the homogeneous stiffness tensor. The internal energy can be calculated from FE results of RVE, by calculating the external work done by the surrounding on the RVE. Due to the periodicity conditions, the traction generated on the opposite edges will be equal and opposite as mentioned in Section 3.4.2. The work done by these traction forces on the RVE will contribute towards the internal strain energy stored in the RVE [43]. In order to calculate the strain energy of the body B_1 with linear elastic material subjected to the displacement $D_1, D_2 \dots D_n$ as shown in Figure 4.12a. Let it be constrained by the another deformable linear elastic body B_2 . Due to the restriction in the deformation of the body B_1 , the force generated at the point of deformation be $P_1, P_2 \dots P_n$. The force generated at a general point, i , will have the generated force versus displacement curve as shown in Figure 4.12b. Assuming, for a

infinitesimally small displacement, the force generation is constant and the body B_1 is under equilibrium. Thus, the work done at the i th node for this displacement is given as in Eq. (4.19)

$$dW_i = P_i dD_i \quad (4.19)$$

The total work done could be evaluated by the integrating Eq. (4.19) from displacement of 0 to D_i which gives Eq. (4.20).

$$W_i = \int_0^{D_i} P_i dD_i \quad (4.20)$$

Now, due to the assumption of the linear elastic material, force generated at i th point can be written as in Eq. (4.21).

$$P_i = K D_i \quad (4.21)$$

Where, K is the stiffness of the body. From Eq. (4.20) and Eq. (4.21), work done by the force can be calculated at the point i , as represented in Eq. (4.22).

$$W_i = \frac{1}{2} K D_i^2 = \frac{1}{2} P_i D_i \quad (4.22)$$

Thus, the total work done by all the forces can be given by Eq. (4.23)

$$W = \frac{1}{2} \sum_{i=1}^n P_i D_i \quad (4.23)$$

This work, W , done by body B_2 on B_1 will be the strain energy stored in the body B_1 . To calculate the strain energy density, work done should be divided by the volume of body B_1 . This is the similar case for the RVEs which are studied in this thesis. RVEs are similar to body B_1 , which are provided displacement but are restricted by the constraints imposed by periodic boundary condition. Thus, similar approach is applied to calculate the strain energy of the RVE. To calculate strain energy from FE analysis, a post processing script was written on python. Through this script, the nodal forces and displacements of nodes at the edges were extracted through output database file of *Abaqus*. The edge nodes were only considered as the forces at the internal node should sum up to zero. The strain energy was calculated through Eq. (4.23). To extract nodal force, **Nforce* variable was extracted from the output database. The script used to evaluate the strain energy is given in Appendix A.2.

Thus, applying 6 load cases on a particular RVE and further, evaluating the internal energy density for each case will enable us to calculate the homogenized stiffness tensor of the RVE. This homogenized stiffness tensor will take account of the defects on the properties of the composite material. The variables like fibre angle distortion, tow width and course width can be changed to evaluate the effect of individual variables on the properties of the composite.

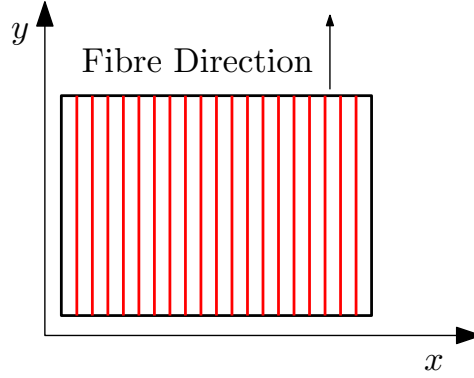


Figure 4.13: Baseline Ply

4.2.3 Knock-down factors

In Section 3.4.3, knock-down factors were introduced. The knock-down factors were evaluated by solving the eigen value problem as shown in Eq. (4.24).

$$(\mathbf{Q}_{hom} - \mathbf{Q}_o)\mathbf{T} = \lambda\mathbf{Q}_o\mathbf{T} \quad (4.24)$$

Here, \mathbf{Q}_{hom} and \mathbf{Q}_o are the homogenized stiffness tensor of RVE with defects and baseline stiffness tensor respectively. λ is the eigen value which can be thought of as the ratio of the change in the baseline stiffness tensor due to the defects to the baseline stiffness tensor. And \mathbf{T} is the vector along which the change has occurred. If the eigen values are multiplied by 100, it gives the percentage change in the stiffness tensor. This is termed as percentage equivalent of the eigen value. Hereon, if λ is referred in the thesis, then it is treated as the diagonal matrix with components of λ at the diagonal position. And if individual components are referred then for the same matrix the components are written as λ_1 , λ_2 and λ_3 . Similar with the case of \mathbf{T} , if vector \mathbf{T} is referred then the vectors is a matrix with each column representing the component of vectors corresponding to respective eigen value. And if the components of the vector \mathbf{T} is referred then the individual vector \mathbf{T}_1 , \mathbf{T}_2 and \mathbf{T}_3 are represented. The representation is given in Eq. (4.25).

$$\lambda = \begin{bmatrix} \lambda_1 & 0 & 0 \\ 0 & \lambda_2 & 0 \\ 0 & 0 & \lambda_3 \end{bmatrix} \quad \mathbf{T} = [\mathbf{T}_1 \quad \mathbf{T}_2 \quad \mathbf{T}_3] \quad (4.25)$$

This section deals with the evaluation of the knock down factors through Eq. (4.24) and from the FE analysis of the RVEs discussed for two different cuts. To evaluate the knock down factors, firstly, a baseline ply has to be selected on which the knock down factors can be applied to get the properties of plies with defect. For this thesis, the baseline ply is shown in Figure 4.13. This ply contains no fibre angular distortion and defects. And the fibres are aligned along the y -axis, thus, it is 0° ply in y -direction. This baseline was chosen because, for all the RVEs discussed for zipper and single sided cuts, if, $\theta = 0$, then all the RVEs will become the baseline ply with no defects and all fibres will be aligned in the y -direction. The evaluation of \mathbf{Q}_o can be done from the material properties and using Eq. (3.4) .

Now, there are two types of cuts and each cut has two RVEs, ideal and with tow drop defects. For both the cuts, zipper and single sided cut, the homogenized stiffness tensor evaluated from ideal RVEs are termed as \mathbf{Q}_θ . Thus, this stiffness tensor, \mathbf{Q}_θ , only accounts for the influence of the fibre angle distortion θ . Similarly, for both cuts, the homogenized stiffness tensor evaluated from RVEs with tow drop defects are termed as \mathbf{Q}_d . Thus, this stiffness tensor, \mathbf{Q}_d , will account for the influence of angle distortion and the tow drop defects. Now, for both the cuts, at a certain angular distortion θ , both RVEs, ideal and with tow drop defects, can be analyzed through periodic homogenization and homogenized stiffness tensor can be calculated. From this analysis, at a certain angular distortion, the effect of angular distortion and tow drop can be evaluated. To evaluate it Eq. (4.26) and Eq. (4.27) can be applied.

$$(\mathbf{Q}_\theta - \mathbf{Q}_o)\mathbf{V}_\theta = \lambda_\theta \mathbf{Q}_o \mathbf{V}_\theta \quad (4.26)$$

$$(\mathbf{Q}_d - \mathbf{Q}_\theta)\mathbf{V}_d = \lambda_d \mathbf{Q}_\theta \mathbf{V}_d \quad (4.27)$$

Here, λ_θ represents, the ratio of change in the baseline stiffness tensor due to fibre angle distortion to the baseline stiffness tensor, and \mathbf{V}_θ represents the vector along which the stiffness changes. Similarly, λ_d represents the ratio of change in the stiffness tensor with only angular distortion due to tow drop defects, to stiffness tensor with only angular distortion, and \mathbf{V}_d represents vector along which the stiffness changes respectively. λ_θ and λ_d multiplied by 100, are equivalent to the percentage change in the stiffness tensor. Both, λ_θ and λ_d , are termed as knock-down factors due to different defects on the baseline composite property. The knock-downs can be evaluated for various values of angular distortion (θ), tow width (t_w) and width of RVE (w).

4.3 Results from Micro-Mechanical Models

4.3.1 Range of variables

The results were generated on different ranges of the variables. Table 4.4 shows the range of variables which were chosen for this research. The range of fibre angle distortion was limited to 12° as reported by *Falco et al* [31]. The choice of tow width and width were dependent upon different AFP machine specifications reported by *Lukaszewicz et al* [9]. The thickness of the ply assumed in this analysis was equal to 0.2mm. Since, the presentation of the results for all the values of the variable is not possible, thus, few RVEs were chosen for which results have been reported. The other results have the similar trend as reported in this research. The chosen RVEs are shown in Table 4.5. For these RVEs, the calculation of the knock-down factors have been shown. Also, some other RVEs are also mentioned in the subsequent section with their specifications for which the specific results are reported.

Variables	Ranges
θ	$1^\circ - 12^\circ$
t_w	6.35mm and 3.175mm
w	90mm-450mm

Table 4.4: Range of variables

-	Zipper Cuts		Single Sided cuts	
Variables	RVE1		RVE2	
θ	5°	5°	5°	5°
t_w	6.35mm	0	6.35mm	0
w	203.00mm	203.00mm	203.00mm	203.00mm
h	291.15mm	291.15mm	72.85mm	72.85mm

Table 4.5: Chosen RVEs

4.3.2 Displacement plots

Figure 4.14 and Figure 4.15 represents the displacement plots of different load cases shown in Table 4.3. These plots were extracted from *Abaqus*. The plots are for RVE1 with defects shown in Table 4.5. The material used for analysis was Material 1. In these plots, U1 and U2 represents the displacement in the x and y direction respectively. In all the figures, the deformed version of the RVE is shown. The displacement shown in the legends are in the millimeters. These plots were checked in order to visualize whether the boundary condition implementation is correct or not. For the loadcase 1, shown in Figure 4.14, the average strain of 0.001 was applied in the x -direction. The opposite edges have the same feature, thus, the periodicity conditions are applied correctly. The maximum displacement in x direction is 0.203mm. The displacement in y -direction, U2, is governed by the poisson's effect. The red and blue bands, in Figure 4.14b, are formed in the resin rich areas. These regions also showed maximum displacement compared to surrounding composite region, which is because the poisson's ratio of resin (0.32) is higher than poisson's ratio for composite part ($\nu_{21}=0.022$). Thus, more displacement is shown near resin rich region compared to surrounding composite material. For the loadcase 2, shown in Figure 4.14, the average strain was applied in the y -direction. This resulted into the maximum displacement in the y -direction equal to 0.356mm. U1 plot, in Figure 4.14d, shows that the displacement are hindered at the tow drop locations, else the region has smooth displacement. The U2 plot, shown in Figure 4.14e, shows that there are waviness on the top and bottom edges. The top and bottom edges are free to move and form any shape. But, it should be such that the difference between the displacement of the top and bottom edge should be constant. Thus, the shape of the top and bottom edge can be of any shape, but the shape should be similar. The shape obtained is similar for top and bottom edges, which implies that periodicity boundary conditions are applied correctly. For the Loadcase 3, shown in Figure 4.14, the average engineering shear strain of 0.001 is applied. Here also, for both plots U1 and U2, the shape of the opposite edges are similar thus, the application of the periodicity boundary condition was correct. Furthermore, loadcase 4, 5 and 6, shown in Figure 4.15 are superposition of the loadcase 1 and 2, loadcase 1 and 3, and loadcase 2 and 3, respectively.

4.3.3 Homogeneous stiffness tensor

In order to calculate the homogeneous stiffness tensor from the FE results, firstly, the script shown in Section A.2, was used to calculate the nodal forces and the displacements, for different load cases, from the output database of the FE analysis. From the nodal forces and displacements data, internal energy is calculated for different load cases, from Eq. (4.22).

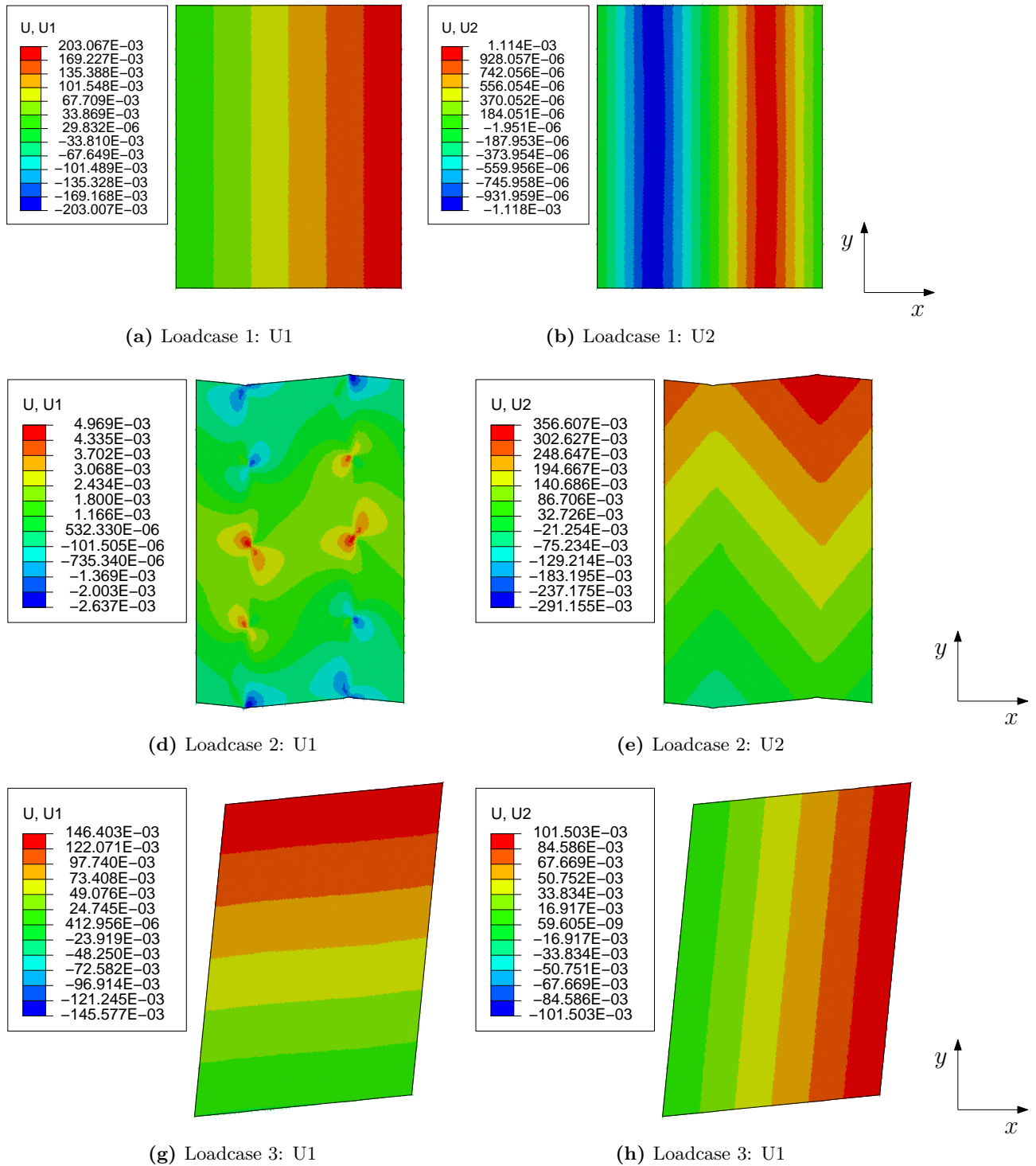


Figure 4.14: Displacement plots for Loadcase 1, 2 and 3. Displacements are in millimeters

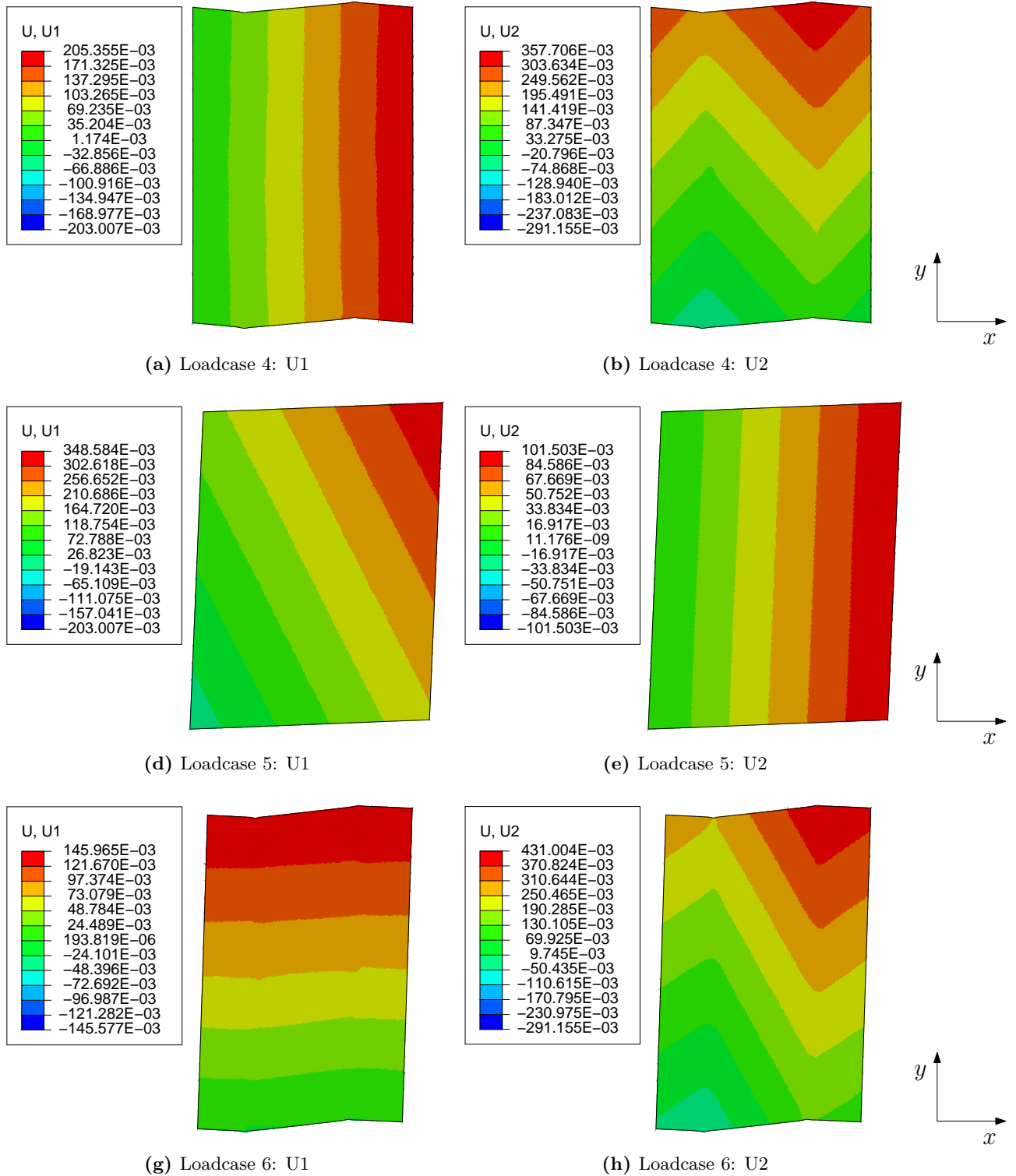


Figure 4.15: Displacement plots for Loadcase 4, 5 and 6. Displacements are in millimeters

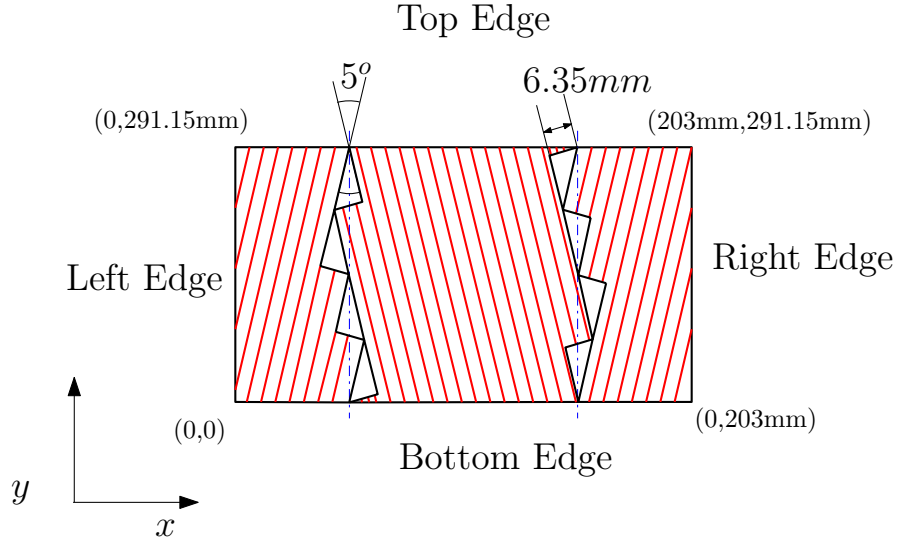


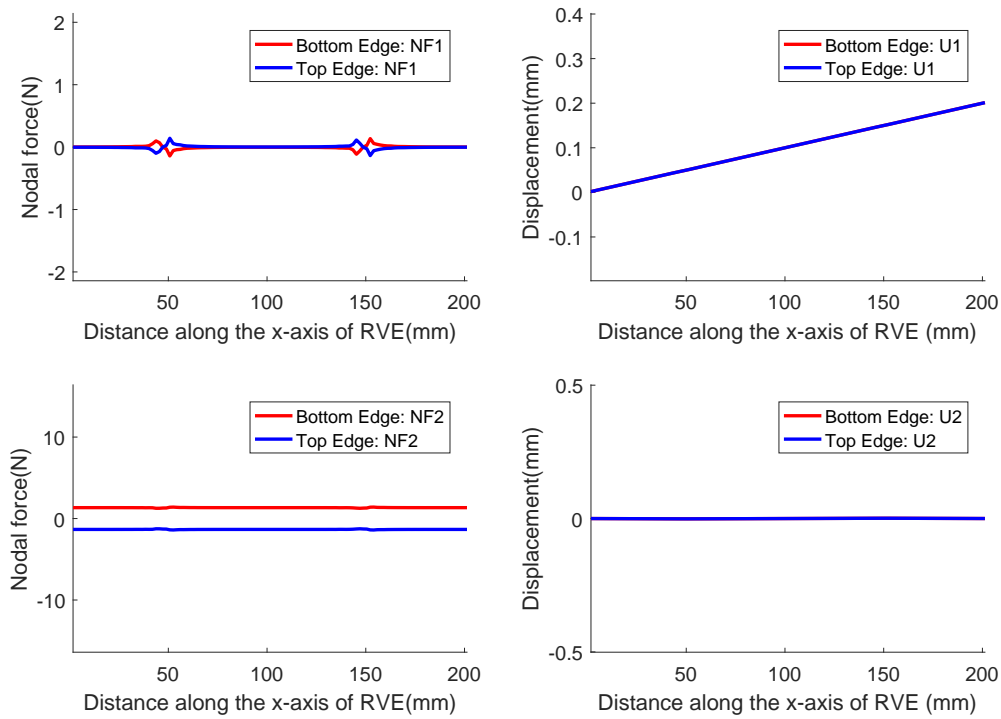
Figure 4.16: Dimensions of zipper cut RVE selected to calculate the homogeneous stiffness tensor.

Thereafter, from Eq. (4.17), the components of the homogeneous stiffness tensor are calculated. Here, in this section, calculation of one homogeneous stiffness tensor is shown. The RVE, for which the homogeneous stiffness tensor is calculated, is the zipper cut RVE with defects. The parameters of this RVE are shown in Figure 4.16. Figure 4.16 shows the coordinates of the corner points and gives the nomenclature to different edges which will be used in further discussion. The nodal forces which will generate due to the applied average strain on the RVE is the in-plane forces. The in-plane forces are termed as NF1 and NF2 in x and y direction. The displacement in x and y directions are termed as $U1$ and $U2$.

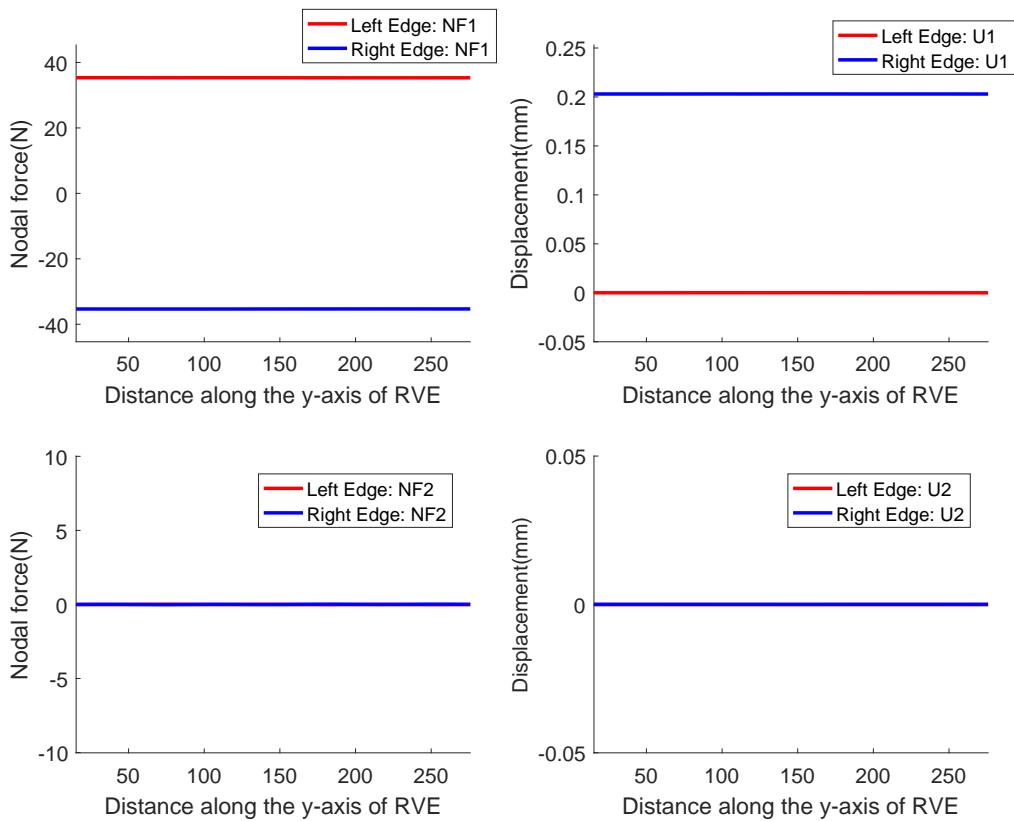
Loadcase 1: $\epsilon_1=0.001$, $\epsilon_2=0$ and $\epsilon_6=0$

The nodal forces and displacements calculated for this case is shown in Figure 4.17a and Figure 4.17b. As it can be seen from Figure 4.17a and Figure 4.17b, that the nodal force generated at the opposite edges are equal and opposite. Also, substituting the value of average strain in Eq. (4.8)-(4.11), it can be inferred that, the displacement $U1$ of Left and Right edge should have a constant difference along the edge, this can be observed in Figure 4.17b, . The displacement $U2$ of Left and Right edge and displacement $U1$ and $U2$ of top and bottom edge are equal. This is because the strain application in those direction is zero. All these conditions suggest that the periodicity conditions are enforced correctly. Now, to calculate the work done, Eq. (4.22) was used and the calculated internal energy of the RVE was equal to $68.12N - mm$. The internal energy density was calculated by dividing this calculated internal energy by the volume of the RVE. The internal energy density was equal to $U = 0.005763 \frac{N}{mm^2}$. Substituting it in Eq. (4.17), Q_{11}^{hom} can be evaluated. The calculated component Q_{11}^{hom} was equal $11525.72MPa$.

Similar calculations can be done for loadcase 2 and loadcase 3. The same procedure of nodal forces and displacements calculation at the edges need to be performed. The figures of the nodal forces for loadcase 2 and loadcase 3 are shown in appendix Section A.3. The calculated components through this procedure were equal to $Q_{22}^{hom} = 148834.63MPa$ and $Q_{66}^{hom} = 5400.91MPa$. For the load cases 4, 5 and 6, the procedure is bit different. For



(a) Loadcase 1: Variation of nodal forces (NF1, NF2) and displacement (U1, U2) at bottom and top edge of the RVE along the x-axis



(b) Loadcase 1: Variation of nodal forces (NF1, NF2) and displacements (U1, U2) at left and right edge of the RVE along the y-axis

Figure 4.17: Loadcase 1

loadcase 4, since both ϵ_1 and ϵ_2 are non-zero, thus, three terms will appear in expression shown in Eq. (4.17). It will look like Eq. (4.28).

$$U = \frac{1}{2}[\epsilon_1 Q_{11}^{hom} \epsilon_1 + \epsilon_2 Q_{22}^{hom} \epsilon_2 + 2\epsilon_1 Q_{12}^{hom} \epsilon_2] \quad (4.28)$$

Now, from loadcase 1 and 2 calculations, the value of Q_{11}^{hom} and Q_{22}^{hom} are known, thus, the value of Q_{12}^{hom} can be calculated from Eq. (4.28). The internal energy density calculation for this case is done through the similar procedure as it was done for the case of loadcase 1. Similarly, loadcase 5 and 6 can be executed. The nodal forces and displacements at the edges for all three cases are also shown in appendix Section A.3. The calculated components are equal to $Q_{12}^{hom} = 3815.92MPa$, $Q_{16}^{hom} = 0.00MPa$ and $Q_{26}^{hom} = -0.67MPa$. Thus, the complete homogeneous stiffness tensor evaluated is shown below.

$$\mathbf{Q}_{hom} = \begin{bmatrix} 11525.72 & 3815.92 & -0.00 \\ 3815.92 & 148834.63 & -0.67 \\ -0.00 & -0.67 & 5400.91 \end{bmatrix} MPa \quad (4.29)$$

4.3.4 Comparison between pixelation and modified defect layer method

As mentioned earlier, the RVEs of zipper cuts with defect were studied from explicit modeling of the defects. However, for the RVE of single sided cuts, the method of analysis has to be chosen in between pixelation and modified defect layer method. In order to compare pixelation and modified defect layer method convergence study was carried out. A general zipper cut RVE with defect was selected. Through which a homogenized stiffness tensor was evaluated by explicit modeling, pixelation and modified defect layer approaches. For convergence study, the mesh size for the case of pixelation and modified defect layer method were reduced to get closer to the stiffness results obtained from explicit modeling case. The convergence to the explicit modeling case was checked because in this case the defects were completely modeled and no assumption was made for properties assignment like linear interpolation of the composite and resin properties as it is used in modified defect layer method. Also, the resin content in the modeled RVE remained constant for any size of the mesh element unlike in the case of pixelation, where the mesh size determines the volume fraction of the defect. The solution from explicit modeling was obtained from mesh with average element size 2.5mm. Below this element size no difference in the components of homogeneous stiffness tensor were observed. To check whether the stiffness tensor obtained from pixelation and modified defect layer method were converging to the tensor evaluated, from explicit modeling Eq. (4.30) was used.

$$(\mathbf{Q}_m - \mathbf{Q}_{ex})\mathbf{V}_m = \lambda_m \mathbf{Q}_{ex} \mathbf{V}_m \quad (4.30)$$

Where, \mathbf{Q}_m is the homogenized stiffness tensor obtained from either pixelation or modified defect layer method. \mathbf{Q}_{ex} is the homogenized stiffness tensor obtained from explicit modeling approach. λ_m is the eigen value which measures the deviation of tensor \mathbf{Q}_m from \mathbf{Q}_{ex} . And \mathbf{V}_m is the vector associated to the eigen values.

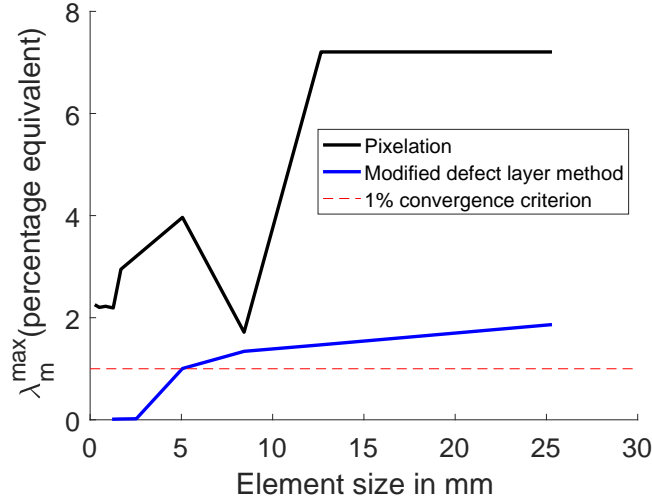


Figure 4.18: Convergence Study: Comparison between pixelation and modified defect layer method.

Solving the eigen value problem, in Eq. (4.30), will result into three eigen values. Only the maximum absolute eigen value were considered. Maximum absolute value of the λ_m was termed as λ_m^{\max} and if this values is less than 1% the results were assumed to be converged. For most of the cases, the convergence to the explicit modeled result were found. However, the value of λ_m^{\max} , for the case of zipper cut RVE, with parameters $\theta = 10^\circ$, $t_w = 6.35mm$ and $w = 101mm$, was not converging for the case of pixelation. The value of λ_m^{\max} , for this RVE obtained for pixelation and modified defect layer method, is shown in Figure 4.18 . For the pixelation case, the value of λ_m^{\max} was equal to 0.022, equivalent to 2.2%, for the element size 0.25mm. And this value did not go further lower to 1%. For the case of modified defect layer method, the value obtained for λ_m^{\max} was equal to 0.011 and 0.0002 (equivalent to 1.1% and 0.2%), for element size 5mm and 2.5mm respectively. Thus, for this particular RVE, pixelation result converged to a result which was 2% offset from the results obtained from explicit modeling. Also, the element size 0.25mm used to reach the result, was 25 times shorter than the minimum defect size of 6.35mm. On the other hand, the result from the modified defect layer method showed convergence to the solution from the explicit modeling case. Also, the element size of 2.5mm was used to reach the complete convergence. It was 2.54 times shorter than the minimum defect size. It could be inferred that the convergence from the modified defect layer method is better than the pixelation approach as for this specific case. Thus, modified defect layer method was used to study single sided cut RVEs with defect and ideal RVEs of zipper and single sided cuts.

4.3.5 Calculations of knock-down factors

In this section, for the chosen RVEs, shown in Table 4.5, results of the homogeneous stiffness tensor have been reported. Also, the knock down factors calculated for different RVEs, from Eq. (4.26) and Eq. (4.27), have been reported. Each RVE has been studied for two materials, Material 1 and Material 2. RVE1 and RVE2 shown in Table 4.5 are two RVEs, ideal and with defects. For RVE1 and RVE2, the calculation of Q_θ and Q_d have been done. Q_θ will

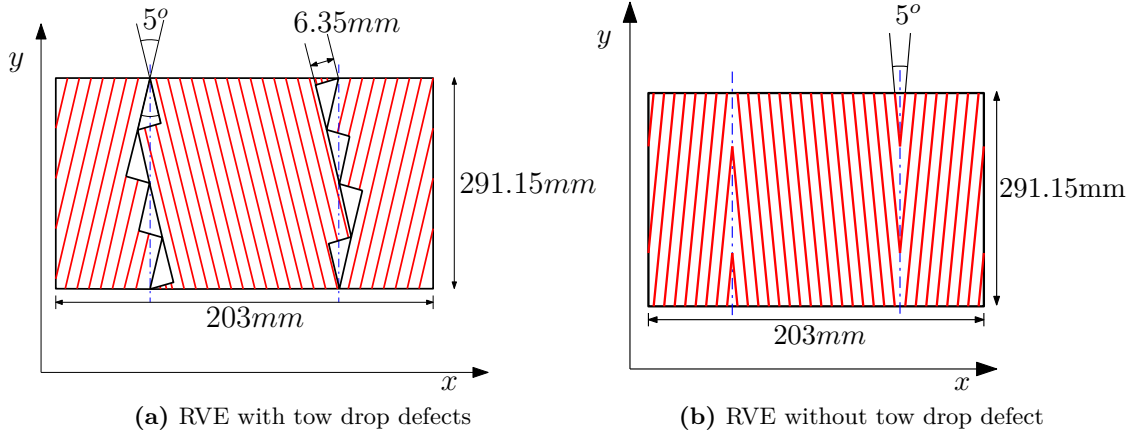


Figure 4.19: Chosen RVE of zipper cut: RVE1

represent the homogeneous stiffness tensor of ideal RVE1 and RVE2. And, similarly, \mathbf{Q}_d will represent the homogeneous stiffness tensor of RVE1 and RVE2 with tow drop defects. The results are presented as follows.

RVE1

For Material 1: The homogeneous stiffness tensors, \mathbf{Q}_θ and \mathbf{Q}_d , calculated for RVE1 and Material 1 are shown in Eq. (4.31).

$$\mathbf{Q}_\theta = \begin{bmatrix} 11490.28 & 3807.37 & 0.00 \\ 3807.37 & 154026.36 & 0.00 \\ 0.00 & 0.00 & 5445.70 \end{bmatrix} MPa \quad \mathbf{Q}_d = \begin{bmatrix} 11525.72 & 3815.92 & -0.00 \\ 3815.92 & 148834.63 & -0.67 \\ -0.00 & -0.67 & 5400.91 \end{bmatrix} MPa \quad (4.31)$$

The components of the RVE are rounded off to second decimal places to take account of the coupling terms. The extension and shear coupling terms in Eq. (4.31) are not completely zero. However, the terms are much smaller than the other terms so they are assumed to be negligible. For the calculation knock-down factors, baseline stiffness tensor has to be evaluated. The baseline stiffness tensor for Material 1 is shown in Eq. (4.32). This tensor will be used to calculate the knock-down factors.

$$\mathbf{Q}_o = \begin{bmatrix} 11483 & 3675 & 0 \\ 3675 & 162175 & 0 \\ 0 & 0 & 5170 \end{bmatrix} MPa \quad (4.32)$$

Substituting the values of \mathbf{Q}_θ , \mathbf{Q}_d and \mathbf{Q}_o from Eq. (4.31) and Eq. (4.32), in Eq. (4.26) and Eq. (4.27). By solving the eigen value problem, the values of λ_θ , λ_d , \mathbf{V}_θ and \mathbf{V}_d can be calculated. By solving these equation three sets of eigen value and eigen vector will be obtained from each equation. The three components of the eigen value λ_θ are termed as λ_{θ_1} , λ_{θ_2} and λ_{θ_3} and, the three components of λ_d are termed as λ_{d_1} , λ_{d_2} and λ_{d_3} . Similarly, the three vectors of \mathbf{V}_θ and \mathbf{V}_d are termed as \mathbf{V}_{θ_1} , \mathbf{V}_{θ_2} , \mathbf{V}_{θ_3} and, \mathbf{V}_{d_1} , \mathbf{V}_{d_2} , \mathbf{V}_{d_3} , respectively. The knock-down values obtained for RVE1 and Material 1 are shown in Eq. (4.33)-(4.36). The

vector components presented in the equations are normalized with the maximum absolute value of its components.

$$\lambda_{\theta_1} = -0.051 \quad \lambda_{\theta_2} = 0.001 \quad \lambda_{\theta_3} = 0.053 \quad (4.33)$$

$$\mathbf{V}_{\theta_1} = \begin{bmatrix} -0.52 \\ 1.00 \\ 0.00 \end{bmatrix} \quad \mathbf{V}_{\theta_2} = \begin{bmatrix} 1.00 \\ 0.01 \\ 0.00 \end{bmatrix} \quad \mathbf{V}_{\theta_3} = \begin{bmatrix} 0.00 \\ 0.00 \\ 1.00 \end{bmatrix} \quad (4.34)$$

$$\lambda_{d_1} = -0.034 \quad \lambda_{d_2} = 0.003 \quad \lambda_{d_3} = -0.008 \quad (4.35)$$

$$\mathbf{V}_{d_1} = \begin{bmatrix} -0.31 \\ 1.00 \\ 0.00 \end{bmatrix} \quad \mathbf{V}_{d_2} = \begin{bmatrix} 1.00 \\ 0.00 \\ 0.00 \end{bmatrix} \quad \mathbf{V}_{d_3} = \begin{bmatrix} 0.00 \\ 0.00 \\ -1 \end{bmatrix} \quad (4.36)$$

Comparing homogeneous stiffness tensors, \mathbf{Q}_θ and \mathbf{Q}_o , from Eq. (4.31) and Eq. (4.32), it can be inferred that due to change in the direction of the fibres from y -axis the reduction in the stiffness property is observed in component Q_{22} of baseline stiffness tensor \mathbf{Q}_o . The reduction in Q_{22} is approximately 5%. Other components in \mathbf{Q}_θ have shown improvement in the properties compared to the baseline stiffness tensor. This behavior is observed because of the misalignment of the fibres from y -axis and aligning more towards the x -axis, as evident from Figure 4.19b. The increase in the Q_{11} and Q_{66} component of \mathbf{Q}_θ is approximately 0.1% and 5% compared to the components of the baseline tensor \mathbf{Q}_o . This behavior is clearly captured by the eigen values λ_{θ_2} and λ_{θ_3} in Eq. (4.33).

λ_{θ_1} shows decrease in the stiffness property by 5.1% in the direction \mathbf{V}_{θ_1} . The vector dominantly affects Q_{22} component in \mathbf{Q}_o . Similarly, λ_{θ_2} and λ_{θ_3} shows an increase of 0.1% and 5.3% in \mathbf{V}_{θ_2} and \mathbf{V}_{θ_3} directions. These vectors dominantly influence the Q_{11} and Q_{66} components of \mathbf{Q}_o . Thus, the eigen values obtained clearly captures the effect on Q_{11} , Q_{22} and Q_{66} . And the vectors give the direction along which the changes are happening. Similar, observations can be drawn by the comparison of \mathbf{Q}_d and \mathbf{Q}_θ from Eq. (4.31). In this case, all the components have decreased with the introduction of tow drop defects except for Q_{11} which has increased by 0.3%. This increase in the property is possible as the stiffness of the resin and of the composite in x -direction are very similar for Material 1. Thus, introduction of resin leads to rise in the properties.

For Material 2: The homogeneous stiffness tensors, \mathbf{Q}_θ and \mathbf{Q}_d , calculated for RVE1 and Material 2 are shown in Eq. (4.37).

$$\mathbf{Q}_\theta = \begin{bmatrix} 9160.56 & 2819.70 & 0.00 \\ 2819.70 & 136869.18 & 0.00 \\ 0.00 & 0.00 & 5041.54 \end{bmatrix} MPa \quad \mathbf{Q}_d = \begin{bmatrix} 8895.05 & 2754.95 & 0.00 \\ 2754.95 & 131811.54 & 0.00 \\ 0.00 & 0.00 & 4829.69 \end{bmatrix} MPa \quad (4.37)$$

The baseline tensor for Material 2 is shown in Eq. (4.38)

$$\mathbf{Q}_o = \begin{bmatrix} 9125 & 2746 & 0 \\ 2746 & 143824 & 0 \\ 0 & 0 & 4800 \end{bmatrix} MPa \quad (4.38)$$

The eigen values and vectors calculated from Eq. (4.26) and Eq. (4.27) are shown in Eq. (4.39)-(4.42)

$$\lambda_{\theta_1} = -0.049 \quad \lambda_{\theta_2} = 0.001 \quad \lambda_{\theta_3} = 0.0503 \quad (4.39)$$

$$\mathbf{V}_{\theta_1} = \begin{bmatrix} -0.46 \\ 1.00 \\ 0.00 \end{bmatrix} \quad \mathbf{V}_{\theta_2} = \begin{bmatrix} -1.00 \\ 0.01 \\ 0.00 \end{bmatrix} \quad \mathbf{V}_{\theta_3} = \begin{bmatrix} 0.00 \\ 0.00 \\ 1.00 \end{bmatrix} \quad (4.40)$$

$$\lambda_{d_1} = -0.038 \quad \lambda_{d_2} = -0.029 \quad \lambda_{d_3} = -0.042 \quad (4.41)$$

$$\mathbf{V}_{d_1} = \begin{bmatrix} -0.0031 \\ 0.0026 \\ 0.0000 \end{bmatrix} \quad \mathbf{V}_{d_2} = \begin{bmatrix} 0.0100 \\ 0.0006 \\ 0.0000 \end{bmatrix} \quad \mathbf{V}_{d_3} = \begin{bmatrix} 0.0000 \\ 0.0000 \\ 0.0141 \end{bmatrix} \quad (4.42)$$

Similar, results were obtained for λ_θ and \mathbf{V}_θ for Material 2, as it was obtained in the case of Material 1. It suggests that the effect of the fibre angle distortion is almost similar for both material set. However, as the tow drop defect were introduced, the components of stiffness tensor \mathbf{Q}_θ reduced more than it was reduced in the case of Material 1. This is because of the stiffness property of the resin introduced in Material 2 case. Since, the resin stiffness properties are much lower than the composite properties in all direction for Material 2 case than in the case of Material 1, thus, the reduction in the properties is observed in all directions.

RVE2

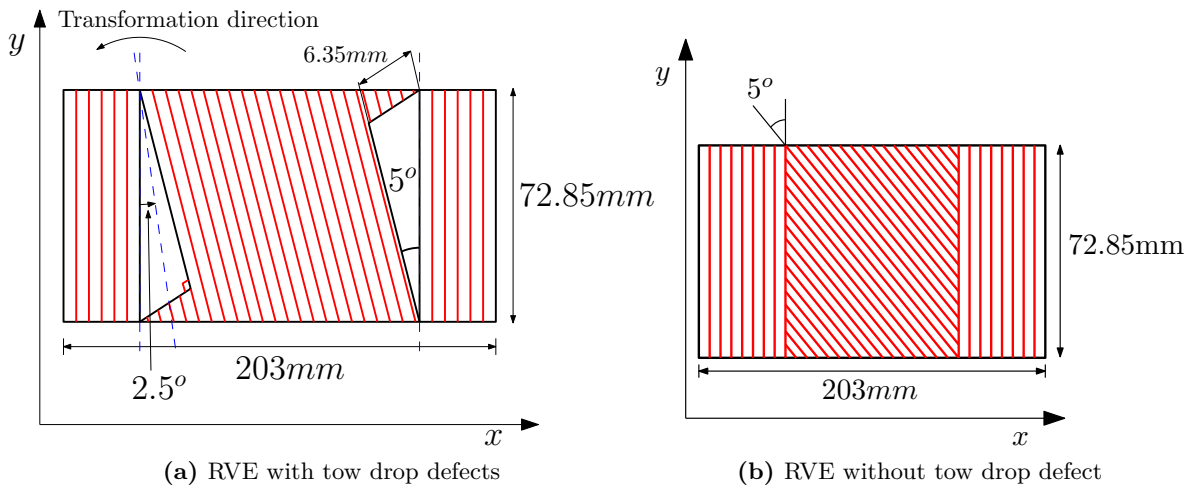


Figure 4.20: Chosen RVE of single sided cut: RVE2

For Material 1: The homogeneous stiffness tensors, \mathbf{Q}_θ and \mathbf{Q}_d , calculated for RVE2 and Material 1 are shown in Eq. (4.43)

$$\mathbf{Q}_\theta = \begin{bmatrix} 11502.14 & 4048.00 & -142.72 \\ 4048.00 & 153976.45 & -5771.71 \\ -142.72 & -5771.71 & 5664.96 \end{bmatrix} MPa \quad \mathbf{Q}_d = \begin{bmatrix} 11524.91 & 4032.45 & -135.91 \\ 4032.45 & 150469.65 & -5460.69 \\ -135.91 & -5460.69 & 5617.24 \end{bmatrix} MPa \quad (4.43)$$

The very first inference from Eq. (4.43) can be made that the coupling terms in the stiffness tensor are not zero. These coupling terms need to be reduced in order to observe the effect of angle distortion and tow drop defects on individual components. To reduce the coupling term the stiffness tensors were rotated and transformed. The rotation of the tensor was done through Eq. (3.5). The stiffness tensor were rotated by angle 2.5° . The rotated stiffness tensor of RVE2 are termed as \mathbf{Q}_θ^r and \mathbf{Q}_d^r . The tensors are shown in Eq. (4.44).

$$\mathbf{Q}_\theta^r = \begin{bmatrix} 11490.63 & 3815.11 & 5.84 \\ 3815.11 & 154453.74 & 310.95 \\ 5.84 & 310.95 & 5432.08 \end{bmatrix} MPa \quad \mathbf{Q}_d^r = \begin{bmatrix} 11514.17 & 3819.78 & 8.26 \\ 3819.78 & 150905.74 & 471.35 \\ 8.26 & 471.35 & 5404.57 \end{bmatrix} MPa \quad (4.44)$$

The stiffness tensors in Eq. (4.44) suggest that the coupling terms are not completely zero but have been reduced. This is because single sided cuts do not have symmetry at the intersection of the two courses. Thus, transformation could reduce the terms but can not fully eliminate it. It can eliminate the individual coupling terms at particular angle but both coupling term can not be eliminated at certain angle simultaneously. Thus, a value of 2.5° was chosen for this case which is half of the angular distortion in the RVE. The rotation of the tensor is in the direction shown in Figure 4.20a. For cases with angular distortion θ , the angle of transformation was $\frac{\theta}{2}$ in the same direction. The tensors in Eq. (4.44), were used for the calculation of the knock-down factors. The knock-down factors calculated from the rotated stiffness tensor are given a superscript 'r'. The baseline stiffness tensor used for the calculation is the same tensor shown in Eq. (4.32). The calculated knock-down factors for this case are given in Eq. (4.45)-(4.48).

$$\lambda_{\theta_1}^r = -0.050 \quad \lambda_{\theta_2}^r = 0.001 \quad \lambda_{\theta_3}^r = 0.052 \quad (4.45)$$

$$\mathbf{V}_{\theta_1}^r = \begin{bmatrix} -0.56 \\ 1.00 \\ -0.05 \end{bmatrix} \quad \mathbf{V}_{\theta_2}^r = \begin{bmatrix} 1.00 \\ 0.02 \\ -0.04 \end{bmatrix} \quad \mathbf{V}_{\theta_3}^r = \begin{bmatrix} 0.00 \\ 0.02 \\ 1.00 \end{bmatrix} \quad (4.46)$$

$$\lambda_{d_1}^r = -0.025 \quad \lambda_{d_2}^r = 0.002 \quad \lambda_{d_3}^r = -0.004 \quad (4.47)$$

$$\mathbf{V}_{d_1}^r = \begin{bmatrix} 0.38 \\ -1.00 \\ 0.28 \end{bmatrix} \quad \mathbf{V}_{d_2}^r = \begin{bmatrix} 1.00 \\ 0.00 \\ 0.08 \end{bmatrix} \quad \mathbf{V}_{d_3}^r = \begin{bmatrix} -0.05 \\ 0.05 \\ 1.00 \end{bmatrix} \quad (4.48)$$

The knock-down λ_θ^r obtained for RVE2 and Material 1, shown in Eq. (4.45), are similar to the knock-down λ_θ for the case of RVE 1 and Material 1, in Eq. (4.33). However, the vectors associated with the respective eigen values are different. The vector \mathbf{V}_θ^r , shown in Eq. (4.46), also consist of the terms which influences the extension-shear coupling terms in the baseline tensor. This shows that influence of the angle distortion on the RVE1 and RVE2 are the same, however, the direction of stiffness tensor change are different due to the different geometries of the RVE1 and RVE2. The effect of resin was different in RVE2 than it was in the case of RVE1. Comparing components of λ_d^r and λ_d , in Eq. (4.47) and Eq. (4.35), it can be inferred that the effect of resin was reduced on the stiffness properties on RVE2 compared to RVE1. The effect of resin was less in RVE2 because of the presence of fibres which are in the direction of fibres of the baseline ply, thus this orientation of fibres tend to increase the stiffness properties of the RVE2. Thus, the property reduction due to the resin was subdued.

It can be also seen from \mathbf{Q}_d^r and \mathbf{Q}_θ^r , that the term Q_{26} was increased by 50%, however, this effect was not captured by the values of λ_d . However, the effect on the components Q_{11} , Q_{22} and Q_{66} was clearly captured by the eigen values. The changes in the components Q_{22} , Q_{11} and Q_{66} were -2.2%, +0.2% and -0.5% and the components of eigen value in percentage form are -2.5%, +0.2% and -0.4%. This shows that the effects of the diagonal terms are given by the eigen values. The effect on the non-diagonal terms are not well captured by it. Thus, the eigen values must be treated as values which shows the effect in the diagonal terms.

For Material 2: The homogeneous stiffness tensors, \mathbf{Q}_θ and \mathbf{Q}_d , calculated for RVE2 and Material 2 are shown in Eq. (4.49)

$$\mathbf{Q}_\theta = \begin{bmatrix} 9173.80 & 3036.29 & -164.18 \\ 3036.29 & 136793.88 & -5146.02 \\ -164.18 & -5146.02 & 5236.66 \end{bmatrix} MPa \quad \mathbf{Q}_d = \begin{bmatrix} 8897.45 & 2948.02 & -151.12 \\ 2948.02 & 131764.70 & -4648.78 \\ -151.12 & -4648.78 & 4960.86 \end{bmatrix} MPa \quad (4.49)$$

It can be inferred from the comparison of \mathbf{Q}_θ and \mathbf{Q}_d tensor that all the components in the \mathbf{Q}_θ have reduced due to the introduction of the tow drop defects. This was expected as the resin properties are much weaker than the composite properties. The knock-down factors were not calculated for RVE2 and Material 2 case.

4.3.6 Knock-down factors for zipper cuts

In Section 4.3.5, the evaluation of the homogeneous stiffness tensor and the knock-down factor for RVE1 was discussed. In this section, knock-down factors of RVEs with different angular distortion are presented. The definition of the various terms remain the same. The knock-down factors were evaluated for two material set, Material 1 and Material 2.

For Material 1:

The results of the eigen values λ_θ for different fibre angle distortion are shown in Figure 4.21. The knock-down factor, λ_θ in Figure 4.21, suggests that the baseline ply properties degrades in one direction and increases in other two directions with increase in θ . This is because the fibres get misaligned from y -direction and gets align more in x -direction with increase in θ . The maximum value of knock-down factors, λ_{θ_1} , λ_{θ_2} and λ_{θ_3} , in form of percentage

equivalent are equal to -23.60%, 0.47% and 30.13%, for maximum angular distortion equal to 12° . The vector associated to λ_θ were comparable to each other for the entire range of the θ . To compare the different vectors Eq. (4.50) was used.

$$\mathbf{V}_\theta^{*T} \mathbf{Q}_o \mathbf{V}_\theta = \mathbf{I} \quad (4.50)$$

Here, \mathbf{Q}_o is the baseline stiffness tensor, \mathbf{V}_θ is the vector evaluated from the eigen value analysis, \mathbf{V}_θ^* is the selected vector which has to be compared to the vector \mathbf{V}_θ , and \mathbf{I} is the identity tensor. For the ideal case, if all the vectors from the analysis are equal to each other then the equality in Eq. (4.50) should hold. However, if the vectors are different to each other than the equality will not hold. The vectors evaluated were comparable suggest that the equality did not hold perfectly but Eq. (4.51) holds true.

$$\mathbf{V}_\theta^{*T} \mathbf{Q}_o \mathbf{V}_\theta \approx \mathbf{I} \quad (4.51)$$

Thus, a set of vectors, \mathbf{V}_θ^{*T} , were selected which were compared against the vectors evaluated for entire range of the angular distortion. For the zipper cuts ideal RVEs, the vector selected for the comparison is shown in Eq. (4.52). These vectors are for the case of $\theta = 1^\circ$ and $w = 406mm$. Each vector is normalized with the maximum absolute value of its components.

$$\mathbf{V}_{\theta_1}^* = \begin{bmatrix} -0.53 \\ 1.00 \\ 0.00 \end{bmatrix} \quad \mathbf{V}_{\theta_2}^* = \begin{bmatrix} -1.00 \\ -0.02 \\ 0.00 \end{bmatrix} \quad \mathbf{V}_{\theta_3}^* = \begin{bmatrix} 0.00 \\ 0.00 \\ 1.00 \end{bmatrix} \quad (4.52)$$

After comparison over the entire range of θ with the selected vector, the maximum deviated result from \mathbf{I} is shown in Eq. (4.53).

$$\mathbf{V}_\theta^{*T} \mathbf{Q}_o \mathbf{V}_\theta = \begin{bmatrix} 1.00 & 0.00 & 0.00 \\ 0.00 & 1.00 & 0.00 \\ 0.00 & 0.00 & 1.00 \end{bmatrix} \quad (4.53)$$

Eq. (4.53) suggests that the deviation of the vectors from each other for the entire range of θ was negligible.

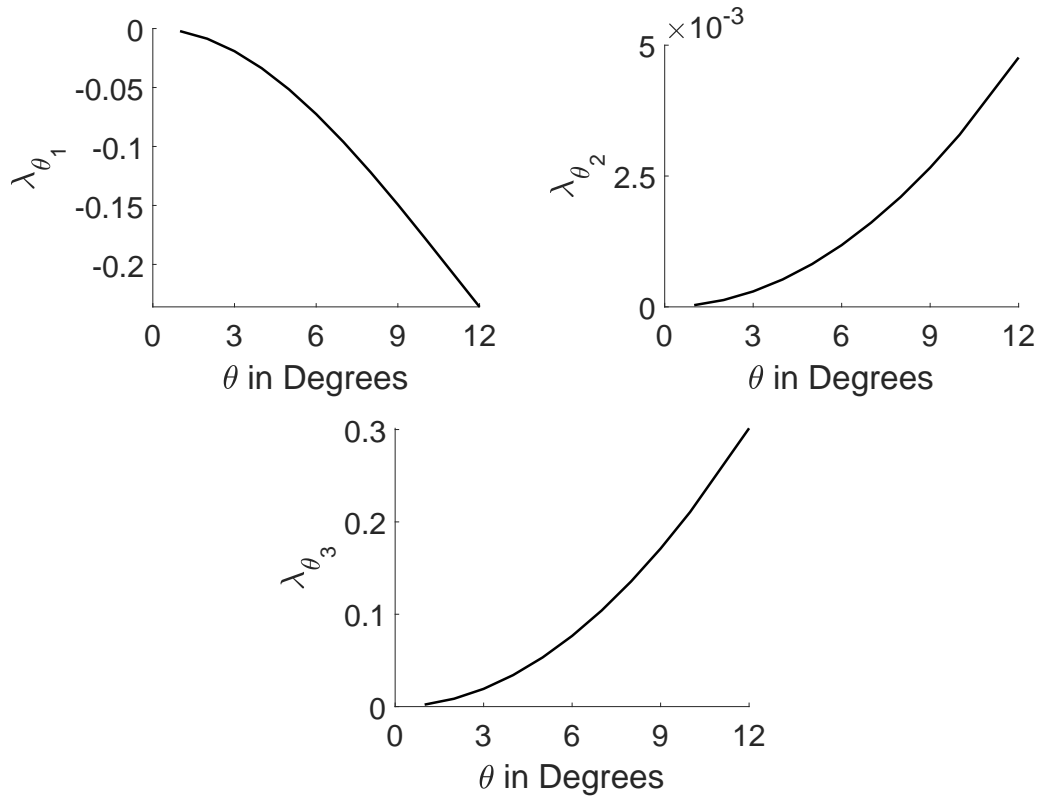


Figure 4.21: Knock-down factors from ideal RVEs of zipper cuts for Material 1

It was found that the knock-down λ_d is linearly dependent upon the volume fraction of defects in a RVE at a certain fibre angular distortion. Figure 4.22 shows λ_d for different values of fibre angular distortion. The slope of the plot for λ_{d_1} and λ_{d_2} case was almost same for different θ values. However, a variation of the slope is observed in the values of λ_{d_3} for different values θ . λ_{d_3} reduces the properties in the shear direction and the properties reduce more with the increase in the angles at same volume fraction of the resin in a RVE. This is because the knock-down factors λ_d is reducing the properties of RVE with angular distortion. At smaller angles θ , the stiffness properties of resin were equivalent to the stiffness properties of composite in perpendicular to the fibre direction and in shear direction. Thus, the impact of resin was small. As the angle increased, the increase in the composite properties were large in the shear direction, upto 30%, however, the rise in properties along x -axis were very small, only 0.5%. Thus, the difference in the properties of the resin and the composite increased rapidly in the shear direction than in the direction along x -axis. Therefore, at large angle more knock-down due to resin was observed. The effect was not observed in the λ_{d_1} case because there was difference of order in the properties of composite and resin in y -direction. Though the properties of composite decreased in y -direction, due to angle change, there was still a difference of order in the stiffness properties between composite and resin. Thus, the impact due to resin in the y -axis direction was similar for higher angle cases. Therefore, the slope was similar.

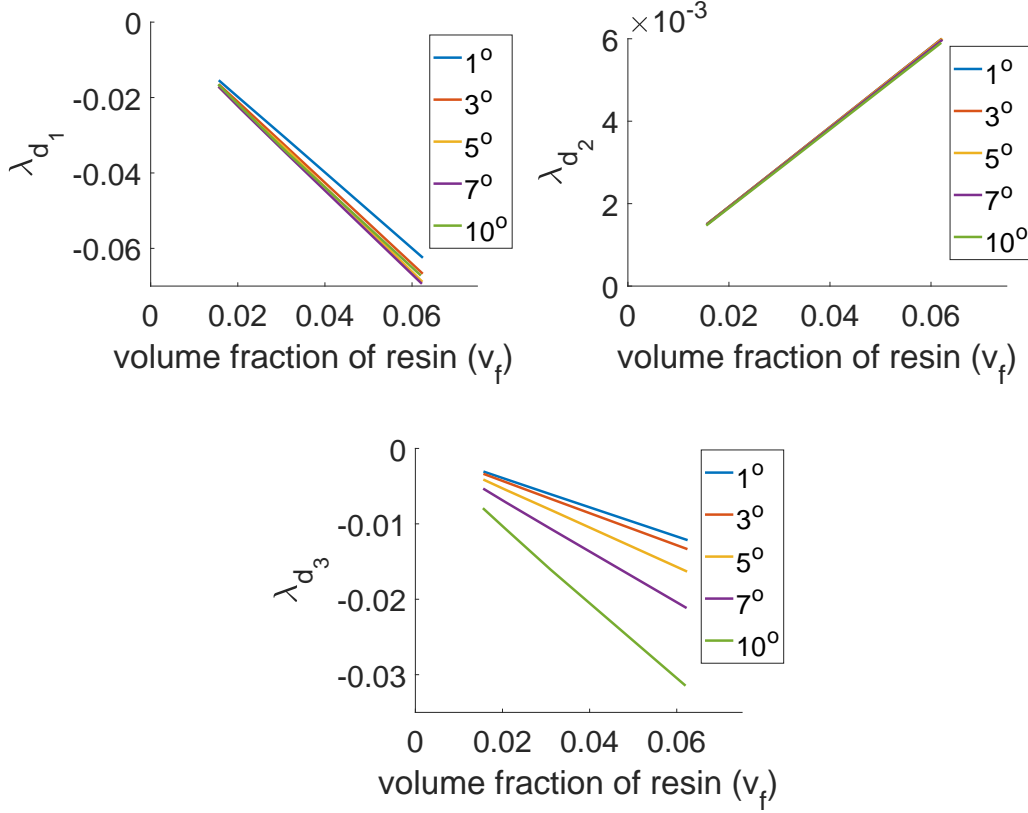


Figure 4.22: Knock-down factors from RVEs of zipper cuts with defects for Material 1

The maximum absolute value of slope obtained for λ_{d1} , λ_{d2} and λ_{d3} are equal to 1.12, 0.096 and 0.51 respectively. It means that for the same volume fraction maximum reduction in the properties will be caused by λ_{d1} . The vector associated to the eigen values also changed with the angle. The vectors, \mathbf{V}_d , were comparable but not equal as it was found in the case of \mathbf{V}_θ . To get the perspective of the direction along which the stiffness property changed, Eq. (4.54) shows the vectors, for the case with $\theta = 1^\circ$, $t_w = 6.35mm$ and $w = 406mm$.

$$\mathbf{V}_{d_1}^* = \begin{bmatrix} -0.32 \\ 1.00 \\ 0.00 \end{bmatrix} \quad \mathbf{V}_{d_2}^* = \begin{bmatrix} 1.00 \\ 0.00 \\ 0.00 \end{bmatrix} \quad \mathbf{V}_{d_3}^* = \begin{bmatrix} 0.00 \\ 0.00 \\ -1.00 \end{bmatrix} \quad (4.54)$$

The vector set in Eq. (4.54) was selected for the vector comparison. The comparison was done from Eq. (4.51). However, instead of the baseline tensor \mathbf{Q}_0 , stiffness tensor \mathbf{Q}_θ was used. The comparison was carried out for different θ and volume fraction of resin. The most deviated result was obtained for RVE with $\theta = 10^\circ$, $t_w = 6.35mm$ and $w = 101mm$, and is shown in Eq. (4.55).

$$\mathbf{V}_d^{*T} \mathbf{Q}_\theta \mathbf{V}_d = \begin{bmatrix} 0.91 & 0.00 & 0.00 \\ 0.00 & 1.10 & 0.00 \\ 0.00 & 0.00 & 1.00 \end{bmatrix} \quad (4.55)$$

The comparison suggests that the matrix is very close to identity tensor. 9% and 10% difference were observed in the first and second diagonal terms. And, the non-diagonal terms are zero compared to the diagonal terms. Thus, the vector deviated from one another but were comparable.

For Material 2:

The knock-down obtained for Material 2 are represented in Figure 4.23 and Figure 4.24. The maximum λ_{θ_1} , λ_{θ_2} and λ_{θ_3} was found for $\theta = 12^\circ$. The values were equivalent to -22.7%, 0.57% and 28.35% respectively. λ_θ results for both Material 1 and Material 2 were almost similar. The difference was observed in the results of λ_d values. λ_d values decreases in all directions as the resin system used is weaker than resin used in Material 1. Also, the variation in the slope of all values λ_d is small for Material 2. This is because for Material 2, the difference between the stiffness properties of the resin and composite is significant in all directions. The maximum absolute value of slope obtained for λ_{d_1} , λ_{d_2} and λ_{d_3} were 1.22, 0.93 and 1.46 respectively. The values of the respective slopes compared to Material 1 have increased. The major change in slope occurred in the values corresponding to λ_{d_2} and λ_{d_3} compared to Material 1 because of the resin properties difference. The slope were 10 and 3 times than the respective slope of eigen values compared to Material 1. The slope for λ_{d_1} has not changed much, approximately increased by 9%, because for both the cases difference in the stiffness property of resin and the composite in y -direction is significant.

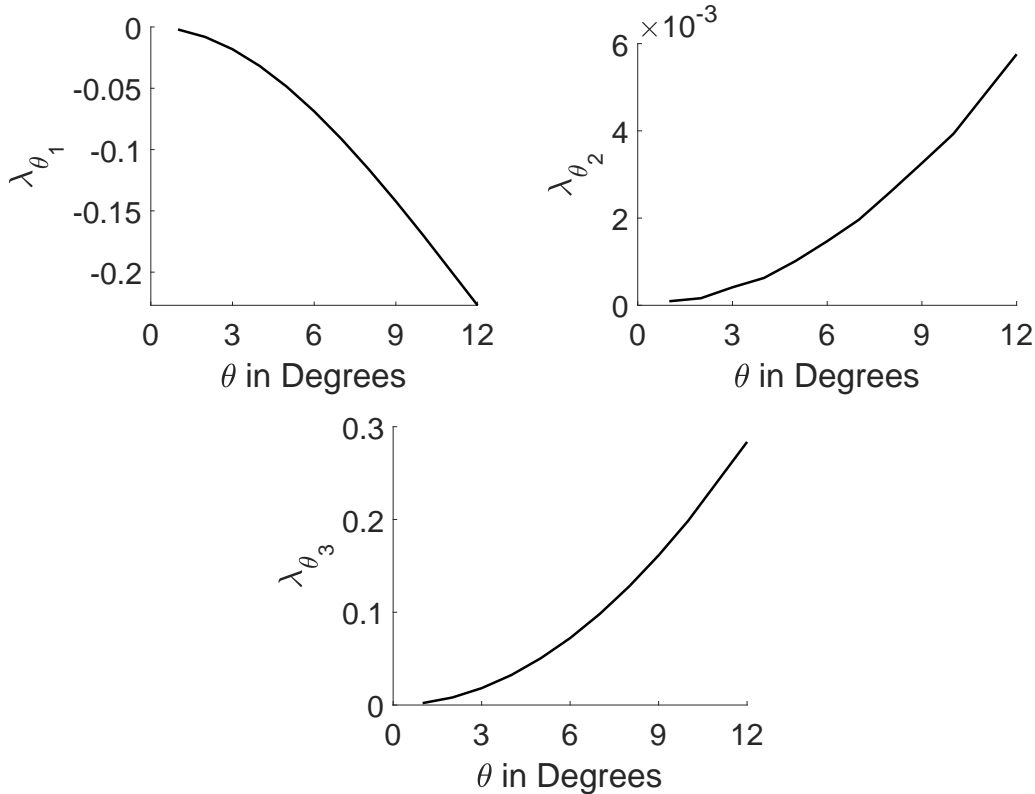


Figure 4.23: Knock-down factors from ideal RVEs of zipper cuts for Material 2

The vectors associated to these eigen values are shown Eq. (4.56) and Eq. (4.57). The com-

ponents of vector \mathbf{V}_θ are shown for the RVE with $\theta = 1^\circ$ and $w = 406mm$. The components of vector \mathbf{V}_d are shown for $\theta = 1^\circ$, $t_w = 6.35mm$ and $w = 406mm$.

$$\mathbf{V}_{\theta_1}^* = \begin{bmatrix} -0.41 \\ 1.00 \\ 0.00 \end{bmatrix} \quad \mathbf{V}_{\theta_2}^* = \begin{bmatrix} 1.00 \\ 0.00 \\ 0.00 \end{bmatrix} \quad \mathbf{V}_{\theta_3}^* = \begin{bmatrix} 0.00 \\ 0.00 \\ 1.00 \end{bmatrix} \quad (4.56)$$

$$\mathbf{V}_{d_1}^* = \begin{bmatrix} -0.56 \\ 1.00 \\ 0.00 \end{bmatrix} \quad \mathbf{V}_{d_2}^* = \begin{bmatrix} 1.00 \\ 0.02 \\ 0.00 \end{bmatrix} \quad \mathbf{V}_{d_3}^* = \begin{bmatrix} 0.00 \\ 0.00 \\ 1.00 \end{bmatrix} \quad (4.57)$$

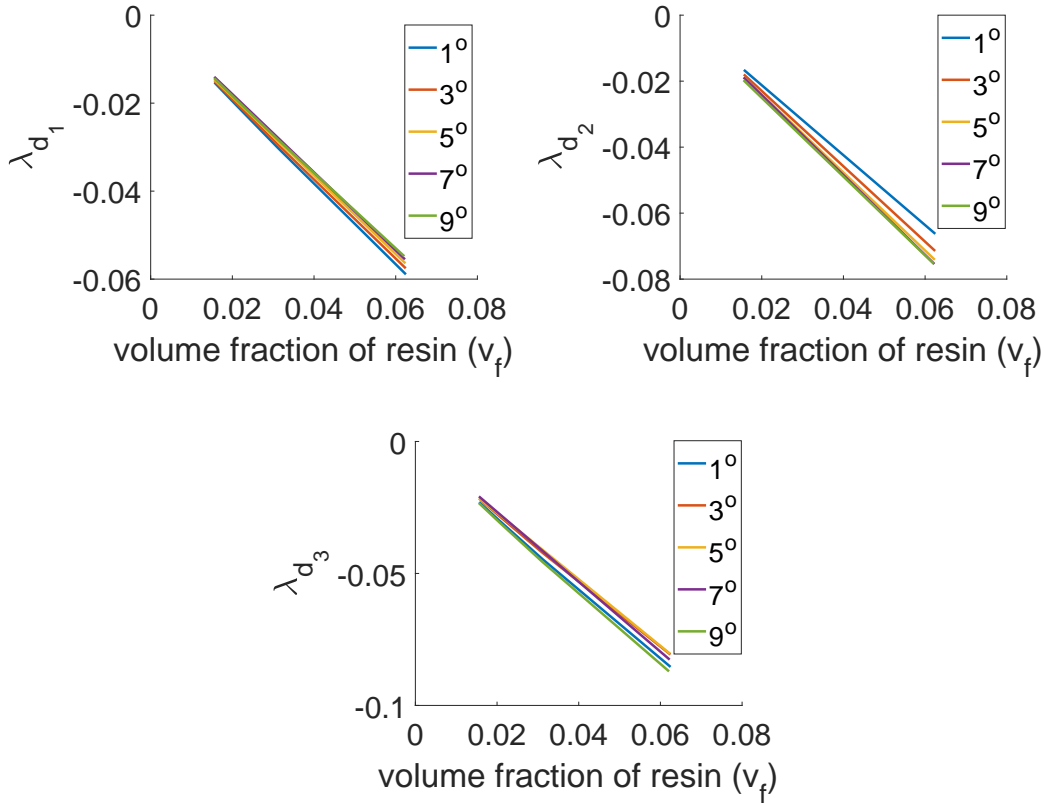


Figure 4.24: Knock-down factors from RVE of zipper cuts with defects for Material 2

The vectors shown in Eq. (4.56) and Eq. (4.57) were used for comparison of different vectors. The comparison results are shown in Eq. (4.58) and Eq. (4.59). The results are similar to the results obtained in Material 1 case. Some non-diagonal terms are visible however, the terms are very small compared to the diagonal terms. The comparison results are shown for most deviated case. Eq. (4.58) shows the comparison with $\theta = 12^\circ$ and $w = 101mm$. Eq. (4.59) shows the result for RVE with $\theta = 9^\circ$, $t_w = 6.35mm$ and $w = 101mm$.

$$\mathbf{V}_\theta^{*T} \mathbf{Q}_o \mathbf{V}_\theta = \begin{bmatrix} 1.00 & -0.01 & 0.00 \\ -0.01 & 1.00 & 0.00 \\ 0.00 & 0.00 & 1.00 \end{bmatrix} \quad (4.58)$$

$$\mathbf{V}_d^{*T} \mathbf{Q}_\theta \mathbf{V}_d = \begin{bmatrix} 0.93 & -0.04 & 0.00 \\ -0.04 & 1.08 & 0.00 \\ 0.00 & 0.00 & 1.00 \end{bmatrix} \quad (4.59)$$

4.3.7 Knock-down factors for single sided cuts

For single sided cuts, the calculations of knock-down factors were done for Material 1. The eigen values, λ_θ^r , are shown in Figure 4.25. The knock-down factors, λ_θ^r , obtained were comparable as it was obtained in the case of zipper cuts. The maximum value of $\lambda_{\theta_1}^r$, $\lambda_{\theta_2}^r$ and $\lambda_{\theta_3}^r$ were equivalent to -21.40%, 0.48% and 26.73% for the case of maximum angle distortion of 12° . The vectors obtained for the respective eigen values were also similar as in the case of zipper cuts. The selected vector for single sided case is shown in Eq. (4.60). The selected vector is from the RVE with $\theta = 1^\circ$ and $w = 406mm$.

$$\mathbf{V}_{\theta_1}^{*r} = \begin{bmatrix} -0.53 \\ 1.00 \\ -0.03 \end{bmatrix} \quad \mathbf{V}_{\theta_2}^{*r} = \begin{bmatrix} 1.00 \\ 0.01 \\ 0.00 \end{bmatrix} \quad \mathbf{V}_{\theta_3}^{*r} = \begin{bmatrix} 0.00 \\ 0.00 \\ -1.00 \end{bmatrix} \quad (4.60)$$

The comparison of the selected vector with the other vectors were carried out and the most deviated case is given in Eq. (4.61). These comparison result were obtained from $\theta = 12^\circ$ and $w = 101mm$. The result shows that the non-diagonal terms are there in the tensor, however, the value of the non-diagonal terms are very less than the diagonal terms. Thus, the vectors obtained were comparable.

$$\mathbf{V}_\theta^{*rT} \mathbf{Q}_o \mathbf{V}_\theta^r = \begin{bmatrix} 1.00 & 0.02 & 0.03 \\ 0.02 & 1.00 & 0.00 \\ 0.03 & 0.00 & 1.00 \end{bmatrix} \quad (4.61)$$

The results of the λ_d^r are shown in Figure 4.26. The same trend in the result are obtained as it was obtained in the zipper cuts. Linear variation of the knock-down factors was obtained with respect to the volume fraction. And similar variation in the slope of $\lambda_{d_2}^r$ plots were obtained. The maximum absolute value of slope obtained for $\lambda_{d_1}^r$, $\lambda_{d_2}^r$ and $\lambda_{d_3}^r$ are 1.22, 0.10 and 0.35 respectively. The vectors corresponding to the λ_d^r , selected for comparison are shown in Eq. (4.62). The vectors are shown for the RVE with $\theta = 1^\circ$, $t_w = 6.35mm$ and $w = 406mm$.

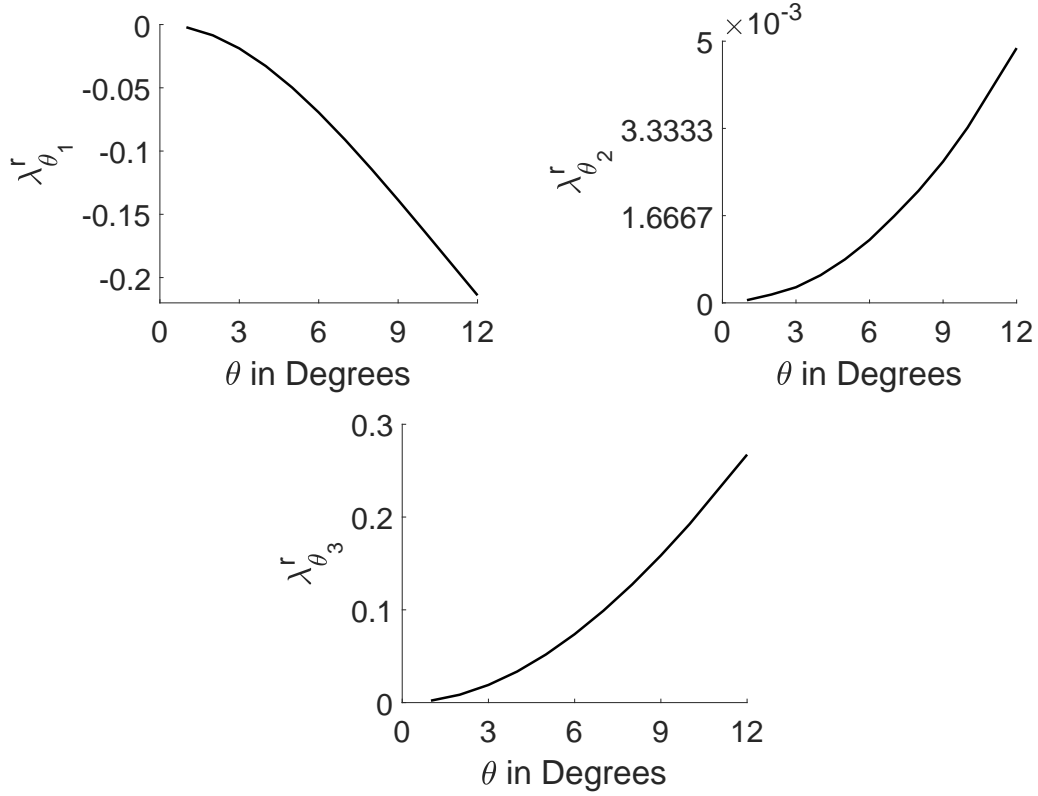


Figure 4.25: Knock-down factors from ideal RVEs of single sided cuts

$$\mathbf{V}_{d_1}^{*r} = \begin{bmatrix} -0.32 \\ 1.00 \\ -0.02 \end{bmatrix} \quad \mathbf{V}_{d_2}^{*r} = \begin{bmatrix} 1.00 \\ 0.00 \\ 0.00 \end{bmatrix} \quad \mathbf{V}_{d_3}^{*r} = \begin{bmatrix} 0.00 \\ 0.00 \\ -1.00 \end{bmatrix} \quad (4.62)$$

The comparison of the selected vector and with the different vector was carried out and the most deviated result are shown in Eq. (4.63). The results are for the RVE with $\theta = 9^\circ$, $t_w = 6.35mm$ and $w = 101mm$. The vector comparison result shows that the non-diagonal terms are no longer smaller than the diagonal terms. Thus, the vectors obtained were not comparable with each other.

$$\mathbf{V}_d^{*rT} \mathbf{Q}_\theta \mathbf{V}_d^r = \begin{bmatrix} 0.86 & -0.36 & 0.03 \\ 0.37 & 1.00 & -0.08 \\ 0.01 & 0.08 & 1.00 \end{bmatrix} \quad (4.63)$$

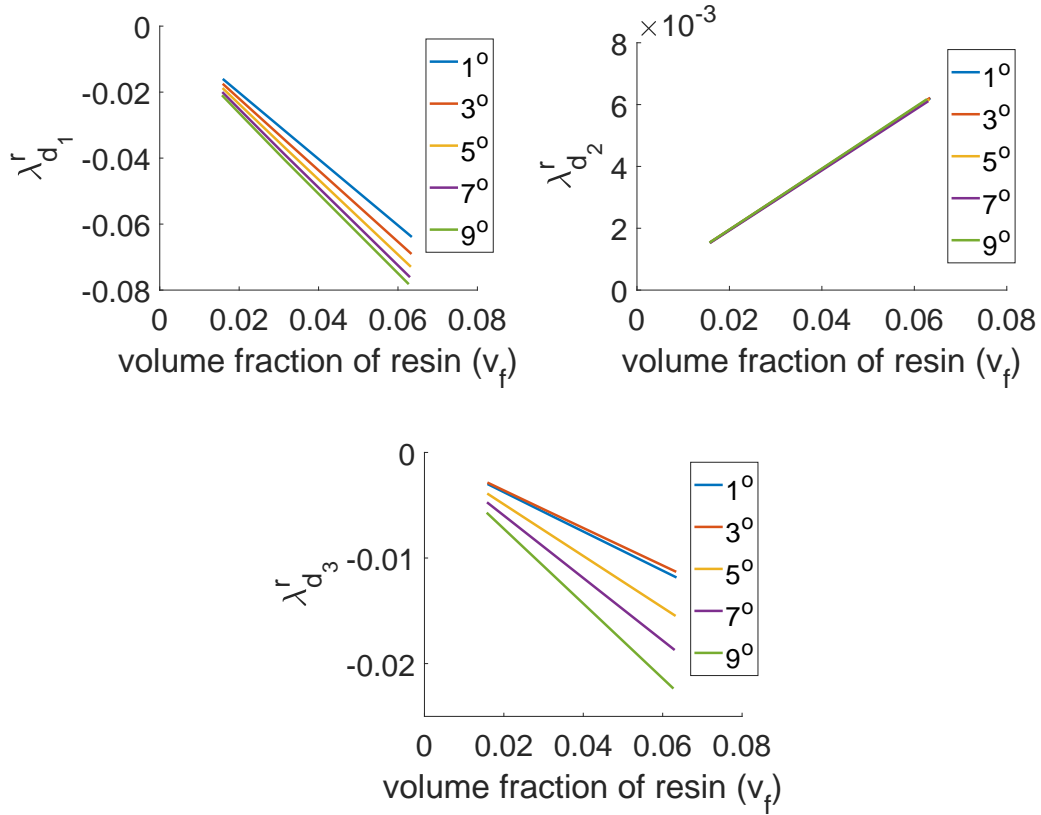


Figure 4.26: Knock-down factors from RVEs of single sided cuts with defects for Material 1

4.4 Correlation Development

The purpose to calculate the knock-down factors was to observe how the geometrical parameters of the defects affect the properties of the composite material. The eigen values λ_θ for zipper cuts suggested that the variation of fibre angle have the same effect on the properties of the composite with Material 1 and Material 2. Even the vectors along which the properties were affected does not change significantly from each other for both material cases. Similar can be said for the case of λ_d results obtained for the zipper cuts. Moreover, λ_d had a linear relationship with the volume fraction of the resin. But, the slope of the relationship was dependent upon the properties of the resin. These trends can be quantified into a simple analytical formula so that the evaluation of the properties could be done through that formula. The analytical formula can be then used to determine the knock-down caused by the defects with any shape, because shape of the tow drop defects may vary inside a VSP depending on the design and production variables. This will avert us to do FE analysis if the properties of certain case need to be obtained. However, from the results of the single sided cuts, it can be inferred that the eigen values λ_θ^r and λ_d^r had the similar behavior as obtained in the zipper cut cases but vectors associated with λ_d^r were not comparable to each other. This shortcoming of vectors not comparable to each other will restrict us to develop an analytical formula for the single sided cuts. Thus, a simple interpolation function will be developed for

the single sided cuts. In this section a method is discussed to develop the analytical formula from the knock-down factors result. It will also elaborate on the point why the mathematical correlation of the single sided cuts was not possible through this method.

In order to develop the correlation, Eq. (4.26) and Eq. (4.27) can be written in general form, as shown in Eq. (4.64).

$$\Delta Q_b V_b = \lambda_b Q_b V_b \quad (4.64)$$

Where, Q_b is termed as base stiffness tensor. ΔQ_b represents the change in the base stiffness tensor. λ_b represents the ratio of the change in the base stiffness to the base stiffness tensor. V_d represents the vector along which the stiffness changes. Now, V_b^T can be multiplied on both side of Eq. (4.64), which results into the Eq. (4.65).

$$V_b^T \Delta Q_b V_b = \lambda_b V_b^T Q_b V_b \quad (4.65)$$

In order to continue, a set of vectors were selected from the results generated such that Eq. (4.66) is satisfied.

$$V_b^{*T} Q_b V_b^* \approx I \quad (4.66)$$

Here, I is the identity matrix. Now, the Eq. (4.65) can be written as represented in Eq. (4.67)

$$V_b^{*T} \Delta Q_b V_b^* \approx \lambda_b I \quad (4.67)$$

Using the set of vectors, Eq. (4.67) can be solved for ΔQ_b . Thus, the selection of the vector will be such that it does not vary and the approximation in Eq. (4.66) holds. For the zipper cut case, this approximation is possible for V_θ^* and V_d^* , however, for the single sided cuts the approximation fails for V_d^{*r} . Thus, the correlation development for single sided cuts was not possible. After the vector selection, the eigen value λ_b has to be known. This value can be approximated by curve fitting the eigen values which were evaluated through the FE analysis in Section 4.3.6. Now, the λ_b evaluated by the polynomial curve fitting can be termed as λ_b^c . And the change in the stiffness can be calculated as shown in Eq. (4.68).

$$\Delta Q_b \approx \Delta Q_b^c = V_b^{*-T} \lambda_b^c I V_b^{*-1} \quad (4.68)$$

Here, ΔQ_b^c is change of the base stiffness tensor, which has been calculated by the correlation. Now, this change can be added to the base tensor and the correlated stiffness tensor can be written as in Eq. (4.69)

$$Q^c = Q_b + \Delta Q_b^c \quad (4.69)$$

Here, Q^c is the approximated stiffness tensor. Through this correlation if the values are calculated for the RVE, then there will be error between the correlated stiffness tensor and the stiffness tensor got from the FE analysis. Let the stiffness tensor from FE analysis be Q^{FE} . In order to calculate the error in the developed correlation, Eq. (4.70) was solved.

$$(\mathbf{Q}^{FE} - \mathbf{Q}^c)\mathbf{V}_e = \lambda_e(\mathbf{Q}^{FE} - \mathbf{Q}_b)\mathbf{V}_e \quad (4.70)$$

Here, λ_e represents the error in the correlation and \mathbf{Q}_b is the base stiffness tensor. Eq. (4.70) suggests that λ_e is the ratio of, the difference in the correlated value and actual value of stiffness tensor from FE analysis, to the difference in the tensor obtained from FE analysis and the base tensor. This means that λ_e compares the order of error in the correlated tensor to the effect of the defect caused by different defects on the base tensor. This ratio should be small in order to get the good correlated value of the stiffness tensor.

4.4.1 Correlation for zipper cuts

The correlation development was done for two materials, Material 1 and Material 2.

For Material 1: The correlation was developed in two stages. Firstly, correlation for the ideal RVEs was developed and then for the RVEs with tow drop defects. The selected vector for the correlation development for ideal RVEs are described Eq. (4.71).

$$\mathbf{V}_{\theta_1}^* = \begin{bmatrix} -0.53 \\ 1.00 \\ 0.00 \end{bmatrix} \quad \mathbf{V}_{\theta_2}^* = \begin{bmatrix} -1.00 \\ -0.02 \\ 0.00 \end{bmatrix} \quad \mathbf{V}_{\theta_3}^* = \begin{bmatrix} 0.00 \\ 0.00 \\ 1.00 \end{bmatrix} \quad (4.71)$$

The approximated function of the eigen values was found by curve fitting the values of λ_{θ_1} , λ_{θ_2} and λ_{θ_3} shown in Figure 4.21. The polynomial obtained with respect to θ are shown in Eq. (4.72). The θ in the expression are in degrees. A superscript 'c' has been given to the eigen values to show that the values are correlated results.

$$\begin{aligned} \lambda_{\theta_1}^c &= (1.26 \times 10^{-6})\theta^4 + (4.466 \times 10^{-5})\theta^3 - (2.39 \times 10^{-3})\theta^2 \\ &\quad + (4.129 \times 10^{-4})\theta - (2.528 \times 10^{-4}) \\ \lambda_{\theta_2}^c &= (1.077 \times 10^{-8})\theta^4 - (1.931 \times 10^{-7})\theta^3 + (3.406 \times 10^{-5})\theta^2 \\ &\quad - (3.401 \times 10^{-6})\theta + (2.47 \times 10^{-6}) \\ \lambda_{\theta_3}^c &= - (3.521 \times 10^{-7})\theta^4 + (8.404 \times 10^{-7})\theta^3 + (2.133 \times 10^{-3})\theta^2 \\ &\quad + (8.483 \times 10^{-6})\theta - (5.341 \times 10^{-6}) \end{aligned} \quad (4.72)$$

Now, Eq. (4.71) and Eq. (4.72), can be substituted in Eq. (4.73) to get the correlation for ideal RVE of zipper cuts with fibre angular distortion of θ .

$$\Delta\mathbf{Q}_{\theta}^c = \mathbf{V}_{\theta}^{*-T} \lambda_{\theta}^c \mathbf{I} \mathbf{V}_{\theta}^{*-1} \quad (4.73)$$

Here, $\Delta\mathbf{Q}_{\theta}^c$ represents the change in the stiffness tensor calculated by the correlation developed. This value can be added to the baseline tensor \mathbf{Q}_o to get the actual value of the stiffness tensor with fibre angle distortion defects, as shown in Eq. (4.74).

$$\mathbf{Q}_{\theta}^c = \mathbf{Q}_o + \Delta\mathbf{Q}_{\theta}^c \quad (4.74)$$

The correlated stiffness tensor, \mathbf{Q}_θ^c , for the ideal RVE of zipper cuts, with $\theta = 5^\circ$ and $w = 203mm$, is shown in Eq. (4.75). This is compared to the actual stiffness tensor \mathbf{Q}_θ calculated by the FE analysis in Eq. (4.75).

$$\mathbf{Q}_\theta^c = \begin{bmatrix} 11490.67 & 3806.69 & 0.00 \\ 3806.69 & 153985.19 & -0.014 \\ 0.00 & -0.014 & 5445.29 \end{bmatrix} MPa \quad \mathbf{Q}_\theta = \begin{bmatrix} 11490.28 & 3807.37 & 0.00 \\ 3807.37 & 154026.36 & 0.00 \\ 0.00 & 0.00 & 5445.70 \end{bmatrix} MPa \quad (4.75)$$

Similarly, for RVEs with defect, the selected vectors are shown in Eq. (4.76).

$$\mathbf{V}_{d_1}^* = \begin{bmatrix} -0.32 \\ 1.00 \\ 0.00 \end{bmatrix} \quad \mathbf{V}_{d_2}^* = \begin{bmatrix} 1.00 \\ 0.00 \\ 0.00 \end{bmatrix} \quad \mathbf{V}_{d_3}^* = \begin{bmatrix} 0.00 \\ 0.00 \\ -1.00 \end{bmatrix} \quad (4.76)$$

Since, λ_d was linearly dependent to the volume fraction of the resin, thus, curve fitting of the slopes was done. Then the slope was directly multiplied to the volume fraction of the resin. sl_1 , sl_2 and sl_3 are slopes of the lines for plots λ_{d_1} , λ_{d_2} and λ_{d_3} shown in Figure 4.22. The maximum values of the slope can also be taken, however, it will give more conservative approximation. The variation of these slopes are dependent upon θ . Thus, the slope were curve fitted for various values of θ . The expression for slope used for correlation development is shown in Eq. (4.77). 'c' superscript means that the curve are approximate function found through curve fitting.

$$\begin{aligned} sl_1^c &= -(0.0033)\theta^2 + (0.0451)\theta + 0.9644 \\ sl_2^c &= (-2 \times 10^{-5})\theta^2 + (6 \times 10^{-5})\theta + 0.0967 \\ sl_3^c &= (0.0035)\theta^2 - (0.0042)\theta + 0.1942 \end{aligned} \quad (4.77)$$

Here, also θ is in degrees. Now, the evaluation of λ_d^c was done through Eq. (4.78).

$$\begin{aligned} \lambda_{d_1}^c &= (-0.0033\theta^2 + 0.0451\theta + 0.9644) \times v_f \\ \lambda_{d_2}^c &= ((-2 \times 10^{-5})\theta^2 + (6 \times 10^{-5})\theta + 0.0967) \times v_f \\ \lambda_{d_3}^c &= (0.0035\theta^2 - 0.0042\theta + 0.1942) \times v_f \end{aligned} \quad (4.78)$$

where, v_f is the volume fraction of the tow drop defect in the RVE. Now, Eq. (4.76) and Eq. (4.78) can be substituted in Eq. (4.79) to calculate the change in the ideal RVE due to tow drop defect.

$$\Delta\mathbf{Q}_d^c = \mathbf{V}_d^{*-T} \lambda_d^c \mathbf{I} \mathbf{V}_d^{*-1} \quad (4.79)$$

The value $\Delta\mathbf{Q}_d^c$ then can be added to the \mathbf{Q}_θ^c as shown Eq. (4.80)

$$\mathbf{Q}_d^c = \mathbf{Q}_\theta^c + \Delta\mathbf{Q}_d^c \quad (4.80)$$

The value of \mathbf{Q}_d^c calculated for the RVE with $\theta = 5^\circ$, $t_w = 6.35mm$ and $w = 203mm$ is shown in Eq. (4.81). The volume fraction in the particular RVE is approximately 3.1%. The value is compared to the \mathbf{Q}_d calculated by FE analysis.

$$\mathbf{Q}_d^c = \begin{bmatrix} 11525.03 & 3817.24 & 0.00 \\ 3817.24 & 148473.37 & 0.25 \\ 0.00 & 0.25 & 5403.41 \end{bmatrix} MPa \quad \mathbf{Q}_d = \begin{bmatrix} 11525.72 & 3815.92 & -0.00 \\ 3815.92 & 148834.63 & -0.67 \\ -0.00 & -0.67 & 5400.91 \end{bmatrix} MPa \quad (4.81)$$

For Material 2: Similar procedure was followed for Material 2, as it was followed in the case of Material 1. The polynomial functions for the eigen value were found from curve fitting from the data shown in Figure 4.23 and Figure 4.24. The eigen value expression found are presented in Eq. (4.82) and Eq. (4.83). and the vectors selected are shown in Eq. (4.84) and Eq. (4.85).

$$\begin{aligned} \lambda_{\theta_1}^c &= (-3.31 \times 10^{-7})\theta^4 + (7.621 \times 10^{-5})\theta^3 - (2.54 \times 10^{-3})\theta^2 \\ &\quad + (1.23 \times 10^{-3})\theta - (9.34 \times 10^{-4}) \\ \lambda_{\theta_2}^c &= (1.17 \times 10^{-8})\theta^4 - (4.614 \times 10^{-7})\theta^3 + (4.534 \times 10^{-5})\theta^2 \\ &\quad - (2.625 \times 10^{-5})\theta + (6.352 \times 10^{-5}) \\ \lambda_{\theta_3}^c &= -(4.905 \times 10^{-7})\theta^4 + (3.811 \times 10^{-6})\theta^3 + (1.99 \times 10^{-3})\theta^2 \\ &\quad + (6.594 \times 10^{-5})\theta - (1.348 \times 10^{-5}) \end{aligned} \quad (4.82)$$

$$\begin{aligned} \lambda_{d_1}^c &= ((-1.658 \times 10^{-5})\theta^4 + 0.000728\theta^3 \\ &\quad - 0.01389\theta^2 + 0.08154\theta - 1.401) \times v_f \\ \lambda_{d_2}^c &= ((-4.795 \times 10^{-7})\theta^4 + (4.084 \times 10^{-5})\theta^3 - 0.0009974\theta^2 \\ &\quad + 0.01427\theta - 0.9433) \times v_f \\ \lambda_{d_3}^c &= ((-2.933 \times 10^{-6})\theta^4 + (-5.583 \times 10^{-5})\theta^3 \\ &\quad + 0.004898\theta^2 - 0.05815\theta - 1.007) \times v_f \end{aligned} \quad (4.83)$$

Here, θ is in degrees and v_f represents the volume fraction in the RVE.

$$\mathbf{V}_{\theta_1}^* = \begin{bmatrix} -0.41 \\ 1.00 \\ 0.00 \end{bmatrix} \quad \mathbf{V}_{\theta_2}^* = \begin{bmatrix} 1.00 \\ 0.00 \\ 0.00 \end{bmatrix} \quad \mathbf{V}_{\theta_3}^* = \begin{bmatrix} 0.00 \\ 0.00 \\ 1.00 \end{bmatrix} \quad (4.84)$$

$$\mathbf{V}_{d_1}^* = \begin{bmatrix} -0.56 \\ 1.00 \\ 0.00 \end{bmatrix} \quad \mathbf{V}_{d_2}^* = \begin{bmatrix} 1.00 \\ 0.02 \\ 0.00 \end{bmatrix} \quad \mathbf{V}_{d_3}^* = \begin{bmatrix} 0.00 \\ 0.00 \\ 1.00 \end{bmatrix} \quad (4.85)$$

For the RVE with $\theta = 5^\circ$, $t_w = 6.35mm$ and $w = 203mm$, the correlated and the actual results from the FE analysis are compared in Eq. (4.86). The volume fraction in the RVE

was approximately equal to 3.1%. The components of the stiffness tensor are comparable for both cases.

$$\mathbf{Q}_d^c = \begin{bmatrix} 8907.46 & 2743.92 & 0.00 \\ 2743.92 & 131618.24 & 0.04 \\ 0.00 & 0.04 & 4853.27 \end{bmatrix} MPa \quad \mathbf{Q}_d = \begin{bmatrix} 8895.05 & 2754.95 & 0.00 \\ 2754.95 & 131811.54 & 0.00 \\ 0.00 & 0.00 & 4829.69 \end{bmatrix} MPa \quad (4.86)$$

4.4.2 Correlation for single sided cuts

As discussed earlier, the correlation development of knock-down factor for single sided cuts was not possible, through the discussed method in Section 4.4. Thus, a simple 2D interpolation of the stiffness tensor components was done. The variables for which the interpolation was done were the angular distortion(θ) and volume fraction(v_f) of the tow drop defects in the RVE. The interpolation was done for Material 1 and Material 2 and it was made as a form of *Matlab* function, which can be used to predict the properties of the RVEs with and without defects. The interpolation functions are shown in Appendix Section A.4. For the interpolation, firstly, the \mathbf{Q}_θ^r was calculated for different angle θ and then \mathbf{Q}_d^r was calculated for different volume fraction by varying tow width and the width of the RVE. These are termed as sample points. Then, 2D interpolation function, *ScatteredInterpolant*, of *Matlab* was used to interpolate the components \mathbf{Q}_θ^r and \mathbf{Q}_d^r based on the sample points. After interpolation, these tensors were rotated by $\frac{\theta}{2}$ to evaluate \mathbf{Q}_θ and \mathbf{Q}_d .

For Material 1: For random RVE with $\theta = 10^\circ$, $t_w = 6.35mm$ and $w = 101mm$, the interpolation results, (\mathbf{Q}_d^i), and the actual results from FE analysis, (\mathbf{Q}_d), are compared in Eq. (4.87). The volume fraction in the RVE is equal to 6.3%. The random RVE means that it should not be the sample point in the interpolation function. For the sample points the interpolation function returns the same value. All the components of the tensor are comparable to each other.

$$\mathbf{Q}_d^i = \begin{bmatrix} 11636.98 & 4624.36 & -357.87 \\ 4624.36 & 129072.48 & -7172.93 \\ -357.879 & -7172.93 & 6350.41 \end{bmatrix} MPa \quad \mathbf{Q}_d = \begin{bmatrix} 11634.14 & 4628.46 & -354.06 \\ 4628.46 & 128955.97 & -7248.33 \\ -354.06 & -7248.33 & 6355.67 \end{bmatrix} MPa \quad (4.87)$$

For Material 2: For same RVE with $\theta = 10^\circ$, $t_w = 6.35mm$ and $w = 101mm$, the interpolation results (\mathbf{Q}_d^i) and the actual results from FE analysis (\mathbf{Q}_d) are compared in Eq. (4.88). The volume fraction in the RVE is equal to 6.3%. The component of the tensors are comparable to each other.

$$\mathbf{Q}_d^i = \begin{bmatrix} 8718.38 & 3342.33 & -362.66 \\ 3342.33 & 113767.34 & -6268.71 \\ -362.66 & -6268.71 & 5442.37 \end{bmatrix} MPa \quad \mathbf{Q}_d = \begin{bmatrix} 8717.93 & 3339.10 & -362.97 \\ 3339.10 & 113726.28 & -6277.96 \\ -362.97 & -6277.96 & 5439.55 \end{bmatrix} MPa \quad (4.88)$$

4.4.3 Error calculations

Only the comparison of the components of the stiffness tensor is not enough. The error in the correlated result should be less than the effect of the defect. Else, correlation would provide spurious result and will not capture the effect of defect. The error calculations were done from the Eq. (4.70), for zipper cuts and single sided cuts, for both Material 1 and Material 2.

For zipper cuts: For Material 1, from substituting the value of the correlated and actual stiffness tensor, from Eq. (4.81), and baseline stiffness tensor for Material 1 in Eq. (4.70), the value of λ_e can be evaluated. The maximum value of λ_e was equivalent to -2.68%. It means that the correlated stiffness tensor has captured approximately 97% of the effect of defect on the baseline stiffness tensor. Now, the error calculations were done for different RVEs for both Material 1 and Material 2. The maximum absolute error obtained was equivalent to 5% for Material 1, for the RVE with $\theta = 10^\circ$, $t_w = 6.35mm$ and $w = 101mm$. The volume fraction of the defect in the RVE was approximately equal to 6.2%. The correlated and actual tensor of the RVE are given in Eq. (4.89).

$$\mathbf{Q}_d^c = \begin{bmatrix} 11581.98 & 4153.78 & 0.01 \\ 4153.78 & 123118.58 & 0.31 \\ 0.01 & 0.31 & 6097.93 \end{bmatrix} MPa \quad \mathbf{Q}_d = \begin{bmatrix} 11582.15 & 4143.46 & 0.00 \\ 4143.46 & 125024.85 & 0.59 \\ 0.00 & 0.59 & 6062.26 \end{bmatrix} MPa \quad (4.89)$$

For Material 2, maximum error of 5% was obtained for RVE, with $\theta = 11^\circ$, $t_w = 6.35mm$ and $w = 101mm$. The volume fraction of the defect in the RVE was approximately equal to 6.2%. The correlated and actual tensor of the RVE are given in Eq. (4.90).

$$\mathbf{Q}_d^c = \begin{bmatrix} 8713.94 & 2861.85 & 0.02 \\ 2861.85 & 105441.07 & 0.19 \\ 0.02 & 0.19 & 5521.14 \end{bmatrix} MPa \quad \mathbf{Q}_d = \begin{bmatrix} 8695.13 & 2937.45 & 0.00 \\ 2937.45 & 107182.96 & 0.00 \\ 0.00 & 0.00 & 5398.57 \end{bmatrix} MPa \quad (4.90)$$

For single sided cuts: Similar, error study was done for the single sided cuts with interpolation function. Random RVEs were tested for Material 1 and Material 2. For Material 1, the maximum error in the function was found for the RVE, with $\theta = 10^\circ$, $t_w = 6.35mm$ and $w = 404mm$. The maximum error was equal to 8%. The stiffness tensor are shown in Eq. (4.91)

$$\mathbf{Q}_d^i = \begin{bmatrix} 11594.51 & 4755.19 & -405.48 \\ 4755.19 & 135167.85 & -8237.45 \\ -405.48 & -8237.45 & 6582.22 \end{bmatrix} MPa \quad \mathbf{Q}_d = \begin{bmatrix} 11590.90 & 4753.35 & -399.91 \\ 4753.35 & 134901.19 & -8298.59 \\ -399.91 & -8298.59 & 6583.43 \end{bmatrix} MPa \quad (4.91)$$

For Material 2, the maximum error was observed for RVE, with $\theta = 6^\circ$, $t_w = 6.35mm$ and $w = 101mm$. The absolute error was equivalent to 4.1%. The interpolated and the FE result are shown in Eq. (4.92)

$$\mathbf{Q}_d^i = \begin{bmatrix} 8627.40 & 2951.45 & -175.86 \\ 2951.45 & 123921.94 & -4732.82 \\ -175.86 & -4732.82 & 4831.51 \end{bmatrix} MPa \quad \mathbf{Q}_d = \begin{bmatrix} 8647.84 & 2956.25 & -177.19 \\ 2956.25 & 124368.58 & -4797.43 \\ -177.19 & -4797.43 & 4848.52 \end{bmatrix} MPa \quad (4.92)$$

Thus, the maximum error observed from the correlation function and interpolation function was less than 10%. It means that minimum 90% of the effect of defect can be captured by the correlation and interpolation functions. Thus, the correlation and the interpolation function can be used to estimate the properties of the RVEs.

Macro-Mechanical Modelling

The aim of this research is to predict the properties of VSP configurations through smearing methodology. However, the predicted results need to be compared with results from complete FE analysis of the VSP for different configurations to verify the results. Thus, a macro-mechanical model of the VSP should be developed to compare the predicted and actual results. For this research macro-mechanical model has been developed for VSP with tow drop defects. The tows were dropped by using single sided cuts and zipper cut strategy as discussed in previous chapter. The FE models produced were analysed under uniform end shortening test. Stiffness properties and buckling load were evaluated through this analysis. The results obtained were later compared with the results reported in the literature in order to verify the model.

5.1 Development of the Model

The complete geometry generation of the VSP models was done through a *Matlab* code. However, the complete *Matlab* code has not been presented in the report. The algorithm used to produce the tow drop defects are reported. As discussed in Section 2.2, in order to generate a VSP through tow drop strategy, the courses have to be shifted in the direction perpendicular to the direction along which the fibre angle changes. For this study, the linear fibre angle variation is chosen for building geometry of every ply in a VSP. Thus, the angle variation along the curvilinear path is given by Eq. (5.1) and the corresponding path equation is given by Eq. (5.2). The expression is same as reported by *Gürdal et al.* [20]. The linear fibre angle variation was chosen as it is easy to control the angles at the center and edges of the plate.

$$\theta^*(x^*) = \begin{cases} T_0 + (T_1 - T_0)\left(\frac{x^*}{d} - k\right), & k: \text{even} \\ T_0 + (T_0 - T_1)\left(\frac{x^*}{d} - k\right), & k: \text{odd} \end{cases} \quad \text{where, } k = \text{floor}\left[\frac{x^*}{d}\right] \quad (5.1)$$

$$y^*(x^*) = \begin{cases} kS + \frac{d}{(T_0 - T_1)} \ln \left[\frac{\cos(\theta^*(x^*))}{\cos(T_0)} \right], & k: \text{even} \\ kS + \frac{d}{(T_1 - T_0)} \ln \left[\frac{\cos(\theta^*(x^*))}{\cos(T_1)} \right], & k: \text{odd} \end{cases} \quad \text{where, } S = \frac{d}{(T_0 - T_1)} \ln \left[\frac{\cos(T_0)}{\cos(T_1)} \right] \quad (5.2)$$

Thus, the first step involved in generating a ply of VSP is choice of the fibre angle at center (T_0) and edge (T_1) location, and dimension of the ply as shown in the Figure 5.1a. Thereafter, tow width (t_w) and number of tows (n_t) in a course are chosen which defines the reference course as shown in Figure 5.1b. The reference course can be different for every ply. The point in the courses are given by the Eq. (5.3).

$$\begin{aligned} x' &= x^* - r \sin(\theta^*(x^*)) & \theta'(x', y') &= \theta^*(x^*) \\ y' &= y^*(x^*) + r \cos(\theta^*(x^*)) & \kappa'(x', y') &= \kappa^*(x^*)/[1 - r\kappa^*(x^*)] \end{aligned} \quad (5.3)$$

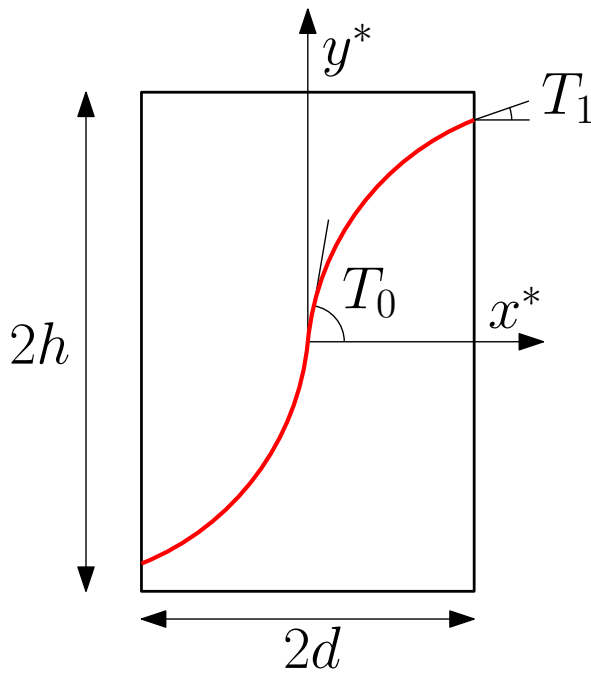
The definition of all the variables remain the same as it was discussed in Section 2.2.2. Since, the centreline of the course, represented in red in Figure 5.1b, should make the angle of T_1 at the edge, therefore, total coverage of the plate with fibres is restricted as shown in Figure 5.1b. Thus, the centreline curve is extrapolated further from the edge of the plate so that the course covers the complete region on the plate as shown in Figure 5.1c.

Thereafter, calculation of the shift distance has to be carried out for every ply. Shift distance is to be chosen in such a way that there are no gaps formation, pre-cutting the tows and post tow dropping there are only tow drop areas left. Thus, for the chosen course path in this research, shift distance is the minimum distance measured between a general point at the lower course edge (B) to the corresponding point on the upper course edge (A) along y' direction as shown in Figure 5.1d. Let the general point, B, on the lower edge of the course have coordinate (x_b, y_b) and the corresponding point, A, on the upper edge of the course have the coordinate (x_b, y_t) . Now, for Eq. (5.4) will be true.

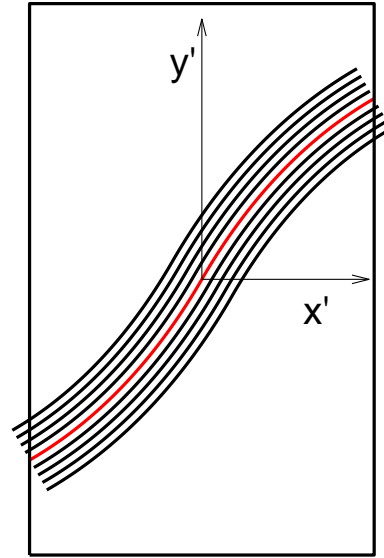
$$(x_b, y_t) \equiv (x_b, y_b + d) \quad (5.4)$$

where, d is the distance between the point A and B along y' -direction. Thus, it can be inferred from Eq. (5.4), calculating the minimum of the function $y_t - y_b$ at same x_b along the x' -axis will give the shift distance, d_s , which is required for no gap in the ply. However, since all the location in the course are parameterized with the x' -coordinate of the reference line (x^*), therefore, in order to calculate y_b , at particular x_b , calculation of the x^* should be made through the Eq. (5.3) and with x^* the corresponding y^* could be calculated from Eq. (5.2) and then, further y_b must be calculated through the Eq. (5.3). The same procedure has to be employed for the calculation of the y_t at same x_b . To calculate the minimum of the function $y_t - y_b$ in the range of x_b from 0 to d , *Matlab* function *Fminbnd* was used. This function finds the minimum of a function in a particular range.

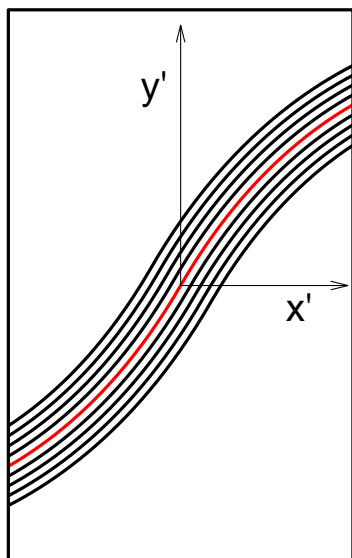
Once the shift distance of the ply is calculated, the reference course is shifted by that distance, as shown in Figure 5.2. The blue and black lines represent the shifted and reference course. It can be observed from Figure 5.2 that the tow lines in each course intersect each other at



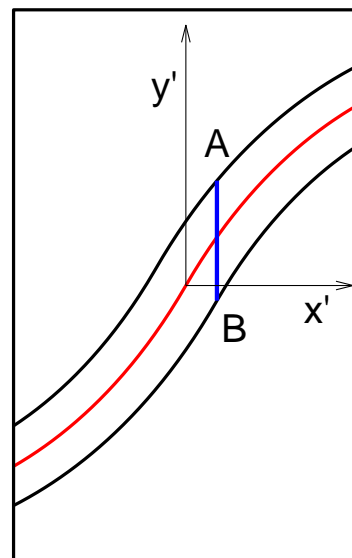
(a) Representation of reference curve of a variable stiffness ply



(b) Reference course of a variable stiffness ply



(c) Reference course covering whole area of plane at the edges



(d) Distance between two extreme course edges measured in y' direction.

Figure 5.1: Representation of a VSP ply

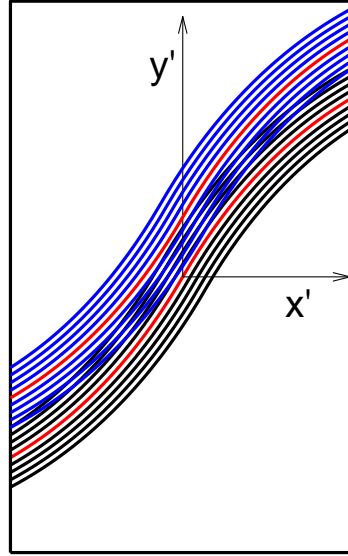


Figure 5.2: Two course which are placed on the plate with shifting method (Blue lines - shifted course, Black lines - reference course)

different location. Thus, these tow lines are cut at intersection points, based on the strategies like single sided tow drop and zipper cut strategy. Both the strategies with which the tows are cut are discussed in the subsequent section.

5.1.1 Single sided cuts

For single sided cuts, the tows are dropped from one course of the intersecting courses. Thus, the intersection has to be calculated between the different tows and the outer edge of one of the course. For this case, the outer edge of the reference course was chosen and the tows in the shifted courses were cut. Now, If there are $2n$ number of tows in the reference course, then there will be $(2n + 1)$ tow edges in the reference course. Thus, if the shifted course is placed, then, the maximum number intersection between the tow edges of the two courses will be equal to $2n$. As the top outer edges of the shifted course will be parallel, which means they do not intersect. Let us suppose that the number of tows in the reference course be $2n$, thus the tow edges can be numbered as, $-n, -(n - 1), \dots, 0, \dots, (n - 1), n$, as shown in Figure 5.3. Thus, the point on the different tow edges in the reference course can be represented as in Eq. (5.5).

$$\begin{aligned} x' &= x^* + it_w \sin(\theta^*(x^*)) \\ y' &= y^*(x^*) + it_w \cos(\theta^*(x^*)) \end{aligned} \quad (5.5)$$

where, i is an indicator which varies from $-n$ to n with step of 1 unit and t_w is the tow width. For $i = 0$, Eq. (5.5) will become reference curve shown in Eq. (5.2). Now, let the shifted and

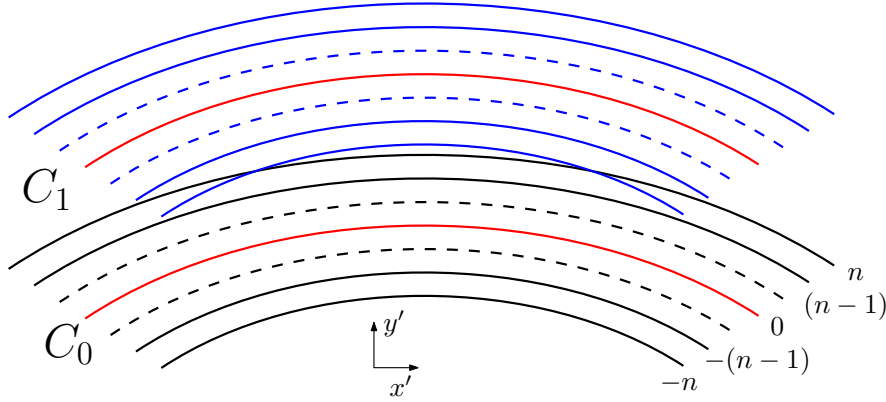


Figure 5.3: Numbering of tow edges of reference course

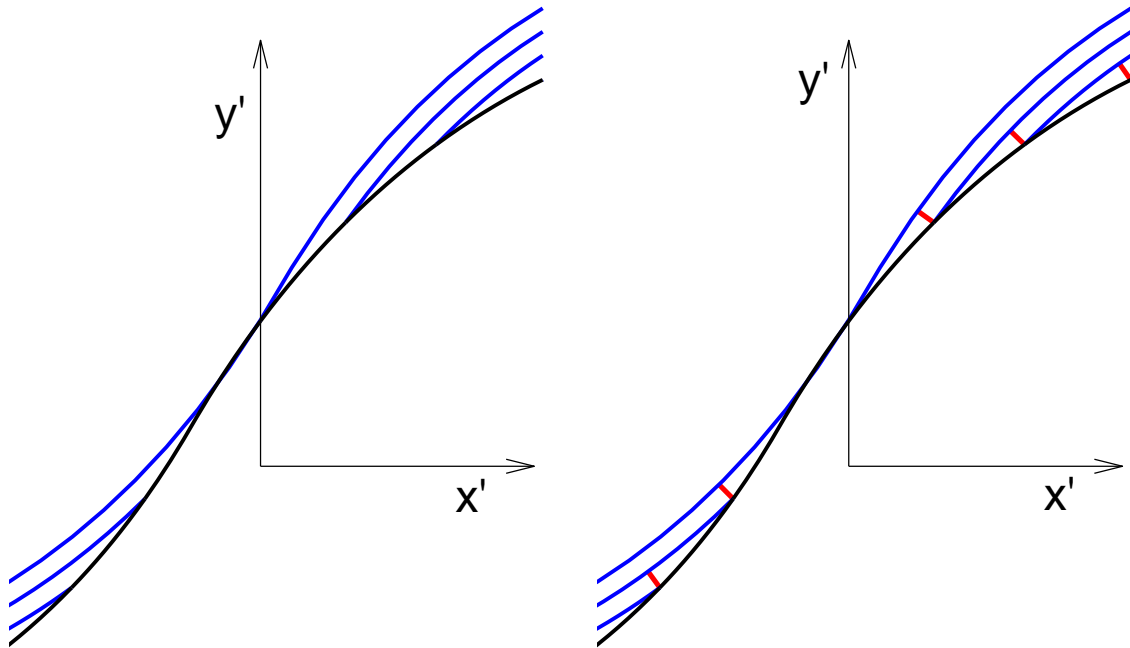
reference course be represented as C_1 and C_0 respectively as shown in Figure 5.3. For the shifted course the tow edges can be labeled, as it is labeled for the reference course. However, the points on the tow edges of the shifted course will be represented as in Eq. (5.6).

$$\begin{aligned} x' &= x^* + jt_w \sin(\theta^*(x^*)) \\ y' &= y^*(x^*) + jt_w \cos(\theta^*(x^*)) + d_s \end{aligned} \quad (5.6)$$

Where, d_s is the shift distance of the ply and j represents the numbering of the tow edges in the shifted course same as reference course. Now, the point of intersection has to be evaluated, between the tow edge n of course C_0 and different tow edges starting from $-n$ to n of C_1 . These point of intersection will be the location at which tow drop will happen in C_1 course. To evaluate this a *Matlab* functions was written. The function generates different tow edges of the courses C_0 and C_1 through Eq. (5.5) and Eq. (5.6) and gets the intersection of these edges through a *Matlab* function called *Fzero*. Once the intersection is found, let us say, for tow edge with number $-n$ in C_1 and tow edge with number n in C_0 , then, the intersection between the tow edge with number $-(n-1)$ in C_1 and tow edge with number n in C_0 is determined. This is done till the intersection goes beyond the plate center. The intersections are represented in Figure 5.4a. The Figure 5.4a shows outer edge of C_0 in black lines. And the tow edges of C_1 in blue lines. Other non-intersecting lines are not shown in Figure 5.4a.

After calculating the intersection points, cut lines are generated. Cut line is the line along which a particular tow is cut. The line is perpendicular to the tow edge at the intersecting point. In order to generate these lines, a point was evaluated on tow edge next to the intersecting tow edge, which lies on the perpendicular drawn on the intersecting tow edge at the intersecting point. It implies, if the $-n$ tow edge of C_1 intersects with n tow edge of C_0 , then the point is evaluated on the $-(n-1)$ tow edge of C_1 . And this process was done for all intersecting tow edges. To do this firstly from the intersection point data, x^* was evaluated from Eq. (5.6). Then, from that x^* value, the corresponding point was evaluated on next tow edge. The cut lines generated are shown in the Figure 5.4b with red lines.

Thus, the region shown in the Figure 5.5a is the tow drop defect area generated due to the intersection of courses. The region can be stored as an array of points and this region could be used further to generate defects on the entire plate. To generate tow drop defects on the



(a) Intersection of the tow edges of two different courses (Blue line - shifted course, Black line- reference course)

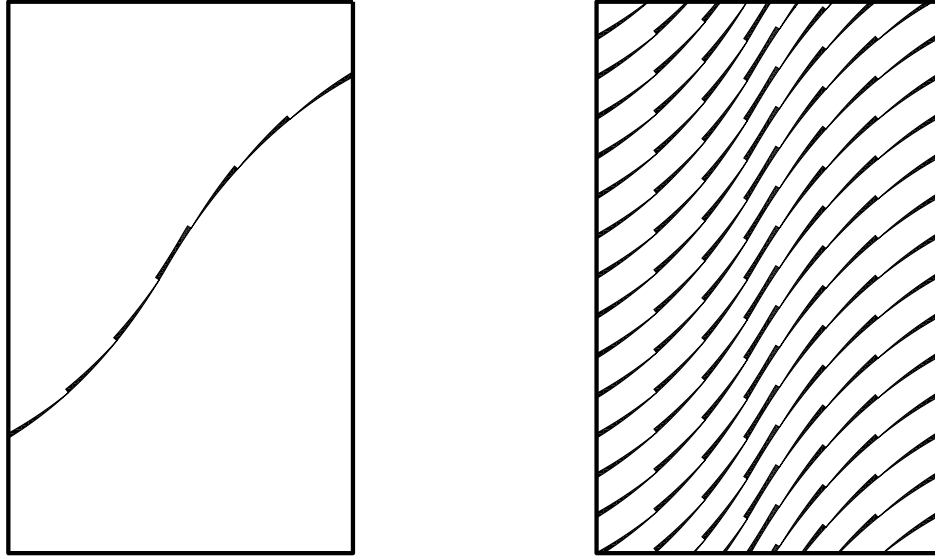
(b) Cut line generation (Red lines - cut lines)

Figure 5.4: Intersecting courses and tow dropping

entire plate the set of defects were translated along y' direction by shift distance. This is done because the lower part of the reference course will be intersected by the shifted course in the negative y' - direction which will result into the same set of defects. And the two sets of defects will be at a distance of shift distance. The array of defects in a ply will be generated which is shown in Figure 5.5b.

5.1.2 Zipper cuts

The generation of the tow drop defects through zipper cut strategy was same as that of the single sided cut strategy. The difference lies in the tow drop algorithm. Unlike single sided cuts, the tows of the C_0 course was also dropped in the zipper cuts case. Firstly, the intersection of the tow edge n of course C_0 and the tow edge $-n$ of course C_1 was evaluated. Then, the first cut was assumed at C_1 course. Thus, the next intersection was evaluated for the tow edge $-(n-1)$ of C_1 and tow edge n of C_0 . And after this the tow were dropped for C_0 . The series of intersection was evaluated through this approach. And the same methodology to develop cut lines was used as in the case of single sided cuts. Similar, to the case of the single sided cuts, tow drop defects were generated as the set of points and it was further translated by the shift distance along y' -axis. The one set of defect generated and the series of defects generated by this strategy are shown in Figure 5.6a Figure 5.6b. Comparing Figure 5.5a and



(a) Tow drop area generated due to intersection of two courses

(b) Tow drop defects generated in a VSP ply through single sided cut strategy

Figure 5.5: The defect generated in the ply with single sided cut strategy.

Figure 5.6a it can be seen that the tow drop area are generated alternately in the case of zipper cuts.

5.2 FE implementation

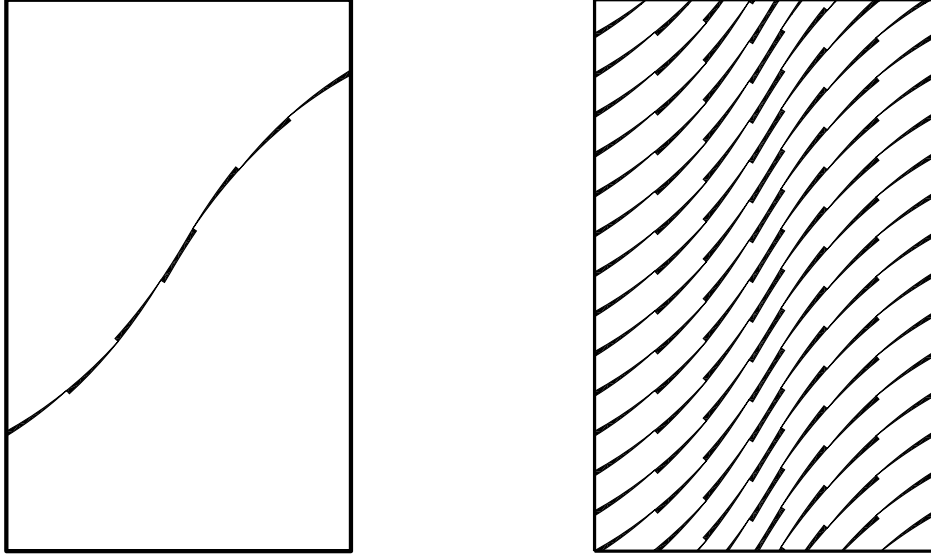
5.2.1 Mesh generation

Square element mesh was generated over the entire panel. The size of the elements used for the study were $3.175mm \times 3.175mm$. The element type were S4R.

5.2.2 Property assignment

Property assignment to the mesh elements was done through the modified defect layer method as discussed in Section 4.2.2. In last chapter, the properties were assigned at ply level. In this case, different plies will be stacked to form the laminate. Thus, for each element, a element stack was made. For a element, the volume fraction of the resin which was covered by it in each ply was evaluated. The property assigned to the element was given based on Eq. (5.7).

$$Q_e = v_f Q_R + (1 - v_f) Q_{\theta'} \quad (5.7)$$



(a) Tow drop area generated due to intersection of two courses

(b) Tow drop defects generated in a VSP ply through zipper cut strategy

Figure 5.6: The defect generated in a ply with zipper cut strategy.

Where, v_f is the volume fraction of the resin in the element, \mathbf{Q}_e is the stiffness tensor assigned to the mesh element, \mathbf{Q}_R is the stiffness tensor of the resin material and $\mathbf{Q}_{\theta'}$ is the composite stiffness tensor at particular angle fibre angle θ' . The value of θ' is evaluated at the centroid of the mesh element for every ply. It is measured with respect to x' -axis. This property value was assigned to the element stack at the same position as that of the ply in the laminate. Thereafter, for each element ABD matrix was calculated. The calculation of the ABD matrix is shown in Section 3.1.1. *General Section Stiffness option of *Abaqus* was used to assign the property to the element. It can also be noticed that $v_f = 0$, in Eq. (5.7), then the element stack will be formed for the ideal VSP case. Thus, the step of volume fraction calculation can be neglected and the result of ideal VSP can also be generated through this method.

5.2.3 Load cases and boundary conditions

From the macro-mechanical models, stiffness properties and buckling load were calculated for VSP. To calculate the stiffness of the VSP uniform end-shortening test was performed. The size of the laminate used for this study was $2d \times 2h$ as shown in Figure 5.7. The dimensions of the panels analyzed were different, thus, a general notation is given. The real dimensions are mentioned in the results. For stiffness evaluation, edge 1 shown in Figure 5.7 was subjected to end-shortening. Uniform displacement in negative y' -direction was applied to the edge. All edges were restricted to displace in out-of-plane direction and edge 3 was additionally restricted to displace in y' -direction. The displacement given to the edge 1 was equivalent to macroscopic average strain of 0.1%. The analysis was linear static, thus, the percentage of

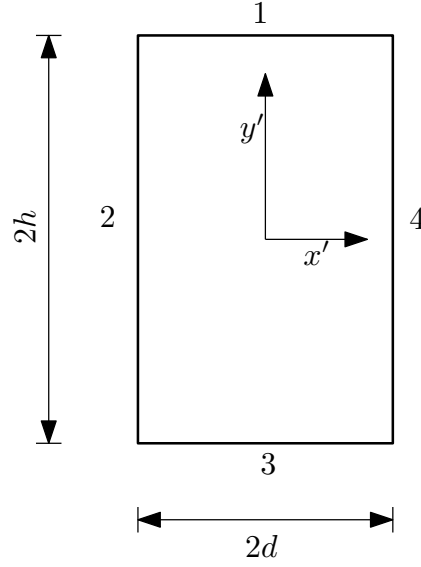


Figure 5.7: Dimensions of panel

strain application to the panel was insignificant. For Buckling analysis, same model was used and boundary conditions were same for all edges. The load application on the edge 1 was changed. A normal shell edge force of 1 N was applied instead of the uniform displacement. Linear perturbation buckling analysis was carried out to calculate the critical buckling load.

5.2.4 Stiffness and buckling Load calculations

All laminates which will be studied in the thesis have symmetric and balanced layup. Assuming plane stress condition, the relation shown in Eq. (5.8) will be true for the structure.

$$\begin{aligned}\epsilon_x &= \frac{1}{E_x}\sigma_x - \frac{\nu_{xy}}{E_y}\sigma_y \\ \epsilon_y &= \frac{1}{E_y}\sigma_y - \frac{\nu_{yx}}{E_x}\sigma_x \\ \sigma_z &= 0\end{aligned}\tag{5.8}$$

Where, E_x and E_y are the effective elastic modulus of VSP in the x' and y' direction. ϵ_x and ϵ_y are the average strain in x' and y' - direction. And σ_x , σ_y and σ_z are the average normal stress in the laminate in x' , y' and z' - direction. Now, due to no restriction in translation of edge 2 and 4 along x-axis, thus, $\sigma_x = 0$ which implies that all the equations in Eq. (5.8) will result down to a simple Eq. (5.9).

$$\epsilon_y = \frac{1}{E_y}\sigma_y\tag{5.9}$$

The average strain in the y' -direction is known. In order to evaluate E_y the calculation of σ_y should be made from the FE results. To calculate σ_y the normal forces along the y' -direction

was calculated. To calculate the normal forces script described in appendix Section A.2 was used. Through the script, normal forces from the edge 1 of the VSP were calculated. After the calculation of the normal forces on edge 1, average stress was calculated in the structure based on the following Eq. (5.10).

$$\sigma_y = \frac{F_y}{t_p \cdot w_p} \quad (5.10)$$

Here, F_y is the normal force calculated from FE analysis in y' -direction. t_p is the thickness of VSP panel and w_p is the width of the panel. Thus, from calculated σ_y and known strain ϵ_y the effective modulus in the y' - direction can be calculated through Eq. (5.9). For the calculation of the buckling load, *Abaqus* software was used to calculate the critical load which leads to buckling. To calculate the buckling load the boundary conditions and loads were applied as described in previous section. Further, the submitted job solves the eigen value problem for the plate and gives the result. These eigen values can be taken as the critical load per length which could lead to buckling. For the case of buckling, the consideration of the thermal effects due to the curing of the material are important, however, for this research the thermal effects are ignored. This research only deals with the linear buckling analysis of the VSP panel without thermal effect.

5.3 Results

In order to verify developed macro-mechanical model, the effective elastic modulus and buckling load were calculated, for the panels which were previously studied in literature. The panels chosen in this research were studied by *Wu et al* [7] and *Fayazbakhsh et al* [6]. The results obtained by analyzing the developed macro-mechanical model was compared to the results reported by them. Also, a comparison between the single sided cut and zipper cuts model is also discussed.

Comparison with results reported by *Wu et al* [7]:

Wu et al [7] studied panel with dimensions, $2h = 660.4\text{mm}$ and $2d = 622.3\text{mm}$. The layup of the panel was $[\pm 45/\pm < 30|60 >_4]_s$. The VSP was build by linear fibre variation. They conducted a experimental and numerical study on the panel. For experimentation, the panel was produced by a course, which contains 16 tows. The tow width of the tows was 3.175 mm. For the numerical study, tow drop defects were not considered in the analysis. The material system used is shown in Table 5.1. They chose $[\pm 45]_{5s}$ as the baseline panel and compared the properties of the VSP panels with the baseline panel. All the elastic properties and buckling load were normalized with the baseline results evaluated from the linear analysis.

Composite		Resin	
E_1	129.8 GPa	E	9.23 GPa
E_2	9.23 GPa	ν	0.36
G_{12}	5.10 GPa		
ν_{12}	0.36		

Table 5.1: Properties of AS4/977-3 Material System

The comparison of the stiffness results from the numerical analysis is shown in Table 5.2. Since, the numerical analysis conducted by *Wu et al* [7] was on the ideal VSP panel, thus, results obtained by ideal VSP panel have been compared. The comparison shows that the stiffness calculated from the developed model is within 1% range of the reported results. Now, in order to compare the results of the tow drop model. The results obtained by the analysis were compared to the experimental results reported by *Wu et al* [7], in Table 5.2. The defect effect row indicates the percentage change in the ideal VSP properties due to the tow drop defect. It could be inferred by the table that the values of the tow drop VSP are within 1% range than the reported results. However, The effect of the defect was not totally captured by the analysis. The total effect of defect reported was 3.8%, however, approximately 50% of the effect was captured by the model. To explain it, the volume fraction of the resin in the panel was evaluated. The volume fraction in the total panel was equal to 2.1%. This volume fraction is comparable to the effect of defect on the ideal VSP calculated by the analysis. Thus, the analysis result captures the effect of the defects accurately as the reduction in the stiffness properties are proportional to the volume fraction present in the panel. However, it can not be inferred from the results that about how much percent of the tow drop defect is captured by the analysis result, because the difference in the numerical value of reported and analysis results is in the order of the effect of defect. Thus, panel with high volume fraction of defect need to be analyzed.

Panel	Reported Results		Analysis Results	Percentage Difference
Ideal	Num.	1.08	1.07	-0.9%
Tow Drop	Exp.	1.04	1.05	0.9%
Defect Effect		3.8%	1.8%	

Table 5.2: Comparison between the stiffness results numerically (Num.) and experimentally (Exp.) calculated by *Wu et al* [7], and the numerical results generated from the analysis of the developed macro-mechanical model

The buckling load of the VSP panel has been compared in Table 5.3. For the ideal VSP, *Wu et al* [7] performed linear and non-linear analysis. And for the non-linear analysis they considered thermal effect generated in the VSP due to the curing. They also concluded that taking account of the non-linearity and thermal effect will result into better prediction of the VSP buckling properties. And the analysis also corresponds well with the experimental results. However, in this research only linear analysis has been performed, thus, linear analysis results of ideal VSP have been compared. For linear analysis case, the result shows that the analysis of the macro-mechanical model over-estimated the buckling load by 2.7% from the reported results. The difference in the value are low, thus, the model can be assumed to give satisfactory result for ideal VSP case.

Panel	Reported Results	Analysis Results	Percentage Difference
Ideal	1.13	1.16	2.7%

Table 5.3: Comparison of the buckling load results of ideal VSP reported by *Wu et al* [7], and the numerical results generated from the analysis of developed macro-mechanical model.

Comparison with results reported by *Fayazbakhsh et al* [6]:

Fayazbakhsh et al [6] studied two VSP panels with dimensions, $2h = 406.4mm$ and $2d = 254mm$. The layup of the panel are shown in Table 5.4. The VSPs were built by constant curvature reference curve. They conducted a numerical study on the panels. The panel geometry was generated by course consisting 8 tows. The tow width was equal to 3.175 mm. Tow drop defects were considered in the analysis. The material system used is shown in Table 5.5. They chose quasi isotropic panel with layup $[45/0/ - 45/90]_{2s}$, as the baseline panel and compared the properties of the VSP panels with the baseline panel. All the stiffness properties and buckling load were normalized with the baseline results evaluated from the analysis.

Label	Configuration
A	$[\pm(47, 0.48)/ \pm(46, -1.57)/ \pm(55, -1.57)/ \pm(52, -1.57)]_s$
B	$[\pm(47, 0.48)/ \pm(42, -1.57)/ \pm(60, -1.57)/ \pm(64, -1.57)]_s$
Baseline	$[45/0/ - 45/90]_{2s}$

Table 5.4: Laminates studied by *Fayazbakhsh et al* [6]

Composite		Resin	
E_1	143 GPa	E	3.7 GPa
E_2	9.1 GPa	ν	0.3
G_{12}	4.8 GPa		
ν_{12}	0.3		

Table 5.5: Material 2 Properties : Material System G40-800/5276-1

Now, the laminate design studied by them was made through constant curvature curve. However, the model generated in this research is for the linear fibre angle curve. Thus, to draw a better perspective of the results from the model developed the angles at the center and edge of the panel were calculated for the laminates which were studied by *Fayazbakhsh et al* [6]. Thereafter, linear fibre angle variation was assumed for the development of the model for the laminates. The complete equivalent configuration analyzed is shown in Table 5.6.

Label	Configuration
A	$[\pm < 47 42 > / \pm < 46 60 > / \pm < 55 68 > / \pm < 52 65 >]_s$
B	$[\pm < 47 42 > / \pm < 42 57 > / \pm < 60 72 > / \pm < 64 76 >]_s$
Baseline	$[45/0/ - 45/90]_{2s}$

Table 5.6: Configuration of Laminates studied in this thesis equivalent to the laminates studied by *Fayazbakhsh et al* [6]

FE analysis of the laminates A and B were performed, for ideal and tow drop case and compared with the results of *Fayazbakhsh et al* [6]. Since, the strategy used by *Fayazbakhsh et al* [6] to generate defects were single sided cuts, thus firstly, the stiffness and buckling results obtained for laminate with single sided cuts. Thereafter, the models with zipper cuts were generated and analyzed. The results from the zipper cuts were compared to the results obtained from single sided cuts.

The results shown in Table 5.7 are the normalized elastic modulus or stiffness results for the ideal VSP case. These results show that the stiffness of the ideal panels studied in this research is slightly lower than the ideal panels studied in the literature. This is due to the reason that in the literature the reference course follows the constant curvature path and in this study the reference course follows linear fibre angle variation. The slight change in the result is due to the reason that different reference courses are chosen for the study. Figure 5.8 shows that the fibre angle distribution of the centreline of the reference course of the ply $(46| -1.57)$ and $< 46|60 >$ along the x' -axis. It clearly shows that the fibre angles are slightly more in the case of the ply reported in the literature. The maximum difference is approximately 0.6%. This trend was observed for all the plies. It shows that the constant curvature curve has slightly more fibre angle with respect to x' -axis, than the linear fibre angle curve at a particular location. This might be the reason for the difference in the stiffness results.

Configuration	Literature Results	Results from analysis	Percentage Difference
A	0.73	0.72	-1.36%
B	1	0.99	-1.00%

Table 5.7: Comparison between the normalized stiffness results of ideal VSP, reported by *Fayazbakhsh et al* [6] and results generated by analysis of the equivalent laminates

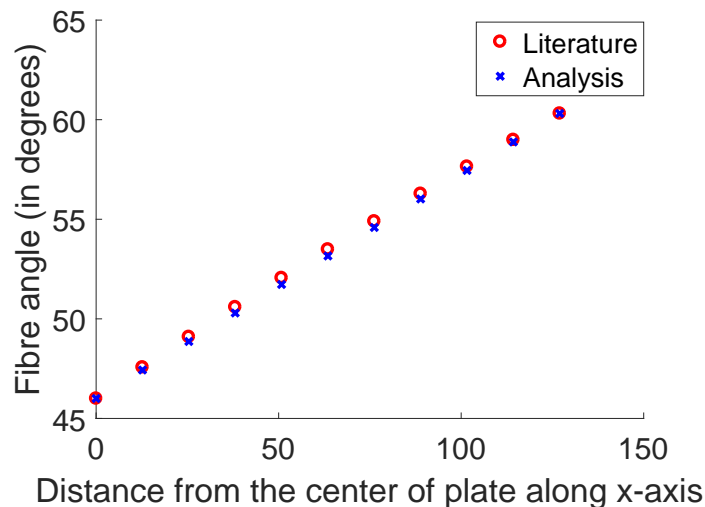


Figure 5.8: Fibre angle of reference curve compared between the ply $(46| -1.57)$ and equivalent studied ply $< 46|60 >$

Table 5.8 shows the stiffness results of panels with tow drop defects. The table also gives the percentage change from the ideal VSP case. It could be observed that the reduction of stiffness is more in the results reported in the literature than for the laminates analyzed in this study. The change is more due to the presence of more percentage of volume fraction of tow drop area in the laminate as shown in Table 5.9. Tow drop areas are generated due to the tow drop at the intersection of the tow edges. The intersection is dependent upon the reference course and tow dropping technique. Now, the reference course is different in the case of literature and this study, but, the tow drop strategy is the same, which is single-sided cuts.

Thus, to investigate rise in the volume fraction in the case of literature results, one such ply is compared to observe the pattern of the tow drop defects. Ply (46|–1.57) and its equivalent ply < 46|60 > have been compared in Figure 5.9. It can be seen from Figure 5.9 that the number of tow drop in the case of ply reported in literature is more than in the case of the equivalent ply studied. Thus, it can be inferred that the fibre angular distortion will be more in the plies studied in literature and will also give rise to more volume fraction of the defects than the equivalent ply studied in this thesis. Combination of both factor will be responsible for greater reduction in the elastic properties of the panel. However, this conclusion is made based on one ply comparison. It was difficult to compare others as the figures of the other plies were not present.

Configuration	Literature Results	Single sided cut results	Zipper cuts results
A	0.61 (-16.4%)	0.66 (-8.3%)	0.66 (-8.3%)
B	0.86 (-14.0%)	0.91 (-8.1%)	0.92 (-7.1%)

Table 5.8: Comparison between the normalized stiffness results of tow drop VSP, reported by *Fayazbakhsh et al* [6] and results generated by analysis of the equivalent laminates. The equivalent laminates were generated from single sided and zipper cut strategy. Percentage difference from the respective ideal VSP is presented in bracket

Configuration	Literature Results	Single sided cuts	zipper cuts
A	12.4	8.3	8.2
B	12.3	8.4	8.2

Table 5.9: Percentage volume fraction of defects, in the panels reported by *Fayazbakhsh et al* [6] and calculated for the equivalent panels generated by single sided and zipper cut strategy

The result shown in Table 5.10 are the buckling load of the ideal panel reported in the literature, for A and B configuration, and the results, which are obtained from the analysis. The result suggests that the buckling load have reduced for A and B configuration with linear fibre angle variation. This change is approximately 3% for both cases. This deviation is due to the choice of the reference course. As the constant curvature curve have higher fibre angles than the linear fibre angle variation, thus, higher buckling load were obtained for constant curvature VSP. The buckling load obtained for the case of tow drop case as shown in Table 5.11. Table also reports the percentage change obtained from the ideal case for respective cases. These results also show similarity with the literature results as the reduction in the buckling load is equivalent to the volume fraction of defects in both cases. Also, for the literature results, the reduction is more than the results from the analysis, this is because of the greater fibre angular distortion and volume fraction generated in the VSP. The rise in the volume fraction is due to more number of tow drops in the ply.

Configuration	Literature Results	Results from analysis	Percentage Difference
A	1.37	1.33	-2.9%
B	1.31	1.27	-3.0%

Table 5.10: Comparison between the normalized buckling load results of ideal VSP, reported by *Fayazbakhsh et al* [6] and results generated by analysis of the equivalent laminates

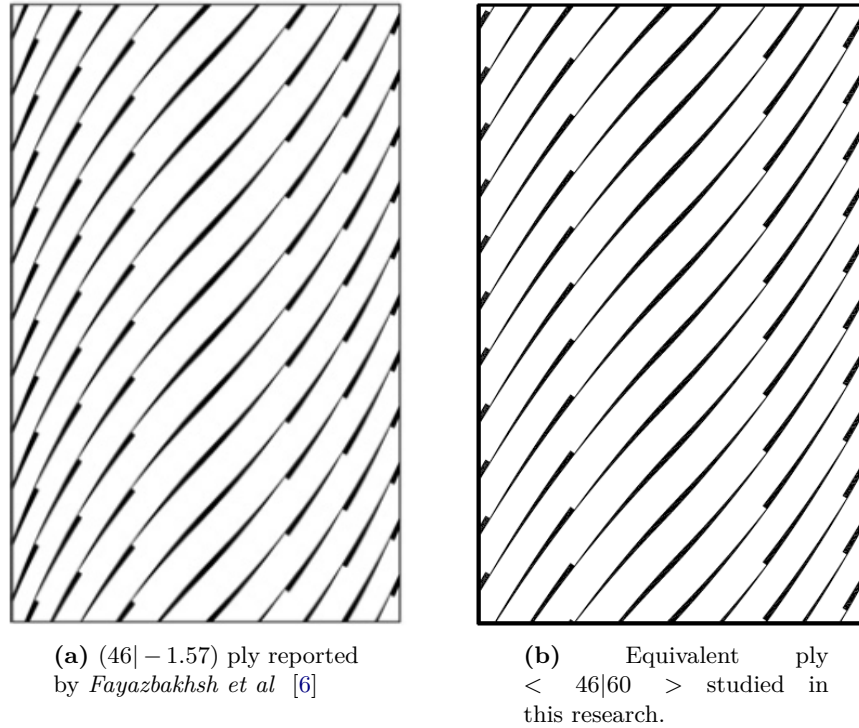


Figure 5.9: Comparison between tow drop area between the reported and equivalent ply

Configuration	Literature Results	Single sided cut results	Zipper cut results
A	1.20 (-12.4%)	1.22 (-8.3%)	1.22 (-8.3%)
B	1.15 (-12.2%)	1.17 (-7.9%)	1.17 (-7.9%)

Table 5.11: Comparison between the normalized buckling load results of tow drop VSP reported by Fayazbakhsh et al [6] and results generated by analysis of the equivalent laminates. The equivalent laminates were generated from single sided and zipper cut strategy. Percentage difference from the respective ideal VSP is presented in bracket

From the results of single sided and zipper cuts, shown in Table 5.11 and Table 5.8 , it could be inferred that no significant improvement in the stiffness properties and buckling load of the panel is observed. Thus, it could be concluded that the zipper cuts do not provide improvement over the single sided cuts for stiffness and buckling load of VSP. Also, it could be said that the fibre angular distortion and the volume fraction generated due to fibre angular distortion, for the case of single sided and zipper cuts, are almost similar for the same center and edge angle.

Smearing Methodology

The smearing methodology takes the advantage of the periodicity of the defect generation in the VSP and use it to predict the effect of the defect on VSP without modeling these defects. Through this methodology determination of fibre angle distortion and volume fraction of defect is done in the VSP. According to these variables the properties are assigned to the FE model with the help of correlation and interpolation functions developed from micro-mechanical model as discussed in Chapter 4. Furthermore, this methodology is applied at lamina and laminate level to evaluate the stiffness and buckling load. These results were compared with the results obtained from the analysis of same lamina and laminate through modified defect layer method as discussed in Chapter 5. Moreover, the applicability of the smearing methodology is discussed.

6.1 Methodology

The methodology involves evaluation of fibre angle distortion in the VSP through fibre angle gradient present in it. And then correlate this fibre angle distortion to the volume fraction that will be generated in the VSP panel. Now, to evaluate the fibre angle distortion a closer look at the intersection of the two course need to be taken. The evaluation of the fibre angle distortion is discussed for both the cuts in subsequent sections.

6.1.1 Single sided cuts

Figure 6.1 shows the representation of a tow cut at the intersection of the outer course edge of the reference curve. The tow edges are represented in red lines and the black lines are the course lines. Now, at the intersection point the normal unit vector to the tow edge is $\tilde{\eta}_{\theta'}$. And the normal unit vector to the course at the intersection point is $\tilde{\eta}_{\theta'+\Delta\theta'}$. Now, if the angle of intersection, i.e., $\Delta\theta'$, is small, thus the two unit vectors could be assumed to be same. Now, for the determination of the $\Delta\theta'$, along the line AB Eq. (6.1) can be written.

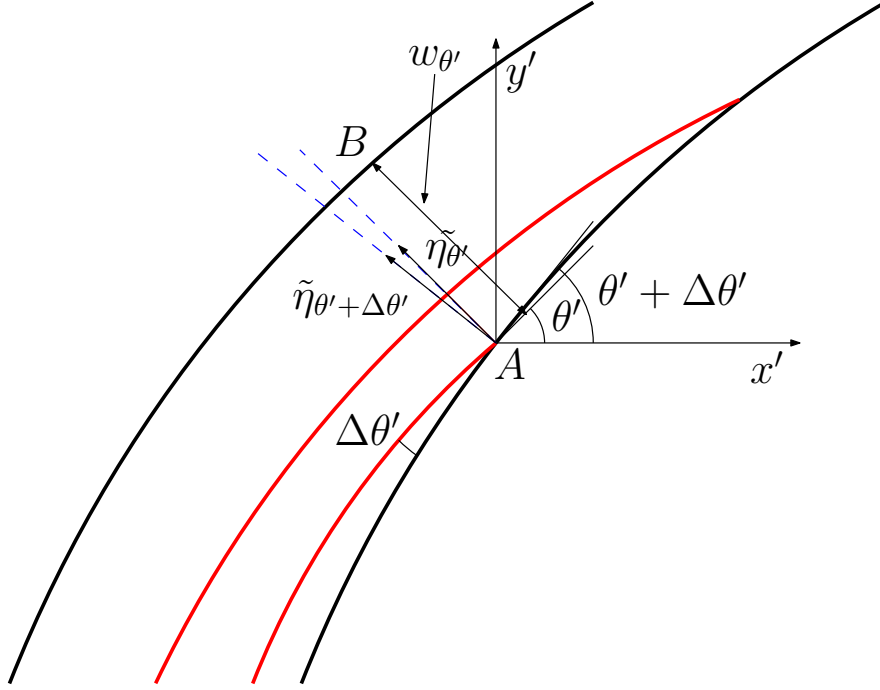


Figure 6.1: The schematic representation of single sided cuts

$$\theta'_B = \nabla\theta' \cdot \tilde{\eta}_{\theta'} w_{\theta'} + \theta'_A \quad (6.1)$$

Here, θ'_A and θ'_B are the fibre angle at the points A and B respectively. $w_{\theta'}$ is the distance between the point A and B. This distance has the maximum value equal to the course width (w_c). However, the tow are dropped at intersection points, thus the distance changes along the course and is represented by $w_{\theta'}$. (\cdot) is the dot product operation between two vectors. Thus, from the Eq. (6.1), $\Delta\theta'$ can be written as in Eq. (6.2).

$$\Delta\theta' = \nabla\theta' \cdot \tilde{\eta}_{\theta'} w_{\theta'} \quad (6.2)$$

The fibre angle distribution on the VSP is dependent on the design variable T_0 and T_1 , thus, gradient of fibre angle distribution, $\nabla\theta'$, can be evaluated by Eq. (6.3).

$$\nabla\theta' = \frac{\partial\theta'}{\partial x'} \hat{e}_1 + \frac{\partial\theta'}{\partial y'} \hat{e}_2 \quad (6.3)$$

Where, \hat{e}_1 and \hat{e}_2 are the unit vectors in x' and y' direction. The normal unit vector to the fibre angle is given by Eq. (6.4).

$$\tilde{\eta}_{\theta'} = -\sin(\theta') \hat{e}_1 + \cos(\theta') \hat{e}_2 \quad (6.4)$$

The evaluation of the distance $w_{\theta'}$ is relatively simpler if the intersection point of the tows was known. However, the objective here is to predict the angle deviation without any knowledge of the intersection location. Thus, this distance was approximated as represented in Eq. (6.5).

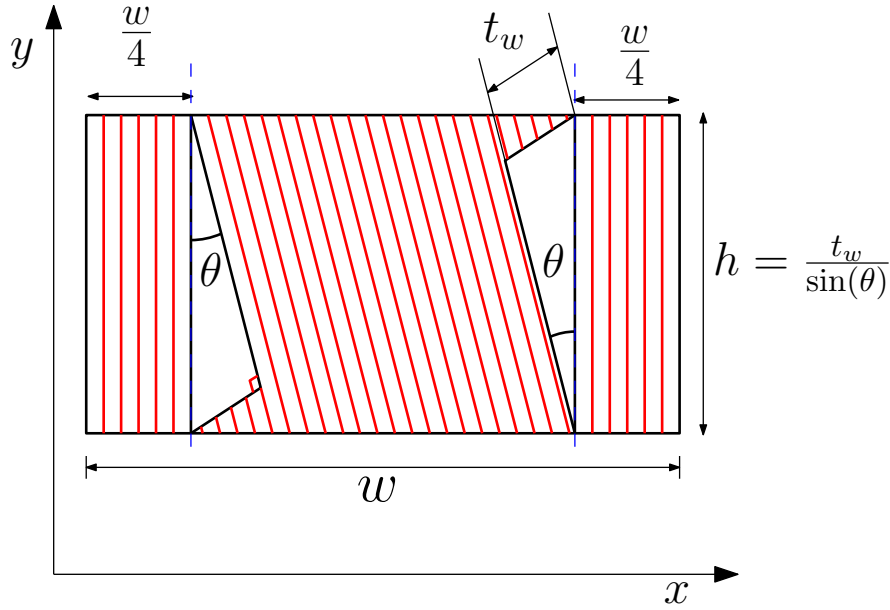


Figure 6.2: RVE for single sided cuts

$$w_{\theta'} \approx d_s \cos(\theta') \quad (6.5)$$

Where, d_s is the shift distance which could be calculated through the methodology discussed in section 5.1. This is a step which require computation, however, the step is used only once in the entire methodology to approximate a single ply. This approximation is based on the motivation that the distance between the two sets of defects in the y' -direction is equal to the shift distance. Thus, in the direction perpendicular to the fibre angle orientation the distance between the courses edges will be approximately equal to the projection of shift distance in the respective direction. Now, to relate this $\Delta\theta'$ to the volume fraction of the defect the micro-mechanical model of single sided cuts with defects should be revisited. The micro-mechanical model developed for the single sided cuts is shown in Figure 6.2. The consideration which need to be satisfied in this micro-mechanical model so that it resembles the defect geometry of the VSP is the following.

1. $\Delta\theta'$ will correspond to the angle θ in micro-mechanical model, which means that the fibre angular distortion in both cases will be equivalent.
2. Tow width (t_w) used for production of the VSP will correspond to the tow width in the micro-mechanical model.
3. The number of tows (n_t) or equivalent course width (w_c) used for production of the VSP should correspond to the width (w) of the micro-mechanical model.

In the micro-mechanical model, to make the substitution of θ and tow width (t_w) can be done easily. However, to make the width, w , of the micro-mechanical model corresponding to the course width in the VSP, Figure 6.3 should be referred.

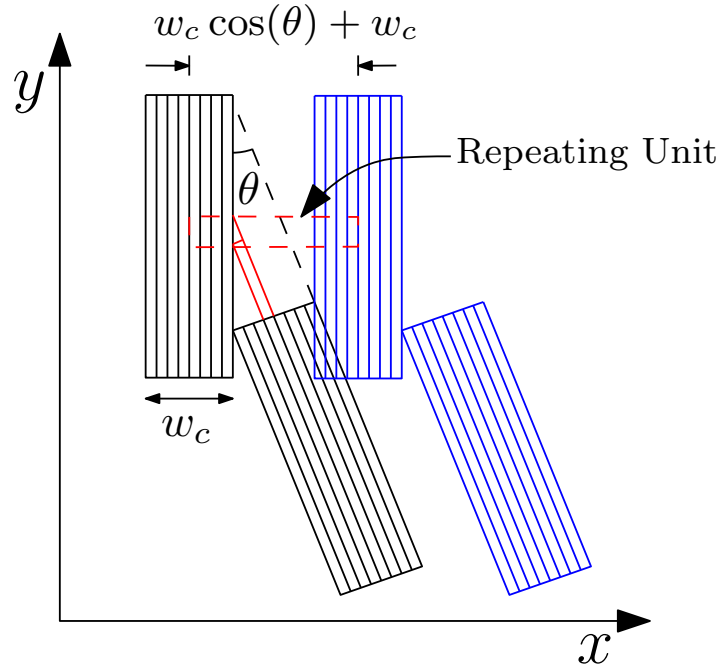


Figure 6.3: Intersection of two courses of equal course width

Figure 6.3 shows that the intersection of the two courses with same course width, w_c , and at an angle θ . The dotted black region forms the outer boundary of the intersection region, where the tows will intersect with other tows and will be cut. In order to generate the repetitive model of the intersection while keeping the course width constant the repetition could be done in by placing blue courses and repeating it in x direction. By doing this a repeating unit, shown in red dotted line will be formed which would be equivalent to the micro-mechanical model shown in Figure 6.2. The width of the model shown in red dot, will correspond to the width of the micro-mechanical model shown in Figure 6.2. Now, from this micro-mechanical model volume fraction of the tow drop area (v_f) can be calculated for the course with equal course width intersecting at an angle θ . The volume fraction of the tow drop area is given by the expression in Eq. (6.6).

$$v_f = \frac{t_w \cos(\theta)}{w_c(\cos(\theta) + 1)} \quad (6.6)$$

Thus, it could be concluded from Eq. (6.6) that the volume fraction of the tow drop area is dependent upon the course width, tow width and fibre angle distortion. Now, to correlate the volume fraction generated in the VSP due to fibre angle distortion Eq. (6.6) can be used. The repetition of the defects in the VSP occurs in the perpendicular direction of the fibre angle, which is along line AB in Figure 6.1. Thus, w_c in the Eq. (6.6) can be replaced by $w_{\theta'}$ for the case of VSP. However, $w_{\theta'}$ will change along the course, thus, the volume fraction would also change along the course. Also, the θ in Eq. (6.6) will be replaced by $\Delta\theta'$. Thus, the volume fraction in a VSP will be dependent upon the fibre angle and the fibre angle distortion. The final expression for v_f to evaluate volume fraction of tow drop will be Eq. (6.7).

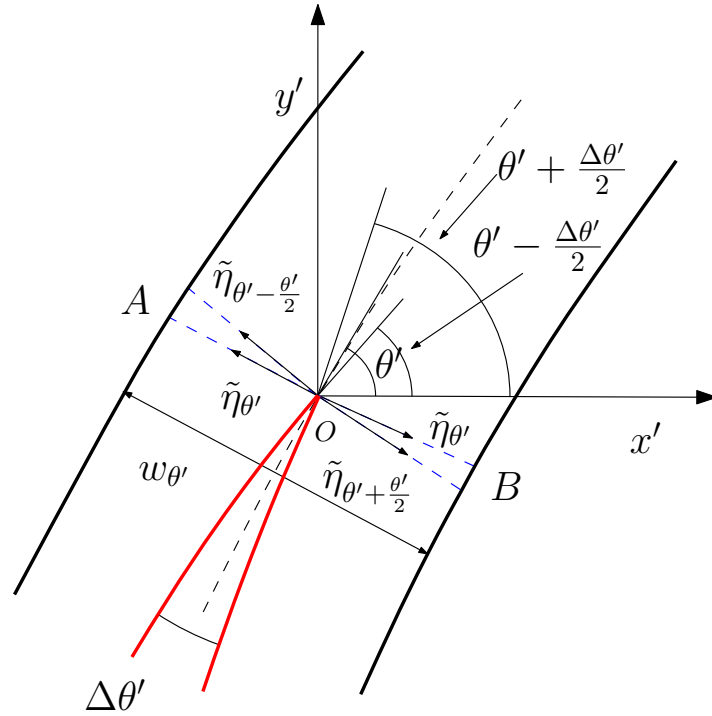


Figure 6.4: The schematic representation of zipper cuts

$$v_f(\Delta\theta', \theta') = \frac{t_w \cos(\Delta\theta')}{w_{\theta'} (\cos(\Delta\theta') + 1)} \quad (6.7)$$

6.1.2 Zipper Cuts

The methodology discussed can be further extended to the zipper cuts. The closer examination of the intersection of two tows of the zipper cut can be done from Figure 6.4. The red line represents the tow edges and the black line represents the center line of courses. Same procedure can be applied here as used in the single sided cuts. The angle difference can be calculated along the line AOB. Eq. (6.8) can be written from Figure 6.4.

$$\begin{aligned} \theta'_B &= \nabla\theta \cdot (-\tilde{\eta}_{\theta'}) \frac{w_{\theta'}}{2} + \theta'_O \\ \theta'_A &= \nabla\theta \cdot (\tilde{\eta}_{\theta'}) \frac{w_{\theta'}}{2} + \theta'_O \end{aligned} \quad (6.8)$$

From Eq. (6.8) the total angle deviation can be written as in Eq. (6.9)

$$\Delta\theta' = \nabla\theta' \cdot \tilde{\eta}_{\theta'} w_{\theta'} \quad (6.9)$$

Eq. (6.9) is same as Eq. (6.2). Thus, the same procedure can be applied to the zipper cuts to calculate the $\Delta\theta'$ as discussed for the single sided cuts. In order to calculate the volume fraction for VSP with zipper cuts, the micro-mechanical model of the zipper cuts should be

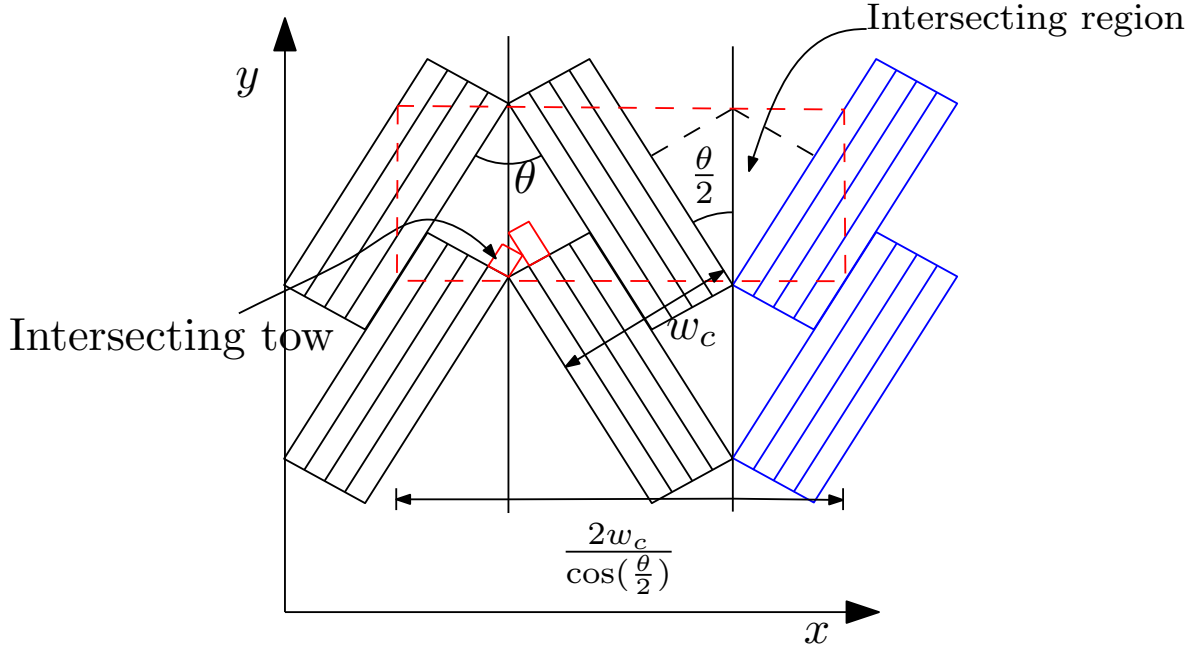


Figure 6.5: Intersection of two courses of equal course width

referred as shown in Figure 6.5. Here also, the width of the micro-mechanical model needs to be according to the course width of the VSP. Figure 6.5 shows two courses intersecting at angle θ with same course width. The intersection of the tows are in the region indicated. The tows could be extended and cut there. The red dotted region is the RVE which is used for zipper cuts. Thus, the width of the RVE will be equal to the width shown in Figure 6.5. Through maintaining this width, course width could be kept constant. Now, the volume fraction for this RVE is indicated in Eq. (6.10).

$$v_f = \frac{t_w \cos(\theta')}{2w_c} \quad (6.10)$$

In order to use this expression for calculation of volume fraction of the resin in the VSP, w_c can be replaced by $w_{\theta'}$ and the fibre angle distortion θ can be replaced by $\Delta\theta'$. Thus, the expression looks like as in Eq. (6.11)

$$v_f(\Delta\theta', \theta') = \frac{t_w \cos(\Delta\theta')}{2w_{\theta'}} \quad (6.11)$$

6.2 FE implementation

6.2.1 Mesh generation

Square mesh was generated on the entire plate as it was done in macro-mechanical model. The size of the elements used for the smearing methodology were $25.4mm \times 25.4mm$. For the analysis, through the defect layer method the size of the element were $3.175mm \times 3.175mm$. The element type were S4R.

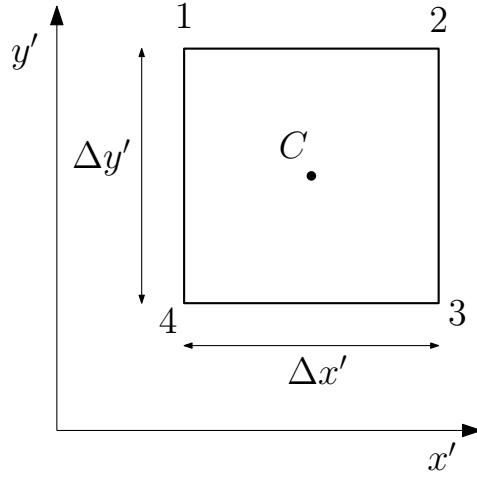


Figure 6.6: An element of the finite element mesh

6.2.2 Property assignment

The property assignment to the elements were done through the correlation developed and interpolation developed in Chapter 4. For each element, element stacking was done. The properties were assigned to the element stack based on the ply properties which were dependent upon the fibre angle distortion and the volume fraction generated due to it. Thus, for each element, fibre angle distortion was calculated from Eq. (6.2) and the volume fraction were calculated from Eq. (6.7) for each ply. And based on these variables the stiffness property was given in the element stack through the interpolation function described in Section 4.4. The procedure described is for the single sided cuts but this can also be done for the zipper cuts with Eq. (6.9), Eq. (6.11) and correlation developed in Section 4.4.

Now, to calculate the fibre angle distortion, fibre angle gradient has to be calculated in an element. The calculation of the gradient of the fibre angle in an element was done through the procedure discussed. For an element shown in the Figure 6.6, the fibre angle at the nodes 1, 2, 3 and 4 were calculated through the Eq. (5.1). Then, the gradient of the fibre angle was calculated at the centroid of the element through the Eq. (6.12).

$$\begin{aligned} \left. \frac{\partial \theta'}{\partial x'} \right|_C &= \frac{\theta'_2 - \theta'_1 + \theta'_3 - \theta'_4}{2\Delta x'} \\ \left. \frac{\partial \theta'}{\partial y'} \right|_C &= \frac{\theta'_1 - \theta'_4 + \theta'_2 - \theta'_3}{2\Delta y'} \end{aligned} \quad (6.12)$$

Thus, after evaluating gradient for the element, the calculation of $\Delta\theta'$ can be done through the Eq. (6.2). The fibre angle at the centroid was used to calculate $\tilde{\eta}_{\theta'}$ and $w_{\theta'}$ in Eq. (6.2). Similarly, v_f in the element can be calculated based on the cuts used for tow dropping, from Eq. (6.7) and Eq. (6.11). The fibre angle at the centroid was used to calculate $w_{\theta'}$ for calculation of the normal vector. This process was repeated for every element and for every ply and ABD matrix was formed for the elements.

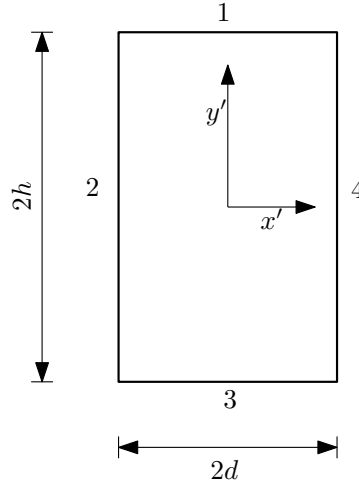


Figure 6.7: Dimensions of the panel

6.2.3 Load cases

Two type of analysis were carried out, one at lamina level and other at laminate level. The lamina level analysis means that laminate was formed of single ply configuration. The laminate level analysis means that the laminate is formed of different ply configuration.

Lamina level analysis: At lamina level, effective elastic modulus calculations were done for different configurations of $[\pm < T_0 | T_1 >]_{4s}$ through modified defect layer method, and for the same configurations the prediction of the effective elastic modulus were made through smearing methodology. The effective elastic modulus calculations are described in Section 5.2.4. The panel considered for analysis is shown in Figure 6.7. The dimensions of the plate were $2d = 254mm$ and $2h = 406.4mm$. Boundary conditions for the analysis were same as described in Section 5.2.4, i.e., all the edges are restricted to move in out of plane direction. Edge 4 is restricted to move in y' -direction and a displacement corresponding to 0.001% average strain in applied to edge 1 in negative y' -direction. Two sets of materials were used for the lamina level analysis. The materials used for the lamina level analysis are shown in Table 6.1 and Table 6.2. The material are referred as Material 1 and Material 2 for the lamina level analysis case. Ideal case of the VSP configurations were also evaluated in order to visualize whether through smearing methodology the effect of defect is captured or not. The results of stiffness were normalized with the baseline laminate $[0]_{8s}$. This baseline laminate has all the fibres aligned in x' -direction. The choice was made as the effective young's modulus will be lowest for this case, thus all the result will be more than 1. Also, the results for the conventional straight fibres were reported to compare the results of VSP plies and striaght fibre plies. The analysis was done for the single sided and zipper cuts.

Laminate level analysis: For the laminate level analysis three laminates were studied. These laminate configurations were studied by *Fayazbakhsh et al* [6] and *Tatting et al* [8]. Two laminate configurations studied by *Fayazbakhsh et al* [6] were made of constant curvature reference course. The equivalent configurations studied in this research are shown in Table 6.3. Effective elastic modulus and buckling load for the laminate configurations were evaluated through smearing approach. The results were compared with the results obtained from modified defect layer method. The dimension of the laminates was $2d = 254mm$ and

Composite		Resin	
E_1	161 GPa	E	11.4 GPa
E_2	11.4 GPa	ν	0.32
G_{12}	5.17 GPa	-	-
ν_{12}	0.32	-	-

Table 6.1: Material 1 Properties : Material system IM7/8552

Composite		Resin	
E_1	143 GPa	E	3.7 GPa
E_2	9.1 GPa	ν	0.3
G_{12}	4.8 GPa	-	-
ν_{12}	0.3	-	-

Table 6.2: Material 2 Properties : Material system G40-800/5276-1

$2h = 406.4mm$. The materials used for these two laminates are shown in Table 6.1 and Table 6.2. These are also referred as Material 1 and Material 2. In the literature, the laminates were analyzed for Material 2. Here, to see the effect of resin on the properties of panels configurations are also analyzed from Material 1. Both single sided and zipper cut strategy were studied for tow drop case. The boundary conditions for the lamina and laminate level analysis were the same. All the edges shown in Figure 6.7 were restricted to move out of plane. Edge 1 was given uniform displacement corresponding to 0.1% macro-strain in negative y' -direction and uniform edge load of 1N/mm for stiffness and buckling calculation respectively. And displacement of edge 4 was restricted in the y' - direction. All the results were normalized by the results of the baseline configurations.

Label	Configuration
A	$[\pm < 47 42 > / \pm < 46 60 > / \pm < 55 68 > / \pm < 52 65 >]_s$
B	$[\pm < 47 42 > / \pm < 42 57 > / \pm < 60 72 > / \pm < 64 76 >]_s$
Baseline	$[45/0/ - 45/90]_{2s}$

Table 6.3: Configuration of Laminates studied in this thesis equivalent to the laminates studied by *Fayazbakhsh et al* [6]

Another laminate with different dimensions, $2d = 381mm$ and $2h = 508mm$, was also analyzed. The layup of the laminate was $[\pm 45/\pm < 45|60 > / \pm < 30|15 > / < 45|60 >]_s$. This layup is the optimized design for maximum buckling load suggested by *Tatting et al* [8]. The material used by them was different than the material models used in this study, though this panel is analyzed to observe the applicability of the smearing approach. The panel was generated with tow width and number of tows equal to 3.175mm and 8. This was different than the panel they studied. The manufacturing parameters considered by them were 3.175mm of tow width and 24 number of tows. These parameter were not selected as the defect generated in the panel was equivalent to 1%. Therefore, the parameters which give rise to more defect were selected to observe the effect of defect captured by the smearing method. The panel was tested for two material models described in Table 6.1 and Table 6.2. The laminate was also analyzed with single sided and zipper cuts for both material models. The results were

normalized by the results obtained for the baseline laminate from respective material models. The baseline laminate layup used is the same quasi-isotropic laminate shown in Table 6.3.

6.3 Results

6.3.1 Lamina results

An additional constraint was applied over lamina geometry which was of the minimum radius of curvature. A minimum radius of curvature of 400mm was chosen for this study. The lamina with minimum radius of curvature greater than 400mm on entire reference course were studied. For reference course, the tow width and number of tows were equal to 3.175 mm and 8. The subsequent section discuss the stiffness results which were generated through modified defect layer method and through smearing methodology.

Results for single sided cuts

For Material 1: The lamina result of single sided cuts for Material 1 are shown in Figure 6.9 - 6.12. The result shows that the normalized elastic modulus (E_y/E_0) of the plate calculated from modified defect layer and smearing method. Here, E_y is the effective elastic modulus in the y' -direction and E_0 is the elastic modulus of the plate with layup $[0]_{8s}$. Also, the actual and predicted volume fraction of tow drop defects in the panel are shown in Figure 6.9 - 6.12. For each figure, center angle, T_0 , is kept constant and edge angle, T_1 , is varied. For all the figures, T_0 and T_1 value is measured from the x' -axis. For Figure 6.9a and Figure 6.9b it can be seen that the results from the modified defect layer method has given more elastic modulus than the ideal case. Also, the modulus value for the straight fibre case, i.e., $T_0 = T_1$, for both cases have shown value less than 1. This is quite surprising result. To explain this behavior, elastic modulus in y' direction of Material 1 was evaluated for different straight fibre laminate with configuration $[\pm\theta_0]_{4s}$. The value of θ_0 will vary from 0° to 90° , measured from x' -axis. These properties will be compared to the elastic modulus of the resin. For $[0]_{8s}$ configuration, the stiffness tensor can be written as in Eq. (6.13), this tensor is calculated by Eq. (3.4).

$$\mathbf{Q}_{S_0} = \begin{bmatrix} 162175 & 3675 & 0 \\ 3675 & 11483 & 0 \\ 0 & 0 & 5170 \end{bmatrix} \quad (6.13)$$

Here, \mathbf{Q}_{S_0} is the stiffness tensor of configuration $[0]_{8s}$. Now, transformation of the stiffness tensor, \mathbf{Q}_{S_0} by angle θ_0 and $-\theta_0$, from Eq. (3.5), and applying Eq. (6.14), the calculation of stiffness tensor of the configuration $[\pm\theta_0]_{4s}$ can be done. Since, all the laminate have equal thickness, thus Eq. (6.14) is valid.

$$\mathbf{Q}_{\theta_0} = \frac{1}{2}(\mathbf{M}(-\theta_0)\mathbf{Q}_{S_0}\mathbf{M}^T(-\theta_0) + \mathbf{M}(\theta_0)\mathbf{Q}_{S_0}\mathbf{M}^T(\theta_0)) \quad (6.14)$$

Here, \mathbf{Q}_{θ_0} is the stiffness tensor of the straight laminate with configuration $[\pm\theta_0]_{4s}$. \mathbf{M} is the transformation matrix dependent upon the angle θ_0 . It is given by Eq. (6.15)

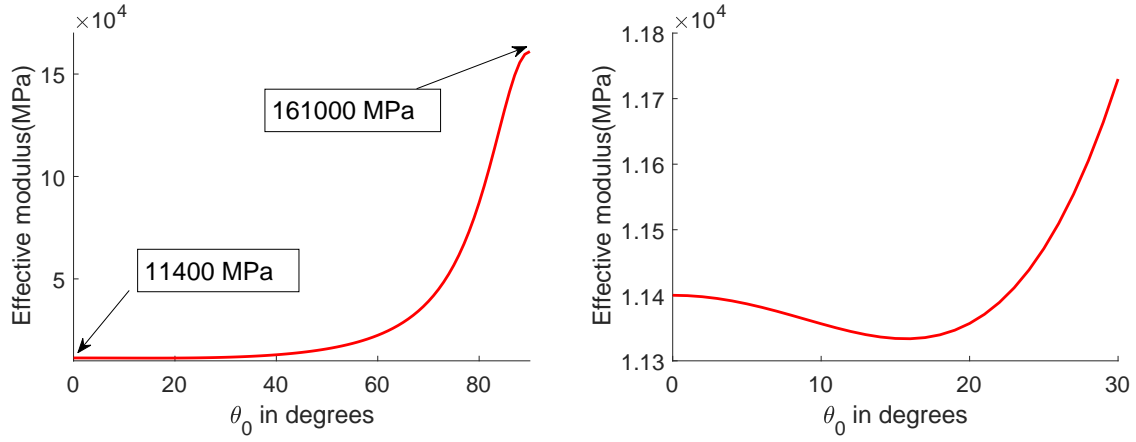


Figure 6.8: Effective modulus of straight fibre panels with configuration $[\pm\theta_0]_{4s}$ in y' direction as a function of θ_0

$$\mathbf{M}(\theta_0) = \begin{bmatrix} \cos^2(\theta_0) & \sin^2(\theta_0) & 2 \cos(\theta_0) \sin(\theta_0) \\ \sin^2(\theta_0) & \cos^2(\theta_0) & -2 \cos(\theta_0) \sin(\theta_0) \\ -\cos(\theta_0) \sin(\theta_0) & \cos(\theta_0) \sin(\theta_0) & \cos^2(\theta_0) - \sin^2(\theta_0) \end{bmatrix} \quad (6.15)$$

Now, taking the inverse of \mathbf{Q}_{θ_0} will give the compliance tensor. The compliance will be a 3×3 matrix. Taking the reciprocal of term at location second column and second row will give the elastic modulus of the panel in the y' direction. Now, performing this procedure for different angle, θ_0 , will give the elastic modulus of the straight panels as the function of θ_0 . The function is shown in Figure 6.8a. The figure shows that the elastic modulus at 0° and 90° are equivalent to the elastic modulus properties of Material 1 in the direction perpendicular to the fibre and along the fibre. The values are equal to 11400MPa and 161000MPa respectively. Now, zooming in the region from angle 0° to 30° as shown in Figure 6.8b, it can be seen that the elastic property decreases initially and further increases after approximately 20° . This dip in the elastic modulus is approximately 0.5% . However, the resin properties are constant for the entire range of the angle, which is 11400MPa . Thus, resin tend to increase the properties of the composite for the cases with $T_0 = 10^\circ$ and $T_0 = 20^\circ$. Thus, the effective modulus of the ideal case is less than the case which has tow drop defects. Also, for the case $T_0 = 10^\circ$, the prediction of effective modulus from the smearing is within 2% range of the results obtained from modified defect layer method, thus the prediction is fairly accurate for the this case. However, the volume fraction prediction is not that accurate. The volume fraction predicted is maximum 68% offset from the result of the modified defect layer method, as shown in Figure 6.9a. Even though the volume fraction is under-predicted, the elastic modulus is predicted fairly accurate. This is because both the material have same elastic modulus, thus, whatever the volume fraction is predicted the value of the properties would be the same. This can be seen for case $T_0 = 10^\circ$ and $T_1 = 0^\circ$. For this case the volume fraction of the resin was approximately 12% , however, the difference obtained in elastic modulus of ideal and tow drop case is 1% . Similar trend were observed for the $T_0 = 20^\circ$, 30° and 40° cases shown in Figure 6.9b, Figure 6.10a and Figure 6.10b. The effect due to the tow drop defect were not more than 3% . And the prediction made by the smearing case was within 1%

range from the result of the modified defect layer approach. Moreover, the prediction of the volume fraction became more accurate for these cases. For different T_1 angles, the maximum difference between the actual and predicted value of volume fraction was 49%, 26% and 7% for the angle, T_0 , equal to 20° , 30° and 40° . This suggest that at higher center angle the volume fraction prediction gets better for different T_1 angles. Now, with the rise in the center angle and bigger difference between the elastic properties of the resin and composite in y' direction, the impact of the tow drop defect becomes visible for the cases, $T_0 = 50^\circ$ and 60° , as shown in Figure 6.11.

For $T_0 = 50^\circ$ case, the effect of the defect on elastic modulus was approximately 2% for edge angles, $T_1 = 30^\circ$ and 40° . The predicted elastic modulus value were within 0.1% range from the values obtained from modified defect layer method. The effect of tow drop defects increased to 4%, 6% and 8% for the case of edge angles, $T_1 = 60^\circ$, 70° and 75° respectively. The rise in the effect of defects is due to the rise in the difference between the stiffness properties of the composite and resin. The predicted elastic modulus values for these cases were 1.5% less than the values obtained from the modified defect layer method. It suggests that the effect of the defects on the elastic properties is over predicted. The maximum deviation of 10% in the value of volume fraction prediction was obtained for lamina with angles, $T_0 = 50^\circ$ and $T_1 = 80^\circ$. The volume fraction was over predicted, however, the under prediction of the elastic properties was 1.5%. It means that the volume fraction of the defect have less influence on the properties than the fibre angular distortion. Thus, effect of the tow drop defect can be segregated in two parts, one is the fibre angular distortion effect and other is the volume fraction effect. The effect of the fibre angular distortion is more than the volume fraction effect on the laminate properties.

For $T_0 = 60^\circ$ case, the effect of the tow drop defect were 3.5%, 3.3%, 5.8%, 9.6% and 13.7% for T_1 equal to 40° , 50° , 70° , 80° and 85° . The prediction of the elastic modulus was within 1% range for all the cases except for the last case, $T_1 = 85^\circ$, for which the predicted value was 2.3% less than the value obtained from modified defect layer method. The volume fraction prediction were accurate for these cases and were within 1.5% range from the actual value. However, the reduction in the elastic modulus was not proportional to the volume fraction in the composite. For $T_1 = 40^\circ$, the volume fraction was 8%, however, the reduction in the elastic modulus was 3.5%. And, for the $T_1 = 80^\circ$ case, the volume fraction is 10.5% and reduction in the properties is 9.6%. The difference in the center angle and edge angle are same for both the case, thus, fibre angle distortion will be approximately same. The difference between the reduction in the properties is due to the effect of resin which is working as the reinforcement for the case with $T_1 = 40^\circ$, but no improvement could be provided by it for the case of $T_1 = 80^\circ$, as the difference in the properties of the composite and resin were high. Thus, volume fraction effect can be positive if the difference in the properties of the composite and resin is low else it will be deteriorating.

For $T_0 = 70^\circ$ case, shown in Figure 6.12, the effect of defects on elastic modulus of ideal cases obtained from modified defect layer method were 6%,6%, 8.3% and 11.5% for T_1 equal to 50° , 60° , 80° and 85° respectively. The prediction from the smearing method was approximately 2% less than the results obtained from modified defect layer method, except for the last one which has deviation of 3.4%. However, all the values were under predicted. Also, the volume fraction prediction deviation was 10% for the case with $T_1 = 85^\circ$. Moreover, for $T_0 = 80^\circ$ case, shown in Figure 6.12, the effect of defect obtained was 10.4%, 7.9%, 7.8% and 8.5% for edge angles 55° , 60° , 70° and 85° respectively. For all the cases, the predicted values were

2% less than the values from the modified defect layer method, except for case of $T_1 = 60^\circ$, in which the deviation was 3.5%. All the values were under predicted. For $T_0 = 80^\circ$, the maximum deviation of 17% in volume fraction prediction is obtained for $T_1 = 60^\circ$ case. For other edge angles the prediction was within 5%. Through these results it can be said that effect of volume fraction prediction is low when the prediction of elastic modulus is made. However, it can not be inferred why this low sensitivity is there. A further study need to be required to investigate it.

For Material 2: The lamina results of single sided cuts for Material 2 are shown in Figure 6.13-6.16. For Material 2 case, the difference between the resin and composite properties are quite significant, thus, the effect of the defects were prominent for the case $T_0 = 10^\circ$ and 20° as shown in Figure 6.13. Since, change is only in the material, thus, the volume fraction obtained from the modified defect layer method and predicted by the smearing method will remain same as discussed for the case of Material 1. For $T_0 = 10^\circ$ case, the effect of defect was 7.5%, 6.8% and 5.9% for $T_1 = 0^\circ, 20^\circ$ and 25° respectively. Through smearing these effect were under estimated by 1%, which suggests that the effect of defect was accurately predicted. However, the volume fraction prediction were offset by maximum 68% than the actual case. This means that the effect of the fibre angular distortion is the major contributor to the effect of defect. For $T_0 = 20^\circ$ case, the effect of defect on the elastic modulus of ideal panels were equal to 6.6%, 6.7%, 6.1% and 4.7% for $T_1 = 5^\circ, 10^\circ, 30^\circ$ and 35° respectively. The prediction through smearing showed 2.5% and 5% variation in the value for the case $T_1 = 30^\circ$ and 35° . For other case, the elastic modulus predicted differed only by 1% from modified defect layer method results. All the results were under predicted. For the case of $T_1 = 35^\circ$, the volume fraction prediction was accurate and varied 1% from the actual value, however, the prediction of the elastic modulus varied by 5%. This suggests that the interpolation function, used for assignment of the properties to the mesh elements for FE analysis of the panel through smearing, has some error, and this error is reflected in the result.

For the case of $T_0 = 30^\circ$, shown in Figure 6.14, the effect of the defect on the elastic properties of ideal lamina were equivalent to 5.2%, 6.0%, 5.3% and 5.5% for $T_1 = 15^\circ, 20^\circ, 40^\circ$ and 50° respectively. Smearing results show that elastic properties have been under estimated for all edge angles. The maximum deviation of the predicted elastic property from the result of modified defect layer method result was 5.5%. It was obtained for the case of $T_1 = 35^\circ$. It can be seen, for this case difference in the predicted and actual result is equivalent to 5.5% and the volume fraction prediction is within 1% range from the actual value. Thus, this is also the case where the interpolation function's errors are visible. However, the prediction are under predicted, thus, it is on the conservative side. Similar results were obtained for case $T_0 = 40^\circ$, shown in Figure 6.14. The effects of tow drop defect on the elastic properties of the ideal panel were 5.5%, 5.0%, 6.2% and 6.7% for $T_1 = 25^\circ, 30^\circ, 50^\circ$ and 60° respectively. The predicted values for all the cases were 5% less than the results from modified defect layer method.

For the case of $T_0 = 50^\circ$, shown in Figure 6.15, the effect of the defects were 4.9%, 6.2%, 6.4%, 8.2% and 10.2% for $T_1 = 30^\circ, 40^\circ, 60^\circ, 70^\circ$ and 75° respectively. The effect of defect increased with the increase in the angle due to rise in the difference between the elastic properties of resin and composite. For this case also the elastic properties were under predicted by approximately 5% for every case. For the case of $T_0 = 60^\circ$, shown in Figure 6.15, the elastic properties calculated from the modified defect layer approach were 6.6%, 6.3%, 7.5%, 10.9% and 15.11% less than the ideal cases for $T_1 = 40^\circ, 50^\circ, 70^\circ, 80^\circ$ and 85° respectively. For this

case, the prediction of elastic modulus through smearing was under predicted for all the edge angles by approximately 3%. The prediction of volume fractions, for all the edge angles, was within 1%, thus, it could be inferred that the error in the interpolation function reduced.

Lastly, for the case of $T_0 = 70^\circ$, shown in Figure 6.16, the effect of defect on elastic modulus had comparatively increased than other cases discussed previously and were equivalent to 8.1%, 7.5%, 9.1% and 12.4% for edge angles equal to 50° , 60° , 80° and 85° respectively. Also, the difference in the predicted and actual result from defect layer method were equivalent to 4.7%, 2.8%, 1.7% and 3.8% respectively. All the results were under predicted. For the case of $T_0 = 80^\circ$, shown in Figure 6.16, the effect of defect on elastic modulus of ideal panels were 11.9%, 9.1%, 8.6% and 9.0% for edge angles equal to 55° , 60° , 70° and 85° respectively. The predicted result from smearing varied less than 3% for each case except for the case of edge angle equal to 60° , in which the variation was 5.3%. Moreover, for the case of edge angle equal to 60° , the volume fraction prediction was more than 17% than the actual result, however, the difference in the elastic modulus results from prediction and defect layer approach was 5.3%. It suggest that the volume fraction effect is less than the fibre angular distortion effect.

From the results of Material 1 and 2 it can be inferred that through smearing, prediction of the elastic properties were maximum deviated by 5% than the values calculated from the modified defect layer approach. And for most of the cases the elastic properties were under predicted. It means that the elastic properties were on conservative side.

Results for zipper cuts

The results of zipper cuts were very similar to the results obtained in the case of single sided cuts. This is because the fibre angular distortion is same for the zipper cuts and single sided cuts, if the angles at the center and at the edges are equal. The equality of the fibre angular distortion is because the shift distance calculated for the plies will be same for the two cases. Also, the fibre angle and gradient of the fibre angle, present in the panel will be same for the two cases. This means that the fibre angular distortion calculated from Eq. (6.2) and Eq. (6.9) will be the same. Moreover, the volume fraction generated corresponding to the fibre angular distortion is almost same for the two cases. This is because the volume fraction is calculated from Eq. (6.7) and Eq. (6.11) for the two cases. Now, the maximum difference between the volume fraction calculated from these expression at same fibre angle and fibre angular distortion is less than 2% for the entire range of the fibre angle distortion from 1° to 12° . This suggests that the volume fraction prediction and the fibre angular distortion prediction will remain the same for single sided and zipper cuts. Due to this reason no remarkable difference was found between the results obtained in previous chapter in Section 5.3. And no significant difference is obtained for the lamina results. The results of the zipper cuts are shown in Appendix Section B.1. However, to generate the results for the zipper cuts correlation developed through knock-down factors were used for the property assignment instead of the interpolation function. It suggests that, for the zipper cuts, an analytical formula can be used instead of the basic interpolation scheme through which the property could be assigned to the mesh element in the FE analysis.

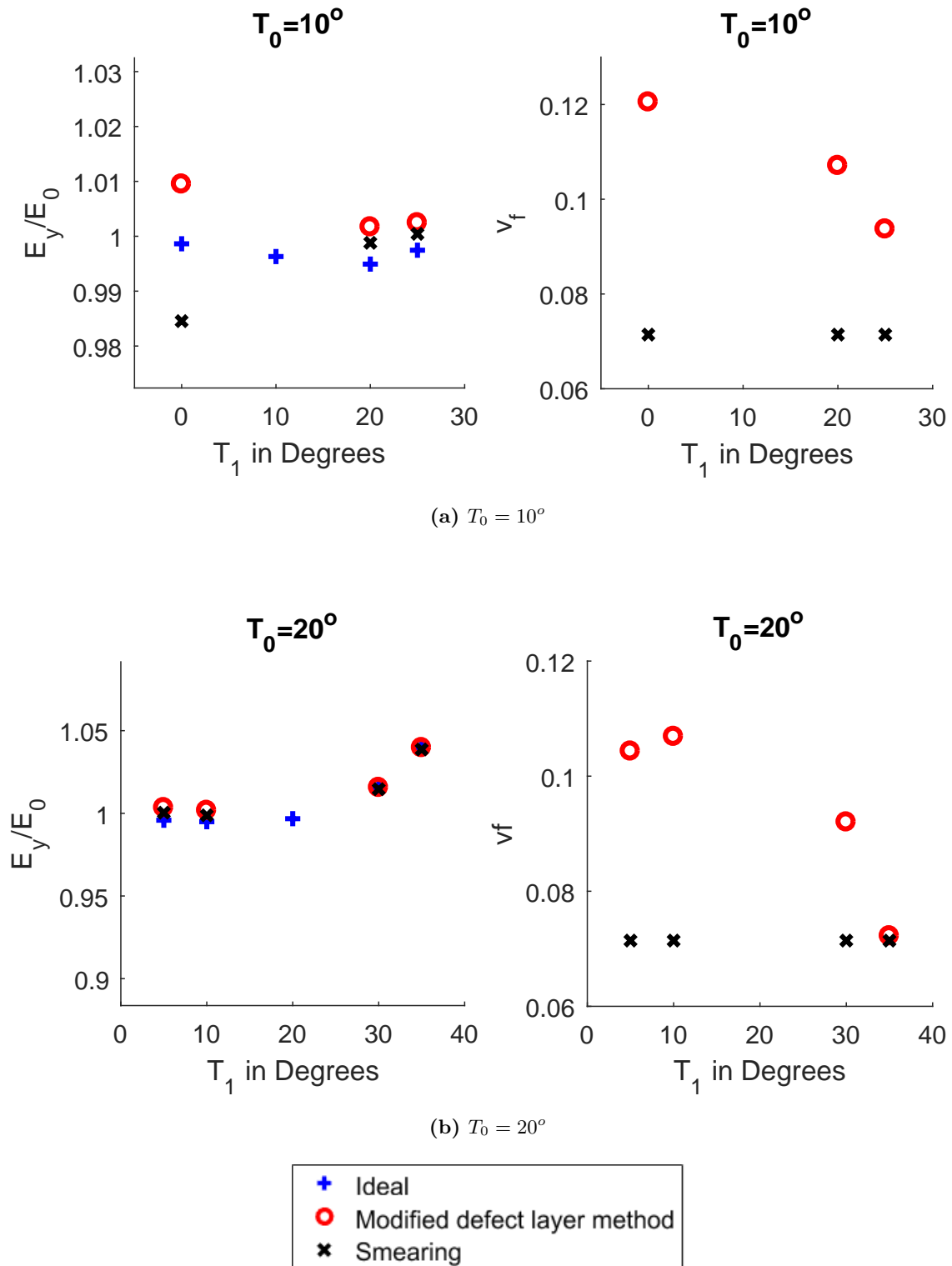


Figure 6.9: Single Sided Cuts (Material 1): Results of normalized elastic modulus (E_y/E_0) and volume fraction of tow drop defect (v_f) obtained from the modified defect layer method and smearing methodology for plies with center angle $T_0 = 10^\circ$ and $T_0=20^\circ$ and for various edge angle T_1 .

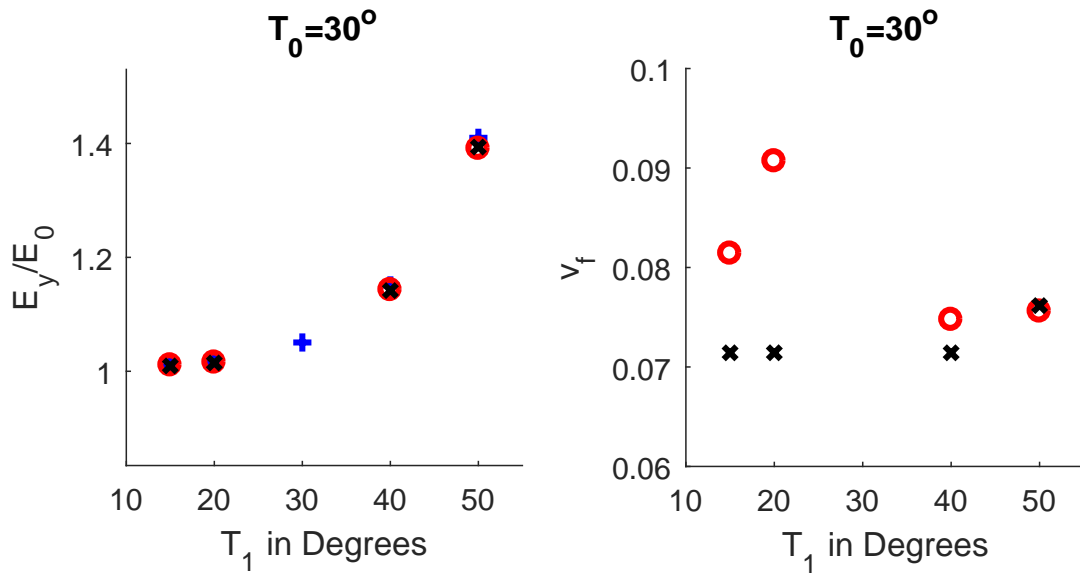
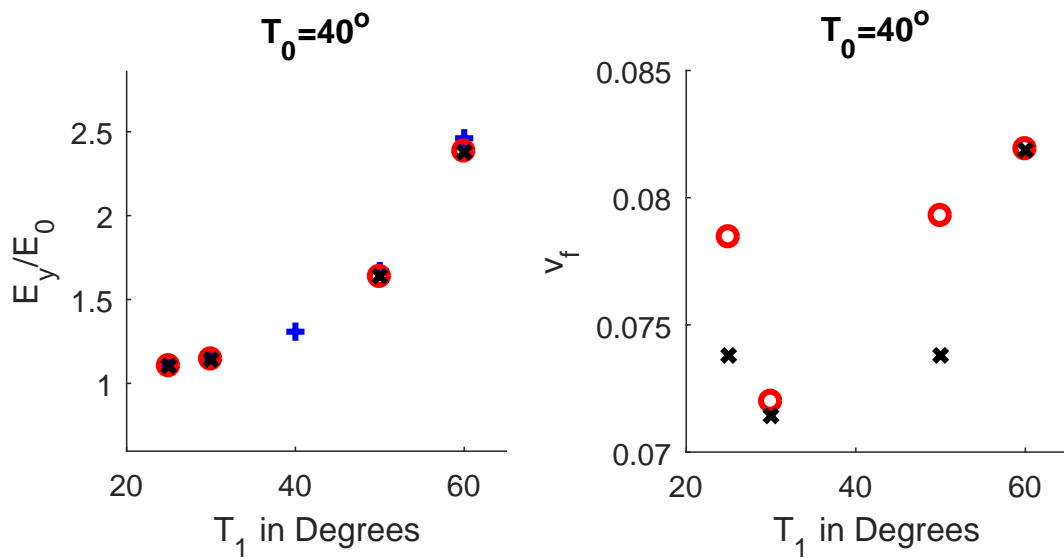
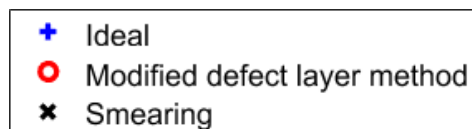
(a) $T_0 = 30^\circ$ (b) $T_0 = 40^\circ$ 

Figure 6.10: Single Sided Cuts (Material 1): Results of normalized elastic modulus (E_y/E_0) and volume fraction of tow drop defect (v_f) obtained from the modified defect layer method and smearing methodology for plies with center angle $T_0 = 30^\circ$ and $T_0 = 40^\circ$ and for various edge angle T_1 .

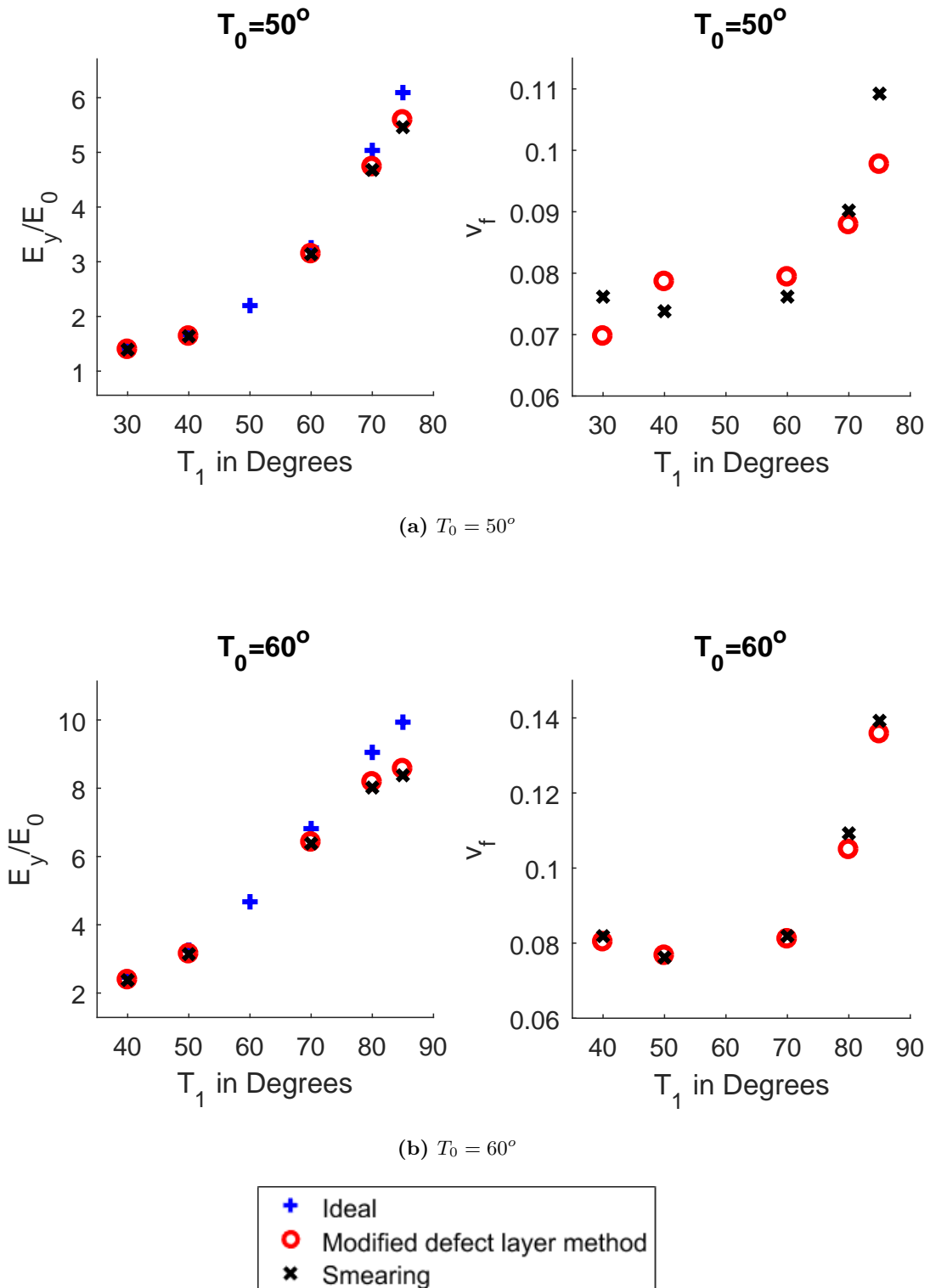


Figure 6.11: Single Sided Cuts (Material 1): Results of normalized elastic modulus (E_y/E_0) and volume fraction of tow drop defect (v_f) obtained from the modified defect layer method and smearing methodology for plies with center angle $T_0 = 50^\circ$ and $T_0=60^\circ$ and for various edge angle T_1 .

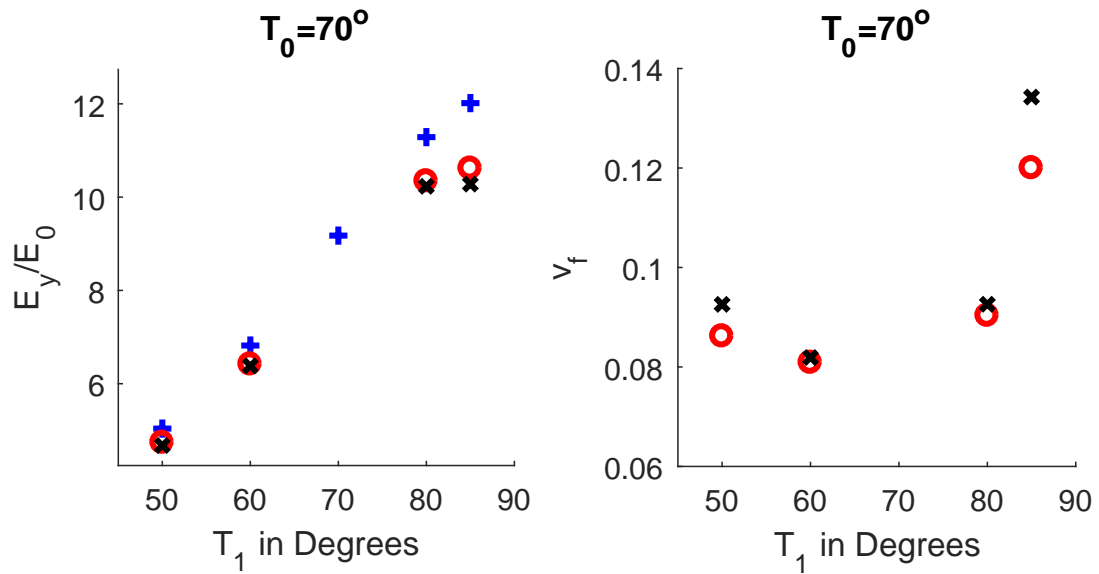
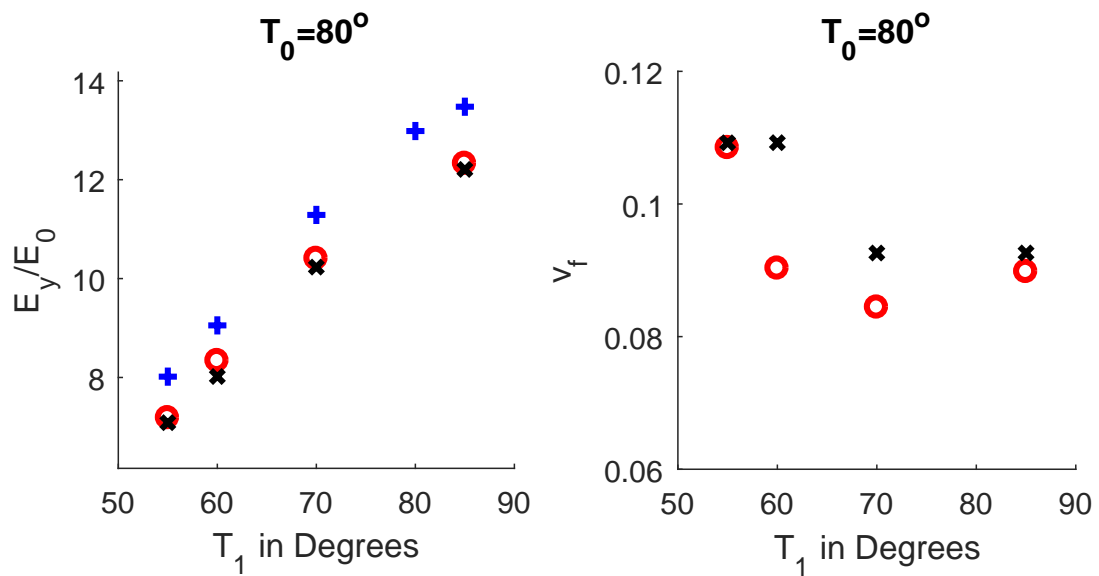
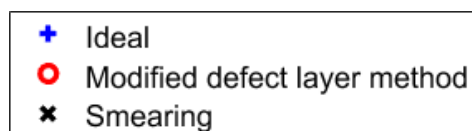
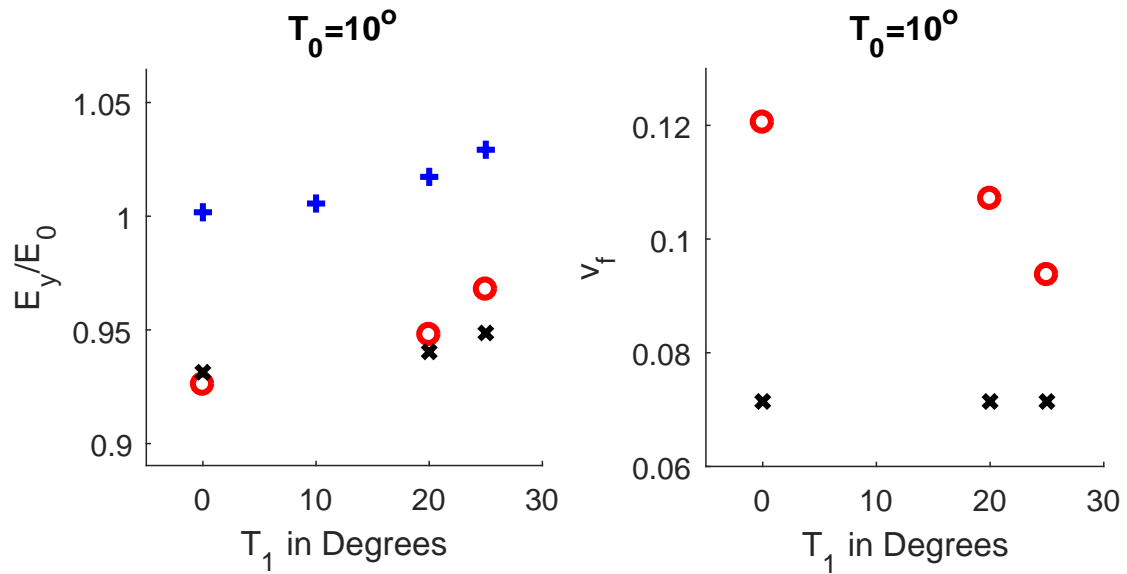
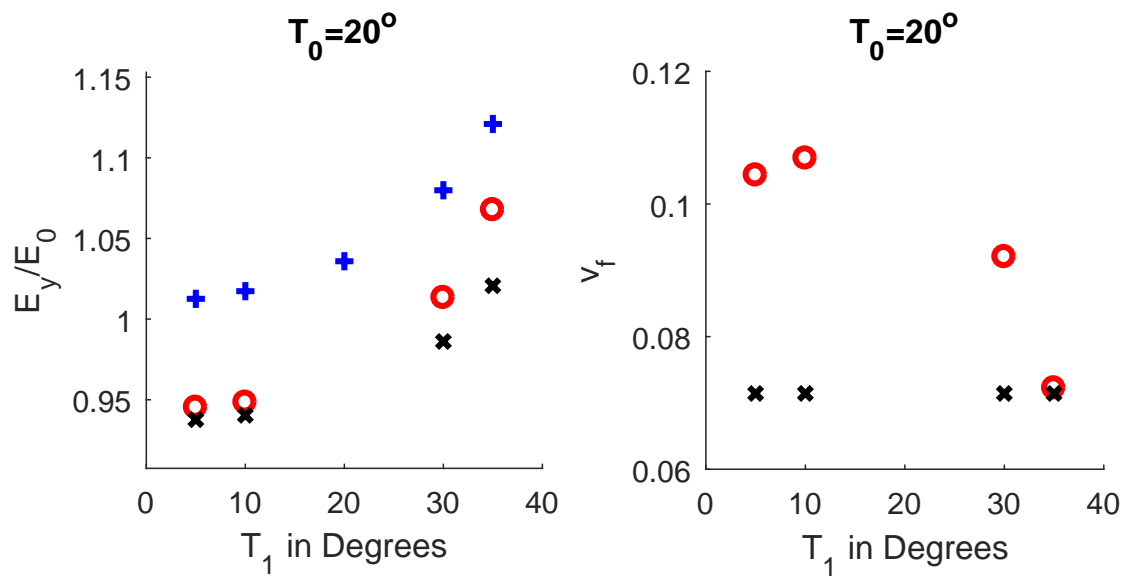
(a) $T_0 = 70^\circ$ (b) $T_0 = 80^\circ$ 

Figure 6.12: Single Sided Cuts (Material 1): Results of normalized elastic modulus (E_y/E_0) and volume fraction of tow drop defect (v_f) obtained from the modified defect layer method and smearing methodology for plies with center angle $T_0 = 70^\circ$ and $T_0 = 80^\circ$ and for various edge angle T_1 .



(a) $T_0 = 10^\circ$



(b) $T_0 = 20^\circ$

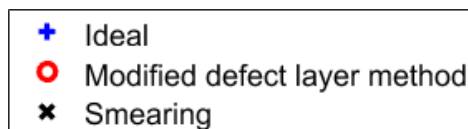
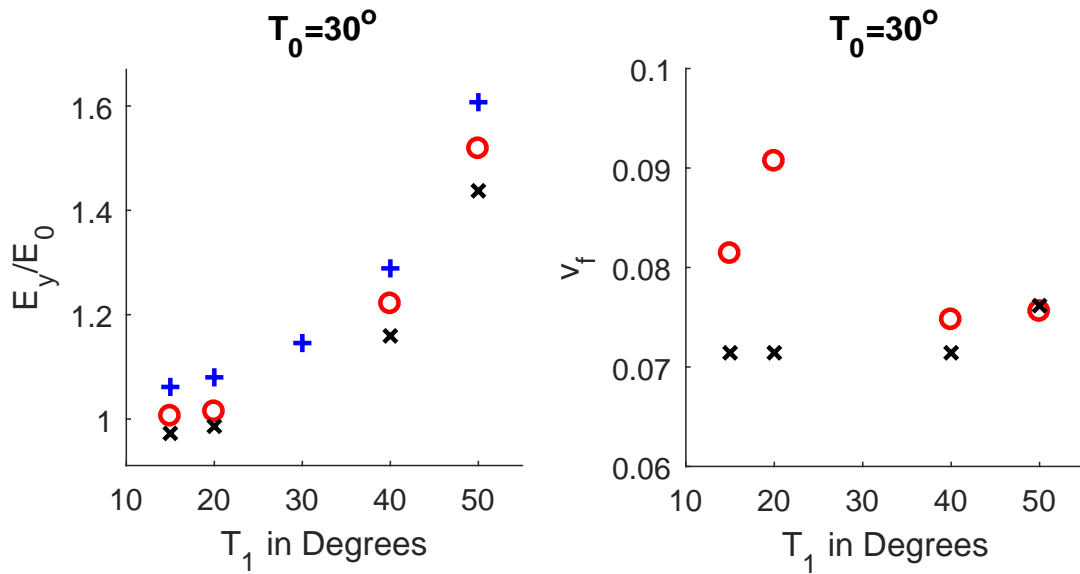
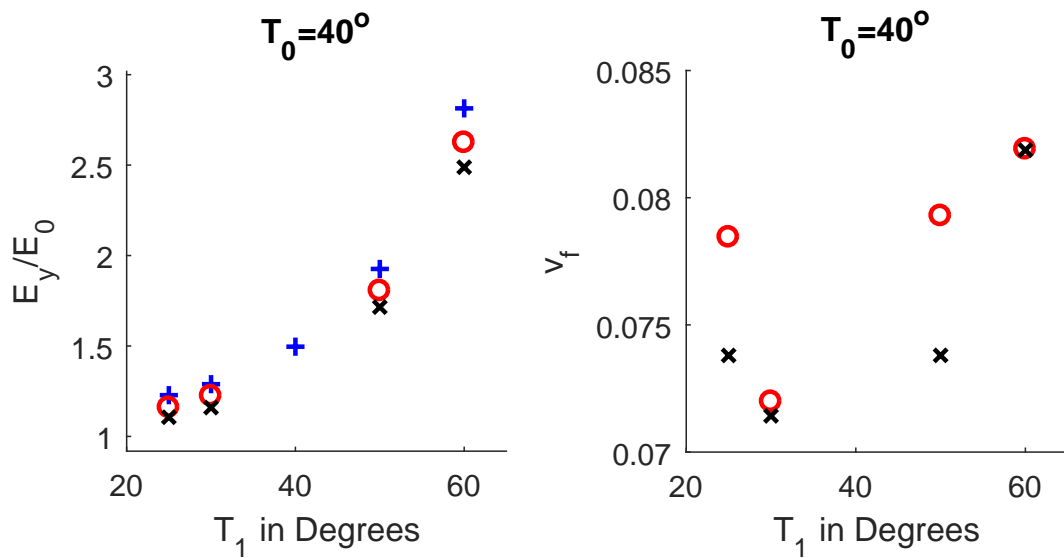


Figure 6.13: Single Sided Cuts (Material 2): Results of normalized elastic modulus (E_y/E_0) and volume fraction of tow drop defect (v_f) obtained from the modified defect layer method and smearing methodology for plies with center angle $T_0 = 10^\circ$ and $T_0=20^\circ$ and for various edge angle T_1 .



(a) $T_0 = 30^\circ$



(b) $T_0 = 40^\circ$

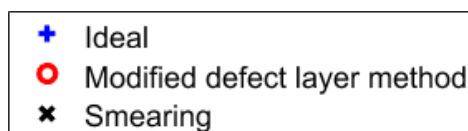


Figure 6.14: Single Sided Cuts (Material 2): Results of normalized elastic modulus (E_y/E_0) and volume fraction of tow drop defect (v_f) obtained from the modified defect layer method and smearing methodology for plies with center angle $T_0 = 30^\circ$ and $T_0=40^\circ$ and for various edge angle T_1 .

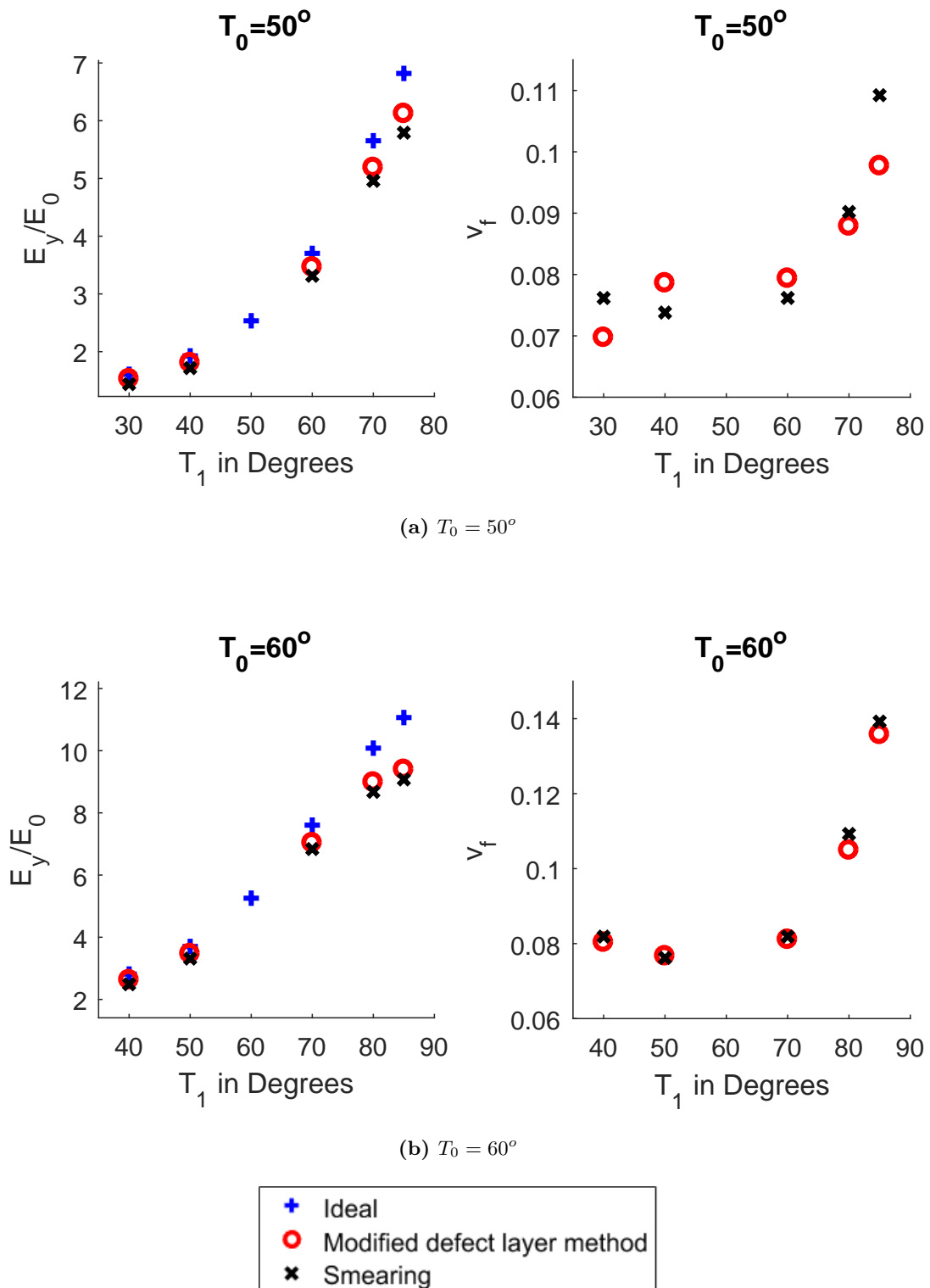
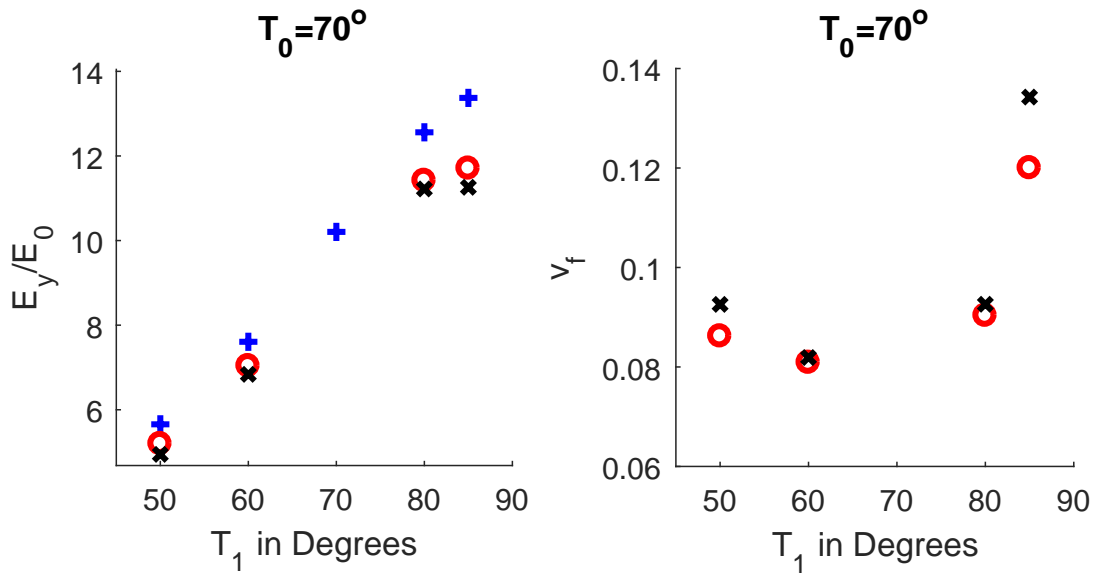
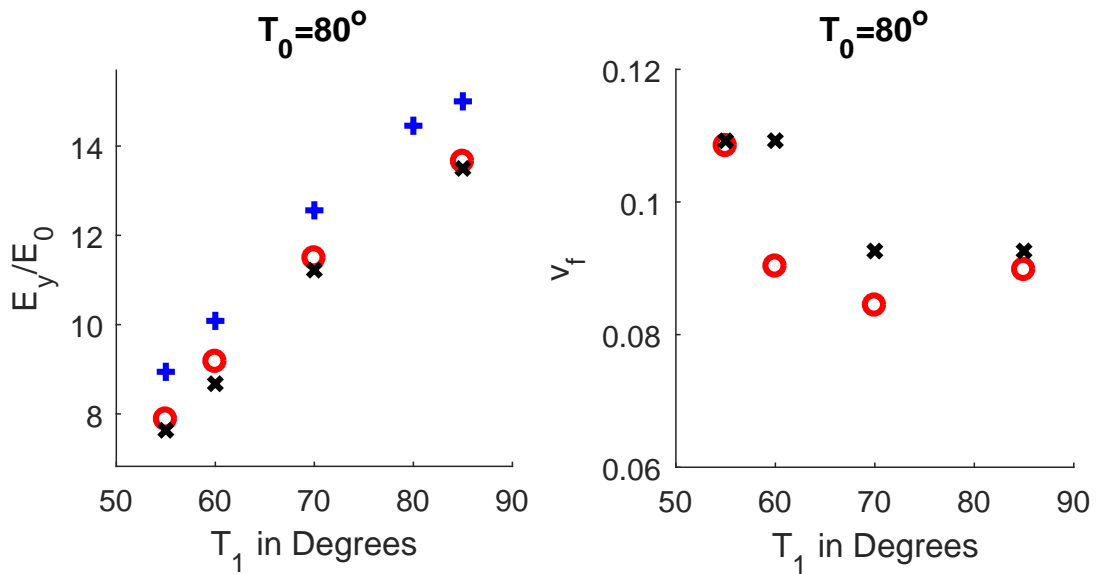


Figure 6.15: Single Sided Cuts (Material 2): Results of normalized elastic modulus (E_y/E_0) and volume fraction of tow drop defect (v_f) obtained from the modified defect layer method and smearing methodology for plies with center angle $T_0 = 50^\circ$ and $T_0=60^\circ$ and for various edge angle T_1 .



(a) $T_0 = 70^\circ$



(b) $T_0 = 80^\circ$

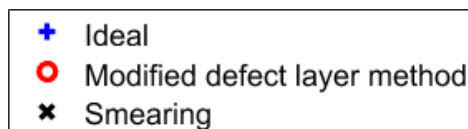


Figure 6.16: Single Sided Cuts (Material 2): Results of normalized elastic modulus (E_y/E_0) and volume fraction of tow drop defect (v_f) obtained from the modified defect layer method and smearing methodology for plies with center angle $T_0 = 70^\circ$ and $T_0=80^\circ$ and for various edge angle T_1 .

Label	Configuration
A	$[\pm < 47 42 > / \pm < 46 60 > / \pm < 55 68 > / \pm < 52 65 >]_s$
B	$[\pm < 47 42 > / \pm < 42 57 > / \pm < 60 72 > / \pm < 64 76 >]_s$
Baseline	$[45/0/ - 45/90]_{2s}$

Table 6.4: Configuration of Laminates studied in this thesis equivalent to the laminates studied by *Fayazbakhsh et al* [6]

6.3.2 Laminate results

The laminates with configurations shown in Table 6.4 were studied through smearing and the results are compared with the results obtained by modified defect layer method. Analysis has been done for two materials. The results are discussed below.

For Material 1: The results of elastic modulus are shown in Table 6.5. The column named DLM shows modified defect layer approach results. Terms in bracket give the percentage difference from the ideal case of VSP. For both A and B cases, the prediction of elastic modulus from the smearing case is less than the result obtained from modified defect layer analysis for both single sided and zipper cuts. It suggests that the predictions are on the conservative side.

Configuration	Ideal VSP	Single sided cut results		Zipper cuts results	
		DLM	Smearing	DLM	Smearing
A	0.70	0.67(-4.2%)	0.66(-5.7%)	0.67(-4.2%)	0.66(-5.7%)
B	0.98	0.92(-6.1%)	0.90 (-8.2%)	0.91(-7.1%)	0.90(-8.2%)

Table 6.5: Normalized elastic modulus results for tow drop VSP from modified defect layer method (DLM) and smearing methodology for Material 1. Percentage in bracket shows the percentage difference between the value and ideal case value.

The results of buckling load are shown in Table 6.6. For both A and B, the prediction of buckling load from the smearing case is more than the result obtained from modified defect layer. Thus, predicted results are on non-conservative side. For laminate A and B, the difference in the buckling load from the ideal case and results from the modified defect layer analysis is less than 8.3%, for both single sided cut and zipper cut cases. Thus, the effect of defect is maximum 8.3% for all cases. Through smearing minimum 5.3% of the effect of defect gets captured for all the cases. Thus, for configuration A and B, through smearing minimum 64% of the effect of defect has been captured by the smearing.

Configuration	Ideal VSP	Single sided cut results		Zipper cuts results	
		DLM	Smearing	DLM	Smearing
A	1.33	1.23(-7.5%)	1.26(-5.3%)	1.22(-8.3%)	1.25(-6.0%)
B	1.28	1.18(-7.8%)	1.21(-5.5%)	1.18(-7.8%)	1.21(-5.5%)

Table 6.6: Normalized buckling load results for tow drop VSP from modified defect layer approach (DLM) and smearing methodology for Material 1. Percentage in bracket shows the percentage difference between the value and ideal case value.

For Material 2: The results of elastic modulus are shown in Table 6.7. For both A and B cases, the prediction of elastic modulus from the smearing case is less than the result obtained from modified defect layer analysis for both single sided and zipper cuts. It suggests that the predictions are on the conservative side. The percentage difference has increased for both the cases compared to the difference obtained in the Material 1 case. This is because the resin properties are weaker than the composite properties in this case.

Configuration	Ideal VSP	Single sided cut results		Zipper cuts results	
		DLM	Smearing	DLM	Smearing
A	0.72	0.66(-8.3%)	0.64(-11.1%)	0.66(-8.3%)	0.65(-9.7%)
B	1	0.91(-9.0%)	0.89(-11.0%)	0.92(-8.0%)	0.89(-11.0%)

Table 6.7: Normalized elastic modulus results for tow drop VSP from modified defect layer method (DLM) and smearing methodology for Material 2. Percentage in bracket shows the percentage difference between the value and ideal case value.

The buckling load results are shown in Table 6.8. For both A and B, the prediction of buckling load from the smearing case is more than the result obtained from modified defect layer. Thus, predicted results are on non-conservative side. For laminate A and B, the difference in the buckling load from the ideal case and results from the modified defect layer analysis is less than 8.3%, for both single sided cut and zipper cut cases. Thus, maximum effect of defect is equal to 8.3% for all cases. Through smearing minimum 6.8% of the effect of defect gets captured for all the cases. Thus, for configuration A and B, through smearing minimum 80% of the effect of defect has been captured by the smearing. Comparing the buckling load result from Material 1 results it can be seen that the effect of defect for buckling case remained almost same. Thus, effect of resin on the buckling load is not that prominent than it is on the elastic modulus properties of the VSP.

Configuration	Ideal VSP	Single sided cut results		Zipper cuts results	
		DLM	Smearing	DLM	Smearing
A	1.33	1.22(-8.3%)	1.24(-6.8%)	1.22(-8.3%)	1.23(-7.5%)
B	1.27	1.17(-7.9%)	1.19(-6.8%)	1.17(-7.9%)	1.19(-6.8%)

Table 6.8: Normalized buckling load results for tow drop VSP from modified defect layer approach (DLM) and smearing methodology for Material 2. Percentage in bracket shows the percentage difference between the value and ideal case value.

Table 6.9 shows that the volume fraction calculated through smearing methodology and modified defect layer method. It shows volume fraction is under predicted for both configuration than modified defect layer method results. Now, the under prediction of the volume fraction and over prediction of the stiffness properties through smearing can be explained by revisiting the lamina results for Material 1 and 2 of single sided and zipper cuts. The effect of the volume fraction was overcome by the fibre angle distortion effect for each case. It was inferred because accurate predictions of elastic modulus were made instead of large variation in the volume fraction prediction. Also, for the accurate prediction of the volume fraction the results of the lamina case were under predicted which was attributed to the error in the correlation and interpolation function. Due to combined effect of these two effect the laminates elastic

properties were under predicted.

Configuration	Single sided cut results			Zipper cuts results		
	DLM	Smearing	Diff.	DLM	Smearing	Diff.
A	8.3	7.8	-6.0%	8.2	7.8	-4.8%
B	8.4	8.1	-3.6%	8.2	8.1	-1.2%

Table 6.9: Percentage volume fraction results for tow drop VSP from smearing methodology. 'Diff.' represents percentage difference between DLM and smearing results.

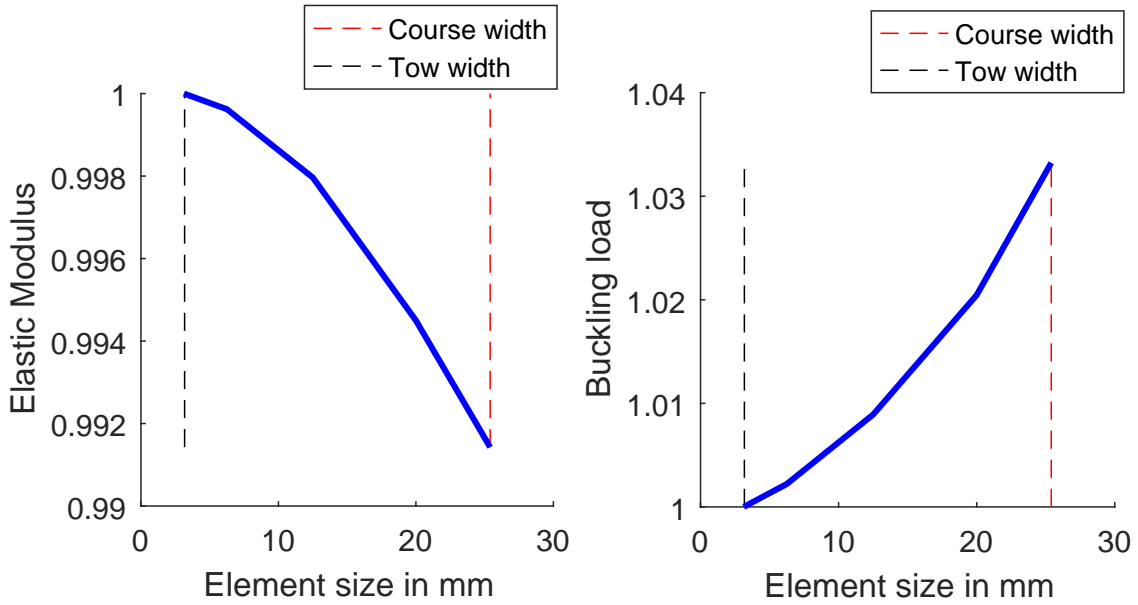


Figure 6.17: Steering effect on the elastic modulus and buckling load

The over prediction of the buckling load result is due to the large element size used to predict the result through smearing. The orientation to the mesh elements are given depending on the position of the centroid of the element. Since, most of the ply in the configuration A and B have higher edge angle than the center angle. It means that the element at the edges will be assigned properties with higher fibre angle orientation. Due to this a major load will be transferred by the edge portion and will lead to higher buckling load. With finer elements the fibre angle variation is captured precisely during the analysis which would reduce the buckling load to the actual solution. To support this argument a high steered panel $[\pm < 30 | 60 >]_{4s}$ with the similar dimension were analyzed with different element sizes. The stiffness and the buckling properties were calculated and the effect of steering was captured. The ideal panel was chosen for analysis so that only the effect of steering is captured. The results are shown in Figure 6.17. The results in the figure are normalized by the results obtained for the mesh size 3.175mm. The convergence criterion followed was that if the results of two consecutive mesh sizes do not differ by 1% then the solution was assumed to be converged. Now, for the stiffness case based on this criterion the results were converged at the course width. However, for the

buckling load results, the convergence did not happen till the element size is close to the tow width which is also the minimum defect size for the manufacturable panels. Thus, coarse meshes do not capture the effect of steering, however, prediction of the stiffness properties can be made accurately than the buckling load. It can also be noticed that the buckling load decreases when the element size decreases. It suggests that for large element the edges behave extra stiffened than at the smaller element size. Moreover, the effect is not that significant. The converged result varied by only 3% from the large size element. However, this difference can be equivalent to the effect of defect and thus give spurious result for the effect of defect. Therefore, over prediction of the buckling load could be because of this effect.

The elastic modulus and buckling load results for the panel with layup $[\pm 45/\pm < 45|60 > / \pm < 30|15 > / < 45|60 >]_s$ are discussed below. The panel was tested for two materials, thus, the results are presented, firstly, for Material 1 and then for Material 2.

For Material 1: The results are shown in Table 6.10. The results suggest that the panel has lower elastic modulus and higher buckling load than the quasi-isotropic panel. Now, from comparing the smearing and modified defect layer method results, it can be inferred that the elastic properties were under predicted and are on conservative side. Whereas, Buckling load is over predicted, the over prediction of the buckling load can be attributed to the not capturing of the steering effect due to the large element size. For this panel, through smearing minimum 76% of the effect of defect on the buckling load is captured for single sided and zipper cut cases. Also, comparing the single sided cuts and zipper cuts suggests that there is no difference between the two strategies. There was a small difference between the values obtained by two strategies, however, due to rounding off the decimals there seems no difference in the two strategy.

Result type	Ideal VSP	Single sided cut results		Zipper cuts results	
		DLM	Smearing	DLM	Smearing
Elastic modulus	0.55	0.52 (-5.4%)	0.51 (-7.2%)	0.52 (-5.4%)	0.51 (-7.2%)
Buckling Load	1.32	1.28 (-3.0%)	1.29 (-2.3%)	1.28 (-3%)	1.29 (-2.3%)
Volume fraction	-	4.04%	3.77%	4.05%	3.77%

Table 6.10: Results obtained by modified defect layer (DLM) and smearing method of optimum laminate reported by *Tatting et al* [8] for Material 1. Percentage in bracket shows the percentage difference between the value and ideal case value.

For Material 2: The results are shown in Table 6.11. Similar to the previous case, for this case, the elastic properties of the ideal panel are less than the baseline panel. However, the buckling properties are more than the baseline panel. The effect on the elastic modulus properties have increased as the resin is weaker in this case. However, the buckling properties remain the same. Thus, it could be said that the effect of the weak resin do not affect the buckling properties and the fibre angle orientation has more effect on the buckling properties than the effect of defect. For this case also elastic modulus the values are under predicted and buckling is over predicted. Through smearing minimum 50% of the effect of defect on the buckling load was captured for the both single sided and zipper cuts. The over prediction of the buckling load is due to non-capturing of the steering effect.

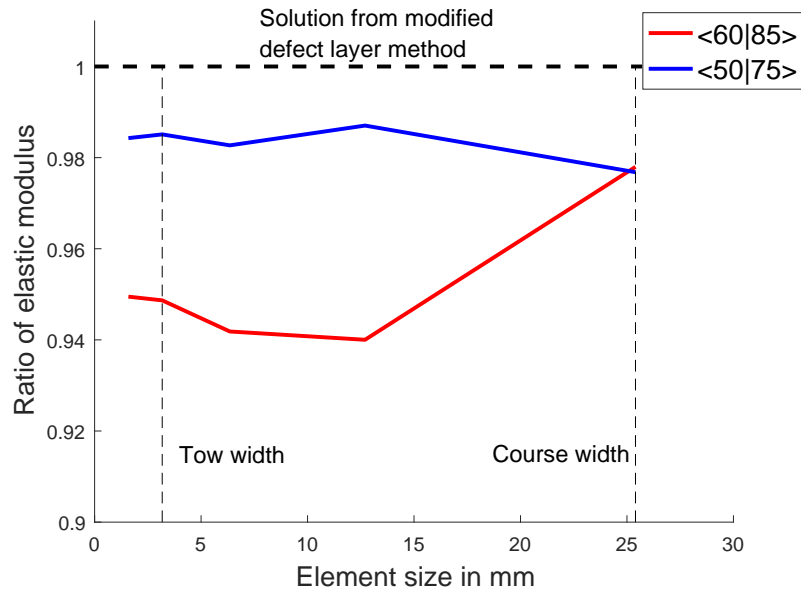


Figure 6.18: Convergence study of smearing methodology

Result type	Ideal VSP	Single sided cut results		Zipper cuts results	
		DLM	Smearing	DLM	Smearing
Elastic modulus	0.55	0.51 (-7.2%)	0.50 (-9.0%)	0.51 (-7.2%)	0.50 (-9.0%)
Buckling Load	1.31	1.27 (-3.0%)	1.28 (-2.3%)	1.27 (-3.0%)	1.29 (-1.5%)
Volume fraction	-	4.04%	3.77%	4.05%	3.77%

Table 6.11: Results obtained by modified defect layer (DLM) and smearing method of optimum laminate reported by *Tatting et al* [8] for Material 2. Percentage in bracket shows the percentage difference between the value and ideal case value.

Computational effort

The Lamina and Laminate results show that the smearing methodology predicts the effect of the tow drop defects reasonably accurate for most of the cases. To produce these results small number of mesh elements were used than modified defect layer method. The choice of the larger element are discussed in this section, also, the computational time involved in obtaining these results from smearing are discussed here. These computational efforts are compared with computational effort required for modified defect layer method. Two cases are presented here for single sided cuts with configuration $[\pm < 60|85 >]_{4s}$ and $[\pm < 50|75 >]_{4s}$. The choice of these configurations was made because effect of tow drop defect on elastic properties were significant. Therefore, the effect of element size would be visible on these configuration. Thus, for these cases smearing methodology was applied for different finite element sizes and convergence of results to the results obtained by modified defect layer method were studied. For the analysis, Material 1 was used.

Figure 6.18 shows ratio of the elastic modulus obtained by smearing to the elastic modulus obtained by modified defect layer method. This ratio was evaluated for different element

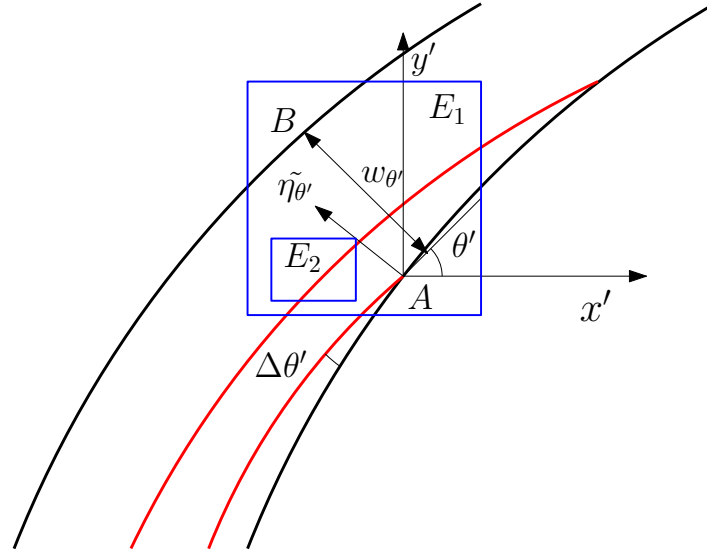


Figure 6.19: Element size comparison in smearing

sizes. For convergence, the ratio of elastic modulus should tend to 1. It could be inferred from Figure 6.18 that the results do not converge to 1. For smaller element sizes, the results converge to certain values lower than 1. However, the results do not change drastically from the initial value obtained from the element size which is equivalent to the course width. The reason for not converging to the solution obtained from modified defect layer method, is the calculation of the fibre angular distortion, $\Delta\theta'$, in the smearing methodology. Since, the fibre angle distortion is calculated through fibre angle gradient across the effective course width, ($w_{\theta'}$), and the volume fraction prediction is based on that course width, thus, the results obtained at element size equivalent to the course width are satisfactory. However, as the element sizes are reduced the gradient of the fibre angles are calculated at much smaller length than the effective course width which implies that the fibre angle distortion are evaluated in the regions, where the fibre angle distortion are not present. Thus, the deviation from the results are obtained.

As shown in Figure 6.19, element E_1 captures the effect of the fibre angle distortion perpendicular to the fibre direction however, a smaller element E_2 does not capture it. Because inside the course there is no fibre angular distortion perpendicular to the direction of the fibre angle. Thus, the results obtained at the higher element sizes, or comparable to the effective course width sizes, are relevant and as the element size reduces the results obtained are more fictitious. Moreover, the element sizes can not be increased as it will not capture the effect of steering fibres as the orientation are given based on the position of the centroid of the element. This implies that the element size equivalent to the course width could be used to evaluate the results. The smearing results which were discussed for different plies in previous sections, were evaluated with element size equivalent to the course width which was 25.4mm for each case. Moreover, the pre-processing time taken by modified defect layer method to give the estimate of result of one ply was equivalent to approximately 450 sec, whereas the smearing methodology takes 10 sec of pre-processing time. These time were evaluated from the running of the *Matlab* code on device with specification- Intel Core i7-5500U, 3.0GHz. It might be possible that the code can be modified and faster results can be achieved but the

effectiveness of the code has not been measured. However, the pre-processing step of determination of location and geometry of tow drop defects has been eliminated. This advantage comes with the loss in accuracy of the results. For the major cases, the stiffness properties are under estimated thus the values are on the conservative side. But, for the buckling case larger element size poses problem because coarser mesh do not capture the fibre steering effect properly. Thus, special care need to be taken to evaluate buckling load of the VSP.

6.4 Applicability of Smearing Methodology

As shown in above results, smearing predicts the results of effective elastic modulus and buckling load comparably well for maximum cases at lamina and laminate level. However, the prediction of the results are subjected to certain choices which has to be made to make this methodology work. One major choice is the element size. For this study, the element size chosen is comparable to the course width size and it is also shown in the convergence study that the choice of the element is made because it captures the fibre angular distortion in the panel. Also, for evaluating the fibre angle distortion through smearing only required information is the fibre angle at the nodes of the element. Thus, this methodology could be applied to the case where the fibre angle distribution is known. The fibre angle distribution can be generated through any reference curve like constant curvature reference curve. It means that defect generated from constant curvature reference curve or other manufacturable curve can also be accounted by this technique. However, only problem in implementing it, is to calculate the shift distance. This is a computational step need to be carried out for every ply of the panel. This is because shift distance is dependent upon the reference curve and course.

Another major problem with smearing is the prediction of accurate volume fraction. The prediction of the volume fraction in some case were offset compared to the modified defect layer method results. This was observed for low fibre steering and low center fibre angle cases, like $\langle 30|20 \rangle$ and $\langle 10|0 \rangle$. For these cases, the tow drops are dependent upon center angle, edge angle and the size of the laminate. The geometry of the tow drop for $\langle 30|20 \rangle$ ply is shown in Figure 6.20a. It shows that the tows are not dropped after one time. However, the calculation of the volume fraction for the case of smearing through micro-mechanical models are based on the assumption that the tow are dropped subsequently in the y - direction as shown in Figure 6.3. This condition is not fulfilled by $\langle 30|20 \rangle$ ply. Thus, the volume fraction of the laminates are not accurately predicted by the smearing case. For the high steering fibre case such as $\langle 60|40 \rangle$ as shown in the Figure 6.20b, the number of tow drops are more and it follows the assumption of the micro-mechanical model that the tows get drop subsequently, thus, the volume fraction prediction is accurate for these cases. Also, for the low steered high center fibre angle VSP such as $\langle 70|80 \rangle$ ply the volume fraction prediction are good comparable to the low steered low center fibre angle VSP ply such as $\langle 30|20 \rangle$. As shown in Figure 6.20c, the $\langle 70|80 \rangle$ ply gets more length across the diagonal of the VSP to cover which results into more tow drop than the case $\langle 30|20 \rangle$ ply. Thus, the volume fraction prediction is accurate for the case $\langle 70|80 \rangle$ ply. From this discussion it could be concluded that the prediction of the volume fraction will be good for the plies with more number of tow drops in the ply than the ply with less number of tow drop case. However, there are other factors which also influence the volume fraction determination. Approximation of the effective course width, w_{θ} and fibre angle distortion calculation through it, can also influence

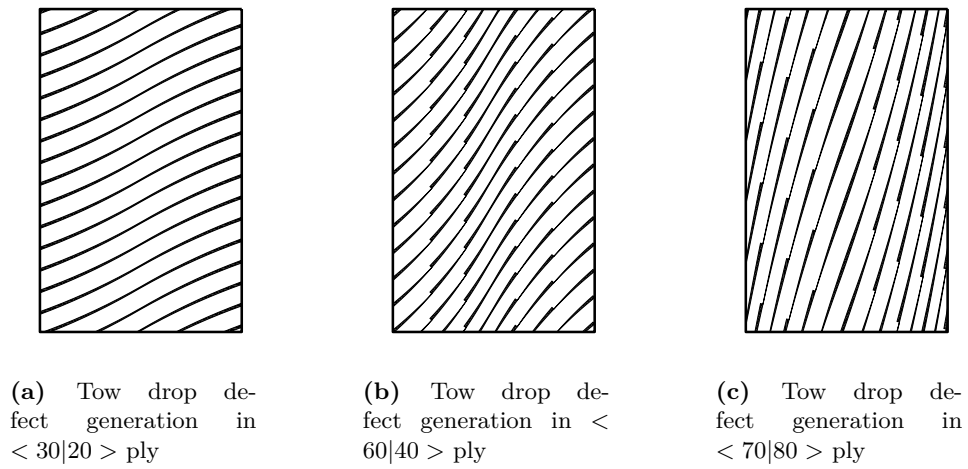


Figure 6.20: Tow drop defects in different VSP plies

the volume fraction determination. The influence of these factors on the volume fraction has not been performed in this research.

Conclusions and Recommendations

7.1 Conclusions

The main objective of the research was to develop a methodology to predict the effect of tow drop defects on the elastic properties and buckling load of the variable stiffness panels. Thus, smearing methodology was developed to take account of the tow drop defects on the properties of the panel. Following conclusions were drawn during the course of the methodology development.

- Tow drop defects are the resin rich area in the variable stiffness panels. The geometry of these defects are dependent on parameters such as fibre angular distortion, tow width and number of tows in a course. Based on the parameters, simple micro-mechanical models of tow drop defects were created and analyzed through finite element method with periodic boundary conditions as discussed in Chapter 4. Through this analysis, homogeneous elastic properties of the simple models were calculated. The homogeneous elastic properties were the average equivalent of the properties of the composite and resin. These properties were compared to the elastic properties of the composite with no defects. The difference in the elastic properties obtained between the composite with defects and without defects was termed as the knock-down factors. The effect of fibre angular distortion, tow width and course width on the knock-down factors was studied. It was found that the knock-down factors were dependent upon fibre angular distortion and volume fraction of the tow drop defects. The relation between the knock-down factors with the fibre angular distortion and volume fraction of tow drop defects was non-linear and linear respectively. The knock-down factors were correlated to these parameters. This process was done for the two material sets. The dependence of the knock-down factors on the fibre angular distortion were found to be less dependent on the material. However, the dependence of the knock-down factor on the volume fraction of the tow drop defects was dependent on the resin properties used. The correlation developed were further used to predict the stiffness properties of variable stiffness panel with different configuration. The maximum error observed between the

developed correlation and the finite element result, for different values fibre angular distortion and volume fraction of defects was 10%.

- To generate the reference results which will be compared to the results obtained from smearing methodology, analysis of the variable stiffness panel through a pre-existing finite element method was carried out. Firstly, a complete model of variable stiffness panel was made. For the model, linear fibre angle variation was assumed in the panel. The procedure to generate the tow drop defects geometries in the variable stiffness panels have been discussed in Chapter 5. The analysis of the complete variable stiffness panel with the tow drop defects was carried out by the pre-existing defect layer method. In defect layer method, the finite element mesh are generated on the panel and based on the volume fraction of the tow drop defects in an element, properties are assigned to the element. Thus, this method involves identification of the tow drop location and geometry. From the analysis, effective elastic modulus and buckling load of different configuration were evaluated. The results were then compared to the results reported by *Wu et al* [7]. They studied variable stiffness panel with linear fibre angle variation. The elastic modulus and buckling load from the analysis of the developed model was within 1% accuracy than the results reported by *Wu et al* [7]. Thereafter, the results from the analysis were compared to the results reported by *Fayazbakhsh et al* [6]. There were difference in the results. This was because, *Fayazbakhsh et al* [6] considered variable stiffness panel with different fibre angle distribution in their study. However, the effect of tow drop defects on the panels was found to be proportional to the volume fraction of the resin present in the panel as it was found in their case. It was concluded based on these comparisons that the full panel model with tow drop defects developed in this thesis could be relied upon and can be further used to analyze different configuration of variable stiffness panels.
- Tow drop defects are generated from the fibre tow cutting operation. The general strategy used is to cut the fibres from one of the two intersecting tows. This is called single sided cut strategy. Shortcoming of this strategy is that the intersection line of the two courses is not properly followed and it also result in to copuling of different degrees of freedom. To overcome these limitation, a new strategy was introduced called zipper cut strategy. In this strategy, fibre tows are cut from both courses of the intersecting courses. It makes the fibres follow the intersecting path in much better way and the tow drop defects are alternatively generated. Panels were generated from the same fibre angle variation but with single sided and zipper cut strategy. The analysis of these two panels showed that there are no remarkable difference in the elastic properties and buckling load of the panels.
- Smearing methodology, discussed in Chapter 6, is finite element based method. Mesh elements were generated on the panel and estimation of the variables like fibre angular distortion and volume fraction of the tow drop defects in a mesh element were made through fibre angle gradient present in the variable stiffness panel. Based on these estimates, the knock-down stiffness properties were assigned to the mesh elements through the correlation developed in Chapter 4. Various configurations at lamina and laminate level were analyzed through this approach. Effective elastic modulus and buckling load were calculated. These results were compared to the results obtained by the full panel analysis performed through defect layer method. Through smearing, the step involved

in defect layer method to identify the position and geometry of the tow drop defects in the variable stiffness panel was completely eliminated. Moreover, the element size used to evaluate the properties from smearing was 8 times more than the element size used to calculate the results from defect layer method. However, there was loss in accuracy of the elastic properties and buckling load results. The results were predicted for two material sets and for both material sets subsequent results were found. For most of the lamina and laminate studied in this thesis, the effective elastic modulus was under predicted than actual results obtained from defect layer approach. This means that the effect of defects was over-estimated and the results were on conservative side. The buckling load results were over estimated than results obtained from the defect layer method. Over estimation was of the order of the effect of defect and minimum 50% of the effect of defect was captured through smearing method for all the laminates studied in this thesis. From comparison of the results obtained from two material sets, it was also found that the stiffness properties depend on the resin properties, however, the effect of this resin properties on buckling was less. Also, smearing methodology only requires the fibre angle distribution to predict the effect of defect, thus, this methodology could be applied to any fibre angle distribution to predict the elastic and buckling response of the panel.

7.2 Recommendations

- The first recommendation from this research would be to generalize the knock down factors which were obtained from the micro-mechanical modeling case. These knock-down should be made geometry dependent not material dependent. Thus, more materials should be analyzed and a conservative knock-down factor can be evaluated from the statistical analysis of different material set.
- In this research, the tow drop defects generated due to the linear fibre angle variation were analyzed and compared with the results obtained by smearing. Smearing involves defect estimation through fibre angle gradients, thus, it can be extended to more general form by estimating the effect of defect in any fibre angle distribution. Therefore, smearing methodology should be applied to evaluate properties of panels with constant curvature, geodesic or general fibre angle distribution.
- Thermal effects and geometric non-linearity effects were not taken into consideration to estimate the buckling load. These effects need to be included in the analysis to account for the curing effects.
- Zipper cut strategy introduced have shown no improvement in stiffness properties and buckling load over the single sided cuts strategy, however, this strategy need to be studied for failure analysis. Furthermore, comparison should be made with the single sided cuts strategy.
- Micro-mechanical models are only used to estimate the stiffness properties of the panels with defects. These models can be used to estimate the failure load of the composite panels. The tow drop areas are the stress concentration site in the variable stiffness panels. Through micro-mechanical models stress concentration can be evaluated at

these sites. These stress concentration can be used to predict the failure of the variable stiffness panels.

References

- [1] Z. Gürdal, B. Tatting, and K. Wu. Tow-placement technology and fabrication issues for laminated composite structures. In *46th AIAA/ASME/ASCE/AHS/ASC Structures, Structural Dynamics and Materials Conference*, page 2017, 2005.
- [2] B.C. Kim, K. Hazra, P. Weaver, and K. Potter. Limitations of fibre placement techniques for variable angle tow composites and their process-induced defects. In *Proceedings of the 18th International Conference on Composite Materials, Jeju, KR*, 2011.
- [3] X. Li, S.R. Hallett, and M.R. Wisnom. Modelling the effect of gaps and overlaps in automated fibre placement (afp)-manufactured laminates. *Science and Engineering of Composite Materials*, 22(2):115–129, 2015.
- [4] M.A. Nik, K. Fayazbakhsh, D. Pasini, and L. Lessard. Optimization of variable stiffness composites with embedded defects induced by automated fiber placement. *Composite Structures*, 107:160–166, 2014.
- [5] P. Suquet. Elements of homogenization for inelastic solid mechanics. *Homogenization Techniques for Composite Media*, 272:193–278, 1987.
- [6] K. Fayazbakhsh, M. A. Nik, D. Pasini, and L. Lessard. Defect layer method to capture effect of gaps and overlaps in variable stiffness laminates made by automated fiber placement. *Composite Structures*, 97:245–251, 2013.
- [7] K.C. Wu, Z. Gürdal, and J.H. Starnes. Structural response of compression-loaded, tow-placed, variable stiffness panels. In *Proceedings of the AIAA/ASME/ASCE/AHS/ASC 43rd Structures, Structural Dynamics and Materials Conference, Denver, CO*, pages 2002–1512, 2002.
- [8] B.F. Tatting, Z. Gürdal, and D. Jegley. Design and manufacture of elastically tailored tow placed plates. Technical report, NASA, Langley Research Center, Hampton, VA, NASA/CR-2002-211919, 2002.

- [9] D.H.J.A. Lukaszewicz, C. Ward, and K. D. Potter. The engineering aspects of automated prepreg layup: History, present and future. *Composites Part B: Engineering*, 43(3):997–1009, 2012.
- [10] C.S. Lopes, Z. Gürdal, and P.P. Camanho. Variable-stiffness composite panels: Buckling and first-ply failure improvements over straight-fibre laminates. *Computers & Structures*, 86(9):897–907, 2008.
- [11] C.S. Lopes, Z. Gürdal, and P.P. Camanho. Tailoring for strength of composite steered-fibre panels with cutouts. *Composites Part A: Applied Science and Manufacturing*, 41(12):1760–1767, 2010.
- [12] A. Sawicki and P. Minguett. The effect of intraply overlaps and gaps upon the compression strength of composite laminates. In *39th AIAA/ASME/ASCE/AHS/ASC Structures, Structural Dynamics, and Materials Conference and Exhibit*, page 1786, 1998.
- [13] A.W. Blom, C.S. Lopes, P.J. Kromwijk, Z. Gurdal, and P.P. Camanho. A theoretical model to study the influence of tow-drop areas on the stiffness and strength of variable-stiffness laminates. *Journal of Composite Materials*, 43(5):403–425, 2009.
- [14] F.H. Abdalla, S.A. Mutasher, Y.A. Khalid, S.M. Sapuan, A.M.S. Hamouda, B.B. Sahari, and M.M. Hamdan. Design and fabrication of low cost filament winding machine. *Materials & Design*, 28(1):234–239, 2007.
- [15] R. Measom and K. Sewell. Fiber placement low-cost production for complex composite structures. In *American Helicopter Society 52nd Annual Forum*, pages 4–6. Washington, DC, 1996.
- [16] M.J. Pasanen, J.P. Martin, R.J. Langone, and J.A. Mondo. Advanced composite fiber placement: process to application. In *Proceedings of the Japan International Sampe Symposium*, pages 1055–1060. Japan Chapter of Sampe, 1997.
- [17] S.S. Yau and T.W. Chou. Strength of woven-fabric composites with drilled and molded holes. In *Composite Materials: Testing and Design (Eighth Conference)*, ASTM STP, Philadelphia, PA, volume 972, page 423. ASTM International, 1988.
- [18] M.W. Hyer and H.H. Lee. The use of curvilinear fiber format to improve buckling resistance of composite plates with central circular holes. *Composite Structures*, 18(3):239–261, 1991.
- [19] M.W. Tosh and D.W. Kelly. On the design, manufacture and testing of trajectorial fibre steering for carbon fibre composite laminates. *Composites part A: Applied Science and Manufacturing*, 31(10):1047–1060, 2000.
- [20] Z. Gurdal and R. Olmedo. In-plane response of laminates with spatially varying fiber orientations-variable stiffness concept. *AIAA Journal*, 31(4):751–758, 1993.
- [21] S. Nagendra, S. Kodiyalam, J.E. Davis, and V.N. Parthasarathy. Optimization of tow fiber paths for composite design. In *Proceedings of the AIAA/ASME/ASCE/AHS/ASC 36th Structures, Structural Dynamics and Materials Conference, New Orleans, LA*, pages 1031–41, 1995.

-
- [22] D.M.J. Peeters. *Design optimisation of practical variable stiffness and thickness laminates*. PhD thesis, Delft University of Technology, 2017.
- [23] K. Croft, L. Lessard, D. Pasini, M. Hojjati, J. Chen, and A. Yousefpour. Experimental study of the effect of automated fiber placement induced defects on performance of composite laminates. *Composites Part A: Applied Science and Manufacturing*, 42(5):484–491, 2011.
- [24] M. Lan, D. Cartié, P. Davies, and C. Baley. Microstructure and tensile properties of carbon-epoxy laminates produced by automated fibre placement: Influence of a caul plate on the effects of gap and overlap embedded defects. *Composites Part A: Applied Science and Manufacturing*, 78:124–134, 2015.
- [25] D.C. Jegley, B.F. Tatting, and Z. Gürdal. Optimization of elastically tailored tow-placed plates with holes. In *Proceedings of the AIAA/ASME/ASCE/AHS/ASC 44th structures, Structural Dynamics and Materials Conference, Norfolk, Va*, pages 2003–1420, 2003.
- [26] D.C. Jegley, B.F. Tatting, and Z. Gürdal. Tow-steered panels with holes subjected to compression or shear loading. In *Proceedings of the 46th AIAA/ASME/ASCE/AHS/ASC Structures, Structural Dynamics and Materials Conference, Austin, TX*, pages 18–21, 2005.
- [27] C.S. Lopes, P.P. Camanho, Z. Gürdal, and B.F. Tatting. Progressive failure analysis of tow-placed, variable-stiffness composite panels. *International Journal of Solids and Structures*, 44(25):8493–8516, 2007.
- [28] Z. Wu, P.M. Weaver, G. Raju, and B.C. Kim. Buckling analysis and optimisation of variable angle tow composite plates. *Thin-Walled Structures*, 60:163–172, 2012.
- [29] G. Raju, Z. Wu, B.C. Kim, and P.M. Weaver. Prebuckling and buckling analysis of variable angle tow plates with general boundary conditions. *Composite Structures*, 94(9):2961–2970, 2012.
- [30] B.H. Coburn and P.M. Weaver. Buckling analysis, design and optimisation of variable-stiffness sandwich panels. *International Journal of Solids and Structures*, 96:217–228, 2016.
- [31] O. Falcó, J.A. Mayugo, C.S. Lopes, N. Gascons, and J. Costa. Variable-stiffness composite panels: Defect tolerance under in-plane tensile loading. *Composites Part A: Applied Science and Manufacturing*, 63:21–31, 2014.
- [32] R. Hill. *Elastic properties of reinforced solids: some theoretical principles*, volume 11. Elsevier, 1963.
- [33] S. Hazanov and C. Huet. Order relationships for boundary conditions effect in heterogeneous bodies smaller than the representative volume. *Journal of the Mechanics and Physics of Solids*, 42(12):1995–2011, 1994.
- [34] K. Terada, M. Hori, T. Kyoya, and N. Kikuchi. Simulation of the multi-scale convergence in computational homogenization approaches. *International Journal of Solids and Structures*, 37(16):2285–2311, 2000.

-
- [35] O. Van der Sluis, P.J.G. Schreurs, W.A.M. Brekelmans, and H.E.H. Meijer. Overall behaviour of heterogeneous elastoviscoplastic materials: effect of microstructural modelling. *Mechanics of Materials*, 32(8):449–462, 2000.
- [36] M. Abdalla, Z. Gurdal, and C. Kassapoglu. Formulation of composite laminate robustness constraint in lamination parameters space. In *50th AIAA/ASME/ASCE/AHS/ASC Structures, Structural Dynamics, and Materials Conference, Palm Springs, California*, page 2478, 2009.
- [37] S.J. Hollister and N. Kikuchi. A comparison of homogenization and standard mechanics analyses for periodic porous composites. *Computational Mechanics*, 10(2):73–95, 1992.
- [38] A.A. Gusev. Representative volume element size for elastic composites: a numerical study. *Journal of the Mechanics and Physics of Solids*, 45(9):1449–1459, 1997.
- [39] X.F. Wang, X.W. Wang, G.M. Zhou, and C.W. Zhou. Multi-scale analyses of 3d woven composite based on periodicity boundary conditions. *Journal of Composite Materials*, 41(14):1773–1788, 2007.
- [40] W. Wu, J. Owino, A. Al-Ostaz, and L. Cai. Applying periodic boundary conditions in finite element analysis. In *Simulia Community Conference, Providence, RI*, pages 707–719, 2014.
- [41] V.D. Nguyen, E. Béchet, C. Geuzaine, and L. Noels. Imposing periodic boundary condition on arbitrary meshes by polynomial interpolation. *Computational Materials Science*, 55:390–406, 2012.
- [42] J. R. Shewchuk. Triangle: Engineering a 2D Quality Mesh Generator and Delaunay Triangulator. In Ming C. Lin and Dinesh Manocha, editors, *Applied Computational Geometry: Towards Geometric Engineering*, volume 1148 of *Lecture Notes in Computer Science*, pages 203–222. Springer-Verlag, May 1996. From the First ACM Workshop on Applied Computational Geometry.
- [43] T.H.G. Megson. *Aircraft structures for engineering students*, volume 4 of *Elsevier Aerospace Engineering Series*. Elsevier Science, 2007.

Appendix A

Appendix A

This appendix is on all the references given in Chapter 4.

A.1 *.poly* file in *Triangle*

Triangle is a free software which can be used to mesh different geometries according to the user requirement. It requires a *.poly* file as an input for which it returns mesh data as an output. The *.poly* file is the combination of two separate data, one is the node data and other is the edge. The node data contains data like coordinates in it and edge data contains connectivity between the different nodes to generate the edges of the geometry. The node generation can be on any part of the geometry and these nodes are not been altered by *Triangle*. However, few of these nodes makes the edges. The procedure to give node data and edge data in a poly file is given below.

Node data input

For the node data input following format has to be followed.

First Line: Number of Nodes <space> Dimensions <space> Attributes <space> Boundary Marker

Remaining Lines: Node number <space> x-coordinate <space> y-coordinate <space> [Attributes] <space> [Boundary Marker]

For the very first line, number of nodes generated by the user is given. Dimensions, indicate the 2D or 3D mesh. '2' must be entered for the 2D meshes. Attributes are the quantities which can be assigned to the nodes. Default value '1' is given. And Boundary marker is used to indicate whether the nodes are on the boundary or not. If the boundary marker in the first line is provided '1', then, for every node it is mandatory to specify the boundary markers. '1' and '0' must be provided for nodes on and not on the boundary. Attributes and boundary marker are the optional input. For the remaining lines, the node numbers are provided. Then, the *x* and *y* coordinate of the nodes are provided. The sample node data given is shown in Figure [A.1a](#).

1	199	2	1	0	201	84	0	
2	1	0.00000000	0.00000000		202	1	20	168
3	2	-6.32583633	0.55343897		203	2	168	169
4	3	-3.18712798	36.42903956		204	3	169	170
5	4	3.13870835	36.98247852		205	4	170	9
6	5	0.00000000	72.85807911		206	5	9	155
7	6	6.32583633	73.41151808		207	6	155	156
8	7	3.18712798	109.28711867		208	7	156	157
9	8	-3.13870835	109.84055763		209	8	157	158
10	9	0.00000000	145.71615822		210	9	158	159
11	10	100.00000000	145.71615822		211	10	159	160
12	11	93.67416367	145.16271925		212	11	160	161
13	12	96.81287202	109.28711867		213	12	161	10
14	13	103.13870835	108.73367970		214	13	10	171
15	14	100.00000000	72.85807911		215	14	171	172
16	15	106.32583633	72.30464014		216	15	172	173
17	16	103.18712798	36.42903956		217	16	173	21
18	17	96.86129165	35.87560059		218	17	19	164
19	18	100.00000000	0.00000000		219	18	164	163
20	19	-50.00000000	0.00000000		220	19	163	162
21	20	-50.00000000	145.71615822		221	20	162	1

(a) Node data input

(b) Edge data input

Figure A.1: Components of *.poly* file

Edge data input

For the edge data input following format has to be followed.

First Line: Number of edges <space> Boundary marker

Remaining Lines: Edge Number <space> Node number 1 <space> Node Number 2 <space> [Boundary marker]

Similar to the node data input, for the edge data in the first line number of edges has to be provided. After that boundary marker has to be specified. For the remaining lines, firstly, the edge number has to be provided and then the connectivity has to be given. Node number of the two nodes has to be given which forms the particular edge. The sample edge data given is shown in Figure A.1b. The first line of the edge data should be right after the node data input.

At the last part of the *.poly* file it has to be specified if there are some discontinuity in the geometry. In this case since there are no discontinuity, thus, '0' has to be entered in the last line.

A.2 Python file for data extraction

This file was used to extract the nodal force, nodal displacement and external work done.

```

1 import odbAccess
2 from odbAccess import *
3 from abaqusConstants import *
4 from numpy import array

```

```

5
6 # Reading of the output file
7 odb = openOdb(path='checkrun.odb')
8
9 # Extraction of the Node attributes
10 allnode = []
11 edgenode = []
12 rightedgenode = []
13 leftedgenode = []
14 bottomedgenode = []
15 topedgenode = []
16
17 allnodeset = odb.rootAssembly.instances['PART-1'].nodes
18 edgenodeset = odb.rootAssembly.instances['PART-1'].nodeSets['EDGENODE'].
    nodes
19 bottomedgenodeset = odb.rootAssembly.instances['PART-1'].nodeSets['
    BOTTOMEDGENODE'].nodes
20 topedgenodeset = odb.rootAssembly.instances['PART-1'].nodeSets['
    TOPEDGENODE'].nodes
21 leftedgenodeset = odb.rootAssembly.instances['PART-1'].nodeSets['
    LEFTEDGENODE'].nodes
22 rightedgenodeset = odb.rootAssembly.instances['PART-1'].nodeSets['
    RIGHTEDGENODE'].nodes
23
24 # Extration of the node label
25 for n in allnodeset:
26     allnode.append(n.label)
27 for n in edgenodeset:
28     edgenode.append(n.label)
29 for n in topedgenodeset:
30     topedgenode.append(n.label)
31 for n in bottomedgenodeset:
32     bottomedgenode.append(n.label)
33 for n in leftedgenodeset:
34     leftedgenode.append(n.label)
35 for n in rightedgenodeset:
36     rightedgenode.append(n.label)
37
38 # Nodal force extraction and output file generation
39
40 outputfile = open('results.txt','w')
41 lastframe = odb.steps['test'].frames[-1]
42 Node = odb.rootAssembly.instances['PART-1'].nodeSets['EDGENODE']
43 NF1Node = lastframe.fieldOutputs['NFORC1'].getSubset(region=Node)
44 NF1ValueNode=NF1Node.values
45 NF2Node = lastframe.fieldOutputs['NFORC2'].getSubset(region=Node)
46 NF2ValueNode=NF2Node.values
47 NF3Node = lastframe.fieldOutputs['NFORC3'].getSubset(region=Node)
48 NF3ValueNode=NF3Node.values
49 NF4Node = lastframe.fieldOutputs['NFORC4'].getSubset(region=Node)
50 NF4ValueNode=NF4Node.values
51 NF5Node = lastframe.fieldOutputs['NFORC5'].getSubset(region=Node)
52 NF5ValueNode=NF5Node.values

```

```
53 NF6Node = lastframe.fieldOutputs['NFORC6'].getSubset(region=Node)
54 NF6ValueNode=NF6Node.values
55
56 disp = lastframe.fieldOutputs['U'].getSubset(region=Node)
57 dispvalue = disp.values
58
59 disprot = lastframe.fieldOutputs['UR'].getSubset(region=Node)
60 disprotvalue = disprot.values
61
62
63 # Energy calculation
64 energy1 = 0
65 energy2 = 0
66 energy3 = 0
67 energy4 = 0
68 energy5 = 0
69 energy6 = 0
70
71 #print edgenode
72
73 for n in edgenode:
74     NF1 = 0
75     for v1 in NF1ValueNode:
76         if v1.nodeLabel == n:
77             NF1 = NF1 + v1.data
78
79     #print (n , NF1)
80     NF2 = 0
81     for v2 in NF2ValueNode:
82         if v2.nodeLabel == n:
83             NF2 = NF2 + v2.data
84
85
86     NF3 = 0
87     for v3 in NF3ValueNode:
88         if v3.nodeLabel == n:
89             NF3 = NF3 + v3.data
90
91     NF4 = 0
92     for v4 in NF4ValueNode:
93         if v4.nodeLabel == n:
94             NF4 = NF4 + v4.data
95
96     NF5 = 0
97     for v5 in NF5ValueNode:
98         if v5.nodeLabel == n:
99             NF5 = NF5 + v5.data
100
101     NF6 = 0
102     for v6 in NF6ValueNode:
103         if v6.nodeLabel == n:
104             NF6 = NF6 + v6.data
105
```

```

106     #print n,NF1,NF2,NF3,NF4,NF5,NF6
107     for u in dispvalue:
108         if u.nodeLabel == n:
109             #print u.nodeLabel,u.data[0],u.data[1]
110             energy1 = energy1 + (NF1 * u.data[0])
111             energy2 = energy2 + (NF2 * u.data[1])
112             energy3 = energy3 + (NF3 * u.data[2])
113     for ur in disprotvalue:
114         if ur.nodeLabel == n:
115             #print u.nodeLabel,u.data[1],u.data[2]
116             energy4 = energy4 + (NF4 * ur.data[0])
117             energy5 = energy5 + (NF5 * ur.data[1])
118             energy6 = energy6 + (NF6 * ur.data[2])
119     outputfile.write('{:5}{:20}{:20}{:20}{:20}{:20}{:20}'.format(n,NF1,
120         NF2,NF3,NF4,NF5,NF6))
121     outputfile.write('\n')
122 # Printing of the output
123 outputfile.write('\n')
124 outputfile.write('\n')
125 outputfile.write('Energy\n')
126 outputfile.write('%f'%(energy1+energy2+energy3+energy4+energy5+energy6))
127 outputfile.write('\n')
128 outputfile.write('Stiffness\n')
129 outputfile.write('%f'%((energy1+energy2+energy3+energy4+energy5+energy6)
130     /(length*height)))
130 print ('yes')
```

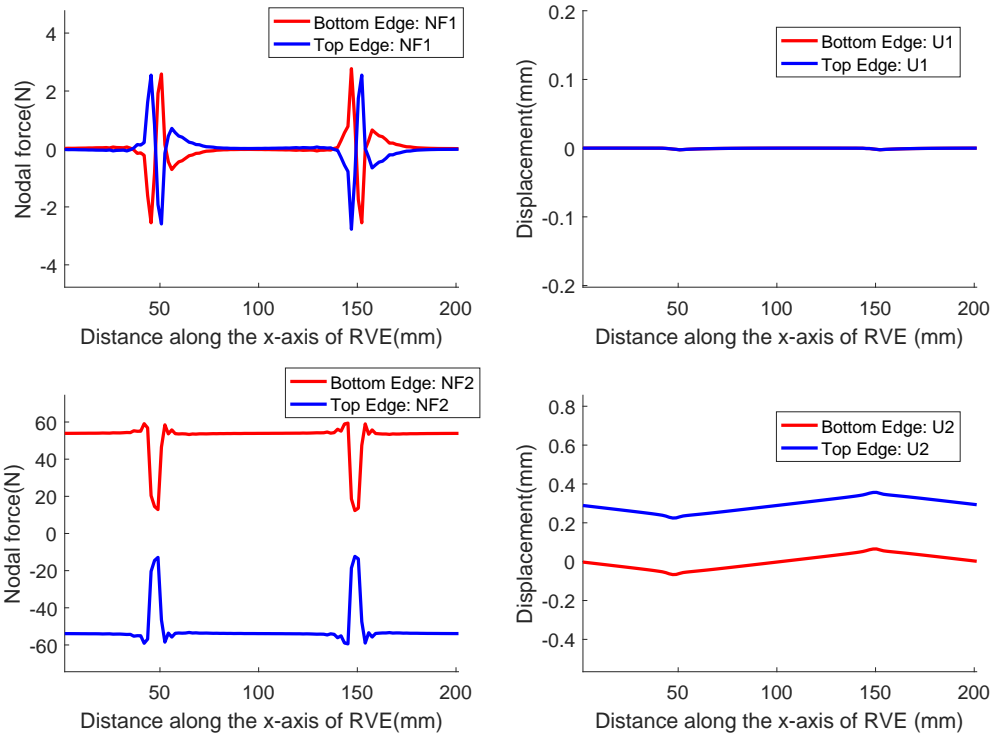
A.3 Nodal forces and displacement plots

In this section, nodal forces and displacements at the edges of the RVE, shown in Figure 4.16, under different load cases are shown in Figure A.2-A.6. In all the figures, the nodal forces at the opposite edges are equal and opposite.

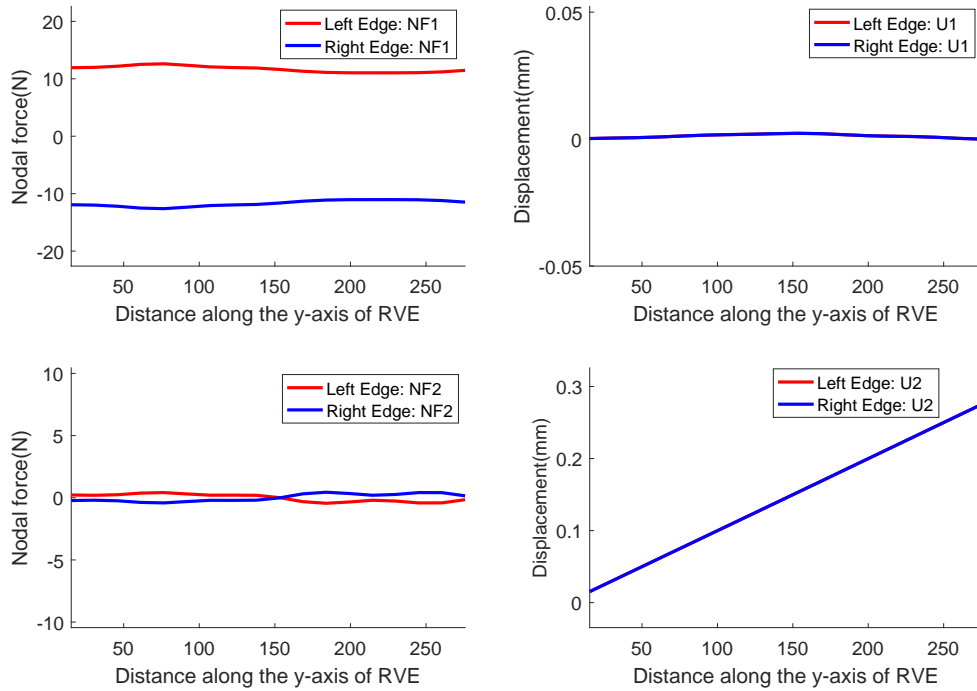
Loadcase 2: $\epsilon_1=0$, $\epsilon_2 = 0.001$ and $\epsilon_6=0$, applying these conditions to periodic boundary condition in Eq. (4.8)-(4.11) suggests that U2 displacement of top and bottom edge should have constant difference and other displacement at opposite edges should be same. This can be seen in Figure A.2a and Figure A.2b.

Loadcase 3: $\epsilon_1=0$, $\epsilon_2 = 0$ and $\epsilon_6=0.001$, applying these conditions to periodic boundary condition in Eq. (4.8)-(4.8), suggests that U1 displacement of top and bottom edge, and U2 displacement of left and right edges should have constant difference and other displacement at opposite edges should be same. This can be seen in Figure A.3a and Figure A.3b.

Loadcase 4, 5 and 6 are the linear combination of the Loadcase 1 and 2, Loadcase 1 and 3 and Loadcase 2 and 3 respectively. The displacement plots of these load cases are also the superposition of the respective loadcases. This can be observed in the displacement plots presented in Figure A.4-A.6. Since, the displacement and nodal forces follow the conditions of periodicity, thus, it can be inferred that the application of periodic boundary condition to the RVE was correct.

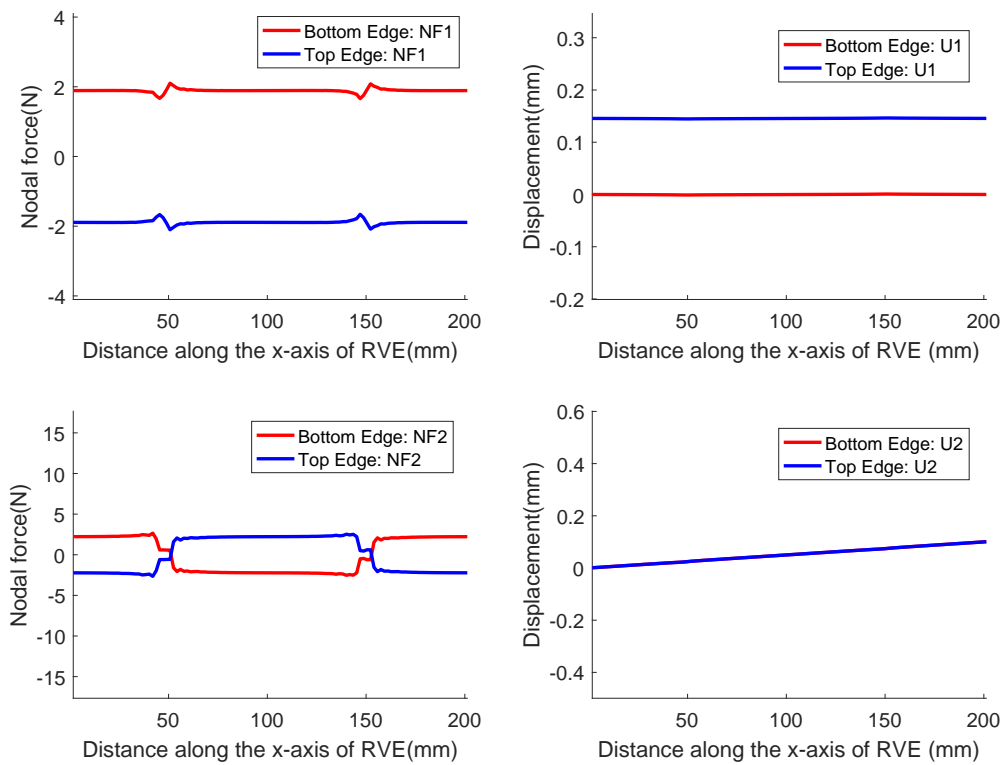


(a) Loadcase 2: Variation of nodal forces and displacements at bottom and top edge of the RVE along the x-axis

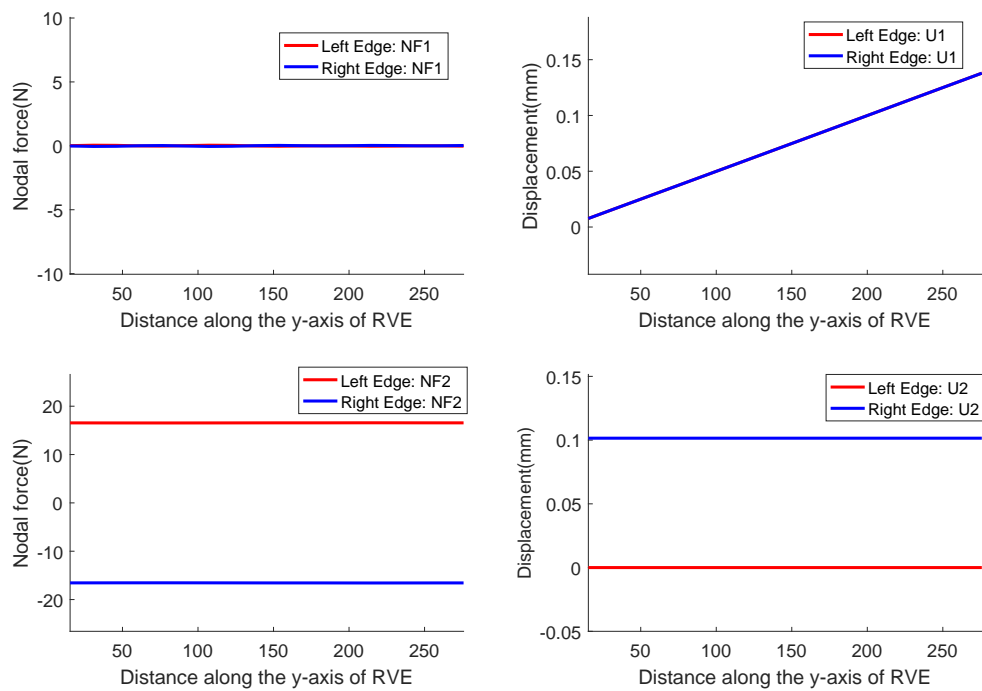


(b) Loadcase 2: Variation of nodal forces and displacements at bottom and top edge of the RVE along the y-axis

Figure A.2: Loadcase 2

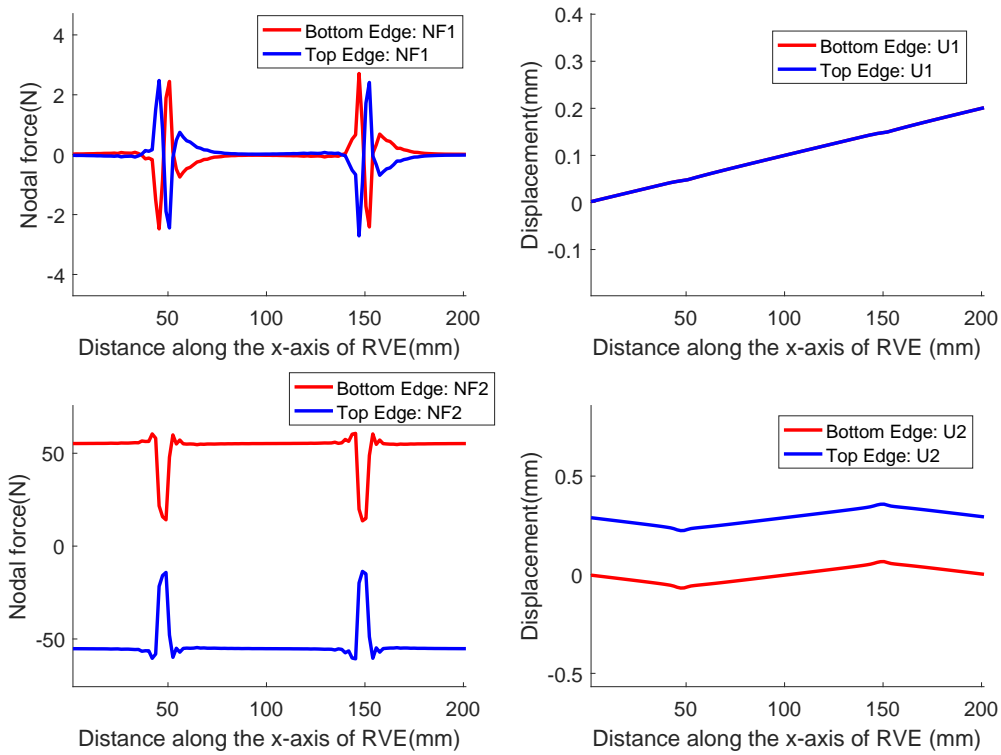


(a) Loadcase 3: Variation of nodal forces and displacements at bottom and top edge of the RVE along the x-axis

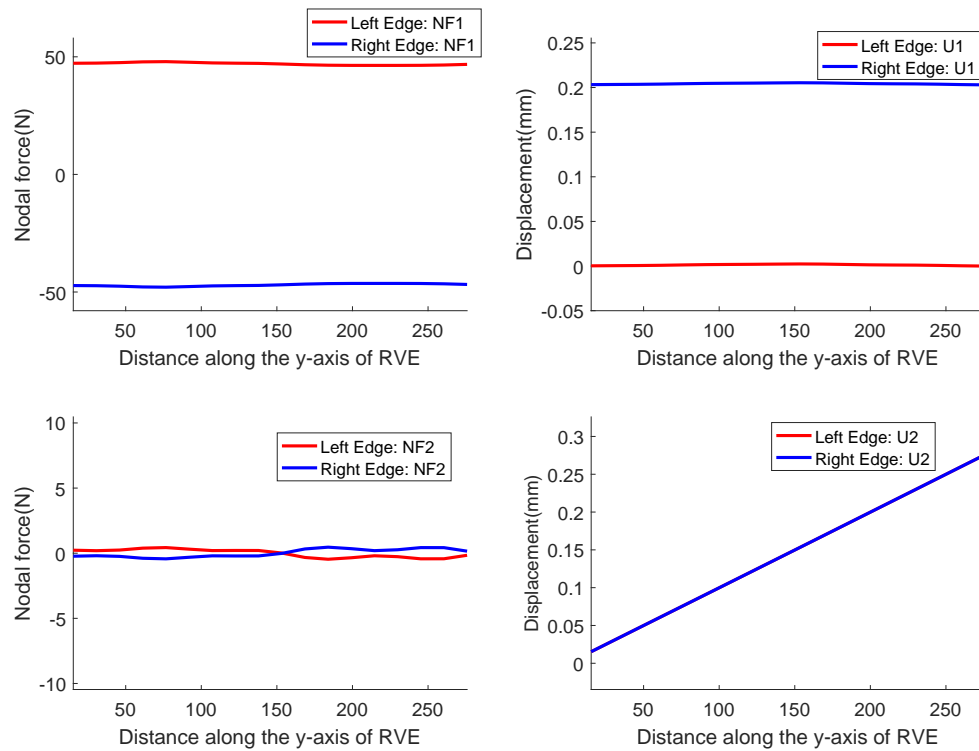


(b) Loadcase 3: Variation of nodal forces and displacements at bottom and top edge of the RVE along the y-axis

Figure A.3: Loadcase 3

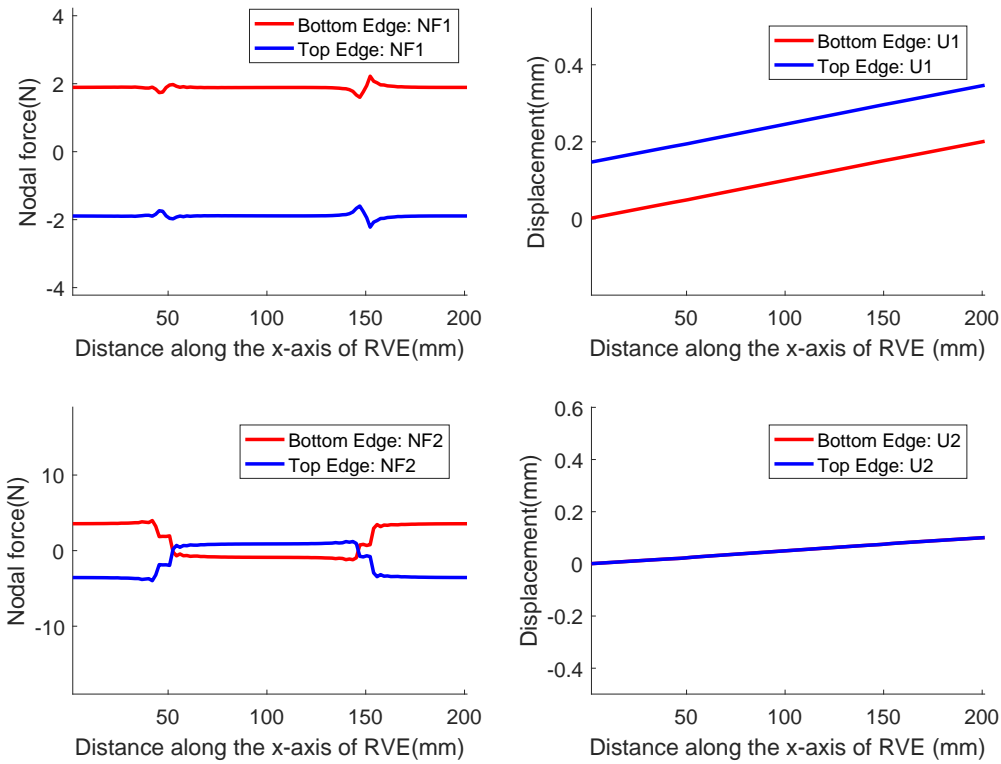


(a) Loadcase 4: Variation of nodal forces and displacements at bottom and top edge of the RVE along the x-axis

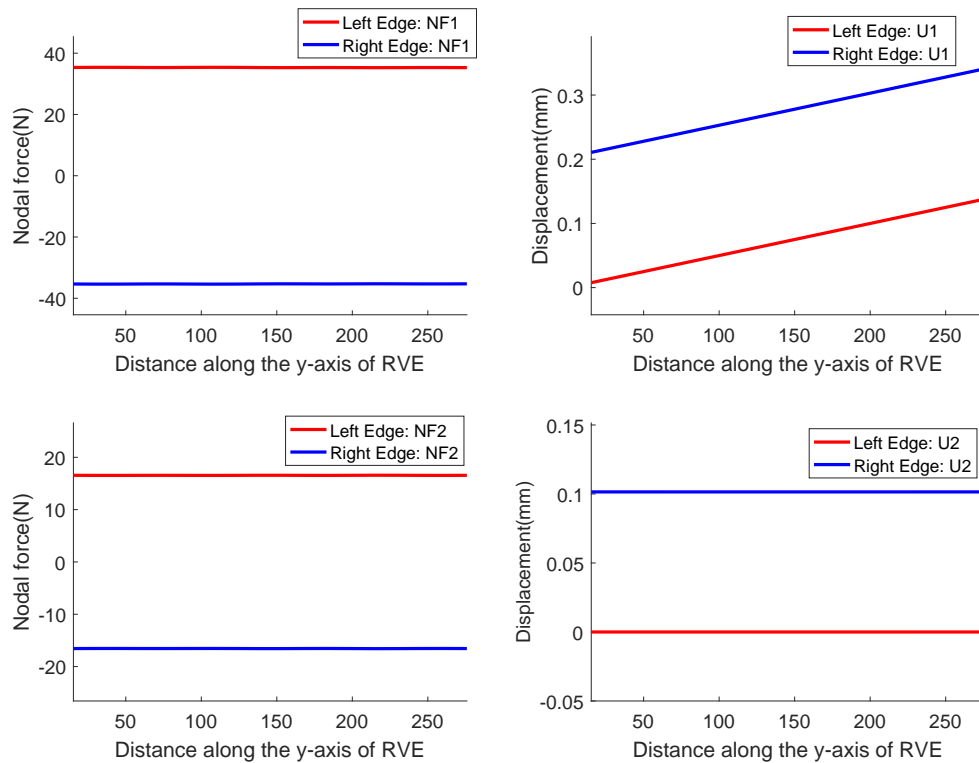


(b) Loadcase 4: Variation of nodal forces and displacements at bottom and top edge of the RVE along the y-axis

Figure A.4: Loadcase 4

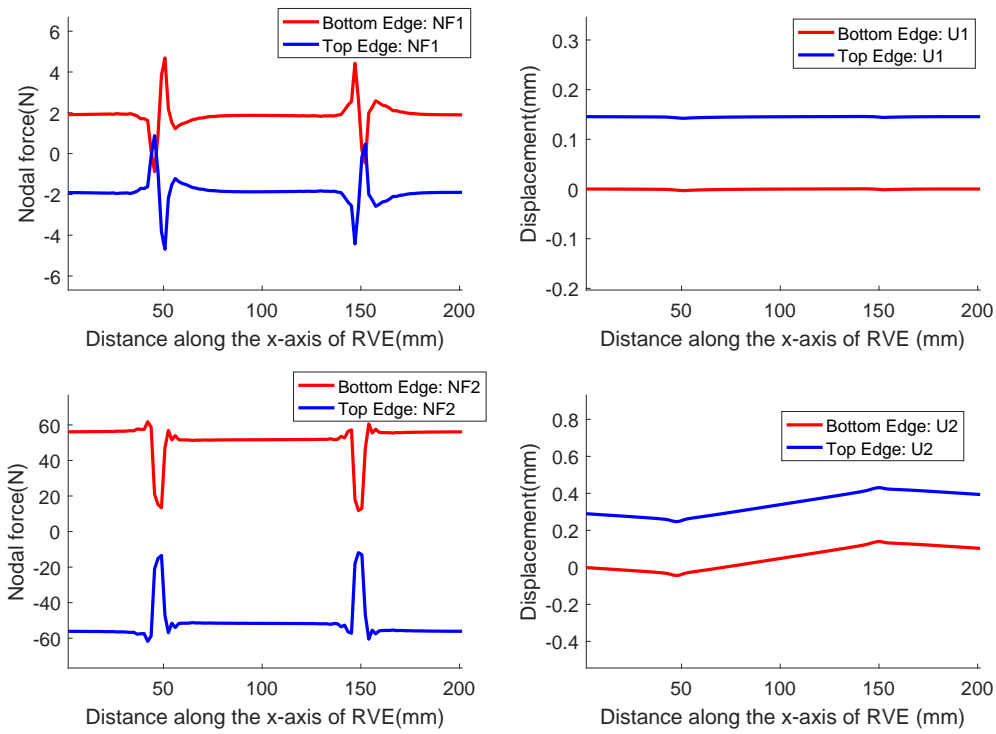


(a) Loadcase 5: Variation of nodal forces and displacements at bottom and top edge of the RVE along the x-axis

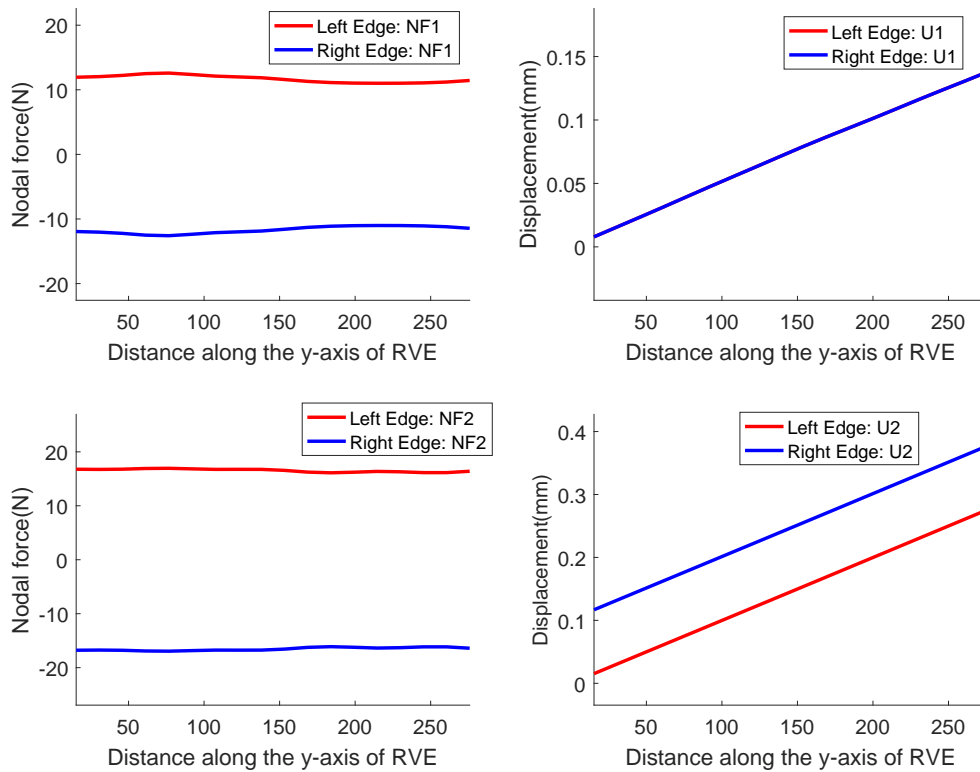


(b) Loadcase 5: Variation of nodal forces and displacements at bottom and top edge of the RVE along the y-axis

Figure A.5: Loadcase 5



(a) Loadcase 6: Variation of nodal forces and displacements at bottom and top edge of the RVE along the x-axis



(b) Loadcase 6: Variation of nodal forces and displacements at bottom and top edge of the RVE along the y-axis

Figure A.6: Loadcase 6

A.4 Interpolation function for single sided cuts

The *Matlab* function developed to get the interpolated result for the RVEs of single sided cuts are shown in this section

A.4.1 Interpolation function for Material 1

```

1  % Interpolation function for the single sided cuts for Material 1
2  %
3  % Input fibre distortion angle and volume fraction for calculation at
4  % specific point
5
6  function Q = homostiffss(angle,geovf)
7
8  % Sample fibre distortion angles
9  sample_angle = [1; 1; 1; 1; 1;...
10 3; 3; 3; 3; 3;...
11 5; 5; 5; 5; 5;...
12 7; 7; 7; 7; 7;...
13 9 ;9; 9; 9 ;9;...
14 12 ;12; 12; 12; 12;
15 15; 15; 15 ;15; 15;...
16 0];
17
18 % Sample volume fraction
19 sample_vf = [0; 0.015872582 ;0.021163443; 0.031745164; 0.063490329;...
20 0; 0.015853244; 0.021137658; 0.031706488; 0.063412975;...
21 0; 0.015814591; 0.021086121; 0.031629182; 0.063258363;...
22 0; 0.01575667; 0.021008894; 0.03151334; 0.063026681;...
23 0; 0.015679552; 0.02090607; 0.031359105; 0.06271821;...
24 0; 0.015528093; 0.020704124; 0.031056186; 0.062112373;...
25 0; 0.015334072; 0.02044543; 0.030668145; 0.06133629;...
26 0];
27
28 % Q11 component at sample point
29 Q11 = [11483.51328; 11501.26247; 11507.19013; 11519.06219;
11554.81794;...
30 11485.69454; 11503.42612; 11509.35118; 11521.2184; 11556.95014;...
31 11490.63137; 11508.26971; 11514.16885; 11525.98549; 11561.57162;...
32 11498.68898; 11516.16446; 11522.01648; 11533.73903; 11569.05004;...
33 11509.46653; 11526.74868; 11532.54556; 11544.15803; 11579.14338;...
34 11534.22682; 11551.08039; 11556.75345; 11568.11774; 11602.35921;...
35 11571.04929; 11587.34748; 11592.85964; 11603.90224; 11637.17572;...
36 11483];
37
38 % Q11 evaluated at specific point
39 Q11f = scatteredInterpolant(sample_angle ,sample_vf ,Q11 ,'natural');
40 Q11p = Q11f(angle ,geovf);
41
42 % Q22 component at sample point

```

```

43 Q22 = [161834.6229; 159272.5255; 158419.5783; 156713.8586;
        151604.3111;...
44 159207.4305; 156521.2464; 155635.8498; 153867.4178; 148580.4282;...
45 154453.7406; 151774.3156; 150905.7393; 149174.8376; 144030.4548;...
46 148348.8536; 145768.4383; 144948.4254; 143318.5987; 138508.2859;...
47 141662.5844; 139255.3266; 138505.85; 137019.9673; 132663.5433;...
48 131765.8041; 129698.711; 129073.523; 127837.6853; 124241.934;...
49 122886.8318; 121182.6458; 120680.4315; 119689.398; 116818.8446;...
50 162176];
51
52 % Q22 evaluated at specific point
53 Q22f = scatteredInterpolant(sample_angle, sample_vf, Q22, 'natural');
54 Q22p = Q22f(angle, geovf);
55
56 % Q66 component at sample point
57 Q66 = [5180.848602; 5165.115637; 5159.895409; 5149.490154;
        5118.538627;...
58 5267.551417; 5250.189332; 5244.438509; 5232.985502; 5199.020363;...
59 5432.078715; 5411.382754; 5404.572789; 5391.030098; 5351.032251;...
60 5661.662614; 5636.393322; 5628.17482; 5611.865338; 5563.945036;...
61 5943.103848; 5912.702582; 5902.958136; 5883.66138; 5827.269589;...
62 6440.526714; 6402.805751; 6390.991565; 6367.656284; 6299.900508;...
63 7011.464999; 6968.088115; 6954.794746; 6928.577193; 6852.736762;...
64 5170;...
65 ];
66
67
68 % Q66 evaluated at specific point
69 Q66f = scatteredInterpolant(sample_angle, sample_vf, Q66, 'natural');
70 Q66p = Q66f(angle, geovf);
71
72
73 % Q12 component at sample point
74 Q12 = [3680.434158; 3685.691002; 3687.454994; 3690.975735;
        3701.543831;...
75 3725.225955; 3729.687414; 3731.337173; 3734.64838; 3744.594527;...
76 3815.110733; 3818.295035; 3819.782971; 3822.811292; 3832.219526;...
77 3950.23347; 3951.847535; 3953.143691; 3955.834831; 3964.607858;...
78 4130.339294; 4130.338022; 4131.456615; 4133.83214; 4142.00559;...
79 4484.01594; 4481.829202; 4482.739583; 4484.744059; 4492.175075;...
80 4934.111216; 4930.238556; 4931.038902; 4932.851806; 4939.885406;...
81 3675];
82
83 % Q12 evaluated at specific point
84 Q12f = scatteredInterpolant(sample_angle, sample_vf, Q12, 'natural');
85 Q12p = Q12f(angle, geovf);
86
87 % Q16 component at sample points
88 Q16 = [0.019165341; 0.369729475; 0.486170601; 0.718804329;
        1.413917303;...
89 1.363916628; 2.425845361; 2.775024492; 3.471909917; 5.553298989;...
90 5.840878281; 7.66665677; 8.256308185; 9.431618728; 12.92960623;...
91 16.05916112; 18.69060132; 19.52108214; 21.17485472; 26.07809571;...

```

```

92 34.02497897; 37.50020205; 38.57100971; 40.70122318; 46.99507783;...
93 80.04524304; 84.81998403; 86.24300264; 89.06806841; 97.38507351;...
94 154.53111107; 160.611053; 162.3705047; 165.8616223; 176.1198217;...
95 0;...
96 ];
97
98 % Q16 evaluated at specific point
99 Q16f = scatteredInterpolant(sample_angle, sample_vf, Q16, 'natural');
100 Q16p = Q16f(angle, geovf);
101
102 % Q26 component at sample points
103 Q26 = [2.528582824; 25.4049434; 32.95846891; 47.97236837;
104         92.13609651;...
105 71.93019941; 144.7968669; 168.6457442; 216.0050293; 355.4160804;...
106 310.954982; 432.2513699; 471.3490248; 548.8476531; 775.8904272;...
107 774.4113333; 937.3327493; 988.8869447; 1090.85887; 1387.881462;...
108 1463.75547; 1658.049425; 1718.359424; 1837.399774; 2182.256727;...
109 2843.304208; 3063.563491; 3130.082399; 3261.066057; 3638.207077;...
110 4491.775356; 4716.538155; 4782.744922; 4912.951356; 5286.637936;...
111 0;...
112 ];
113 % Q26 evaluated at specific point
114 Q26f = scatteredInterpolant(sample_angle, sample_vf, Q26, 'natural');
115 Q26p = Q26f(angle, geovf);
116
117 % Q matrix formation at specific point
118 Qp = [Q11p, Q12p, Q16p; Q12p, Q22p, Q26p; Q16p, Q26p, Q66p];
119
120 cn = cosd(-angle/2);
121 sn = sind(-angle/2);
122
123 Mn = [cn*cn, sn*sn, 2*cn*sn; sn*sn, cn*cn, -2*cn*sn; -cn*sn, cn*sn, (cn*cn)-(sn*
124         sn)];
125 % Rotation of the matrix
126 Q = Mn*Qp*Mn';
127 end

```

A.4.2 Interpolation function for Material 2

```

1 % Interpolation function for the single sided cuts for Material 2
2 %
3 % Input fibre distortion angle and volume fraction for calculation at
4 % specific point
5 function Q = homostiffssdl(angle, geovf)
6
7 % Sample fibre distortion angles
8 sample_angle = [1; 1; 1; 1; 1;...
9 3; 3; 3; 3; 3;...
10 5; 5; 5; 5; 5;...
11 7; 7; 7; 7; 7;...
12 9; 9; 9; 9; 9;...

```

```

13 11; 11; 11; 11; 11;...
14 13; 13; 13; 13; 13;...
15 15; 15; 15; 15; 15;...
16 0];
17
18 % Sample volume fraction
19 sample_vf = [0.0625; 0.03125; 0.020833333; 0.015625; 0;...
20 0.0625; 0.03125; 0.020833333; 0.015625; 0;...
21 0.0625; 0.03125; 0.020833333; 0.015625; 0;...
22 0.0625; 0.03125; 0.020833333; 0.015625; 0;...
23 0.0625; 0.03125; 0.020833333; 0.015625; 0;...
24 0.0625; 0.03125; 0.020833333; 0.015625; 0;...
25 0.0625; 0.03125; 0.020833333; 0.015625; 0;...
26 0.0625; 0.03125; 0.020833333; 0.015625; 0;...
27 0];
28
29 % Q11 component at sample point
30 Q11 = [8597.959756; 8867.396764; 8960.629269; 9007.875949;
31 9152.357694;...
32 8610.455717; 8875.631244; 8967.022123; 9013.349563; 9155.259855;...
33 8624.08254; 8885.149931; 8975.30029; 9021.015829; 9160.456816;...
34 8638.784883; 8896.758649; 8985.930325; 9031.126772; 9169.412456;...
35 8656.017471; 8911.601252; 8999.931645; 9044.692614; 9181.795692;...
36 8676.492211; 8930.083152; 9017.690154; 9062.088932; 9197.933801;...
37 8700.499655; 8952.501594; 9039.543225; 9083.66561; 9219.278414;...
38 8730.381145; 8981.420459; 9068.137635; 9112.105598; 9246.674447;...
39 9152];
40
41 % Q11 evaluated at specific point
42 Q11f = scatteredInterpolant(sample_angle, sample_vf, Q11, 'natural');
43 Q11p = Q11f(angle, geovf);
44
45 % Q22 component at sample point
46 Q22 = [134070.4985; 138796.2656; 140374.1044; 141163.1763;
47 143533.3158;...
48 131286.9922; 136261.657; 137927.6172; 138762.1752; 141292.863;...
49 127170.1755; 132121.5292; 133792.8671; 134632.7707; 137220.5349;...
50 122205.7201; 126957.7349; 128576.8424; 129393.534; 131956.4064;...
51 116974.4991; 121398.6159; 122919.2985; 123689.0249; 126147.7302;...
52 111879.143; 115902.7489; 117295.5884; 118002.6; 120298.2861;...
53 107141.9769; 110740.6759; 111992.9457; 112629.9006; 114726.348;...
54 102838.8317; 106025.5222; 107138.137; 107704.7967; 109592.2262;...
55 143824];
56
57 % Q22 evaluated at specific point
58 Q22f = scatteredInterpolant(sample_angle, sample_vf, Q22, 'natural');
59 Q22p = Q22f(angle, geovf);
60
61 % Q66 component at sample point
62 Q66 = [4332.728148; 4558.066271; 4638.582862; 4680.044341;
63 4809.626377;...
64 4428.514232; 4644.248019; 4721.723501; 4761.540796; 4885.29434;...

```

```

63 4571.760666; 4788.598695; 4866.240547; 4906.087915; 5030.003278;...
64 4765.132842; 4985.942204; 5064.940373; 5105.508064; 5232.06275;...
65 5003.14956; 5228.31667; 5308.948364; 5350.393039; 5480.149328;...
66 5279.829272; 5508.216074; 5590.084858; 5632.192935; 5764.658956;...
67 5590.398621; 5820.354641; 5902.822793; 5945.250378; 6079.256236;...
68 5931.999018; 6161.667128; 6243.992098; 6286.339362; 6420.642265;...
69 4800];
70
71 % Q66 evaluated at specific point
72 Q66f = scatteredInterpolant(sample_angle ,sample_vf ,Q66 , 'natural' );
73 Q66p = Q66f(angle ,geovf );
74
75 % Q12 component at sample point
76 Q12 = [2627.323151; 2685.941845; 2706.357254; 2716.774281;
        2749.18257;...
77 2664.780296; 2716.92925; 2735.495176; 2744.968315; 2775.008933;...
78 2726.996232; 2775.762914; 2792.895355; 2801.580523; 2829.63544;...
79 2822.289965; 2867.432222; 2882.969109; 2890.810467; 2916.955492;...
80 2954.970241; 2995.952241; 3009.782223; 3016.727507; 3041.394399;...
81 3127.507645; 3164.266198; 3176.435638; 3182.498229; 3204.762361;...
82 3339.730544; 3372.508215; 3383.143941; 3388.395312; 3409.332682;...
83 3592.332501; 3621.733716; 3631.076581; 3635.643322; 3654.936805;...
84 2746];
85
86 % Q12 evaluated at specific point
87 Q12f = scatteredInterpolant(sample_angle ,sample_vf ,Q12 , 'natural' );
88 Q12p = Q12f(angle ,geovf );
89
90 % Q16 component at sample points
91 Q16 = [0.732373989; 0.453497314; 0.374392736; 0.334351138;
        0.263361996;...
92 1.515117542; 1.383281872; 1.340523807; 1.321932139; 1.648007896;...
93 6.219702406; 6.478167104; 6.605129435; 6.678154236; 6.889813587;...
94 16.92330828; 17.6363264; 17.95861418; 18.13488311; 18.44524209;...
95 35.63046563; 36.85497738; 37.38435036; 37.6705848; 38.52074386;...
96 64.21167368; 65.95434782; 66.68788416; 67.08320061; 67.8392827;...
97 103.9354251; 106.0792914; 106.9719422; 107.4536599; 108.5700471;...
98 156.9526303; 159.4462802; 160.4785104; 161.0361007; 162.1329932;...
99 0];
100
101 % Q16 evaluated at specific point
102 Q16f = scatteredInterpolant(sample_angle ,sample_vf ,Q16 , 'natural' );
103 Q16p = Q16f(angle ,geovf );
104
105 % Q26 component at sample points
106 Q26 = [94.45572359; 53.586653; 37.72228105; 29.37832555; 2.126338777;
107 385.7310015; 238.1309603; 182.6381857; 153.6197817; 61.09990678;
108 817.7957157; 566.180779; 472.0065788; 422.847041; 264.5262469;
109 1400.155219; 1064.897203; 939.5370039; 874.0976941; 661.58523;
110 2122.284133; 1730.624435; 1584.123631; 1507.622733; 1256.126908;
111 2957.23108; 2535.143425; 2377.252404; 2294.783534; 2020.772305;
112 3874.765462; 3443.414804; 3282.124571; 3197.887098; 2914.726028;
113 4845.995226; 4420.651155; 4261.816407; 4178.896024; 3897.288247;

```

```
114 0];
115
116 % Q26 evaluated at specific point
117 Q26f = scatteredInterpolant(sample_angle, sample_vf, Q26, 'natural');
118 Q23p = Q26f(angle, geovf);
119
120 % Q matrix formation at specific point
121 Qp = [Q11p, Q12p, Q16p; Q12p, Q22p, Q23p; Q16p, Q23p, Q66p];
122
123 cn = cosd(-angle/2);
124 sn = sind(-angle/2);
125
126 Mn = [cn*cn, sn*sn, 2*cn*sn; sn*sn, cn*cn, -2*cn*sn; -cn*sn, cn*sn, (cn*cn)-(sn*
      sn)];
127
128 % Rotation of the matrix
129 Q = Mn*Qp*Mn';
130 end
```

Appendix B

Appendix B

B.1 Lamina results for zipper cuts

The lamina results for zipper cuts are presented in this section. The lamina results were generated for two material sets Material 1 and Material 2. The results for Material 1 are presented in Figure [B.1-B.4](#) and the results for Material 2 are presented in Figure [B.5-B.8](#)

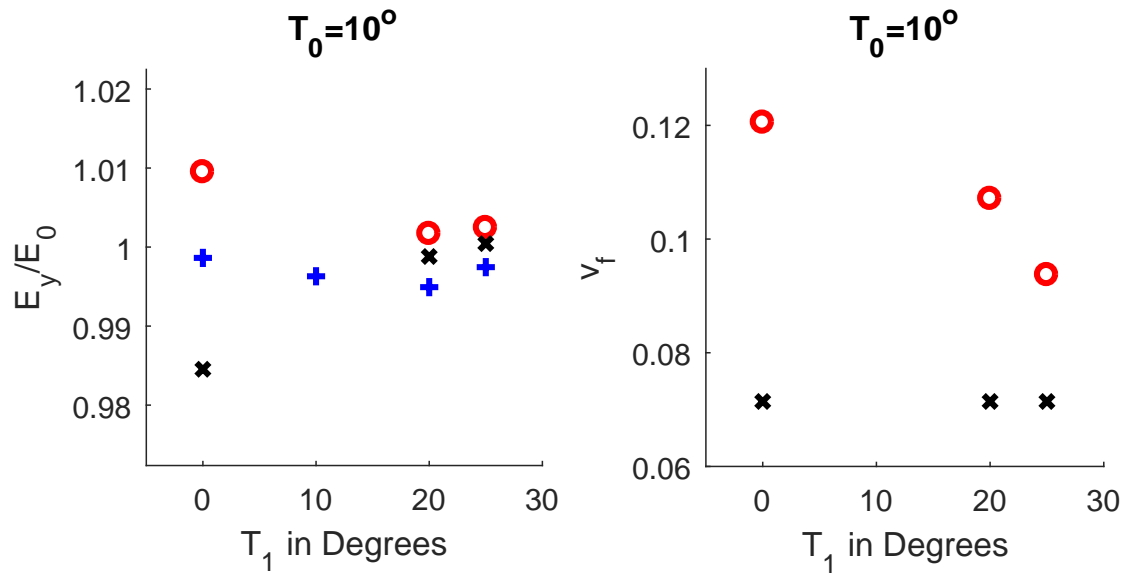
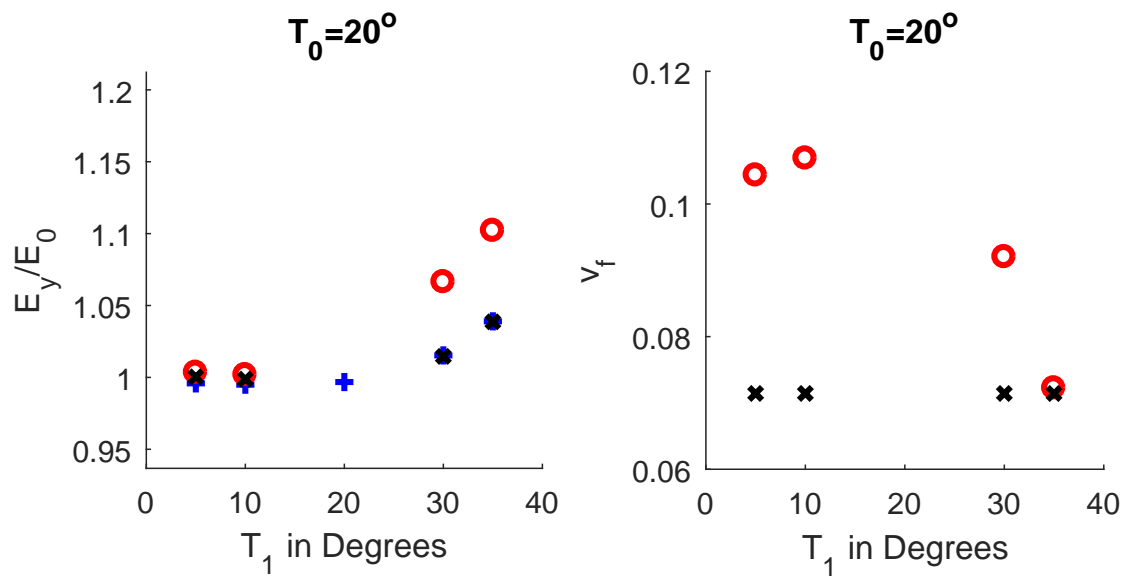
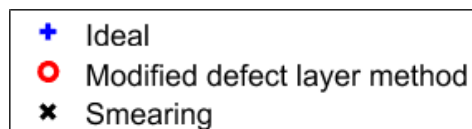
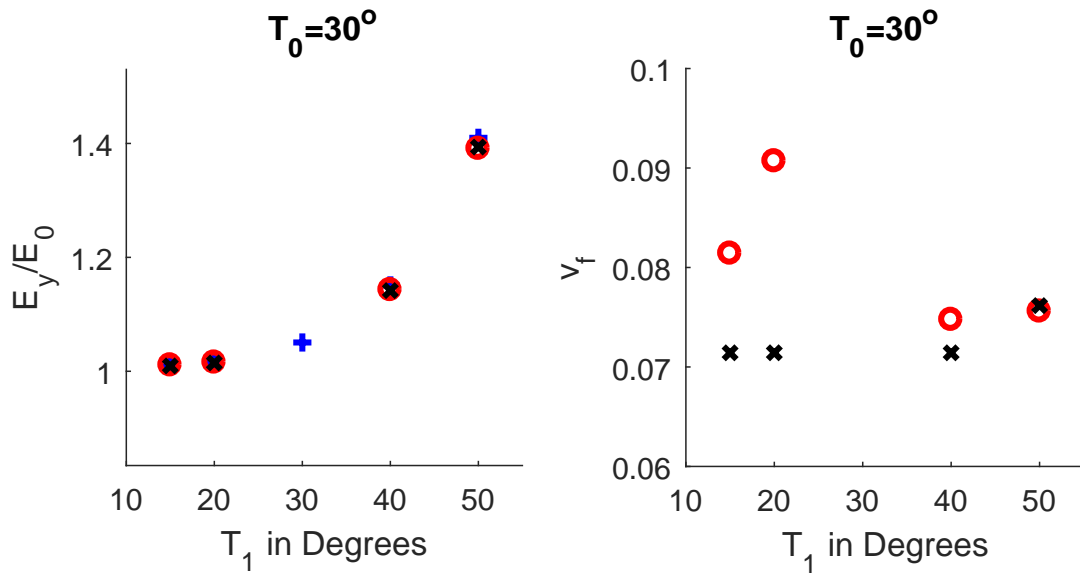
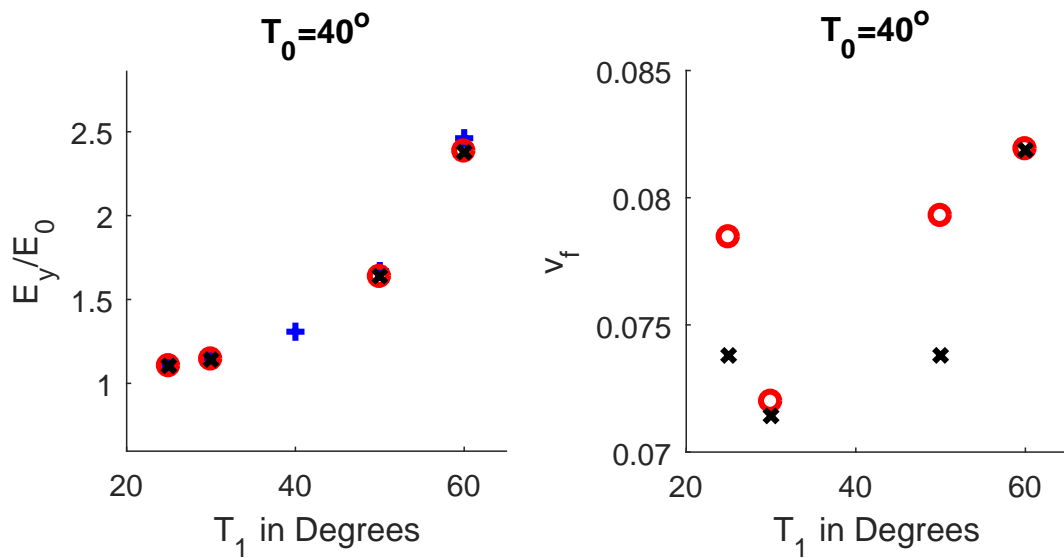
(a) $T_0 = 10^\circ$ (b) $T_0 = 20^\circ$ 

Figure B.1: Zipper Cuts (Material 1): Results of normalized elastic modulus (E_y/E_0) and volume fraction of tow drop defect (v_f) obtained from the modified defect layer method and smearing methodology for plies with center angle $T_0 = 10^\circ$ and $T_0 = 20^\circ$ and for various edge angle T_1 .



(a) $T_0 = 30^\circ$



(b) $T_0 = 40^\circ$

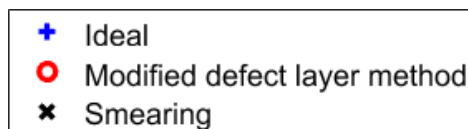


Figure B.2: Zipper Cuts (Material 1): Results of normalized elastic modulus (E_y/E_0) and volume fraction of tow drop defect (v_f) obtained from the modified defect layer method and smearing methodology for plies with center angle $T_0 = 30^\circ$ and $T_0=40^\circ$ and for various edge angle T_1 .

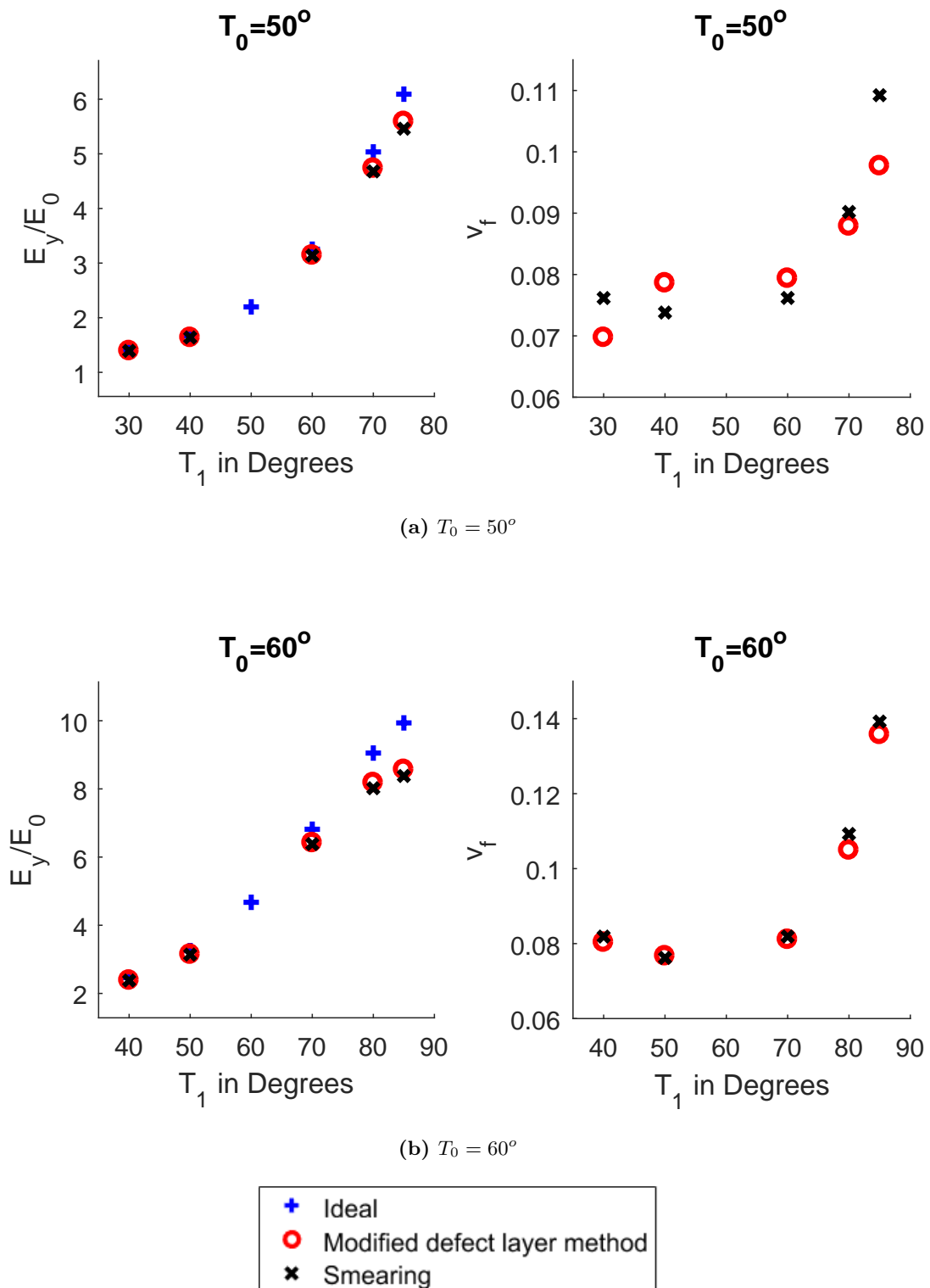
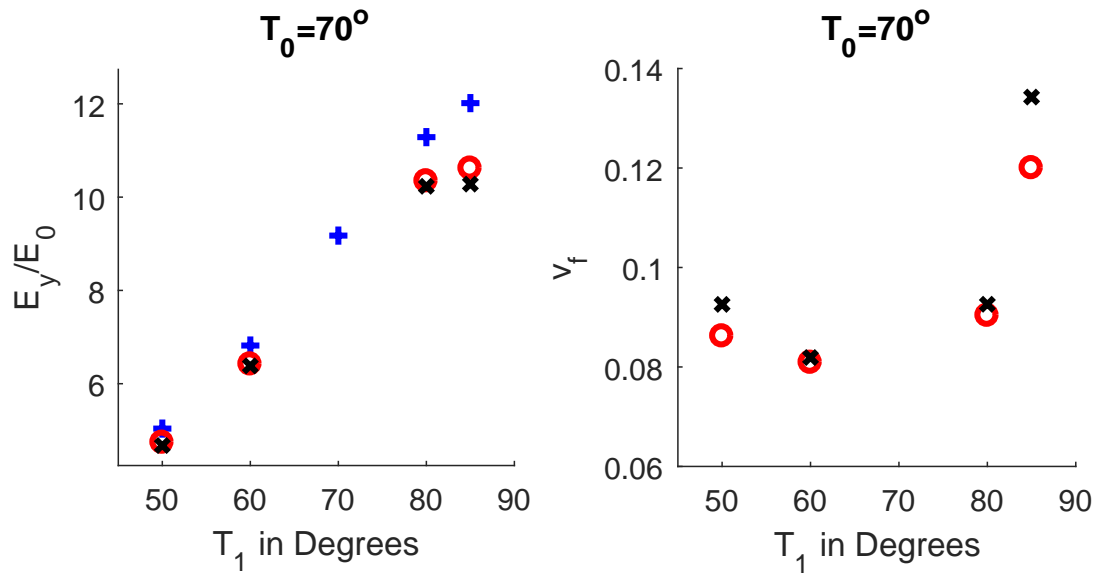
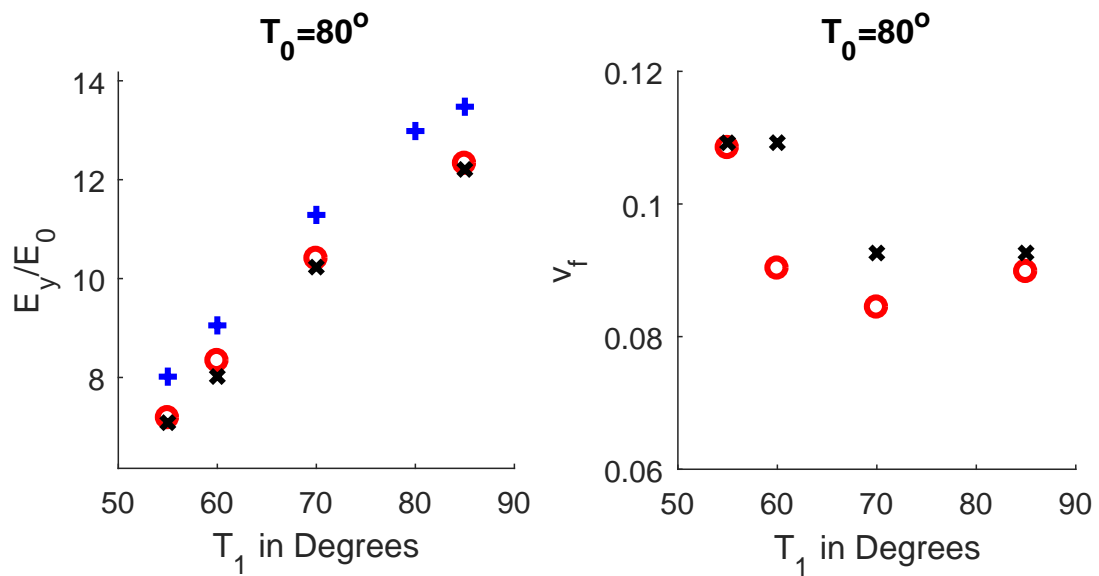


Figure B.3: Zipper Cuts (Material 1): Results of normalized elastic modulus (E_y/E_0) and volume fraction of tow drop defect (v_f) obtained from the modified defect layer method and smearing methodology for plies with center angle $T_0 = 50^\circ$ and $T_0=60^\circ$ and for various edge angle T_1 .



(a) $T_0 = 70^\circ$



(b) $T_0 = 80^\circ$

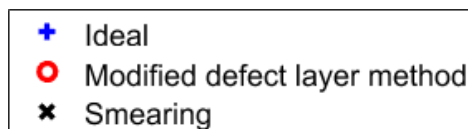
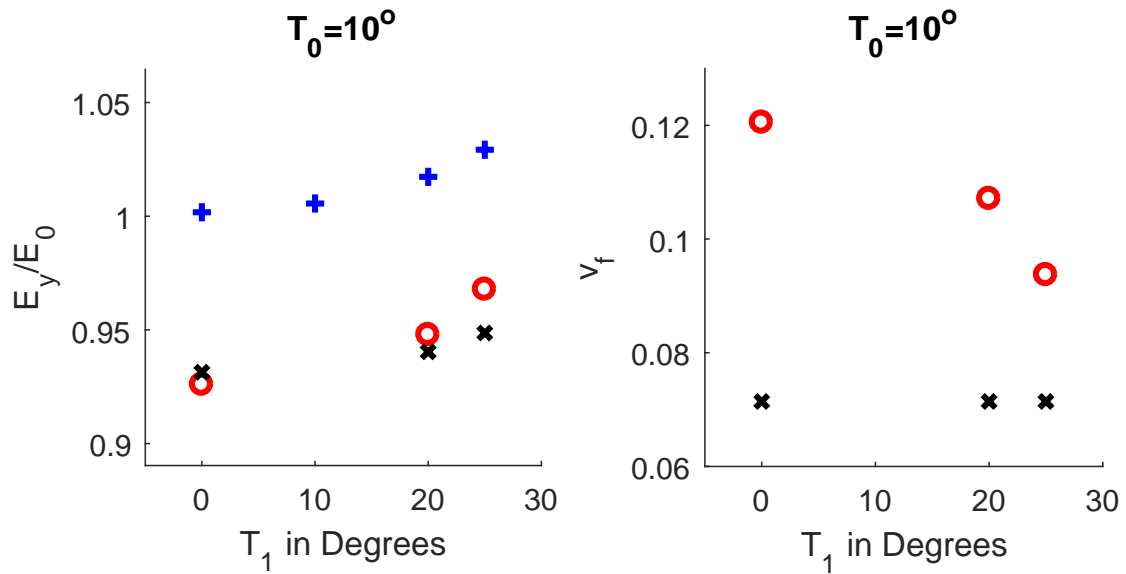
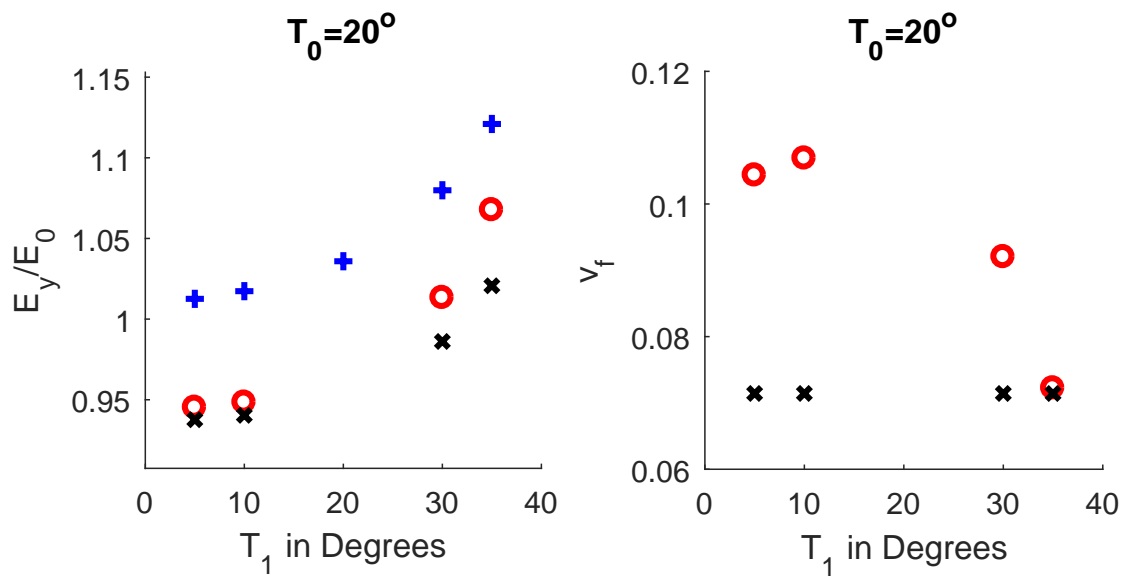


Figure B.4: Zipper Cuts (Material 1): Results of normalized elastic modulus (E_y/E_0) and volume fraction of tow drop defect (v_f) obtained from the modified defect layer method and smearing methodology for plies with center angle $T_0 = 70^\circ$ and $T_0=80^\circ$ and for various edge angle T_1 .



(a) $T_0 = 10^\circ$



(b) $T_0 = 20^\circ$

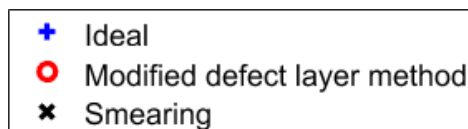
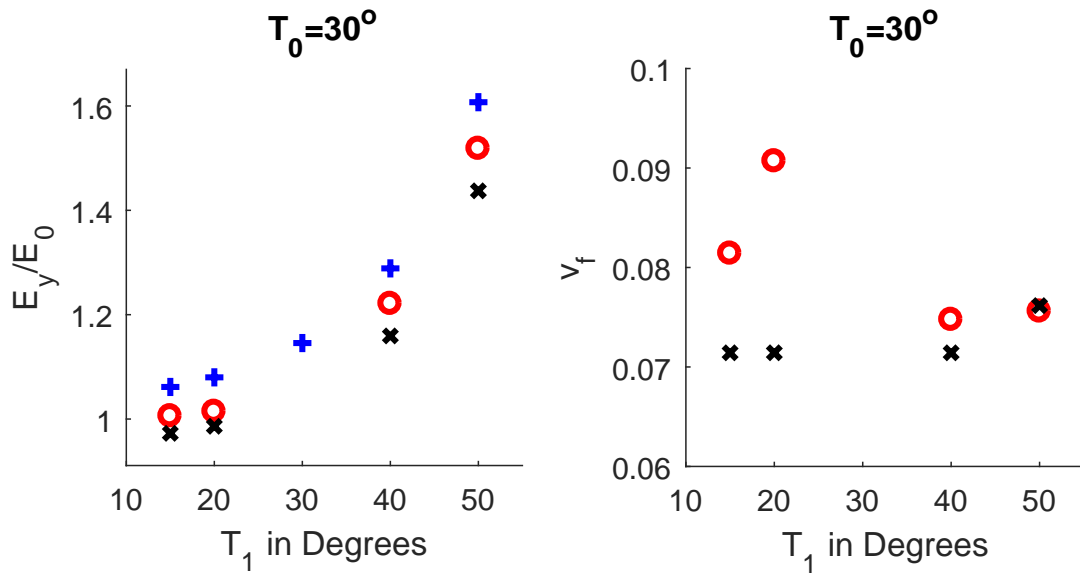
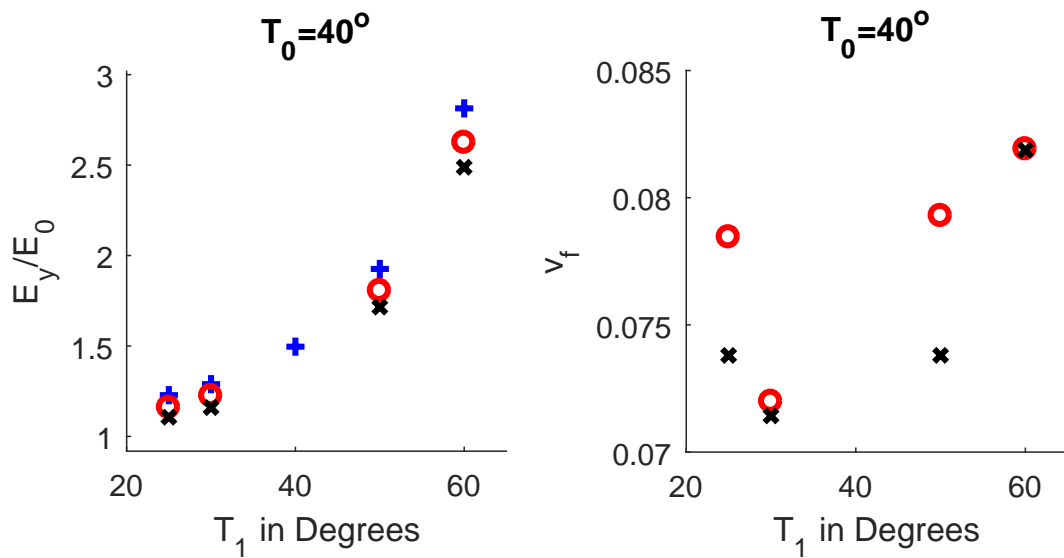


Figure B.5: Zipper Cuts (Material 2): Results of normalized elastic modulus (E_y/E_0) and volume fraction of tow drop defect (v_f) obtained from the modified defect layer method and smearing methodology for plies with center angle $T_0 = 10^\circ$ and $T_0=20^\circ$ and for various edge angle T_1 .



(a) $T_0 = 30^\circ$



(b) $T_0 = 40^\circ$

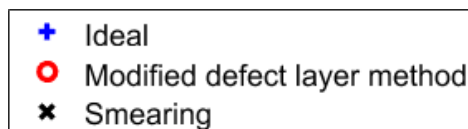
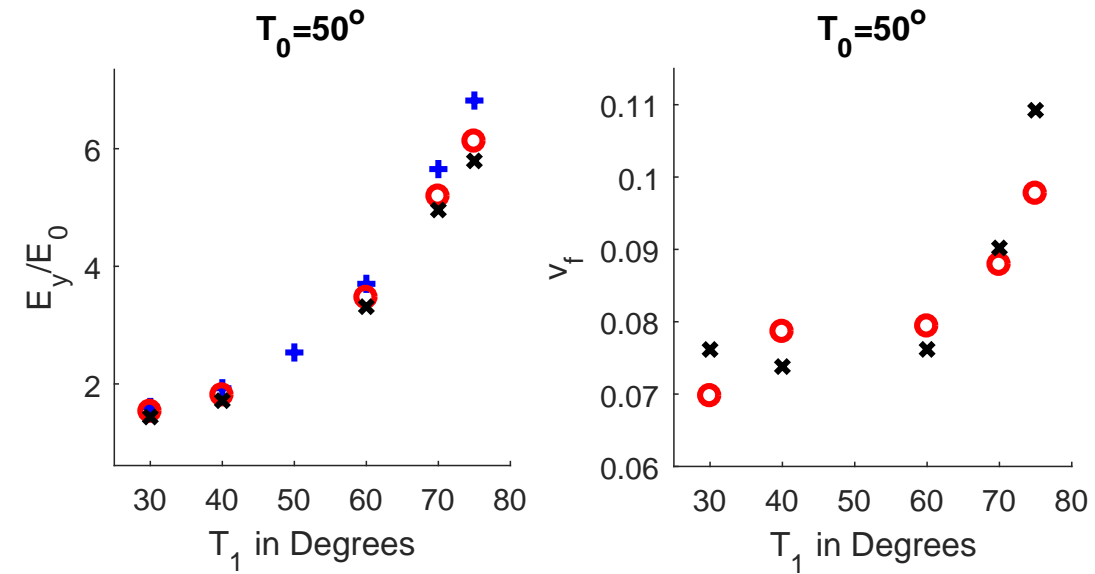
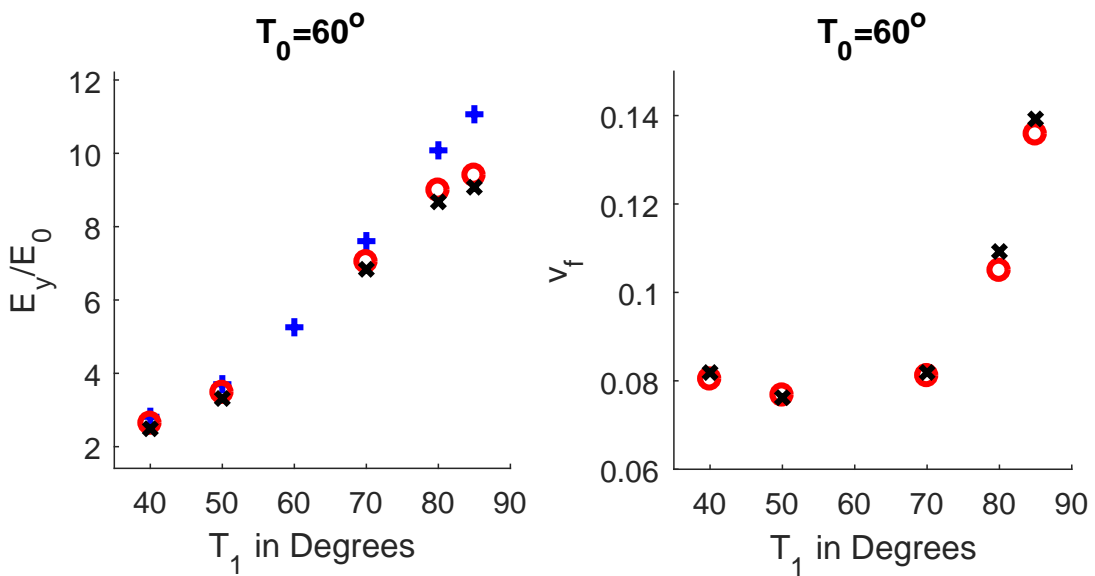


Figure B.6: Zipper Cuts (Material 2): Results of normalized elastic modulus (E_y/E_0) and volume fraction of tow drop defect (v_f) obtained from the modified defect layer method and smearing methodology for plies with center angle $T_0 = 30^\circ$ and $T_0=40^\circ$ and for various edge angle T_1 .



(a) $T_0 = 50^\circ$



(b) $T_0 = 60^\circ$

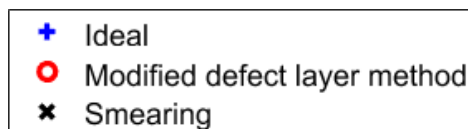
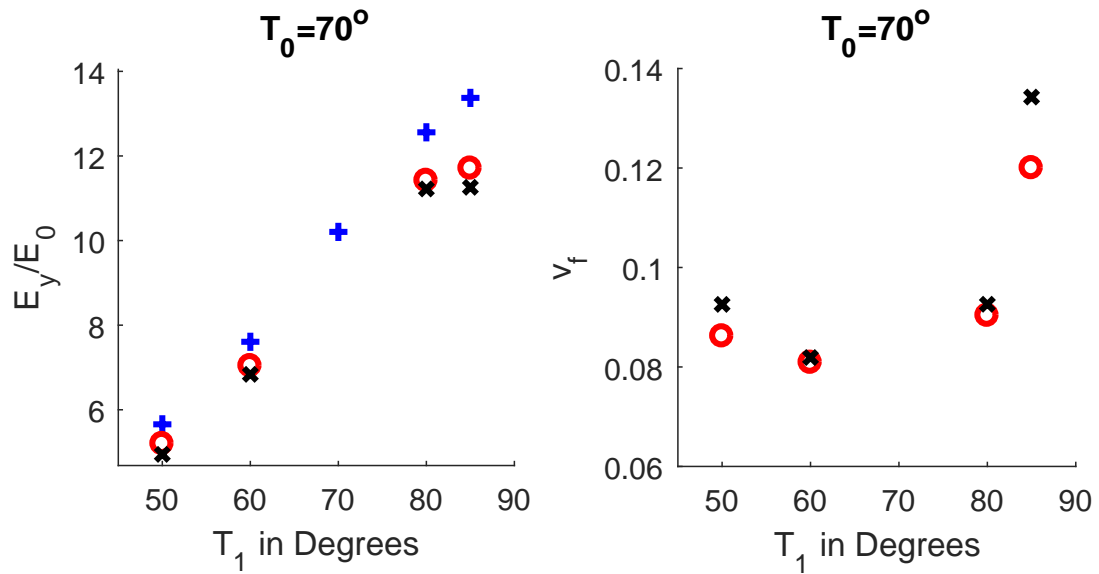
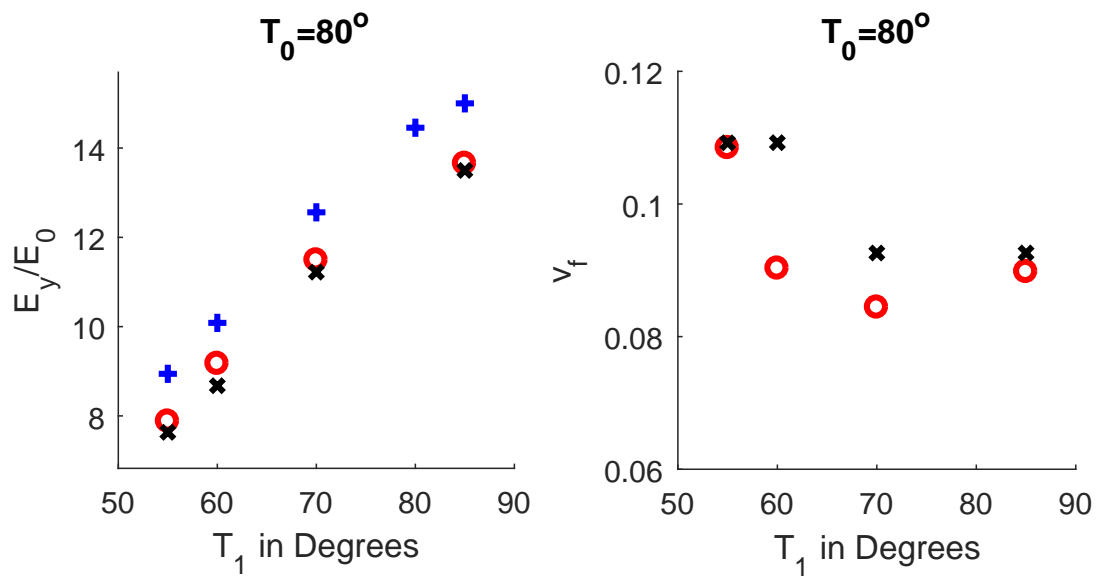


Figure B.7: Zipper Cuts (Material 2): Results of normalized elastic modulus (E_y/E_0) and volume fraction of tow drop defect (v_f) obtained from the modified defect layer method and smearing methodology for plies with center angle $T_0 = 50^\circ$ and $T_0=60^\circ$ and for various edge angle T_1 .



(a) $T_0 = 70^\circ$



(b) $T_0 = 80^\circ$

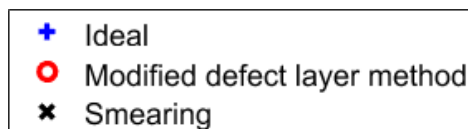


Figure B.8: Zipper Cuts (Material 2): Results of normalized elastic modulus (E_y/E_0) and volume fraction of tow drop defect (v_f) obtained from the modified defect layer method and smearing methodology for plies with center angle $T_0 = 70^\circ$ and $T_0 = 80^\circ$ and for various edge angle T_1 .